SYNOPTIC-SCALE DYNAMICS AND MODELING OF EXTREME PRECIPITATION EVENTS IN KENYA

Zur Erlangung des akademischen Grades eines
DOKTORS DER NATURWISSENSCHAFTEN

von der KIT-Fakultät für Physik
des Karlsruher Instituts für Technologie (KIT)

genehmigte
DISSERTATION

von
MSc. Joseph Karianjahi Njeri
aus Kahuro, Muranga County,
Kenia

Datum der mündlichen Prüfung: 17.05.2019
Referent: Prof. Dr. Andreas H. Fink
Korreferent: Prof. Dr. Peter Knippertz

Abstract

Extreme and contiguous precipitation events over Kenya are usually catastrophic leading to loss of lives, destruction of infrastructure and impact food security. This work documents synoptic-scale dynamics of these events using case studies with a view to understanding their initiation, evolution and dissipation including representation in models that resolve convection explicitly. As such, various data platforms are used ranging from satellite-based products e.g. TRMM-3B42, CALIPSO/CloudSat overpasses, Advanced Microwave Sounding Unit (AMSU) and Microwave Humidity Sounder (MHS) and SEVIRI Infrared brightness temperatures at 10.8μ (BT) as well as surfaces rain-gauges, Meteorological Terminal Air Report (METAR) and the European Center for Medium Range Weather Forecasts (ECMWF) reanalysis products. The latter is used to diagnose the synoptic-scale dynamics of extreme precipitation events. A convection-permitting model known as the ICOsahedral Nonhydrostatic modelling framework (ICON) is used to simulate these events.

Atmospheric preconditions to deep moist convection and viability of the ICON nested set-up to represent the 24-hour accumulated precipitation between 0600–0600 UTC (A06) were the main goals of this work. Three cases were chosen based on an objective method that compared the extremity and contiguity of a precipitation event from both satellite and surface observations where agreement between both observations was strictly required. However, where this agreement was not attainable especially due to scarcity of surface observations, satellite-based observations were adopted. The first and the second cases were selected from the Coastal and Lowlands regions of Kenya on 14 May 2007 and 29 October 2011 respectively while the third case was selected from the Central Highlands of Kenya on 29 December 2012.

The Coastal and Lowlands cases were found to be dynamically similar in that they were found to have been associated with large-scale atmospheric processes. The events appeared to have been either initiated or amplified by a superposition between a Kelvin wave and an equatorial Rossby wave creating a low pressure system. In contrast, the Central Highlands case appeared to have been a locally forced system characterised by intense daytime heating that created a low pressure system. The low pressure system observed from all cases induced low-level winds towards the region resulting in convergence that promoted the ascent of air to the Level of Free Convection (LFC).

Within the limitations of ERA5 data in terms of reproducing thermodynamic instabilities and local forcings, the atmosphere appeared to have been conditionally unstable in all the cases studied. This was inferred from the high amounts of warm and unsaturated air in the lower levels of the atmosphere advected from the anomalously warm ocean requiring just a trigger mechanism to release instability. Indeed, a moisture flux between the surface and the mid-levels advected sufficient moisture promoting accumulation of total column water that surpassed the 98^{th} percentile. The persistent moisture flux aided the longevity of the event for hours. For the Lowlands and Central Highlands cases, frictional convergence was found to have played a key role while for the Central Highlands case, orographic lifting was found to have been the major dynamic process that rendered the warm and unsaturated parcels in the lower levels positively buoyant.

This study revealed the underestimation of upward and downward motion by ERA5 reanalysis model where Convective Available Potential Energy (CAPE) amounts were largely underestimated. However, CAPE anomalies in the period 1979–2018 revealed that for these events, CAPE was anomalously higher relative to climatology of ERA5. A Lagrangian analysis of moisture in all cases indicated that moisture uptake took place in the neighbouring anomalously warm western equatorial Indian Ocean. This analysis further revealed the role of diabatic processes in the development and growth of the convective systems through the exchange of moisture between the Ocean and the atmosphere leading to release of instability over the region.

The convection-permitting ICON model, however, could not adequately represent A06 in all cases as it produced very intense but isolated convection. However, the model reproduced the location of the precipitation object to a considerable degree of skill. Representation of Cloud Top Temperatures (CTT) observed from satellite failed as well with the model producing too warm clouds with temperatures above 250 K during the time window of the most intense convection. This was partly attributed to the quality of initial data from ECMWF in forcing the model. It is suggested that, perhaps with a higher quality initial and boundary data, the results might improve. It is therefore left as an open question and perhaps a future endeavor, whether a different ICON model set-up would greatly improve the results.

Contents

Acronyms

A06	24-hour accumulated precipitation between 0600–0600 UTC
AEW	African Easterly Waves
AFSS	Asymptotic Fractions Skill Score
AMSR-E	Advanced Microwave Scanning Radiometer for Earth Observing Systems
AMSU	Advanced Microwave Sounding Unit
AMSU-B	Advanced Microwave Sounding Unit - B
Apr.	April
Aug.	August
BT	SEVIRI Infrared brightness temperatures at 10.8μ
C3S	Copernicus Climate Change
CALIOP	Cloud-Aerosol Lidar with Orthogonal Polarization
CALIPSO	Cloud-Aerosol Lidar and Infrared Pathfinder Satellite Observations
CAPE	Convective Available Potential Energy
CCKWs	Convectively Coupled Kelvin Waves
CCL	Convective Condensation Level
CIN	Convective Inhibition
CLAAS	CLoud property dAtAset using SEVIRI
CM-SAF	Satellite Application Facility on Cloud Monitoring
CMORPH	NOAA Climate Prediction Center Morphing Technique Global Precipitation Analyses
CMPI5	Coupled Model Intercomparison Project phase 5
CP	Convection-Permitting

CPR	Cloud Profiling Radar
CTT	Cloud Top Temperatures
DAAD	Deutscher AkademischerAustauschdienst
Dec.	December
DJF	December-January-February
DREF	Disaster Relief Emergency Fund
DWD	Deutscher Wetterdienst
ECDF	Empirical Cumulative Distribution Function
ECMWF	European Center for Medium Range Weather Forecasts
EDA	Ensemble of Data Assimilation
EEA	Equatorial East Africa
EIG	Eastward Inertio Gravity waves
EL	Equilibrium Level
ENSO	El-niño Southern Oscillation
ER	Equatorial Rossby
ERA5	European Center for Medium Range Weather Forecasting Version 5
ERAI	ECMWF Reanalyses Interim
EU	European Union
EUMETSAT	EUropean Organisation for the Exploitation of MEteorological SAtellites
Feb.	February
FSS	Fractional Skill Score
GCM	Global Climate Model
GCMs	Global Climate Models
GDP	Gross Domestic Product
GPM	Global Precipitation Mission
HT	Latent heat
ICON	ICOsahedral Nonhydrostatic modelling framework
IFRC	International Federation of Red Cross and Red Crescent Societies
IFS	Integrated Forecast System

IOD	Indian Ocean Dipole
IODM	Indian Ocean Dipole Mode
IODMI	Indian Ocean Dipole Mode Index
IPCC	Intergovernmental Panel on Climate Change
IR	Infrared
ITCZ	Inter-Tropical Convergence Zone
Jan.	January
Jul.	July
Jun.	June
KASS-D	Karlsruhe African Surface Station Database
KMS	Kenya Meteorological Services
KRCS	Kenya Red Cross Society
LAGRANTO	Lagrangian Analysis Tool
LCL	Lifting Condensation Level
LFC	Level of Free Convection
LNB	Level of Neutral Buoyancy
LSB	Land-Sea Breeze
MAM	March-April-May
Mar.	March
MCS	Mesoscale Convective Systems
METAR	Meteorological Terminal Air Report
MGIR	Merged Geo-Infrared
MHS	Microwave Humidity Sounder
MJO	Madden Julian Oscillation
MPI-M	Max-Planck Institute for Meteorology in Hamburg
MRG	Mixed-Rossby-Gravity Waves
MRG	mixed Rossby-gravity
MSE	Moist Static Energy
MSG	Meteostat Second Generation
MSL	Mean Sea Level
MSLP	Mean Sea Level Pressure

N–S	North – South
NACOSTI	National Commission for Science, Technology and Innovation
NCAR	National Center for Atmospheric Research
NE	North Easterlies
NOAA	National Oceanic and Atmospheric Administration
Nov.	November
NWP	Numerical Weather Prediction
Oct.	October
OND	October-November-December
PCA	Principal Component Analysis
PR	Precipitation Radar
RCM	Regional Climate Model
RH	Relative Humidity
RMM1	Real-time Multivariate MJO series 1
RMM2	Real-time Multivariate MJO series 2
RRTM	Rapid Radiative Transfer Model
SAL	Structure-Amplitude-Location
SE	South Easterlies
Sep.	September
SEVIRI	Spinning Enhanced Visible and Infrared Imager
SP	Surface Pressure
SSMI	Special Sensor Microwave Imager
SSMIS	Special Sensor Microwave Imager/Sounder
SST	Sea Surface Temperatures
TD	Tropical Disturbance
TEJ	Tropical Easterly Jet
TMI	TRMM Microwave Imager
TMPA	TRMM Multi-Satellite Precipitation Analysis
TRMM	Tropical Rainfall Measuring Mission
UNHCR	United Nations High Commissioner for Refugees
VIRS	Visible Infrared Scanner

WIG	westward propagating inertio-gravity
WMO	World Meteorological Organization
WS1	Deep convective clouds
WS2	Relatively deep convective clouds
WS3	Shallow clouds
WS4	Convectively suppressed weather state

List of Symbols

$\bar{x}$	21-day precipitation mean centered on event date
$\Delta\bar{x}$	Domain spatial resolution
$\Delta\bar{x}$	Effective mesh size of the ICON model
Δt	Domain temporal resolution
η	Absolute vorticity
κ	Ratio of R to c_p
κ_d	κ for dry air
$\mathbf{V}$	wind vector
ω	Vertical velocity
ϕ	Spectral response of an instrument
π	Exner function in ICON
ρ	Density
θ	Potential temperature
θ_e	Equivalent potential temperature
θ_e^*	Saturated equivalent potential temperature
θ_L	Estimated dry potential temperature at LCL
θ_v	Virtual potential temperature
ζ	Relative vorticity
B	Radiance
c_i	Conditional instability
c_p	Specific heat capacity at constant pressure
c_{pd}	Specific heat capacity of dry air at constant pressure
D	Wind divergence

D_{mod}	Domain area of precipitation in the model
D_{obs}	Domain area of precipitation in observations
e	Vapour pressure
e_s	Saturation vapour pressure
f_0	Frequency of observations
f_m	Frequency of forecast
F_w	Vertically integrated moisture flux divergence
f_q	Observed fractional quantity coverage over a domain
g	Acceleration due to gravity
gz_{700}	Geopotential height at 700 hPa
h	Height
h_s	Height at 2m above the surface
h^*_{700}	Saturated MSE at 700 hPa
i	index (count)
k	Number of bisection steps
K_h	Horizontal component of the kinetic energy
k_λ	wave number
L_1	Normalized distance between the centres of mass of modeled and observed precipitation fields while computing SAL
L_2	Discriminant for overlapping precipitation patterns with the same centre of mass while computing SAL
l_e	Equilibrium level
l_f	Level of free convection
L_{ss}	Spatial scale skill score
L_v	Latent heat of vapourisation
n	Last contributing time step to a calculation
n_c	Number of cells
n_d	Distance from the centre of mass
n_e	Number of edges
N_l	Length of the largest side in a domain in calculation of FSS

p	Pressure
p_0	Initial Pressure
Q	Dynamical quantity
q	Specific Humidity
q_{2m}	Specific humidity at 2m above the surface
q^*_{700}	Saturated specific humidity at 700 hPa
$Q^{'}_t$	Anomaly from the mean
R	Specific gas constant for air
r	Mixing ratio of water vapour
R_d	Specific heat capacity for dry air
r_e	Radius of the earth
R_b	Plank function
R_{rad}	Observed radiance
R_{thresh}	Precipitation threshold upon which precipitation patterns are curved
sfc	Surface
$Shear_{deep}$	Wind shear between the surface and 200 hPa
$Shear_{shallow}$	Wind shear between the surface and 500 hPa
T	Temperature
t	Time
T_d	Dew point temperature
T_L	Estimated temperature at LCL
T_{2m}	Temperature at 2m above the surface
T_{700}	Temperature at 700 hPa
T_b	Equivalent brightness temperature
u	Zonal component of wind
v	Meridional component of wind
v_c	Central wave number
v_h	Horizontal wind component in ICON
v_n	Horizontal velocity component normal to the triangle edges

v_t	Reconstructed tangential velocity component
V_{mod}	Scaled volume in the model
V_{obs}	Scaled volume in the observation
w	Vertical wind component
x	Precipitation variable
x_i	Precipitation at time step i
x_{anom}	Deviation from the mean
x_{case}	0600 to 0600 UTC accumulated precipitation during day of event
x_{ex}	Precipitation exceedance from a given percentile
x_{per}	A given percentile

Chapter 1

Introduction and motivation

Precipitation is a major driver for East African economies and Kenya in particular. In fact, the latter's major economic activity is agriculture which determines to a considerable extent, the Gross Domestic Product (GDP). As such, understanding the dynamical characteristics of precipitation from formation, growth, maturity to dissipation, is important for near-accurate real time forecasting. Statistical forecasting of seasonal rainfall over East Africa which is carried out at regional levels (Chen and Georgakakos, 2015) can be complemented by a sound dynamical approach which this work attempts to achieve through case diagnosis.

Extreme precipitation events are usually catastrophic over Kenya. They cause major damage to infrastructure, crops and usually result into major humanitarian crisis with cases of homes being swept away by raging flood waters among other consequences (figure 1.1a-1.1e). It is noteworthy that reproduction of extreme precipitation in dynamical models especially over east Africa has been an ongoing process. Efforts of complementing the statistical approaches to seasonal prediction of precipitation by use of a dynamical approach has been made (Satti et al., 2017; Endris et al., 2013) while understanding of the representation of diurnal cycle of extreme convection over Lake Victoria using a 4 Km convection-permitting model has been attempted (Woodhams et al., 2018). Nonetheless, more work still needs to be done to improve the already available infrastructure.

Extreme weather events (droughts and floods) have always wreaked havoc Kenyan communities especially those who live in lowland areas and areas near large-water bodies (FEWSNET, 2011). The drought situation in Kenya seems to be a recurring affair according to media reports, with dozens of people within various parts of Kenya succumbing to the March 2019 drought. In fact, there has been a decline in the amount of seasonal precipitation over the years over east Africa especially during the March to May season (Lyon, 2014; Lyon and DeWitt, 2012; Williams and Funk, 2011). Reasons advanced for this general drying trend include the decadal variability of the Indo-Pacific warm pool and Walker circulation due to shifts of sea surface temperatures over the Pacific. It is peculiar to highlight that since Kenya lies within the deep tropical belt, the expectation is that precipitation should be as much as in other tropical areas e.g. over the Amazon and over the equatorial Congo forest. This is usually not the case for reasons elucidated under section 3.4.

The events such as the 1997/98 El-Ninõ event (Indeje et al., 2000) and the May 2007 heavy precipitation event over the Kenyan coast whose characteristics are analysed and documented in a subsequent section are few of the cases where the motivation to investigate and document the dynamical characteristics of extreme precipitation events is derived. In

Figure 1.1: *Some of the effects of extreme precipitation over Kenya in April 2018. a) A vehicle swept away by raging floods in Mandera County, Northern Kenya. b) A submerged refugee camp in eastern Kenya. c) Crops destroyed by flash floods as families are rescued. d) Infrastructural damage caused by floods in Northern Kenya rendering roads impassable and e) A highway submerged by floods in Nairobi (source: Kenya Red Cross official twitter page).*

fact, there is a general agreement in model simulations from the Intergovernmental Panel on Climate Change (IPCC) Fourth Assessment Report (AR4) and from the Coupled Model Intercomparison Project phase 5 (CMPI5)(Taylor et al., 2012) that there is going to be an increase in precipitation over east Africa in the coming years under a warming climate implying Kenyan rains (which are usually embedded within the Inter-Tropical Convergence Zone (ITCZ)), will become more enhanced (Held and Soden, 2006).

Apparently, there appears to be minimal studies over Kenya on dynamical characteristics associated with extreme precipitation events. Most studies which exists are mainly focused on seasonal to annual precipitation variability (Ogallo, 1989, 1988; Okoola, 1999a; Okoola et al., 2008; Camberlin and Philippon, 2002; Hastenrath, 2000; Yang et al., 2015) with few studies focussing on intraseasonal characteristics of precipitation and their predictability (Gitau et al., 2013). The plausible reason for this seasonal-scale research bias is because the most important meteorological information is precipitation as it drives the agricultural agenda.

Occurrence of major extreme precipitation events is much more pronounced during both the long (March-April-May (MAM)) and the short (October-November-December (OND)) rainy seasons. Through organisation of the low level flow, high amounts of warm and moist air from the Indian Ocean as well as from the Congo can be advected to the region initiating deep convection especially over the highlands which act as trigger mechanisms through the lifting of air to the Level of Free Convection (LFC). Further lifting and pronounced condensation leads to deep moist convection resulting in enhanced rains over these regions.

Numerical studies by Mukabana and Piekle (1996) provided a ground upon which understanding of diurnal cycle of convection over Kenya can be understood. The studies opined that more active convection develops in regions where the large-scale monsoonal winds in the lower troposphere converges with the local mesoscale circulations embedded in the large-scale flow. Large-scale flow advects more moisture inland as compared to mesoscale flow implying more moisture is transported to the region by the monsoon winds from the Indian Ocean. Large-scale monsoon flow usually controls the locations and movement of the convergence/precipitating zones over Kenya. As for topography, Mukabana and Piekle (1996) found that it has a significant impact on the diurnal precipitation pattern over the country through the generation of anabatic-katabatic winds with a strong diurnal cycle. Topography also modifies the large-scale temperature, moisture, and wind flow as well as inhibiting a substantial amount of the moisture-laden monsoonal winds from reaching farther inland. The numerical studies also found that large water bodies, e.g. Lake Victoria, Lake Turkana and the Indian Ocean, usually create strong Land-Sea Breeze (LSB) circulations with an intense diurnal cycle that contributes to the overall precipitation pattern in Kenya. Thus both large-scale monsoonal and mesoscale circulations are important components of the diurnal rainfall regime over the country.

During the Short Rains, there exists an outstanding zonal-vertical circulation cell over the equatorial Indian Ocean that is usually absent during the Long Rains season (Mutai and Ward, 2000; Hastenrath et al., 2011; Mutai et al., 2012). During the end of the Long Rains season, the upper level easterlies (usually at 200 hPa) are relatively weak. The Long Rains season tends to benefit from a south easterly flow from the neighbouring Indian Ocean advecting warm and moist air from the western Indian Ocean.

Surface winds are generally convergent over the coastlines but divergent inland due to the easterly acceleration when going through the Turkana channel (Yang et al., 2015). During extremely wet seasons, a local cyclonic circulation centered around 5°S, 35E° at the 700 hPa level exists with low wind intensities which extends to the western Indian Ocean where they pick up moisture and transport it inland. Southerlies from the Mozambique channel tend to promote the surge of cold air equatorward (Okoola, 1999b).

It is not lost to many Kenyans as well as their east African neighbours of the destructive nature of the 1997/1998 El-Ninõ event that brought misery-inflicting floods and the drought episodes associated with the 1999 La-Ninã event (Ngecu and Mathu, 1999; Indeje et al., 2000). The biggest impact of the El-Ninõ event of 1997/98 was felt by maize farmers as the crop yield during the season of October to mid February (Short Rains season) dropped drastically by a record 65% (Karanja and Mutua, 2000). The severe floods caused loss of life through landslides and drowning, damage to housing and infrastructure including contributing to the outbreak of Rift-Valley fever after Dec. 1997 among other damaging impacts (Odada and Olago, 2002). This El-Ninõ event re-energised investigations geared towards understanding its causes. Saji et al. (1999) and Webster et al. (1999) brought to the fore the circulation anomaly characteristics in the east and west of the equatorial Indian Ocean as one of the primary factors contributing to these events.

It is therefore not trivial to undertake research leading to the understanding and prediction of extreme precipitation events especially over the tropics since they have devastating impacts. The understanding is required to counter the poor representation and predictability of such events in models and against a data-sparse continent. The precursors gathered in such research can be used for the benefit of society through calibration of regional weather and climate models to render the latter more responsive to such eventualities.

Chapter 2

Area of Study

2.1 Geographical boundaries

The area of study is Kenya located within the region 33°–42°E and 5°N–5°S of the globe and forming part of the equatorial east African region. Kenya therefore straddles the equator as shown in figure 2.1a and 2.1b. The regions of interest for this thesis namely, the Coastal Lowlands, the Lowlands and the Central Highlands are demarcated with pink, red, and blue dotted outlines respectively. The rain-gauge stations used in this study are sourced from Karlsruhe African Surface Station Database (KASS-D) and are annotated on the map and explained in figure 2.1c and Table A.1.

It is bordered by Ethiopia to the north, South Sudan to the north-west, Uganda to the west, Tanzania to the south west, equatorial Indian Ocean to the south east, and Somalia to the east. Figures 2.1a and 2.1b detail the region of study with the various physical features and relief (colors). Bordering countries are also shown in text.

2.2 Physical features

The region of study lies within the highlands and lowlands zones of East Africa. However, the greater east African region is characterized by a complex topography where land areas can rise from below 200 meters in the coastal plains to over 3000 meters above Mean Sea Level (MSL) further inland. Generally, the western and central regions of Kenya are referred to as the highlands areas as terrain over these regions rises from below 1000 meters over the lake basin to highs of between 3000 and 5000 meters within the highlands. These zones are also the most agriculturally productive with cash-crops like coffee and tea being grown by a majority of small-scale farmers. Generally, the terrain rises gradually from the east African coastline next to the western equatorial Indian Ocean in a north-westward fashion. In fact, the highest mountains over the African continent are located within the east African region e.g. Mt. Elgon (4321m), Mt. Kilimanjaro (5895m), Mt. Ruwenzori (5109m) and Mt. Kenya (5199m). The Aberdare ranges over the central highlands are located at an altitude of about 3000 meters above MSL. From the highlands, the altitude gradually drops westward towards the lake basin region to an altitude of about 1130 meters above MSL.

The Kenyan highlands are separated from the Ethiopian highlands to the north by a steep valley where wind-jets exceeding 30 m s^{-1} (and in some occasions 50 m s^{-1}) dominate. This corridor of this jet-maxima, which exist throughout the year is known as

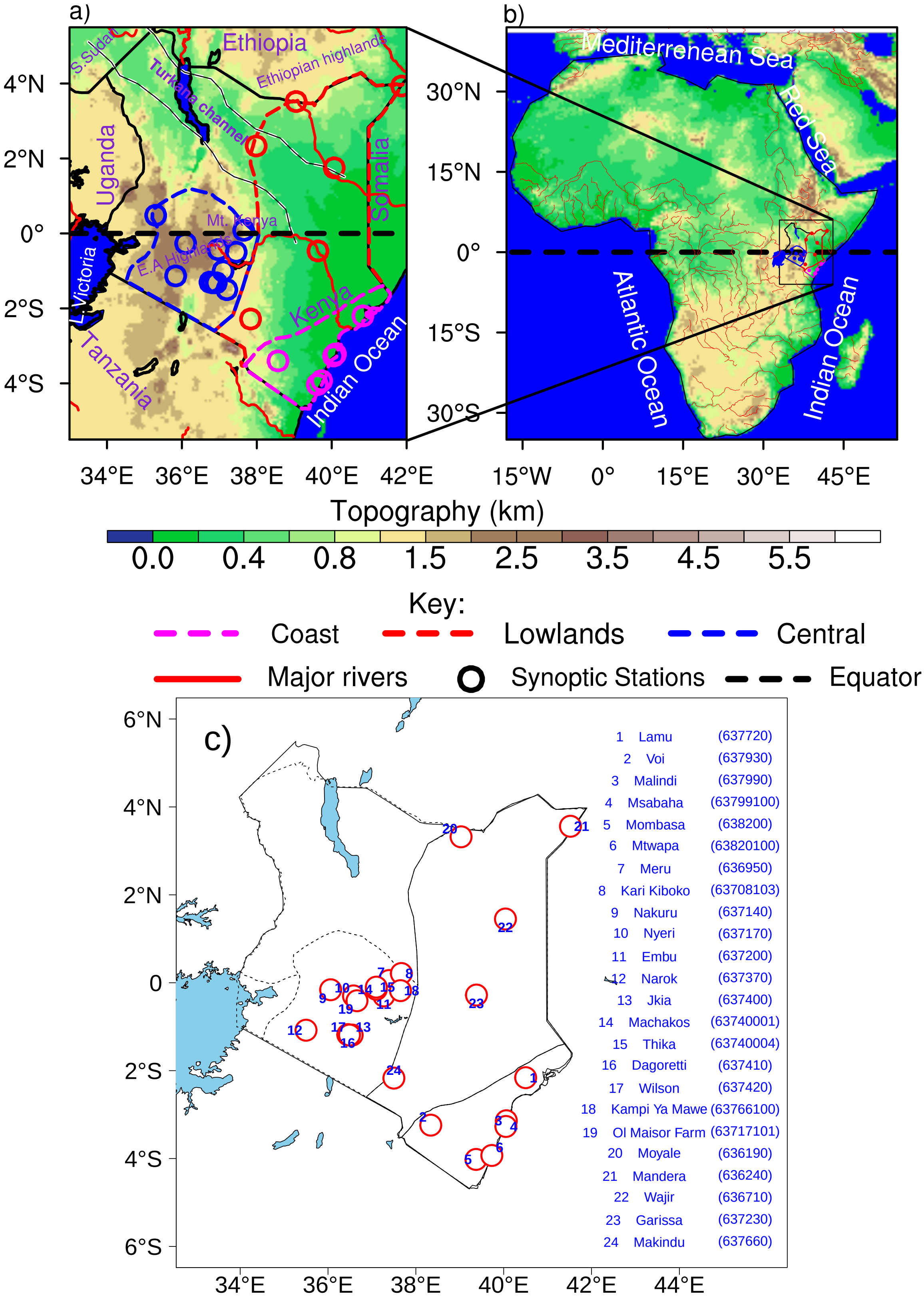

Figure 2.1: a) Area of study showing the local relief (colors) and water features (blue). The pink, red and blue dashed outlines demarcate the three regions whose extreme precipitation is diagnosed in this study namely the Coastal Lowlands, the Lowlands and the Central Highlands respectively. Also shown are the synoptic stations over the three regions used later in the study. b) A map showing the location of the study area within the African continent. c) Spatial distribution of synoptic stations shown in a) with names and IDs annotated to the right of the figure. For more details about the stations, see Table A.1. (Source: Author's analysis of KASS-D and NOAA elevation data).

the Turkana channel (Kinuthia and Asnani, 1982). The channel is shown both in text and with two purple lines in figure 2.1a.

One of the largest fresh water bodies in the world, Lake Victoria, is located within the east African region. With a surface area of about 68,800 Km^2 (Vanden and Bernacsek, 1990), this is the largest lake in Africa and the third largest in the world. The lake modulates the diurnal cycle of precipitation over the surrounding areas as has been confirmed by high resolution convection-permitting models (Woodhams et al., 2018). Towards the south-western part of Tanzania is Lake Tanganyika (not shown in figure 2.1) which is the deepest fresh water lake after Lake Baikal (Anyah et al., 2006). The presence of these large water bodies and rough terrain present a stage where local and large-scale climate drivers interplay with each other to create the variance observed in weather and climate over the region (Sun et al., 1999a,b; Anyah et al., 2006).

Orography determines the locations of the permanent and semi-permanent upper tropospheric troughs and ridges within the regime of westerlies, convective rain, development and sustainability of mesoscale circulations, blocking and channeling effects within low-level jet streams (Indeje et al., 2000). The Somali and the Turkana jets are examples of high speed low-level winds as a result of channeling effects. More about jets and other weather drivers are discussed in chapter 3.

Chapter 3

General Literature Review

3.1 Circulation mechanisms and convection

Historical observational studies over Kenya show that diurnal variation of precipitation in East Africa is largely determined by mesoscale flows and the interaction between synoptic-scale and mesoscale flows where synoptic-scale circulations interact with the local mesoscale systems to determine the location of convergence zones (figure 3.1). Large-scale monsoonal winds control the intensity, movement and locations of the convergence complexes and precipitation (Asnani and Kinuthia, 1979). Kenya is affected by two monsoon flows located over the Indian Ocean namely the south-easterly (South Easterlies (SE)) and the north easterly (North Easterlies (NE)) monsoon flows. The NE airstream occurs during the Northern Hemisphere winter (Dec.–Feb.) and has its origin over the Arabian anticyclone located over the Arabian peninsula (Trenberth, 1976). It is usually dry and warm having a slight contact with a cold ocean and a long trajectory overland. The south easterly monsoon happens during the northern hemisphere summer, emanating from the Mascarene anticyclone located over the southern Indian Ocean. Due to the long trajectory over Ocean, the current is usually cool and moist. However, this moist current does not contribute much to rainfall over Kenya as its usually diffluent over the region (Forsdyke, 1944). During the rainfall seasons (long and short seasons i.e. MAM and OND seasons respectively), there exists an intense surface heating with ITCZ exhibiting maximum influence due to the convergence of SE and NE winds over Kenya (Okoola, 1999a; Johnson, 1962).

Diurnal cycle of mesoscale circulations have been studied numerically by Mukabana and Piekle (1996). Terrain-induced mesoscale circulations caused by differential thermal heating depicted a situation where horizontal velocity convergence occur in low-elevation areas as katabatic drainage winds flow downslope from the highlands during morning hours with a corresponding low-level horizontal divergence over the highlands. The low-level horizontal convergence over low-elevated areas (e.g over Lake Victoria, Turkana channel and the Indian Ocean) result in rising motion and subsequent convective precipitation. The convergence over the lake is as a result of nonlinear interaction between two mesoscale circulations namely, the land-lake breeze and the katabatic downslope drainage winds. During afternoon hours, the situation is reversed with low-level velocity divergence occurring over the low-elevated areas and convergence over highlands. This is a result of the strong sea breeze over the coastal region coupled with the anabatic upslope winds which converge over the highlands. This mesoscale interaction (sea-breeze and anabatic flow) advects heat, moisture and momentum far inland. Thus, the highlands are usually

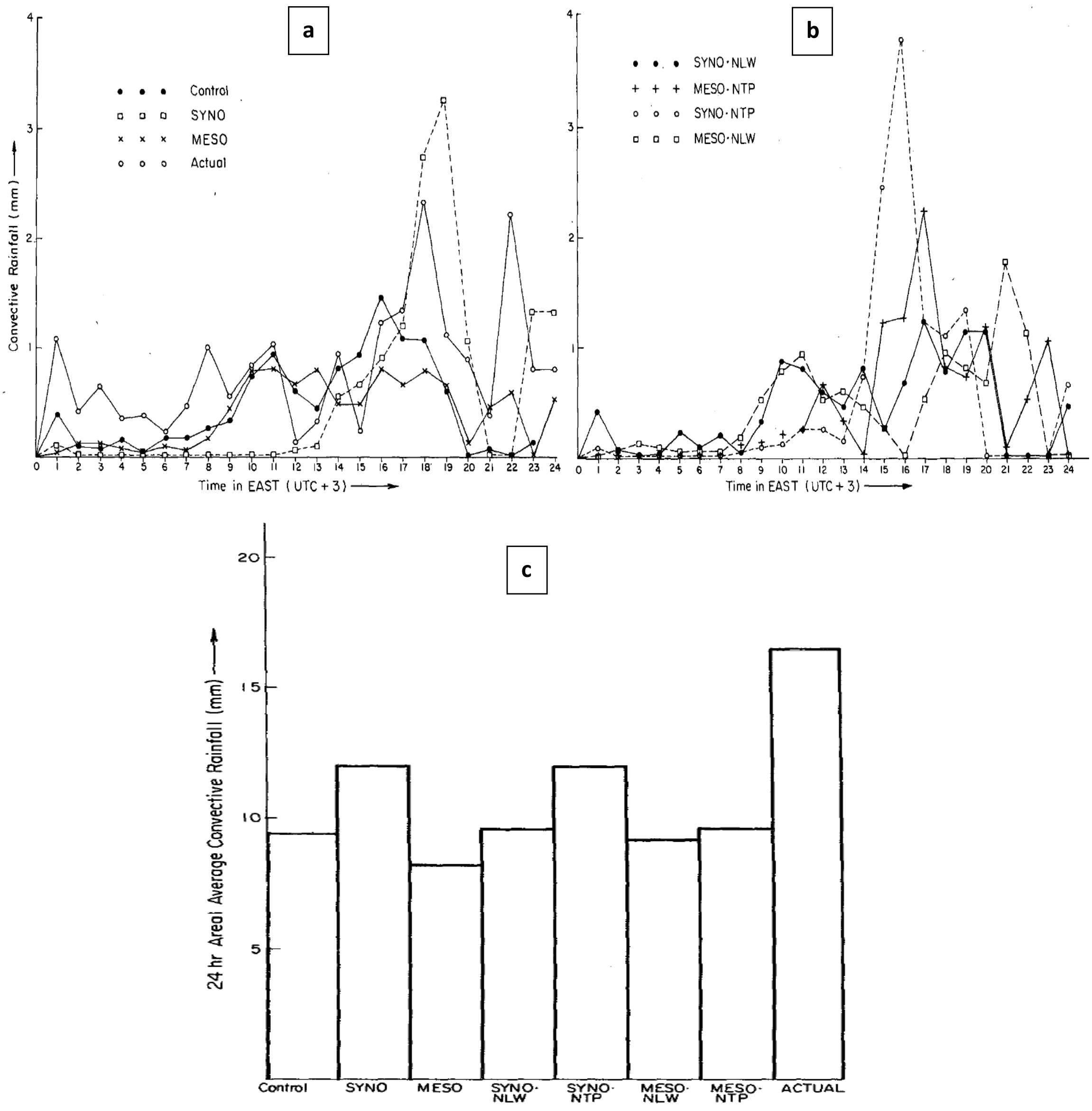

***Figure 3.1:** Time series of convective precipitation for **a:** different simulations and **b:** different sensitivity experiments versus the actual observed average rainfall over Kenya on 14 Apr. 1985. **c:** A histogram showing grid-averaged 24-hour convective precipitation for different experiments and the actual observed average rainfall over Kenya on 14 Apr. 1985. The abbreviations are defined as follows: **Control**: Control experiment using full physics and moist convection in simulating large-scale flow fields. **MESO**: Experiment without synoptic-scale monsoonal flow. **SYNO**: Experiment without terrain and land water contrasts to eliminate the effect of thermally induced local circulations. **SYNO.NLW**: synoptic-scale monsoonal simulation with topography but without land-water contrast. **SYNO.NTP**: Synoptic-scale monsoonal flow with land-water contrasts but no topography. **MESO.NLW**: Mesoscale simulation with topography but no land-water contrast. **MESO.NTP**: Mesoscale simulation with land-water contrast but no topography. Taken from Mukabana and Piekle (1996).*

likely to precipitate over the afternoons while the lowlands are more likely to experience convective precipitation in the early mornings. Figure 3.1 is a summary of the interaction between synoptic-scale and mesoscale flow in a controlled experiment over Kenya (Mukabana and Piekle, 1996). Studies on the mechanisms responsible for convection and precipitation over Kenya dates back to the 1970's and 1980's with numerical modeling studies of Fraedrich (1972) and Okeyo (1986) and recently in the 1990's with the numerical simulation studies of Mukabana and Piekle (1996). Mesoscale numerical studies by Okeyo (1986) found that the presence of Lake Victoria serves to provide energy and moisture by moistening the lower atmosphere above the highlands by as much as 2g/kg as well as warming it by about 5°C and therefore raising the condensational heating by 5°C/day. As such, precipitation is usually higher by 1.2 mm during day-time over the highlands than if the lake was absent.

3.2 Mechanisms of mesoscale convection

Studies on propagating mesocale convection producing precipitation events on a sub-daily to daily scales appears scanty over Kenya and, indeed, over the Equatorial East Africa (EEA). Yet, this is a region that is characterised by the most intense thunderstorms (Laing et al., 2011). Some of the few studies on extreme convection over the EEA suggest that, organised deep convection consists of coherent structures that are characteristic of systems that propagate under a broader range of atmospheric conditions. Usually, convection is triggered by daytime heating of elevated terrain and LSB which, over East Africa, is a source of elevated heating which tends to increase vertical shear and horizontal vorticity (Grabowski and Moncrieff, 2004; Laing et al., 2011). Organised convection is usually a result of regeneration of convection through multiple diurnal cycles with a westward propagation. Propagating convection over EEA takes place in an environment characterised by moderate low-level shear accompanied by a southwesterly monsoonal flow and midlevel easterly jets (Mekonnen and Rossow, 2018; Laing et al., 2011). EEA is also characterised by equatorially trapped Kelvin waves with phase speeds of 12–22 ms^{-1} (Wheeler and Kiladis, 1999; Laing et al., 2011; Gruber, 1974; Kiladis et al., 2009). However, dry phases of Kelvin waves usually disrupt propagation of mesoscale convection although during the wet phases, mesocale convection is more widespread especially during the active phase of the Madden Julian Oscillation (MJO) with limited westward propagation. Deep convection over EEA is more frequently initiated in the leeward sides of high terrain during mid- to late afternoon and the maximum frequency in cold clouds is observed downstream of the mountain ranges of the African Rift Valley over the Congo basin (Laing et al., 2011). Figure 3.2 shows how a Mesoscale Convective Systems (MCS) develops over the mountains of East Africa and propagates westward.

Recent works of e.g. Mekonnen and Rossow (2018) suggests that though the effect of African Easterly Waves (AEW) on the initiation of mesoscale convection is unclear, intradiurnal activity, atmospheric instability, and specific humidity usually precede the development of well-organized convection over the Ethiopian highlands. The study found that atmospheric instability favours the development of high frequency scattered, isolated convection to the east of Ethiopian highlands that is followed by a perpetual large increase in instability and increasing humidity which supports highly organized large-scale convection.

Mekonnen and Rossow (2011) observed that stronger latent heating and negative radiative cooling over eastern African are associated with larger and better organized

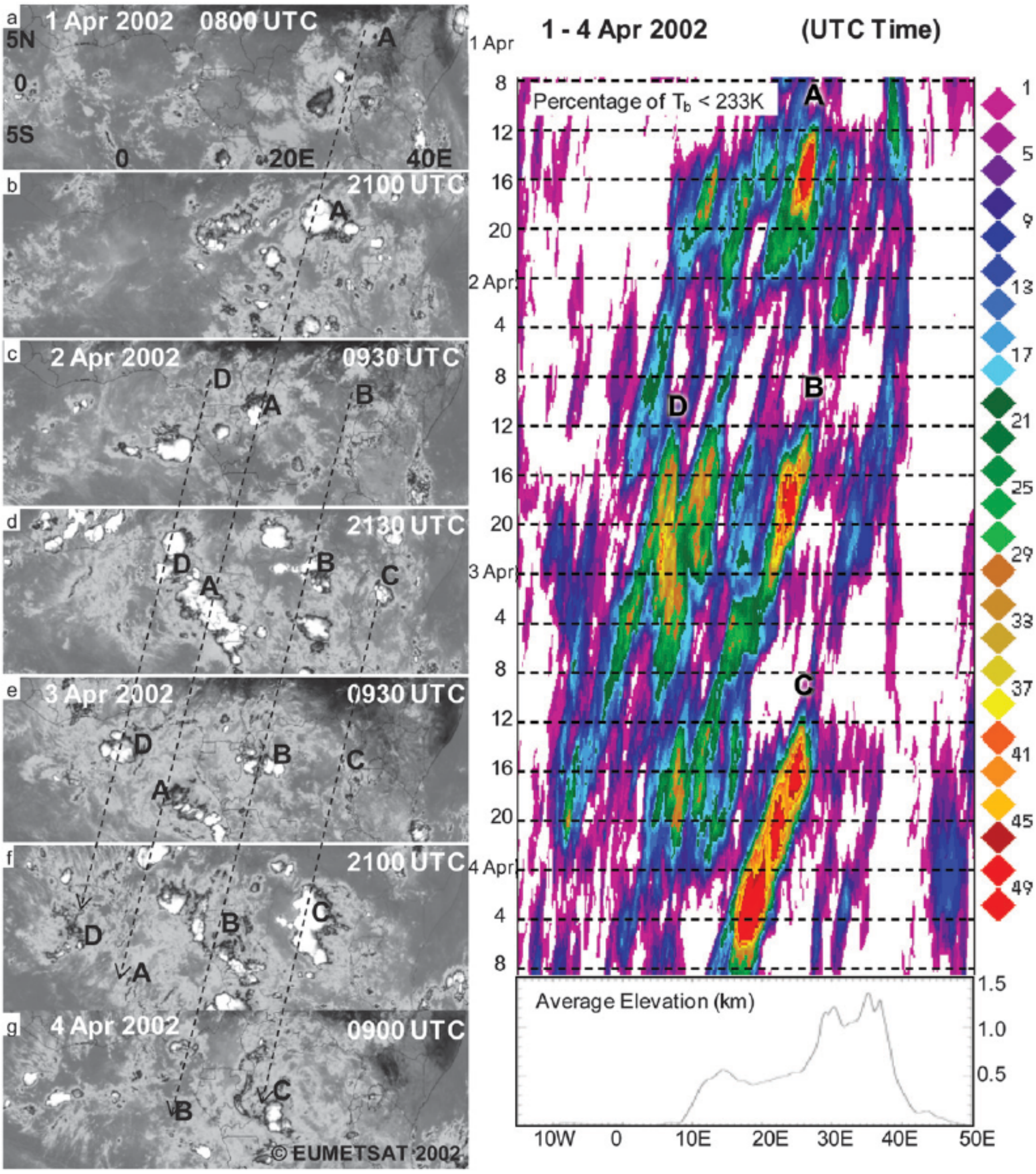

Figure 3.2: *(left) Enhanced Infrared images and (right) associated cloud streaks between 1–4 Apr 2002. Averages of percentage of* $T_b < 233K$ *are taken between 7.5°S–7.5°N. Dashed black lines on the satellite images link systems that form episodes and are marked by letters A, B, C and D to match the Hovmöller diagram. Average elevation (km) is drawn below the Hovmöller diagram. Figure taken from Laing et al. (2011).*

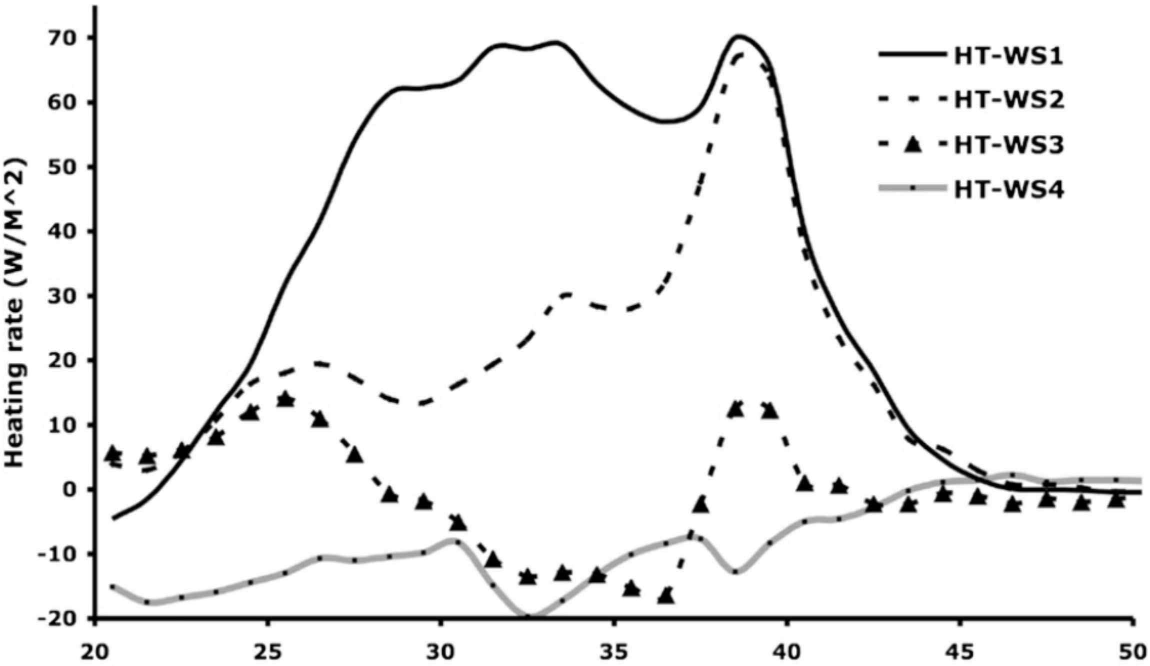

Figure 3.3: Composite anomalies of latent heat release (HT) for June–August season between 1997–2004 regressed against weather states namely, Deep convective clouds (WS1), Relatively deep convective clouds (WS2), Shallow clouds (WS3) and Convectively suppressed weather state (WS4) at the base point 5°–15°N, 30°–40°E at day 0, the time of maximum relative frequency of occurrences of weather states, for Central and East African region (averaged in 5°–15°N). The latent heating associated with each weather state is shown in the legend. Figure taken from Mekonnen and Rossow (2011).

convective clouds than weaker and scattered convective clouds (see figure 3.3). This study observed that less organized convective clouds emanating over the Arabian Sea produce a chain of events that lead to better organized mesoscale convective systems just to the west of Ethiopian highlands.

3.3 Teleconnections and extreme precipitation over East Africa

The most devastating heavy rains over Kenya and East Africa occured in the Short Rains of 1997/1998 due to the El-niño Southern Oscillation (ENSO) (Indeje et al., 2000). Okoola et al. (2008) found that before this El-Niño event, a ridge of high pressure towards the eastern coast of South Africa intensified and propagated eastwards leading to the strengthening of moisture-laden easterly winds reaching the East African coast. The study also found that zonal wind component along the longitude 40°E showed shears in the flow that were associated with the development of a trough in the lower troposphere around which southerlies moved towards the north. Thus, the convergence of the (cold and continental) southerlies with the (warm and wet) easterlies near the East African coast initiated instability that can explain the evolution of the El-Ninõ event of 1997/98.

Prior to these events, the year 1961 recorded the heaviest rainfall event which saw massive flooding in many parts of East Africa through to the Indian subcontinent causing significant economic difficulties as well as prolonged increases in lake levels across East Africa (Odingo, 1962; Mörth, 1967). Past studies have advanced the idea of a dipole mode in atmospheric circulation in the Indian Ocean as the principal driver to these extreme rainfall events over Kenya and East Africa (Saji et al., 1999; Webster et al., 1999). In their analysis of the 1961 rainfall event, Reverdin et al. (1986) studied the year to year variability of the surface observations in the equatorial Indian Ocean. The study identified the years 1961, 1963 and 1967 as anomalous with a large dipole mode over the Indian Ocean characterised by negative Sea Surface Temperature (SST) anomalies over the far east of the ocean and positive anomalies towards the center. The circulation was dubbed the Indian Ocean Dipole Mode (IODM) defined as a Sea Surface Temperatures (SST) gradient between the western and eastern equatorial Indian Ocean. The study noted that large-scale circulation patterns from the Pacific during these extreme rainfall events was normal and therefore the sources of the extreme rainfall event was restricted to the Indian Ocean. Saji et al. (1999) defines this reversal in SST gradient using the difference in SST anomaly between the tropical western Indian Ocean and the tropical south-eastern Indian Ocean and refer to it as an Indian Ocean Dipole Mode Index (IODMI). The IODMI has been used as a predictor of seasonal rainfall over East African Short Rains with some degree of success by Owiti et al. (2008). The Indian Ocean Dipole (IOD) and the coupled IOD-ENSO influence have also been linked with some of the wettest periods in the region e.g. the 1961 and 2006 floods over East Africa (Black et al., 2003; Bowden and Semazzi, 2007). Over the East African coast, Okoola et al. (2008) found that the circulation features common during extreme rainfall episodes consisted of a weakening or reversal of the east-west (Walker type) circulation over the Indian Ocean, enhanced convergence between trade winds and westward-moving disturbances in the surface field.

Flohn and Burkhardt (1985) linked extreme rainfall events with an anomalous surface flow caused by an SST anomaly over western equatorial Indian Ocean. Webster et al. (1999) note that during the period between June (July) of 1997, strong, cool (warm) SST anomalies initiated over the eastern (western) part of the equatorial Indian Ocean getting to below $-2°$C in Nov. and over $+2°$C in Feb. 1998. These anomalies brought about a reversal in the circulation characteristics over the Indian Ocean normally triggered by an SST gradient that in normal seasons requires a low level westerly flow of winds. An easterly flow ensued characterised by a vertical motion over the western side and subsidence over the eastern side. Other studies have also confirmed a strong relationship between the dipole mode and the East African Short Rains (Latif et al., 1999) used ensemble Global Climate Model (GCM) experiments forced by SST anomalies to show the strong response of the 1997/98 El-Ninõ event (with exception of Oct. and Nov. of 1997) with the IODMI whose effect was stronger than the El-Ninõ related SST anomalies in the Pacific.

A complex structure resulting from incoherent topography and nearness to large water bodies, e.g. Lake Victoria and the Indian Ocean render the weather in the East African region difficult to predict. Interannual variability of rainfall emanate from complex interactions of forced and free atmospheric variations (Mutai and Ward, 2000). SST forcings, quasi-stationary systems (e.g. the ITCZ, migratory synoptic-scale disturbances of extra-tropical regions on the borders of the tropical regions, e.g. blocking highs and cold lows, migratory synoptic-scale disturbances over tropical regions, e.g. easterly waves, equatorial waves, intra-seasonal waves, mesocale disturbances among other factors are responsible for weather over Kenya and the greater East African region.

3.4 Rainfall climatology and variability

Rainfall distribution over Kenya and the larger East Africa is irregular due to various factors ranging from local to global scale. The variability is also common within relatively short distances (Nicholson, 1996; Ogallo, 1989) among others. The local factors are more dominant than global factors (Nicholson, 1996; Ogallo, 1989; Okoola, 1999b; Ininda, 1995; Gitau et al., 2013; Indeje et al., 2000). They include but not limited to the presence of large water bodies especially the proximity to the Indian Ocean and Lake Victoria, the highlands e.g. Mt. Kenya (5199m), Mt. Elgon (4,321m) at the Kenya-Uganda border, Mt. Kilimanjaro (5,895m) of Tanzania and the Aberdare ranges of Kenya, the Ruwenzori mountains (5,109m) of Uganda, the presence of the great Rift-Valley among others factors (Nicholson, 1996; Ogallo, 1989; Okoola, 1999b; Ininda, 1995; Gitau et al., 2013; Indeje et al., 2000). These factors are central to the huge variance of convection over the region as synoptic-scale weather factors interact with the locally induced circulations to create a complex weather regime.

Variability of weather over Kenya, and by extension, the East African region changes significantly over short distances due to the factors mentioned in the preceding paragraph. Figure 3.4, taken from Karianjahi (2012), shows the annual cycle of precipitation over three gauge stations within Kenya chosen to represent close but inhomogeneous regions. A 30-year monthly rain-gauge data set was used to calculate the annual precipitation cycle. Figure 3.4a shows the annual cycle of precipitation over the Central Highlands, 3.4b over the Lake basin and 3.4c over the coastal lowlands. It is clear from the figure that the highlands are characterised by two peaks of rainfall maxima (bimodal rainfall regime) centered around Apr. and Nov. responding to the passage of the ITCZ (Okoola, 1999a,b; Okoola et al., 2008), while the Lake basin, situated a mere 300 Km from the highlands, has a maxima centered in Apr. and a weak maxima during the months of Aug. to Nov. reflecting the abundance of the synoptic ITCZ signal during the Long Rains season (Apr.) and the influence of other local factors during the second phase of ITCZ passage across the region in Oct./Nov. (Short Rains season). The variability during the months of Aug. to Oct./Nov. can be attributed to the nearness to the Lake as well as advection of moist air from the Congo basin whose influence tends to dominate the synoptic-scale influences. Over the coastal region, about 300 Km from the highlands, the peak is found during May and another significantly weak peak during Nov. This is just but to show how the various physical features interact to create an incoherent weather and climate regime across short distances.

The factors above have led past researchers to formulate ways geared towards description of rainfall variability over the East African region. Most studies have used statistical methods to regionalize East African region into homogeneous rainfall zones. The most common statistical methods used in the works of Bärring (1988); Ogallo (1989); Ininda (1995); Indeje et al. (2000) among few others involved collecting as many rain-gauge stations with as much data as feasibly possible across the region, aggregating the data into seasonal totals and applying an Empirical Orthogonal Function analysis on the data set. This produces modes of variability where the first few modes describing the most variability are cut-off based on some tests of significance and later used to align the gauge stations based on their principal component scores. The stability of the Principal Component Analysis (PCA) patterns are then tested using composite analysis and inter-station correlation. Usually, one station that is most representative of the clustered pool is adopted as the eventual representative of the delineated region (Indeje et al., 2000). Other researchers who have sought to identify modes of seasonal precipitation include Dyer (1977) over southern Africa, Basalirwa (1995) over Uganda and Schreck and Semazzi (2004) over East Africa.

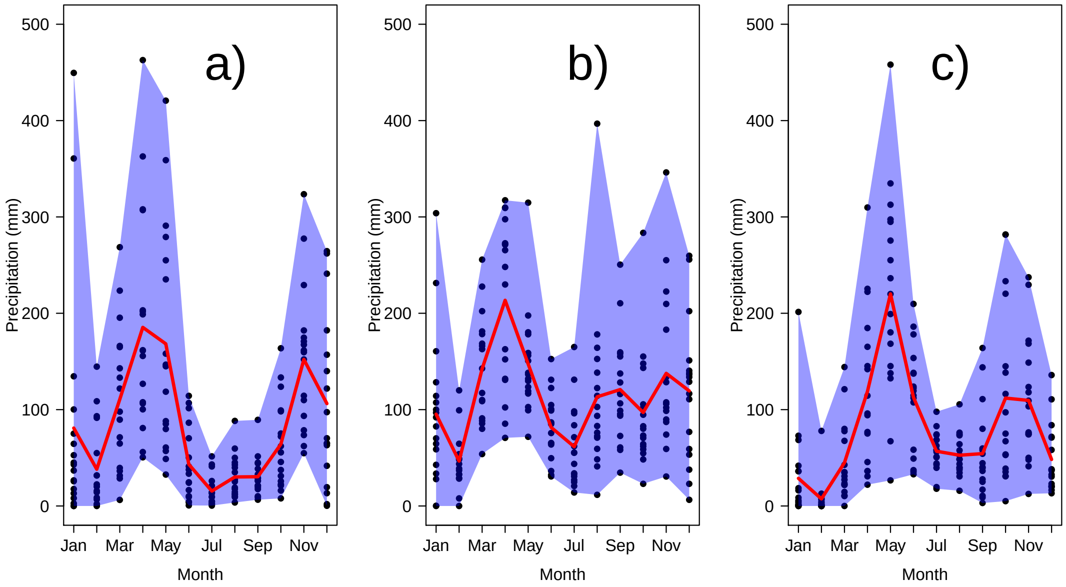

Figure 3.4: *Rainfall climatology for (a) Dagoretti, representing the highlands (b) Kisumu, representing the lake basin climatology and (c) Mombasa, representing the coastal rainfall climatology. The climatology is based on an average of 30 years of rainfall records between 1961-1990. The red curve represents the mean for each month while the black dots represents the individual values for each month in the entire period. The blue shading encloses the highest and lowest monthly precipitation values. Notice the almost similar pattern for Mombasa and Nairobi with the former reporting the highest mean amount of precipitation in May and the latter in April during the Long Rains. Also, the coastal station has a less peaked mean than Nairobi in Oct. (Karianjahi, 2012)*

3.5 Walker-type circulation over the Indian Ocean

During boreal autumn season, there exists an equatorial zonal circulation cell characterised by an ascending arm over the eastern Indian Ocean near Indonesia and a sinking arm over the western Indian Ocean near the equatorial East African coast as shown in figure 3.5. Rains during this season are found to have a very steep negative correlation with the Indian Ocean equatorial westerlies, pressure and vertical velocity while maintaining a positive correlation with pressure and vertical velocity over the eastern Indian Ocean as well as with the South East trade winds as has been shown by the works of Hastenrath et al. (2010) and Mutai et al. (2012). As a result, enhanced (deficient) rains during the boreal autumn season are promoted when the equatorial surface westerlies are weak (strong) accompanied by weak (strong) subsidence over the western (eastern) part of the Indian Ocean. The powerful zonal-vertical cell results in a strong surface westerly jet over the equatorial Indian Ocean known as the Wyrtki jet (Wyrtki, 1973).

During the Long Rains seasons however, the outstanding zonal-vertical circulation cell over the equatorial Indian Ocean that dominates the boreal autumn is overwhelmingly absent (Hastenrath et al., 2011). During the end of the Long Rains season, the upper level (200mb) easterlies are relatively weak compared to during the Short Rains season. As a result, a zonal vertical circulation cell observed during *mvua ya vuli* (boreal autumn season) is not apparent during *mvua ya masika* (boreal spring season) (Hastenrath et al., 2011). In contrast, the boreal spring season tends to benefit from south easterly flow from the neighbouring Indian Ocean that advects warm and high θ_e-air from the western Indian Ocean as SSTs are usually the highest here throughout the year as has been shown by Yang et al. (2015). Surface winds are generally convergent over the coastlines but divergent

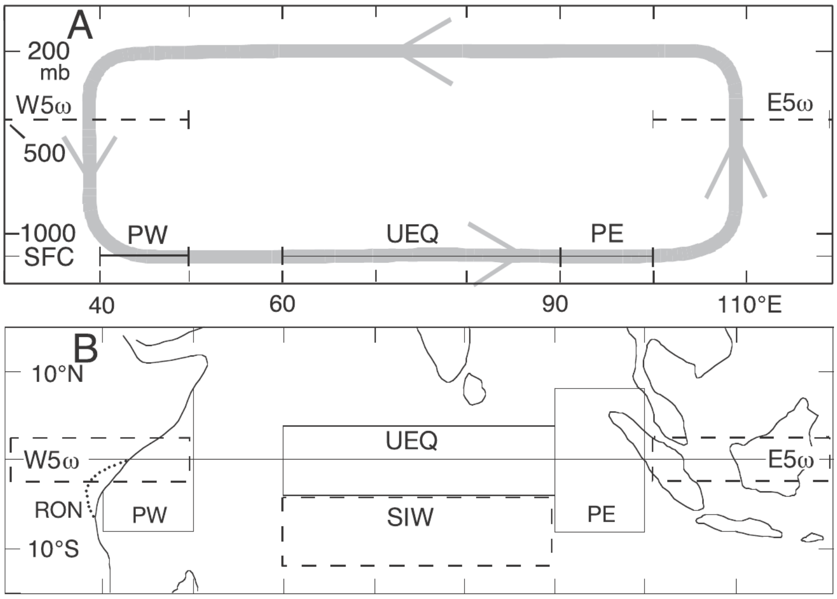

__Figure 3.5:__ a) Zonal-vertical cross section of the circulation during the Short Rains season over the equatorial Indian ocean and b) Spatial locations of the various circulation indices involving pressure on the surface and at 200mb as well as vertical velocity at 500mb levels. PW: pressure to the west (8°N–8°S, 40°–50°E), PE: pressure to the east (8°N–8°S, 90°–100°E), UEQ: Surface westerlies (4°N–4°S, 60°–90°E), SIW: South Indian Ocean trade winds (4°–12°S, 60°–90°E), W5ω: vertical velocity to the west (2.5°N–2.5°S, 30°E–50°E), and E5ω: vertical velocity to the east (2.5°N–2.5°S, 100°–120°E) and RON: Rainfall index for Oct. – Nov.. Figure taken from Mutai et al. (2012).

inland due to the easterly acceleration when going through the Turkana channel (Yang et al., 2015). During anomalously wet boreal spring season, there exists a local cyclonic circulation centered at 5°S, 35°E at the 700mb level with low wind intensities. The closed circulation extends to the western Indian Ocean, picks up moisture and discharges it over the mainland given the slowing winds in the closed cell. The southerlies (northerlies) from the Mozambique channel promote (inhibit) the surge of cold air equatorward. During anomalously dry (wet) boreal spring season, the wind intensity at 700mb level is enhanced (suppressed) and no (a) local cyclonic circulation is observed in the neighbourhood of the region. However, an anticyclonic (cyclonic) circulation located at the intersection of Ethiopia, Kenya and Somalia tends to dominate dry (wet) boreal spring seasons (Okoola, 1999b) suppressing (promoting) advection of equatorial westerlies from the Congo towards the region at 700mb. SST anomalies over the western equatorial Indian Ocean are generally warmer (colder) than normal while the eastern Atlantic SSTs are generally colder (warmer) than normal during anomolously wet boreal spring seasons (Okoola, 1999b; Yang et al., 2015).

3.6 Conditional instability and deep moist convection

The lower atmosphere of Kenya, and indeed, that of East Africa is convectively stable throughout the year except during the Long and Short Rains season when the SSTs are at their highest (Xu and Emanuel, 1989) and Yang et al. (2015) among others. This conditional instability situation requires mechanisms to trigger convection. It is therefore not uncommon for the region to experience suppressed rains during out-of-season periods since large-scale trigger mechanisms are largely absent. Conditional instability is defined by Yang et al. (2015) and Cook and Seager (2013), as the difference between the surface Moist Static Energy (MSE) and the saturated MSE at the 700 hPa level. At this level, the atmosphere is clearly above the boundary layer in this topographically complex region. The definition of the surface MSE, the 700 hPa saturated MSE and conditional instability are defined in section 5.2.4.2 in the data and methods chapter by equations 5.10, 5.11 and 5.12 respectively.

Using this definition, a north-south Indian Ocean gradient near the Kenyan coastline is such that during boreal winter (Dec. to Feb.), there is an advection of very low θ_e air into the region from the cold northern Indian Ocean while during the boreal summer, the region is replete with cold and dry air from the cool Indian Ocean emanating from both winds coming from the winter hemisphere as well as the coastal upwelling associated with the Somali Jet. However, during both Long and Short Rains, the low-level winds are much weaker and have very little impact on the surface air MSE over the region. The SSTs are also at their highest during the two rainy seasons. Throughout the year, the south western Indian Ocean is much cooler than the east and this triggers a west-east gradient in temperature and winds. This off-shore circulation establishes a situation where the adjacent land is denied the possibility of developing a high sub-cloud θ_e which suppresses precipitation in the region leading to the semi-arid/arid conditions in the region (Yang et al., 2015). Divergence pattern in general is such that convergence is common at the surface with divergence at about 850mb level accompanied by another convergence in the upper levels (Yang et al., 2015).

3.7 Detection of deep convection by satellite imagery

Few studies have been conducted over the East African region centered on tracking of large and organised convective systems using satellite imagery. However, many studies have been conducted especially over the west African region that quantify organised convection. Recent works of Redl et al. (2015) and Engel et al. (2017) over west Africa adopted microwave channels of 150 and 157-GHz of the Advanced Microwave Sounding Unit - B (AMSU-B) and MHS to detect deep moist convection. Redl et al. (2015) opine that microwave window channels are able to delineate deep continental convection. Engel et al. (2017) using the microwave channels were able to locate deep convective systems causing heavy precipitation over Niger, Burkina Faso and Senegal. Limitations of instruments which carry the sensors are that they are usually mounted on polar-orbiting satellites which means that a consistent tracking may not be feasible as satellite overpasses are irregular. The Spinning Enhanced Visible and Infrared Imager (SEVIRI) instrument is a great candidate to track deep convective systems on regular and high temporal resolution of 15-mins as it is mounted on a geostationary satellite. The only disadvantage is that the instrument can only detect cloud top temperatures as it is a passive sensor. Since temperature is a function of height, one can infer the height of a system from the temperature data received but cannot infer hydrometeors. Hong et al. (2005) provide methods of detecting deep tropical convective clouds and overshooting convection from measurements at the three water vapour channels namely 183.3±1, 183.3±3, and 183.3±7 GHz of the AMSU-B. In short, the differences in brightness temperatures between the three channels are suitable for detecting deep convective clouds while an order relation between the different sizes can be suitable for determining overshooting towers.

3.8 The Role of CAPE/CIN in convection

Deep convection results into intense precipitation. For this to occur, high rate of condensation is required prompting the release of relatively high amounts of latent heat to the atmosphere. Deep convection is promoted by mechanisms that lift air parcels to the LFC. As air parcels rise adiabatically (without exchange of heat with the environment), they expand and cool. The cooling proceeds until the air parcel condenses. Thus, since Relative Humidity (RH) depends on temperature, the cooling of the air parcels result in increases in RH. The vapour pressure exerted by the air parcels nears the saturation vapour pressure during the ascent. Equation 3.1 shows the relationship between RH and both pressures just mentioned.

$$RH = \frac{e}{e_s} * 100\% \tag{3.1}$$

Bolton (1980) provides the equation for saturation vapour pressure as shown by equation 3.2.

$$e_s(T) = 6.112 \exp\left(\frac{17.67}{T + 243.5}\right) \tag{3.2}$$

where T is the temperature of air in °C. As the parcel rises adiabatically, $T \longrightarrow T_d$ (dew point temperature) and $RH \longrightarrow 100\%$. At $T = T_d$, condensation begins and this defines the base of cumulus cloud. Any further lifting of the saturated air parcel happens at a rate less than the adiabatic lapse rate since the latent heat released by the air parcels warms the parcel. The rate is known as the saturated adiabatic lapse rate. Since air parcels within the East African region are stable with respect to dry adiabatic lapse rate but unstable with respect to moist adiabatic lapse rate (essentially the definition of conditional instability), a mechanism is necessary to lift the parcels to the LFC. Beyond this point, the parcels continue to ascend on account of their own buoyancy as they find themselves warmer than the immediate environment. Convective Available Potential Energy (CAPE) is released in the process until the parcels reach the equilibrium level beyond which the parcels become colder than their environment and sink. CAPE is a measure of the amount of potential energy present between the LFC (or the Convective Condensation Level (CCL), for convective lifting) and the Equilibrium Level (EL) or the Level of Neutral Buoyancy (LNB). CAPE can also be said to be a measure of the maximum kinetic energy per unit mass of air parcel achieved by moist convection implying that it is an estimate of the maximum possible updraft velocity (Murugavel et al., 2012). The higher the amount of CAPE, the higher is the possibility for deep convection (Bhat et al., 1996). Thermodynamic diagrams e.g. a Skew T-log P diagram can be a good tool to measure graphically the amount of CAPE.

The path of a rising saturated air parcel between the LFC and the point where it crosses the environmental temperature curve gives the amount of CAPE. Convective Inhibition (CIN) is the amount of energy below LFC preventing the air parcel from rising freely. It is the energy required by an unsaturated air parcel to overcome the stable layer between the surface and the LFC. The parcel has to overcome CIN through some atmospheric processes e.g, low-level convergence, or surface insolation to rise freely. A thermodynamic diagram is a powerful tool to forecast deep convection. Figure 3.6 is a cartoon that shows how a thermodynamic diagram can aid in the forecasting of a thunderstorm. Shown on the figure are the dew-point and environmental temperature curves with LCL, CIN, LFC, CAPE among other thermodynamic lines shown. CAPE and CIN are measures of instability in the atmosphere. For an unstable atmospheric layer, CAPE increases with increase in either temperature and moisture within the boundary layer. Though previous studies on CAPE

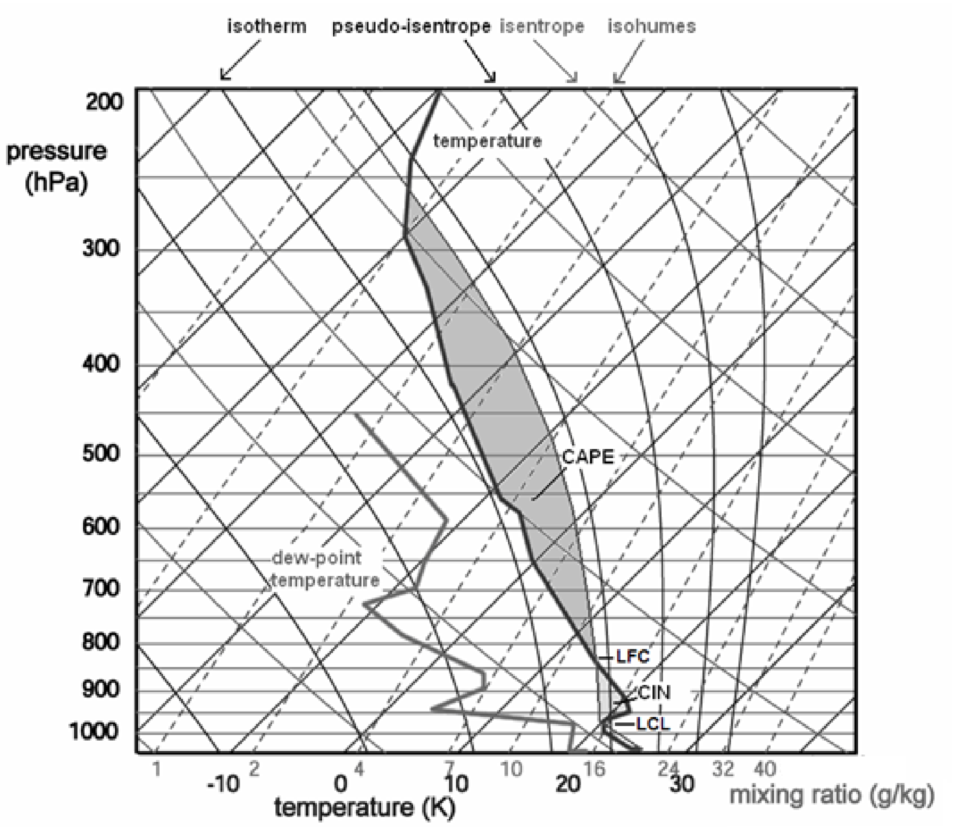

Figure 3.6: A Skew-T log-P model where environmental and dew-point temperatures are plotted for forecasting purposes. Shown on the diagram are isotherms, isentropes (dry adiabatic lines), pseudo-isentropes (pseudo-adiabatic lines) and isohumes (lines of equal mixing ratio). A parcel from the surface having an initial temperature of 26°C and a dew-point temperature of 21°C has been plotted and CIN and CAPE calculated graphically. Illustration taken from `http://www.estofex.org/guide/1_2_2.html` *accessed on 22 Sep. 2018.*

have shown that large scale convection over the tropical regions are driven by large-scale processes and therefore CAPE plays unimportant role (Emanuel, 1987; Neelin et al., 1987; Xu and Emanuel, 1989; Yano and Emanuel, 1991; Emanuel, 1993; Emanuel et al., 1994), good correlations between CAPE and rainfall around the ITCZ and mountainous regions over Africa have been found by (Monkam, 2002). However, many studies outside the African region have shown little promise to the relationship between CAPE and rainfall. McBride and Frank (1999) found negative correlation between CAPE and the Australian monsoon and so did Yano et al. (2005) and Sobel et al. (2004). Studies carried out in the United States attempting to associate rainfall on CAPE proved unsuccessful (Peppler and Lamb, 1989; Zhang, 2002).

3.9 Modeling studies of precipitation over the region

Atmospheric modeling is the science of simulating the atmosphere and its evolution in space and time from some initial state. For the accuracy and reliability of the model results, the initial data must be defined at the highest spatial and temporal resolution possible. Global Climate Models (GCMs) are widely used over East Africa especially to project future climate scenarios on seasonal, annual to decadal time-scales. GCMs are the most appropriate for simulating future climate change scenarios. They are capable of modeling the evolution of the atmosphere in response to external forcings such as increase in greenhouse gases like carbon dioxide, increase in SST and soil moisture. Their resolutions are usually coarse both in spatial and temporal scales with some having a spatial resolution as coarse as 300 Km. This is not an ideal resolution when accurate understanding of the local/regional phenomena that trigger weather and climate is at stake. At coarse resolutions in the order of 300 Km, the magnitude and extent of extreme weather events such as cyclones or floods are not realistically reproduced. Local factors that affect weather e.g. steep topography and water bodies compromise the effectiveness of GCM since they happen at scales way smaller than a GCM's grid box. A solution to this difficulty has always been to combine GCMs with high-resolution regional climate models in a process known as 'nesting'. This way, GCM simulates the response of the general circulation to the large scale forcings while the Regional Climate Model simulates the effects of sub-GCM-grid scale forcings and provides fine scale regional information. In essence, a Regional Climate Model (RCM) provides all the important components of the climate system. The fact that they usually cover a limited area of the globe, RCM's are ideal for probing regional climate processes and variability especially within the complex lower boundary layer (Wang et al., 2004). Usually the initial conditions and lateral boundary conditions of the RCM are obtained from the GCM or observations. However, unlike the GCM which once configured evolves from the initial conditions, a RCM is heavily dependent on information at the domain boundary (lateral boundary conditions) provided by a Global model or by observations.

A reliable weather and climate model incorporates all physical features that influence the atmospheric processes in the real world. Dynamical models attempt to achieve this task by solving a set of equations that describe atmospheric motions, physical processes and the evolution of meteorological variables that define the state of the atmosphere e.g. temperature, wind speed, humidity and pressure. To achieve their task, dynamical models have a set of five pillars, namely;

1. A closed set of hydrodynamical equations that are based on conservation laws. Closed means there exists as many unknowns as there are equations. In section 5.3.1, this set of conservation equations is illustrated. The equations define the conservation of motion (equation 5.18), conservation of mass (equation 5.20) and the conservation of moisture (water substance, equation 5.21)

2. A method of solving these equations, or *method of solution*. The most widely used methods of solution are finite differencing techniques and spectral methods.

3. Initial conditions. The model requires to be initialized by a set of initial data. This data has to be quality-checked and modified dynamically, a process known as *data assimilation* before driving the model.

4. Boundary conditions. These are the conditions imposed on the perimeters of model domain at the top, bottom and laterally. The conditions can be in form of data values or equations.

5. Parameterization. Physical processes which cannot be fully resolved by the model need to be approximated using objective schemes. These unresolved processes at sub-grid scales include radiative processes (e.g. scattering, absorption, reflection and transmission of solar radiation), boundary layer turbulence, cumulus convection, cloud, rainfall and cloud-radiation interaction.

RCM's have been applied over many parts of the globe. Over the African continent, they have been applied with relatively promising results (Rowell et al., 1996; Ward et al., 1993; Indeje et al., 2000; Anyah et al., 2006). Over East Africa, RCM's have been applied by Sun et al. (1999a,b); Indeje et al. (2000); Anyah et al. (2006); Anyah and Semazzi (2007) among others. Sun et al. (1999a,b) used a 60 Km resolution RCM to investigate rainfall over East Africa while Anyah et al. (2006) used an enhanced version of the RegCM3 modified at North Carolina State University for multi year simulations of the East African climate. Indeje et al. (2000) used the National Center for Atmospheric Research (NCAR) Regional Climate Model (RegCM2) to perform simulations where he reiterated the advantages of the nesting approach in improving regional climate simulations. The model was able to reproduce well the Turkana lowlevel jet shown in figure 2.1. After application in prognostic mode, the RegCM2 quite well captured the 3-months forecast of the extreme seasonal anomalies with the 1997 ENSO event. Schreck and Semazzi (2004) clearly showed how a highly resolved RCM could be utilised to resolve the detailed characteristics associated with the East Africa climate variability.

3.10 Convection-Permitting (CP) models

Regional to global models which parameterize convection are not adequate in reproducing processes that are smaller than their resolutions e.g. diabatic heating processes. Hence, Convection-Permitting (CP) models which resolve convection explicitly are of more added value in representing these processes. Some of the potential benefits of using a convective-permitting numerical models are elucidated in Finney et al. (2019) and Woodhams et al. (2018) as follows:

- Explicit representation of precipitation and diabatic heating from moist convection which is not possible in models that parameterize convection.
- Explicit representation of precipitation leads to improvement in the intensities and diurnal cycle of rainfall compared to outputs from models that adopt parameterization.
- Sub-daily characteristics of convection evolve much more realistically in a convection-permitting model and forecasts are much more improved compared to global models especially over the tropics.
- Convective storms are more realistic in CP models than in models which unresolve convection.

Over East Africa, few studies have used CP models to understand evolution of convection. A recent study by Woodhams et al. (2018) found that CP models produce more realistic subdaily evolutions of convection and precipitation than global models over Lake Victoria. However, these CP models require more in situ observations for data assimilation into the models and for verification.

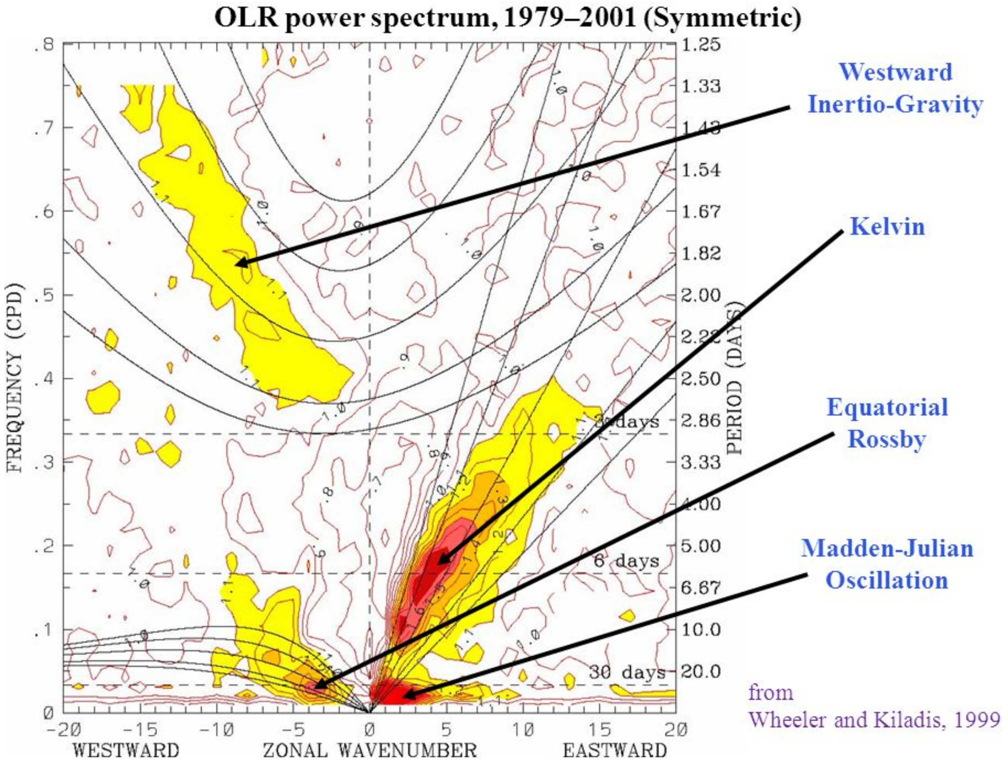

from
Wheeler and Kiladis, 1999

Figure 3.7: *Various tropical waves namely Kelvin, Equatorial Rossby, MJO and Inertio-Gravity waves filtered within the wave-number-frequency domain. For more details, see Wheeler and Kiladis (1999).*

3.11 Influence of equatorial waves over East African precipitation

Clearly, the East African precipitation has some degree of linkage to synoptic wave features especially during the long and Short Rains season. Equatorial waves are a potential source of rainfall predictability within the tropical region as they can be considered preferred eigenmodes of the tropical atmosphere. When these waves interact with precipitation, they are referred to as convectively coupled waves (Wheeler and Kiladis, 1999).

Various equatorial waves are identifiable based on their wavelength and period signatures as well as in their influence on dynamic-thermodynamic environment. The theory of these waves emanate from the solutions of the shallow-water equations which is a theory that describes wave propagation trapped at the equator (figure 3.7). The waves include Equatorial Rossby (ER) waves, mixed Rossby-gravity (MRG) waves, Eastward Inertio Gravity waves (EIG) and westward propagating inertio-gravity (WIG) waves (Matsuno, 1966). Two more waves have been identified within the tropical belt but are not solutions of the shallow water equations namely, MJO (Madden and Julian, 1971b) and Tropical Disturbance (TD)s including easterly waves (Riehl, 1945).

MJO has been found to have a major influence on precipitation over East Africa. It is a 30–60 day oscillation (figure 3.7) centered around the equator (Madden and Julian, 1971b, 1972, 1994b) and manifests as an eastward propagating large-scale disturbance in convection, zonal winds, and upper level velocity potential (Hendon and Salby, 1994). The wave feature usually develops over the western Indian Ocean and propagates eastward as a series of convection towards the Pacific Ocean where it disappears after encountering regions of cold waters. It pops up again over the tropical Atlantic and west Africa (Madden and Julian, 1971b, 1972). Infact, Wheeler and Hendon (2004) categorized the MJO's eastward propagation into eight phases where each phase corresponds to the geographical position of its active convective center. Each phase lasts for six days (figure 3.8) Research

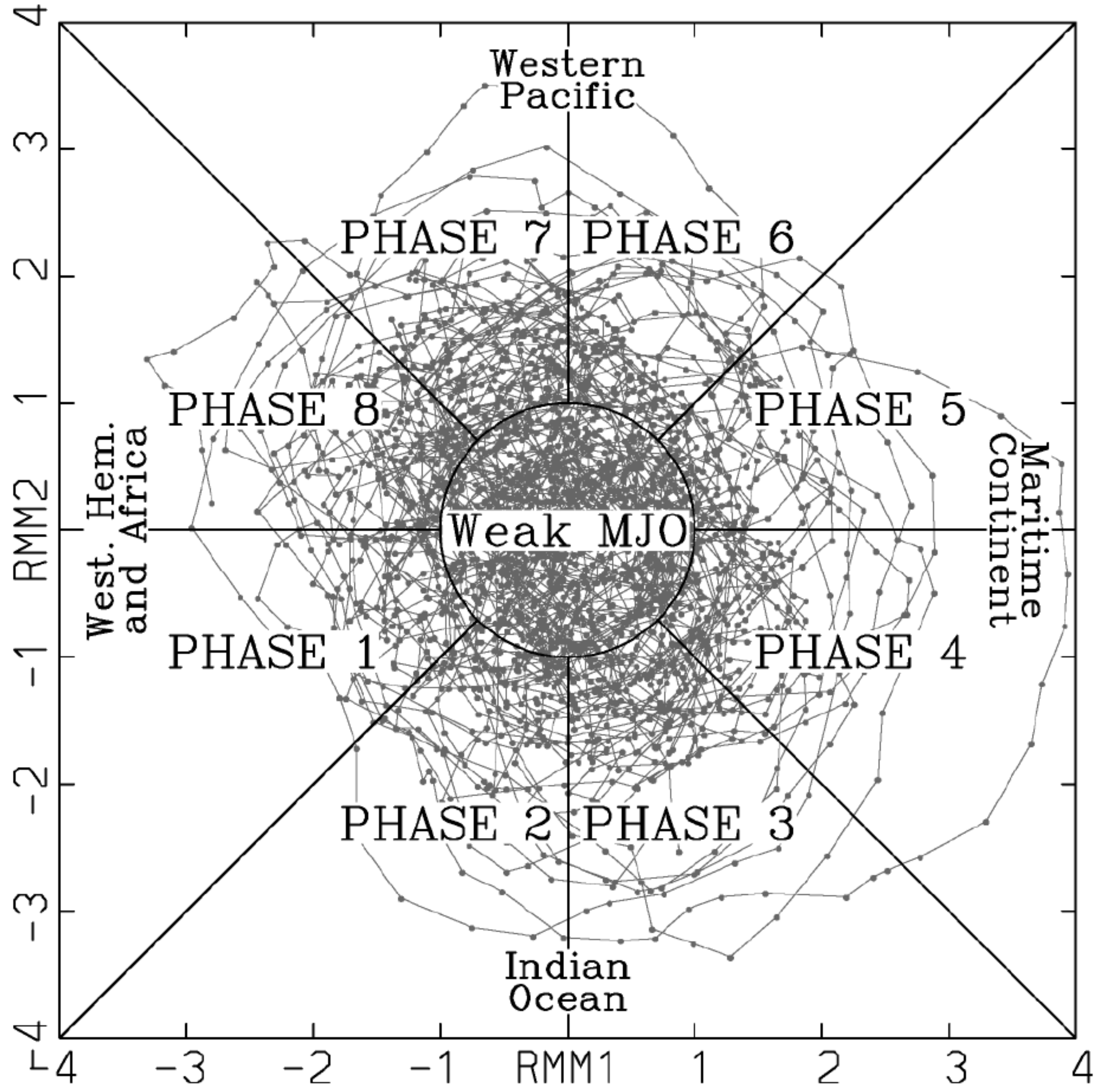

Figure 3.8: *Real-time Multivariate MJO series 1 (RMM1), Real-time Multivariate MJO series 2 (RMM2) phase space points for all available days in December-January-February (DJF) season from 1974–2003. Eight defined regions of the phase space are labeled, as is the region considered to signify weak MJO activity. Also labeled are the approximate locations of the enhanced convective signal of the MJO for that location of the phase space, e.g. the "Indian Ocean" for phases 2 and 3. Figure taken from Wheeler and Hendon (2004).*

on the relationship between MJO and precipitation at various scales over East Africa has been conducted rather extensively. Recent studies of Hogan et al. (2015); Berhane and Zaitchik (2014); Pohl and Camberlin (2006a,b) among others have documented exhaustively, the influence of MJO on East African precipitation patterns during the on and off rainfall seasons. Berhane and Zaitchik (2014) observed that East African rains during the months of Nov. and Dec. (Short Rains) and March and May (Long Rains) are enhanced over East Africa over contiguous regions when the MJO convective center lies between

20° and 140°E longitude and the influence is strongest when the center is located at 70°E. Dry precipitation anomalies are observed when the MJO convective centered is located between 140°E and 10°W (figure 3.9).

Mutai and Ward (2000) diagnosed the tropical circulation before, during, and after the rainfall spells by an investigation of how the intra-seasonal teleconnection structure relates to the seasonal atmospheric teleconnection structure. Gitau et al. (2013) also delved into the investigation of the intraseasonal statistics of rainfall over equatorial East Africa. Both studies showed that the MJO (Madden and Julian, 1971a, 1994a) which have a spectral signature of about 30 to 60 days have the highest impact on intraseasonal spells of precipitation.

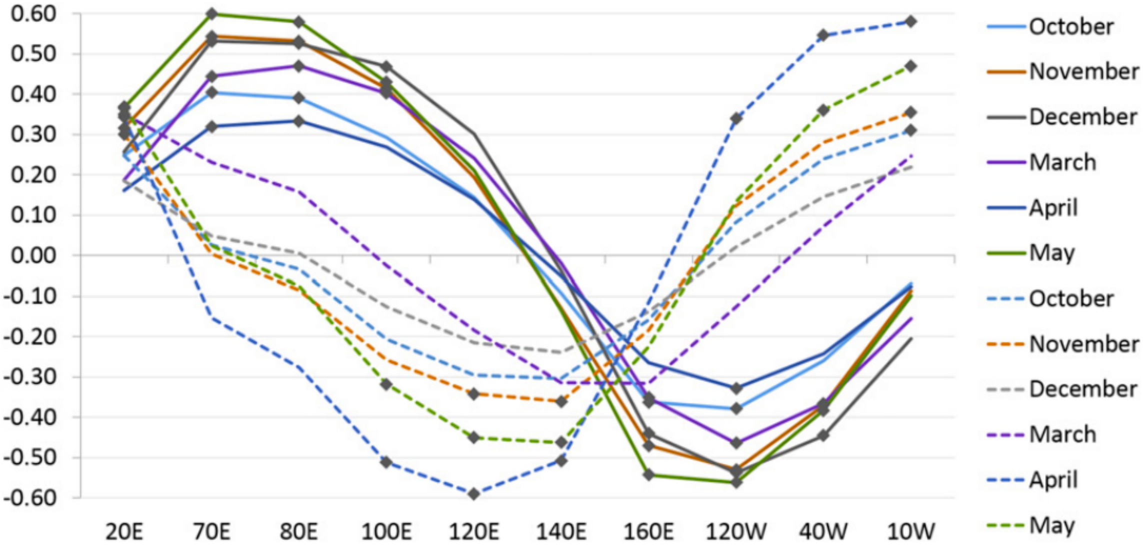

Figure 3.9: Correlation of area averaged precipitation over East Africa with each MJO index. Regions used for each month are 12°–2°S, 34°–38° for Mar.; 6°S–5°N, 30°–38°E for Apr. and May; 2°S–8°N, 30°–38°E for Oct.; 4°S – 4°N, 32°–38°E for Nov.; and 10°S–2°N, 32°–38°E for Dec. Solid lines are correlations with concurrent MJO indices, while dashed lines are correlations with MJO indices at a lead of two pentads. Diamonds show correlations that are significant at the 90% confidence level using the reduced degrees of freedom resulting from autocorrelation. Figure taken from Berhane and Zaitchik (2014).

Kelvin waves which are eastward propagating with a period of about 2.5–20 days corresponding to wave numbers 1–14 and shallow water depth 8–90 m (Wheeler and Kiladis, 1999) have been observed to modulate precipitation on the synoptic to intraseasonal time scale (figure 3.7). During March–May season, they have been found to significantly influence rainfall over the central African region (Laing et al., 2011; Nguyen and Duvel, 2008; Sinclaire et al., 2015). Active convection over East Africa is preceded by eastward propagating Convectively Coupled Kelvin Waves (CCKWs) which subsequently trigger westward-moving AEW(Mekonnen and Thorncroft, 2016). Westward moving equatorial waves originating from the Tropical Easterly Jet (TEJ) over the South Asian region and propagating with a period of about 4 days have an impact on synoptic convection over East Africa as has been shown by Mekonnen and Thorncroft (2016). Recently, Schlueter et al. (2019) found that MJO, ER and Kelvin waves are equally important in modulating rainfall on a time scale of three days over the EEA.

Generally, Kelvin and Equatorial Rossby waves have lesser impact on rainfall than MJO with Mixed-Rossby-Gravity Waves (MRG) and EIG having the least influence over the East African region Fink et al. (2018).

Chapter 4

Research questions

The main goal of this study is to diagnose extreme precipitation events over Kenya with a view to developing precursors that can aid in future forecasting of such extreme events. As such, the following are the formulated research questions that inform the pursuit of this work.

1. Within the TRMM period (1998–2014), what has been the most extreme precipitation event in terms of magnitude and spatial contiguousness over Kenya?
2. How did remotely sensed data respond compared to the rain-gauge stations in terms of rainfall magnitude and temporal distribution? Are the two data sources interchangeable for the purposes of rainfall representation over Kenya?
3. Is the ECMWF reanalysis model (which is used largely in many National hydro-meteorological centers across the globe) able to capture the events both in spatial extent, temporal distribution and magnitude?
4. Are the events a result of propagating organised convective systems or from isolated and scattered convection caused by local direct solar heating? In case of the former, what is the vertical extent of these systems?
5. In terms of the event-triggers, are these extreme and contiguous precipitation events locally or synoptically forced or are they a result of a complex interaction between synoptic influences and local factors?
6. During the formation of these extreme precipitation events, what dynamic and thermodynamic preconditions are necessary for their formation, development, maturity, duration and dissipation?
7. Can these extreme and contiguous precipitation events be readily reproduced by state-of-the-art high resolution weather and climate models that resolve convection explicitly (Convection-Permitting models)?

To be able to answer these questions, the following specific objectives are formulated.

i) Determine the strength and magnitude of the cases against climatology.

ii) Identify the large-scale synoptic/dynamic factors and their interactions with the local factors in promoting the evolution of the events.

iii) Investigate the sources of moisture and the ensuing thermodynamic evolution leading up to the cases.

iv) Assess the reproducibility of these extreme events in a Convective-Permitting model.

Chapter 5

Data and Methods

This section describes the data and methods used to diagnose extreme precipitation over Kenya.

5.1 Data

5.1.1 Rain Gauge data

Precipitation data (*in situ*, satellite and reanalysed) are used extensively in this work. 30 daily rain gauge records (observations are made between 06 and 06 UTC (0900 local time)) are available from KASS-D and shown in Table A.1 with their corresponding geographic locations in space shown in figure 2.1. For the diagnosis of extreme events, the period between 1998 and 2014 is employed deliberately to coincide with TRMM Multi-Satellite Precipitation Analysis (TMPA) data products which start in 1998. It is noted that Kenya lacks a dense network of surface stations. However, the available stations have less than 10% of data gaps and are also homogeneous. The stations are nevertheless adequate in representing the various climatic characteristics over Kenya.

5.1.2 TRMM products

To minimise the challenges of sparseness in rain gauge data, the study adopts a unique platform that characterizes tropical rainfall with remote sensors from space known as Tropical Rainfall Measuring Mission (TRMM). TRMM (in operation between 1997 and 2014) was a joint satellite mission between the United States and Japanese government to monitor precipitation in the tropics and subtropics and to estimate its latent heating (Wilheit, 2003). It was first launched in 1997 e.g. Okamoto (2003). TRMM has since been replaced by a new platform of satellites known as the Global Precipitation Mission (GPM) (2015 to date). Instruments onboard the TRMM satellite included the Precipitation Radar (PR) which scans at 13.8 GHz, the TRMM Microwave Imager (TMI) which is a 9-channel passive microwave radiometer as well as a Visible Infrared Scanner (VIRS) which is a 5-channel visible/infrared radiometer. TRMM 3B42 algorithm combines TMI, Advanced Microwave Scanning Radiometer for Earth Observing Systems (AMSR-E), Special Sensor Microwave Imager (SSMI), Special Sensor Microwave Imager/Sounder (SSMIS), AMSU, MHS, and the microwave-adjusted Merged Geo-Infrared (MGIR) to arrive at a final multisatellite measurement product known as the TMPA whose units are in mm/hr. It has a temporal and spatial resolution of 3-hour and 0.25° respectively. It is extensively used in this study as a proxy for rainfall where raingauges are untenable or sparse.

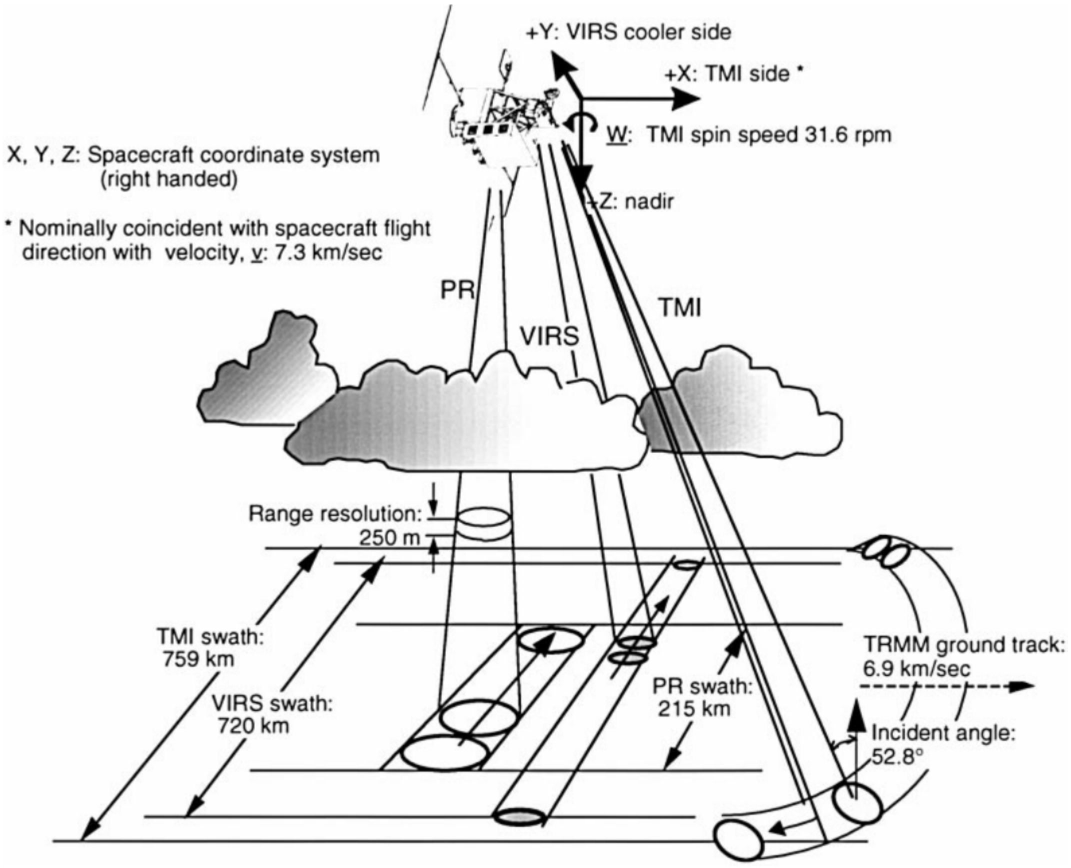

Figure 5.1: *Low earth-orbiting TRMM satellite showing the scanning geometry of the PR, TMI, and VIRS (Kummerow et al., 1998).*

The study also employs, where available, the level 2 products, namely, 2A12, 2A23, 2A25 and 2B31. Product 2A12 is a direct derivation from TMI which has a larger swath width than PR. The product contains such information as surface rain rates and vertical hydrometeor profiles on a pixel by pixel basis. It is derived from the TMI brightness temperature data using the Goddard Profiling algorithm GPROF2010. 2A23 product contains information from PR measurements which has a shorter swath width. The product detects rainfall and records "rain" or "no rain" accordingly. In case rain is detected, the algorithm is able to distinguish convective from stratiform precipitation which aids in classifying precipitation-causing systems. Broadband signals and storm heights are also provided in this product. The algorithm for this product follows the works of e.g. Schumacher and Houze (2003). 2A25 product contains a copy of all products of 2A23 but also provides the vertical profile of rainfall causing systems in a 3 dimensional platform. Thus, it is possible to distinguish surface rain from rain occuring at a height of say 5 Km from the surface. Product 2B31 (also called TRMM combined) derives vertical hydrometeor profiles using data from PR radar and the TMI. It also calculates the correlation-corrected mass-weighted mean drop diameter and its standard deviation as well as latent heating. 2B31 product estimates high resolution radar rain, see Haddad et al. (1997). The TRMM low-orbiting satellite mission infrastructure showing all the 3 major instruments (PR, VIRS, and TMI) and their swath widths is shown in figure 5.1. The image is taken from Kummerow et al. (1998).

5.1.3 CMORPH

NOAA Climate Prediction Center Morphing Technique Global Precipitation Analyses (CMORPH) precipitation estimates (Climate Prediction Center, 2011) are also used in this study. They aid in the sub-daily evolution of precipitation as their temporal resolution is 30 minutes. They are useful in this study in terms of providing additional information to the METAR reports at weather station where available.

5.1.4 ECMWF model precipitation data

The European Center for Medium Range Weather Forecasting Version 5 (ERA5) model precipitation products at a spatial and temporal resolution of 0.3° by 0.3° and one-hour are also used in the study. Also deployed are the ECMWF Reanalyses Interim (ERAI) model precipitation datasets at 6-hourly and 0.75° temporal and spatial resolution. Details about the ECMWF model are outlined in section 5.1.6.

5.1.5 Other satellite-based products for deep convection

Deep convection products used in the study include products from geostationary and polar-orbiting satellites.

5.1.5.1 Meteosat products

Observations of only one narrowband infrared channel with a central wavelength of 10.8μm of the imaging radiometer SEVIRI aboard the geostationary Meteostat Second Generation (MSG) satellites operated by EUropean Organisation for the Exploitation of MEteorological SAtellites (EUMETSAT) (Schmetz et al., 2002) are exclusively used. SEVIRI has, besides this single narrowband channel, a total of 11 narrowband and 1 broadband high resolution visible channel. Data from the primary scan service are utilised exclusively. The data has an image update cycle of 15 min with an orbital position at 0° longitude. The 10.8μm IR channel is only influenced by atmospheric gases and mostly shows the radiative signature of the clouds and the surface. It is therefore assumed that these brightness temperatures correspond to the cloud-top temperature for optically thick clouds, but are significantly warmer for cirrus clouds e.g. Rempel et al. (2017). Since the raw data from MSG SEVIRI comes in pixel counts, they are converted to brightness temperatures using the fomulas in appendix C.1. The CLoud property dAtAset using SEVIRI (CLAAS)-2 dataset, prepared and archived by the Satellite Application Facility on Cloud Monitoring (CM-SAF), see Stengel et al. (2014) is also used in this work. It is derived from SEVIRI sensor onboard METEOSAT Second Generation (MSG) satellites. The CLAAS product provides satellite-based characteristics of clouds. The data are provided on the native SEVIRI resolution of 15 minutes repeat cycle and 3 Km nadir resolution to 11 Km which is the edge of field of view. There are also in addition to these high resolutions of data, coarser temporal resolutions of mainly daily and monthly averages on a resolution of 0.05°. A summary of CLAAS-2 characteristics and a comprehensive evaluation are documented in Benas et al. (2017). We use the Cloud Physical Properties (CPP) product which categorises clouds into nine sub-categories namely, clear skies, fog, water-only laden clouds, supercooled droplets, mixed phase clouds, opaque ice clouds, cirrus clouds, overlapping clouds and overshooting tops.

5.1.5.2 CloudSat and CALIPSO

Data from the CloudSat and Cloud-Aerosol Lidar and Infrared Pathfinder Satellite Observations (CALIPSO) are also used in this study to characterize the vertical distribution of cloud properties. Both satellites are part of the A-Train constellation of 5 satellites (including Aura, PARASOL and Aqua) and take measurements at almost the same geolocation once in every 16 days. CloudSat is always ahead of CALIPSO by about 15 secs. They are nadir-viewing sun-synchronous satellites orbitting the Earth at an approximate height of about 705 Km , a velocity of about 7 Km/s and with an inclination angle of 98°. CloudSat carries a 94-GHz Cloud Profiling Radar (CPR) calibrated in a such a way to accurately and optimally profile the vertical distribution of clouds through an atmospheric column. It probes the atmosphere 15 seconds ahead of CALIPSO, see Im et al. (2006). CloudSat is sensitive to light rain and drizzle. The CPR has a vertical resolution of 0.48 Km and across-track resolution of 1.7 Km. The 2B-GEOPROF (Release 04 or R04) identifies levels sampled by CloudSat that contain significant radar echo from hydrometeors and provide estimates of radar reflectivity factor for each of these volumes e.g. Marchand et al. (2008). CloudSat, however, has an issue arising from surface clutter contamination as a result of radar bins within 750m of ocean surface. Thus, such radar bins are excluded as they are not reliable. CALIPSO carries the Cloud-Aerosol Lidar with Orthogonal Polarization (CALIOP) which operates at a dual wavelength of 532 and 1064 nm. At a horizontal resolution of 333m and a vertical resolution of 30m (below 8.2 Km latitude) and about 60m (between 8.2 and 20.2 Km), CALIOP is sensitive to optically thin layers and become fully attenuated in the presence of clouds with optical thickness greater than 3 e.g. Hu et al. (2009).

Specifically, this study uses the CloudSat Level 2 standard data products namely, the 2B-GEOPROF (Mace et al., 2007) and the 2B-GEOPROF-LIDAR (Mace et al., 2009). The 2B-GEOPROF products contains the radar reflectivity factor and cloud mask information in the vertical column sampled by the CPR while the 2B-GEOPROF-LIDAR products contains information on hydrometeor layer base heights and the layer top for different layers in each CPR vertical scan profile. The latter integrates the CALIPSO (lidar) and CPR (radar) data to estimate the cloud layer in each of the vertical radar bins.

5.1.5.3 Advanced Microwave Sounding Unit (AMSU) and Microwave Humidity Sounder (MHS)

For microwave data, the AMSU and the MHS data products from National Oceanic and Atmospheric Administration (NOAA) polar-orbiting satellites are used to investigate the characteristics of deep clouds. The instruments perform radiation measurements in several channels ranging from 23.8 to 183±7 GHz. AMSU-A has 15 channels ranging from 23.8 to 89 GHz usually called the temperature channels while AMSU-B has 5 channels ranging from 89±0.9 to 183.31±7 GHz known as the water vapour channels as within these frequencies, deeper penetration into the cloud is possible.

AMSU-B, on board NOAA-15, -16 and -17 satellites, is a scanning radiometer with a cross-track scan and an instanteneous field of view of 1.1° which translates to 16 Km by 16 Km in nadir view. Each scan line in AMSU-B has 90 pixels equivalent to a distance of 2120 Km (Kidwell et al., 2009). The MHS has the channels 89, 157, 183.3±1, 183.3±3, and 190.31 GHz at the nadir frequency of 15 by 15 Km with a single scan containing 90 pixels (Puranik and Karekar, 2004). Probing of the atmosphere for moisture can be done within the 3 moisture channels of 183±1, ±3 and ±7.

For the purposes of this study, the AMSU-B and MHS instruments at channel number 150 and 157Ghz (channels along the water vapour absorption lines) are particularly useful as they provide the grounds to probe the atmospheric moisture content of the atmosphere.

5.1.6 ECMWF dynamical fields

ERA5 model products (Hersbach and Dee, 2016) are adopted to extensively diagnose all extreme cases relevant to this study. ERA5 is the latest and fifth generation of European reanalyses produced by the ECMWF and a key element of the Copernicus Climate Change (C3S) and which receives funding from the European Union (EU). ERA5 is going to be the ultimate replacement to the existing ERA-Interim reanalysis before the end of 2019, from 1979 to the current day. Later, an extension of ERA5 back to 1950 is envisaged. ERA5 adds different characteristics to ERA-Interim reanalysis, which makes it richer in term of climate information. The following reasons make ERA5 model data more powerful than its predecessor, ERA-Interim:

1. It uses a state of the art model and a data assimilation scheme ensuring that the product is able to use modern parameterizations of Atmospheric and ocean processes compared to older versions used in ERA-Interim.

2. It is able to use a variational bias scheme for satellite data and ozone, aircraft and surface pressure data.

3. It benefits from reprocessed data sets that were not ready yet during the production of ERA-Interim.

4. It prides a more improved temporal and spatial resolution of one hour and 0.3 degree (about 31 Km) and 137 vertical levels than its predecessor, ERA-Interim, which has a 6-hourly and 0.75° (about 79 Km) temporal and spatial resolution respectively with 60 vertical levels.

5. It provides an estimate of uncertainty through the use of a 10-member Ensemble of Data Assimilation (EDA) at a much coarser resolution of about 63 Km and 3-hourly resolutions.

For the purposes of this study, several two-dimensional (2D) and vertical profile (pressure level) variables from the model are used. 2D variables include total surface precipitation, mean sea level pressure (MSLP), horizontal and vertical moisture fluxes and divergence, CAPE and SSTs. Pressure level variables include horizontal winds (u and v), relative vorticity, relative and specific humidity. For stations lying within a zone where radiosonde ascents are done operationally the raw data from these operational stations are used for the purposes of atmospheric sounding. However, for regions where these operation soundings are absent, the ERA5 reanalysis data of pressure levels, temperature, specific humidity and horizontal winds are adopted for the purposes of analysing the vertical profile of the atmosphere.

5.2 Methods

This section describes the methods used to address the objectives of the study.

5.2.1 Case selection of extreme events

Since this study focuses extensively on the characteristics of the environmental synoptic and meso-scale conditions promoting or inhibiting development of deep convection systems over a contiguous region, percentile-based statistics are initially used to select cases of extreme precipitation. Stations are first categorized based on the regions identified by Indeje et al. (2000). Figure 2.1 shows these regions. However, for the purposes of this thesis, only the coast, lowlands and central regions are considered. To identify a date for diagnostic analysis, both TRMM and gauge data are subjected to percentile-based analysis. The 98^{th} and the 80^{th} percentile thresholds are adopted. In the first case, all gauge data above the 98^{th} percentile are considered per region. The difference between the observed and the percentile is then computed. All differences equal to or less than zero are masked. The total in these differences is then calculated for only those stations whose differences are above zero. This total, as well as the number of stations used for every date, are captured. The same procedure is applied to TRMM pixels within the same period where the total in differences as well as the number of pixels used are noted. For reasons of identifying contiguous precipitation areas per region, the TRMM pixels are sorted in a decreasing order. The dates associated with the first few cases are identified and the intersection between them and those identified from gauges are recorded. A similar procedure is applied for the 80^{th} percentile threshold on gauge and 98^{th} percentile on TRMM. The cases are also carefully chosen to reflect the rainfall seasons namely, MAM, and OND. As such, attempts are made to capture at least two contiguous extreme precipitation scenarios in both cases where possible. However, since the country is prone to data scarcity, extreme precipitation from the TRMM data is adopted for such regions. The vast lowlands region, for example, has only 8 stations. It is noted that in such a situation, there is a likelihood to have non-coherence among the gauge stations even when a wide enough MCS is present as it can be missed by a majority of the stations. It is therefore more prudent to adopt a TRMM-based extreme precipitation case in such circumstances to ensure coherence for large regions. The most ideal case from both criterion forms the basis of dynamical analysis. Appendix B.1 provides a summary of the methodology outlined under this section.

5.2.2 Extremity of the event against climatology

Once the cases have been selected as described in subsection 5.2.1, the event's anomaly from climatology, x_{anom}, is assessed by way of calculating the mean of 21 days centered around the event for all the years with available data and subtracting this mean from the day value, x_{case}. The percentile exceeded or equalled by a pixel/station value against its climatology for daily precipitation is also determined. Percentiles of interest are namely 98^{th}, 99^{th}, 99.5^{th} and 100^{th}. The mean and percentile exceedance equations are shown in equations 5.1 and 5.2

$$x_{anom} = x_{case} - \frac{1}{N}\sum_{i=1}^{n}\sum_{j=-10}^{j=10} x_{ij} \tag{5.1}$$

$$x_{ex} = x_{case} - x_{per} = \begin{cases} 0, & x_{ex} \leq 0 \\ x_{ex}, & x_{ex} > 0 \end{cases} \tag{5.2}$$

where $\bar{x}$ is the climatological mean considering 20 days centred on the event, N is the total number of observations, $j = -10, -9, ..., 10$ are the indices of individual precipitation values per year while $i = 1, 2, ..., n$ are the years. x_{case} is the precipitation value on the day of event while x_{ex} are the exceedances from a given percentile.

5.2.3 Synoptic development and dynamics

Once the cases are selected as discussed in section 5.2.1, what then follows is an investigation into the synoptic drivers and dynamics that precipitated the occurrence of the event. Analysis techniques for these factors are discussed in subsections 5.2.3.1, 5.2.3.2 and 5.2.3.3.

5.2.3.1 Evolution of convection

Loops of SEVIRI Infrared (IR) brightness temperatures and visible reflectances preceding the the events are inspected to identify the spatial extent of the extreme event. Deep convection is characterised by low brightness temperatures and high fractions of visible reflectances. Inspection of certain cloud types e.g. opaque ice, cirrus and overshooting tops from CLAAS algorithm is intended to give insights to the vertical extent of the layers of convection.

5.2.3.2 Mean Sea Level Pressure and the structure of wind flow

Mean Sea Level Pressure (MSLP) is an indicator of regions likely to experience convergence. As such, deep pressure troughs (surface lows) are likely to characterise the development of an extreme precipitation event. Low-level winds are then expected to be predominant in such a deep low pressure zone. Horizontal winds at low levels (between 1000 to 600mb depending on topography) and at upper levels (about 200mb level) are inspected to monitor convergence below and divergence aloft. The rotational wind (relative vorticity) as well as vertical velocity are analysed too. Cyclonic centers are usually associated with rising motion. The fomulars for divergence (convergence) and relative voriticity are given by equations 5.3 and 5.4.

$$D = \nabla \cdot \mathbf{V} = \frac{\partial u}{\partial x} + \frac{\partial v}{\partial y} \tag{5.3}$$

$$\zeta = \mathbf{k} \cdot \nabla \times V = \frac{\partial v}{\partial x} - \frac{\partial u}{\partial y} \tag{5.4}$$

Additionally, the vertical shear of the horizontal wind for a mid and deep layer is calculated as shown in equation 5.5 and 5.6 (see Kutty and Gohil (2017))

$$Shear_{mid} = \frac{V_{sfc} - V_{500}}{sfc - 500} \tag{5.5}$$

$$Shear_{deep} = \frac{V_{sfc} - V_{200}}{sfc - 200} \tag{5.6}$$

where V corresponds to the net wind speed at a particular altitude (sfc, 500, and 200 hPa, where sfc is the lowest pressure level just above the terrain).

5.2.3.3 Analysis of the influence of equatorial waves

An analysis of the influence of synoptic-scale atmospheric waves to the extreme precipitation is done. The equatorial waves have the ability to trigger or suppress convection. The waves to be analysed include Kelvin waves, The equatorial Rossby waves, tropical waves (e.g. the Easterly waves), and the Madden Julian Oscillation (MJO). A methodology on how to perform wave filtering is outlined in Wheeler and Kiladis (1999) with the routine to carry out the filtering adopted from Knippertz et al. (2017). Specifically, the routine is written by Andreas Schluetter (IMK-TRO).

5.2.4 Analysis of preconditions for deep moist convection

According to Doswell et al. (1996), deep and moist convection requires three ingredients, namely:

1. Sufficient quantities of moisture especially within the boundary layer as well as within the lower layers of the atmosphere.
2. An atmosphere where the environmental lapse rate is greater than the moist-adiabatic lapse rate to trigger ascent of moist air parcels (an unstable atmosphere).
3. A lifting mechanism to lift the air parcels to the level of free convection.

Methods used to analyse these preconditions are highlighted in the subsections that follow namely, 5.2.4.1, 5.2.4.2, 5.2.4.3 and 5.2.7.

5.2.4.1 Moisture content analysis and transport

Relative humidity over the region of interest is examined to assess the amount of moisture available especially in the lower layers. In a subsequent analysis (discussed under section 5.2.7) trajectory analysis is carried out through a Lagrangian method to identify the sources of moisture. SSTs from the neighbouring Indian Ocean are inspected to gather information about the state of moisture availability. Higher SST's translate to higher amounts of evaporation. In case the prevailing winds are onshore, the water vapour is advected inland where, if the conditions are sufficient, can trigger convection. Moisture fields are analysed in terms of their horizontal and vertical fluxes and divergence. Of importance is the vertical integral of water vapour flux divergence computed as shown in equation 5.7 (Doswell et al., 1998).

$$F_w = -\int_{p_0}^{p} \nabla \cdot (q\mathbf{V}) \frac{dp}{g} \tag{5.7}$$

where q is the specific humidity, p_0 is the surface pressure, and $\mathbf{V}$ is the horizontal wind. Related to water vapour is the potential temperature (θ) and the equivalent potential temperature (θ_e). θ compares the temperatures at different pressure levels and paths that rising and sinking air parcels will take while θ_e can in addition to what θ does, indicate the moisture content of the atmosphere. Equation 5.8 and 5.9 shows how θ and θ_e are evaluated. The formulas are taken from Bolton (1980).

$$\theta = T\left(\frac{p_0}{p}\right)^{\kappa} \tag{5.8}$$

Where θ is the potential temperature, T is the absolute temperature, p_0 and p are the pressures at 1000hPa and at a particular level while κ is the ratio of the gas constant R and specific heat capacity of air at constant pressure c_p.

$$\begin{aligned}\theta_e &= \theta_L \exp\left[\left(\frac{3036}{T_L} - 1.78\right) r(1 + 0.448r)\right] \\ \theta_L &= T\left(\frac{p_0}{p-e}\right)^{\kappa_d}\left(\frac{T}{T_L}\right)^{0.28r} \\ T_L &= \frac{1}{\frac{1}{T_d - 56} + \frac{log_e(\frac{T}{T_d})}{800}} + 56\end{aligned} \tag{5.9}$$

Where θ_L is the dry potential temperature at the LCL, T_L is approximated temperature at LCL, T is temperature of air at pressure p, T_d is the dew point at pressure p, p is the pressure, p_0 is the reference pressure (1000hpa), e is the water vapour pressure, $\kappa_d = \frac{R_d}{c_{pd}}$ is the ratio of the specific gas constant to the specific heat of dry air at constant pressure (which has a value of 0.2854) and r is the mixing ratio of water vapour mass per unit mass.

5.2.4.2 Conditional instability

As explained in section 3.6, the Yang et al. (2015)'s criteria of conditional instability was adopted. The surface MSE, saturated MSE at 700 hPa and the conditional instability during the cases were calculated using the formulas in equations 5.10, 5.11 and 5.12 respectively.

$$h_s = c_p T_{2m} + L_v q_{2m} \tag{5.10}$$

$$h^*_{700} = c_p T_{700} + L_v q^*_{700} + g z_{700} \tag{5.11}$$

$$c_i = h_s - h^*_{700} \tag{5.12}$$

where h_s is the 2m surface MSE, h^*_{700} is the saturated MSE at 700hPa, c_i is the conditional instability, c_p is the specific heat capacity of dry air at constant pressure, T_{2m} the 2-meter surface air temperature, T_{700} is the 700hPa air temperature, L_v is the latent heat of vapourization, q_{2m} is the surface specific humidity, $q^*_7 00$ is the saturation specific humidity at 700hPa, g is the gravitational acceleration and z_{700} is the height of the 700 hPa layer above the surface.

5.2.4.3 Convective Available Potential Energy/Convective Inhibition

CAPE which is the energy available for air parcels from the LFC to the level of free buoyancy is evaluated at each grid point using equation 5.13.

$$CAPE = g \int_{lf}^{le} \left(\frac{\theta - \bar{\theta}}{\bar{\theta}}\right) dz \tag{5.13}$$

For CIN, the formula is as given in equation 5.14

$$CIN = g \int_{sfc}^{lf} \left(\frac{\theta - \bar{\theta}}{\bar{\theta}}\right) dz \tag{5.14}$$

where θ is the potential temperature of a rising air parcel, $\bar{\theta}$ is the potential temperature of the environment, and sfc, lf and le are the surface, LFC and the equilibrium level for the rising air parcel. Both CAPE and CIN are given in units of $\mathrm{JKg^{-1}}$.

5.2.5 Local rate of change and advection

The total change with time of a variable in the Eulerian frame can be split between the changes that occur locally (at a fixed point) and those caused by advection. For a quantity Q, its total rate of change is given by equation 5.15 (see Holton and Gregory (2012)).

$$\frac{dQ}{dt} = \frac{\partial Q}{\partial t} + \mathbf{V} \cdot \nabla Q \tag{5.15}$$

where $\frac{dQ}{dt}$ is the total change, $\frac{\partial Q}{\partial t}$ is the local rate of change and $\mathbf{V} \cdot \nabla Q$ is the advection term. Advection of a variable, e.g. temperature can explain sudden increases/decreases on the variable's magnitude during unexpected times. An increase in temperature on a clear-skied night over tropical regions might be triggered by a nightime advection from a nearby water body.

5.2.6 Calculation of anomalies

Where it is deemed necessary, dynamical fields are associated with a corresponding anomaly in the period 1979–2018. The computation of this anomaly is based on the consideration of a time-stamp relevant to the calculation pivoted within a ten-day window. For example, to compute the anomaly field of a dynamical quantity, Q, at time-stamp t, we apply equation 5.16.

$$Q_t^{'} = Q_t - \frac{1}{N}\sum_{i=1}^{n} Q_i \tag{5.16}$$

where i is the time index (or count that starts from $i = 1$ to $i = n$). N is the number of time-stamps.

5.2.7 Lagranto (Lagrangian Analysis Tool)

The publicly available LAGRANTO software developed by Wernli and Davies (1997) is used in this thesis to calculate trajectories of humidity from source to rainiest regions.

5.2.7.1 Background

The software uses the Lagrangian approach to calculate trajectories. Lagranto is made to work with ECMWF datasets as well as COSMO model data. There are three adaptations of the lagranto model. The LAGRANTO.ECMWF version, e.g. Sprenger and Wernli (2015), is used to compute air-parcel trajectories based on 6-hourly ERA-Interim as well as 1-hourly ERA5 data on a regular latitude/longitude grid. LAGRANTO.COSMO, e.g. Miltenberger et al. (2013), is the version that is made to be compatible with COSMO output data while LAGRANTO.OCEAN, e.g. Schemm et al. (2017), is the latest member of the Lagranto family adapted to compute ocean-parcel trajectories based on ECMWF's Ocean Reanalysis data. As opposed to the Eulerian approaches used by models where the state of the atmosphere is described at a particular time, the strength of the lagranto tool lies on the usage of a Lagrangian approach that describes the temporal evolution of atmospheric variables along the pathway of a single air parcel.

Lagranto tool has been used recently by Zschenderlein et al. (2018) to investigate the dynamics of the 2016 heat wave over Europe. Sprenger and Wernli (2015) used the tool to identify warm-conveyor belts while Wernli and Davies (1997) used it to analyse the structure of extratropical cyclones. Over Africa, Reiff et al. (1986) used trajectory-based calculations to verify belts of dust over the Sahara desert while D'Abreton and Tyson (1996) used a trajectory approach over southern Africa to determine pathways of moisture.

LAGRANTO.ECMWF version is adopted for this study. We use the relatively high resolution ERA5 pressure-level model data (1-hour and approximately 30 Km temporal and spatial resolution respectively) to drive the lagranto analysis. This analysis aids in tracing the source regions of moisture and the subsequent paths followed towards the target region. Since the method is able to trace various fields, we use it here to infer adiabatic and diabatic changes in air parcels by calculating potential temperature along the trajectory as has been done recently by e.g. Zschenderlein et al. (2018) and Bieli et al. (2015). This is key in aiding the identification of areas of adiabatic subsidence and ascent as well as inferring diabatic changes in air caused by e.g. condensation, turbulent surface fluxes and radiative processess.

5.2.7.2 Lagranto set-up

Lagranto is entirely based on shell scripts that can perform both forward and backward trajectories, e.g. Sprenger and Wernli (2015). During the time when this thesis was being written, the software was downloadable from Wernli H. and Sprenger M. (2018). The site documents all the types of lagranto versions and how to work with the lagranto tool. Basically, an air parcel is traced over time with changing wind conditions where Eulerian data is acquired during this trajectory period. Backward trajectory mode of Lagranto is used here where the starting point is taken as the rainiest grid point of ERA5 at a certain pressure level. A **start file** is created containing the grid point and pressure levels where initialization of the trajectory is desired. Table 5.1 is an example of a lagranto startfile.

Once the *start file* has been created, all meteorological variables of interest are calculated along the trajectories for subsequent time steps. For both cases in this thesis, the pressure levels shown in Table 5.1 are adopted. The Lagranto is set-up such that any trajectory that goes through topography is lifted so that the entire trajectory flow is always above the surface. Pressure level is capped to 500hPa since the essence is to capture processes that occur within the region of high specific humidity where deep moist convection usually takes place.

5.3 Numerical Simulation of precipitation

Numerical simulation of precipitation fields discussed before is carried out. A Numerical Weather Prediction (NWP) model is a suite of computational scripts and algorithms that solves equations that govern atmospheric dynamics for the purposes of making predictions. We utilize the ICON model in this study to assess the representation of the 06 to 06 UTC daily precipitation totals for the events selected in section 5.2.1.

Table 5.1: *Table showing how a typical* start file *from Lagranto looks like. The* start file *for the rainiest ERA5 grid point for the lowlands case study is shown here for illustration purposes only.*

	Lon	**Lat**	**Plevel (hPa)**
1	38.500	2.500	500.000
2	38.500	2.500	550.000
3	38.500	2.500	600.000
4	38.500	2.500	650.000
5	38.500	2.500	700.000
6	38.500	2.500	750.000
7	38.500	2.500	800.000
8	38.500	2.500	850.000
9	38.500	2.500	900.000
10	38.500	2.500	950.000

5.3.1 ICON model: A brief description

The **ICO**sahedral **N**onhydrostatic model (ICON) is a new state-of-the-art global NWP model at Deutscher Wetterdienst (DWD). It was initially launched in Jan. 2015 as a replacement of the operational global model *GME*. ICON is developed jointly by DWD and the Max-Planck Institute for Meteorology in Hamburg (MPI-M).

The development of the model was inspired by the need to develop a nonhydrostatic dynamical core so that the model can be applied over the full range of spatial resolutions relevant to NWP. The model allows for the conservation of atmospheric variables that are naturally conserved e.g. mass, heat and moisture, to address the problem of forecast quality. Discretization of the model equations of ICON is implemented on icosahedral-triangular Arakawa-C grid where the mass points are located in the circumference of each triangular cell. The horizontal velocity component is defined at the edge midpoints. The grid generation is based on the successive refinement of a spherical icosahedron. In the root division step, the edges of each basic triangle are divided into n equal arcs. After connecting all the new edge points by great circle arcs yields n^2 spherical triangles inside the original triangle. The step is followed by k bisection steps where each triangle is further divided into four smaller triangles. The resulting total number of cells n_c and edges n_e is then given by equation 5.17

$$n_c = 20n^2 4^k \quad n_e = 30n^2 4^k \tag{5.17}$$

The corresponding effective mesh size of the model grid is then computed as $\Delta\bar{x} = \sqrt{\frac{4\pi r_e^2}{n_c}}$ where r_e denotes the radius of the earth. A much more elaborate description of the icosahedral-triangular Arakawa-C grid discretization with graphical illustrations can be found in Wan et al. (2013).

In terms of the dynamical core, the ICON model solves the fully compressible nonhydrostatic Navier-Stokes equations of motion, using a set of prognostic variables. The basic equation system is shown in equations 5.18, 5.19, 5.20 and 5.21 representing the equation of motion, conservation of mass, conservation of heat and conservation of moisture.

$$\frac{\partial v_n}{\partial t} + \frac{\partial K_h}{\partial n} + (\zeta + f)v_t + w\frac{\partial v_n}{\partial z} = -c_{pd}\theta_v\frac{\partial \pi}{\partial n} + F(v_n) \tag{5.18}$$

$$\frac{\partial w}{\partial t} + \mathbf{v_h} \cdot \nabla w + w\frac{\partial w}{\partial z} = -c_{pd}\theta_v\frac{\partial \pi}{\partial z} - g \tag{5.19}$$

$$\frac{\partial \rho}{\partial t} + \nabla \cdot (\mathbf{v}\rho) = 0 \tag{5.20}$$

$$\frac{\partial \rho\theta_v}{\partial t} + \nabla \cdot (\mathbf{v}\rho\theta_v) = \tilde{Q} \tag{5.21}$$

To simplify the implicit numerical treatment of the terms representing vertical sound wave propagation, equation 5.21 is rewritten as 5.22.

$$\frac{\partial \pi}{\partial t} + \frac{R_d}{c_{vd}}\frac{\pi}{\rho\theta_v}\nabla \cdot (\mathbf{v}\rho\theta_v) = \hat{Q} \tag{5.22}$$

The prognostic variables of the equation system are the horizontal velocity component normal to the triangle edges, v_n, the vertical wind component, w, density, ρ, and virtual potential temperature, θ_v. The reconstructed tangential velocity component is denoted as v_t, and to be consistent with the model code, it is assumed that (v_t, v_n, w) form a right-handed system. $\mathbf{v_h}$ and $\mathbf{v}$ denote the horizontal and 3D wind vector, respectively. ζ is the vertical vorticity component, f is the coriolis parameter, $K_h = \frac{1}{2}(v_n^2 + v_t^2\ )$ is the horizontal component of the kinetic energy while π is the Exner function. c_{pd} and c_{vd} are the specific heat capacities of dry air at constant pressure and volume respectively while $R_d = c_{pd} - c_{vc}$ is the gas constant of dry air. g is the gravitational constant and $\frac{\partial}{\partial n}$ denotes a horizontal derivative in edge-normal to direction. $F(v_n)$ denotes the source terms for horizontal momentum (e.g. physics parameterizations), while $\tilde{Q}$ and $\hat{Q}$ denote the diabatic heat sources.

5.3.2 Grid-nesting

The grid-nesting approach in ICON is a classical one-way nesting. To get rid of unrealistic wave perturbations at the nest boundaries, the mesh-size ratio is fixed to a value of 2, which implies that one triangular cell is subdivided by edge bisection into four small triangular cells. To ensure numerical stability with explicit time-stepping, the time step in nested domain is reduced in proportion to the mesh refinement ratio. Vertical nesting is available too implying that a nested domain may have a lower top level than the parent domain. The ICON model can also be used in a limited-area mode in which the lateral boundary conditions are prescribed from external data. The workflow at model runtime is as follows:

1. Integrate one time step in the parent domain
2. Compute the lateral boundary condition for the nested domain
3. Integrate two time steps in the nested domain
4. Provide feedback from the nested domain to the parent domain

For nested setups, the time step, Δt, is multiplied by a factor of 0.5 for each nesting level. Δt should be specified for the coarsest domain only. The initial and boundary conditions for the outer domain are the ERA-Interim reanalysis and Integrated Forecast System (IFS) operational analysis. As mentioned before, the lateral boundaries of the inner domains (domain 2 and domain 3) are updated every 120 seconds.

The boundary update mechanism provides the inner domains with up-to-date lateral boundary conditions at each time step. The boundary conditions required are v_n, w, ρ, θ_v, and q_k. Once provided at a time t, the prognostic equations shown in equations 5.18, 5.19 and 5.20 are solved incrementally. The physical parameterizations used in ICON have been partly imported from the COSMO model and partly from the Integraged Forecast System (IFS). The parameterization schemes in ICON include the five-category cloud microphysics scheme that is operational in the COSMO-EU (Doms and Schättler, 2004; Seifert, 2008), the TKE-based turbulence scheme (Raschendorfer, 2001), and the TERRA land-surface scheme (Heise et al., 2006). From IFS, ICON has imported the moist convection scheme (Bechtold et al., 2008), the subgrid-scale orography scheme (Lott and Miller, 1997), the nonorographic gravity-wave drag scheme (Orr et al., 2010) and the Rapid Radiative Transfer Model (RRTM) radiation scheme (Mlawer et al., 1997). This and more information about the ICON model can be found in Zängl et al. (2015).

The Limited-Area-Mode (LAM) setup of ICON is used for simulations in this study. ICON has the capability for static mesh refinement in horizontal directions. This is achieved through a multi-grid approach which implies that one or more additional high resolution domains (*child domain*) can be overlaid on a coarser domain (*parent domain*) a technique known as *nesting*. The three domains in this study namely domain 1 (coarsest, $\Delta\bar{x} = 13.5Km$, $\Delta t = 120s$), DOM02 (less coarse, $\Delta\bar{x} = 6.5Km$, $\Delta t = 60s$), and DOM03 (finest, $\Delta\bar{x} = 3.5Km$, $\Delta t = 30s$) are adjusted as to not feedback on each other. We therefore have a one-way nesting set-up. The nested domain in this study is split into three blocks as shown in figure 5.2. The coarsest domain (dark blue) provides boundary data to the finer (red) domain which provides boundary data to the finest domain. The resolutions in ICON are known as R3B07, R3B08, and R3B09 corresponding to $\Delta\bar{x} = 13Km$, $\Delta\bar{x} = 6.5Km$ and $\Delta\bar{x} = 3.25Km$ resolutions. At a resolution such as the one in domain 3 of 3.25 Km, explicit representation of convection is possible.

5.3.3 Evaluation of model outputs

Prediction of rainfall occurence is much easier than predicting the amount in a given location e.g. Doswell et al. (1996). Thus, suitable methods for evaluation of a model performance in simulating rainfall should bear this in mind. Two spatial based evaluation methods were adopted for this study namely, the SAL spatial verification method applied to precipitation outputs and the Fractional Skill Score (FSS) method applied to evaluate cloud top temperatures. The methods are described in subsequent sections.

5.3.3.1 The SAL spatial verification score

The SAL spatial verification method (Wernli et al., 2008) is a superior method of evaluating model performance based on its ability to cure the grid point to grid point comparison between model and observations which can lead to heavy double penalty as each grid point can be penalized twice. For example, assuming that a precipitation object was forecast at location x but measured at location $x + \Delta x$, a false alarm would inevitably be made for location $x + \Delta x$ and as a consequence, a miss would be produced

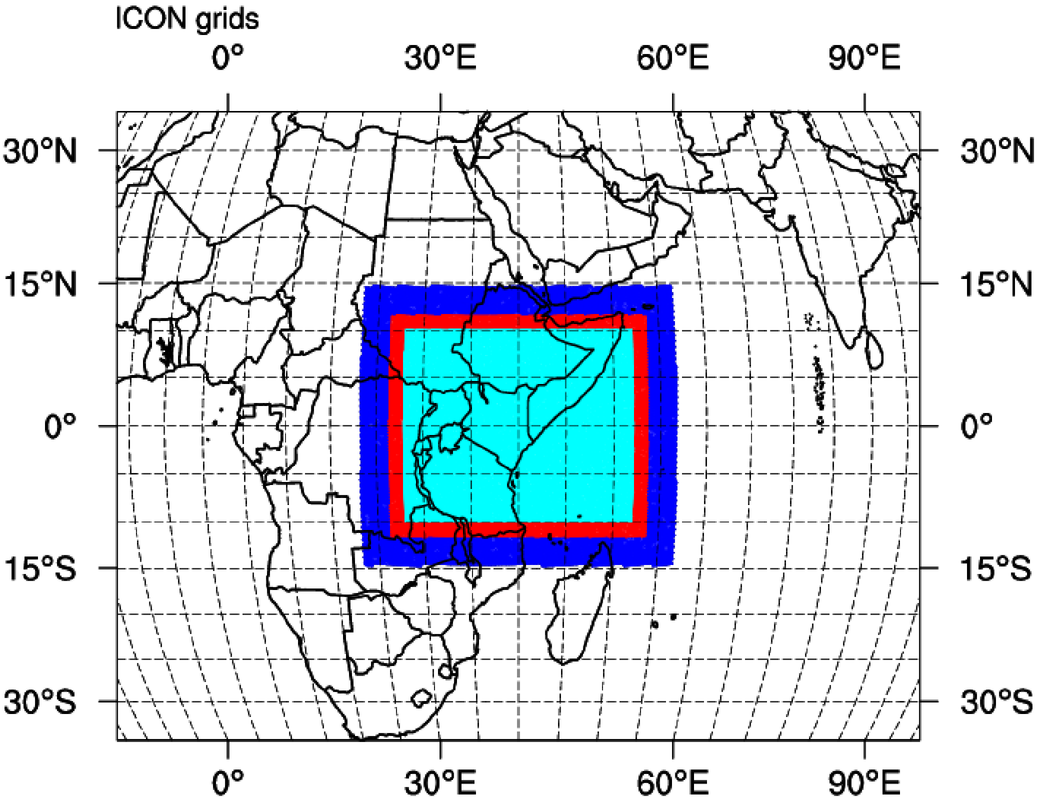

Figure 5.2: *The structure of the the nested domain. The dark blue domain is domain 1 (R3B07) which is the coarsest with a model resolution of* $\Delta\bar{x} = 13Km$ *and* $\Delta t = 120s$*. The red domain is domain 2 (R3B08) the coarser domain with a resolution of* $\Delta\bar{x} = 6.5Km$ *and* $\Delta t = 60s$ *while the light blue zone is the finest resolution domain (R3B09) at* $\Delta\bar{x} = 3.5Km$ *and* $\Delta t = 30s$*.*

at location x. This mere shift in precipitation area is penalized twice in this case. The SAL method, which is an object-based verification method, attempts to link precipitation objects between the model and observations. *Eye-ball* method can actually detect these linkages but SAL attempts to transform the method to an objective detection algorithm.

SAL compares features between model and observations in structure (S-component), amplitude (A-component) and location (L-component). Both model and observations must have the same horizontal grid spacing and be available in the same area. To calculate S- and L- components, the Wernli et al. (2008) procedure is adopted as follows:

a) Identify the domain area of precipitation

b) Define a threshold R_{thresh} upon which precipitation patterns shall be carved out. Recommended threshold is to use $\frac{1}{15}$ of the 95^{th} percentile of all grid point values in the precipitation field for values greater than 0.1 mm.

c) Based on the threshold, create a Boolean matrix where "0" stands for precipitation values less than R_{thresh} and "1" stands for precipitation values greater than or equal to R_{thresh}.

d) Use a clustering algorithm to define precipitation patterns.

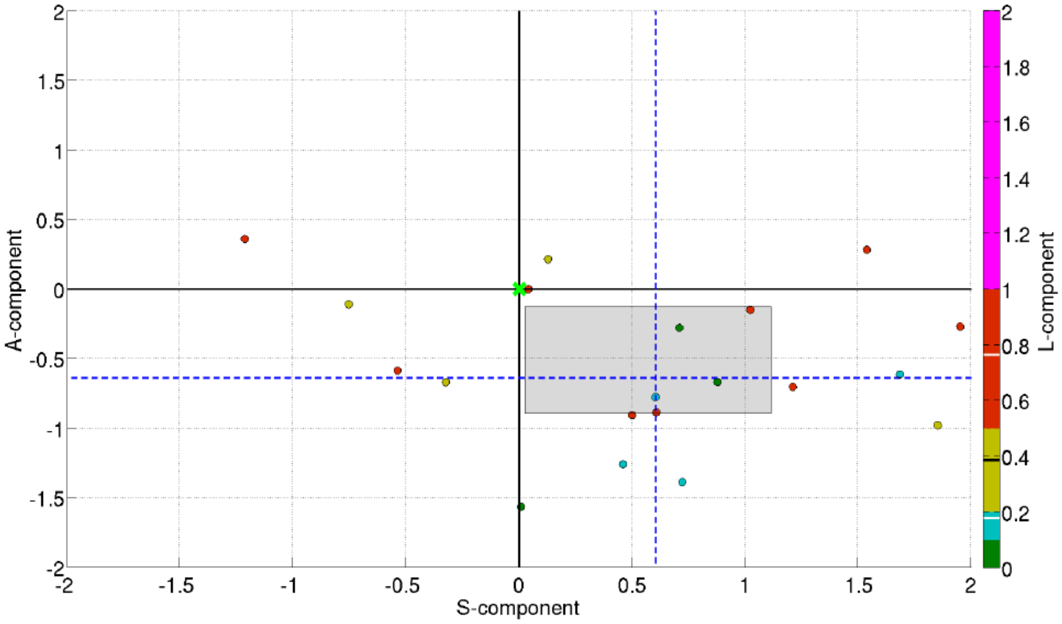

Figure 5.3: *Example of a SAL plot. The S-component is represented through the x-axis, the A-component through the y-axis and the L-component is marked with a colorbar. The interquartile range for each component is represented through the grey rectangle (for S and A) and through the bold white bars in the colorbar (for L). The median values for all SAL components are shown by the blue dashed lines (for S and A) and by the bold black bar in the colorbar (for L). Figure taken from Röhner (2016)*

e) Compute the size (number of grid points), the integrated precipitation amount (sum of precipitation) and a scaled volume (precipitation sum divided by the max precipitation) for each pattern of precipitation with more than three grid points.

f) The A-component which signals over- or under-estimation of precipitation within the domain D is given by

$$A = \frac{2(D_{mod} - D_{obs})}{D_{mod} + D_{obs}} \tag{5.23}$$

g) The S-component which gives information about size and shape of both precipitation fields is derived through the weighted means of all patterns (scaled volumes V_{mod} and V_{obs}) where orientation is not taken into account. Its given by:

$$S = \frac{2(V_{mod}) - V_{obs}}{V_{mod} + V_{obs}} \tag{5.24}$$

h) Determine the center of mass of each pattern and the total mass center for both precipitation fields, x.

i) Compute the L-Component using the weighted averaged distance, r, between the individual mass centers and the total mass center. The first location component, L_1, measures the normalized distance between the centers of mass of the modeled and observed precipitation fields while the second location component, L_2 aims to distinguish patterns with same center of mass but overlapping as to insinuate one predicted precipitation object. They are formulated as follows.

$$L_1 = \frac{x^2_{mod} + x^2_{obs}}{d} \tag{5.25}$$

$$L_2 = \frac{2|r_{mod}^2 + r_{obs}^2|}{d} \tag{5.26}$$

Finally, the location component is given as:

$$L = L_1 + L_2 \tag{5.27}$$

S- and A-components have a range of values within $-2 \leq x \leq 2$ while the L-component has a range between 0 and 2. A perfect match arises between model and observations if all components of SAL are zero. if $S < 0$ $S > 0$, the precipitation patterns in the model are smaller (larger) than in the verification field. For $A < 0$ ($A > 0$), the precipitation patterns in the modeled field are weaker (stronger) than in the verification field. The larger the L, the more the spatial variance between the precipitation patterns in the modeled and the verification field. Visualization of the SAL is usually done using a 2-D plot where A- and S-components are the ordinate and abscissa respectively while L-component is usually shaded with a color (see figure 5.3.)

5.3.3.2 Fractional Skill Score (FSS)

This spatial verification score introduced sufficiently by Roberts and Lean (2008) and expanded upon by Roberts (2008) was adopted to verify high resolution ICON cloud top temperatures against the satellite-based SEVIRI IR brightness temperatures. The method is intended to give a variation of skill with spatial scale from high resolution forecasts. To compute FSS, the following steps are taken:

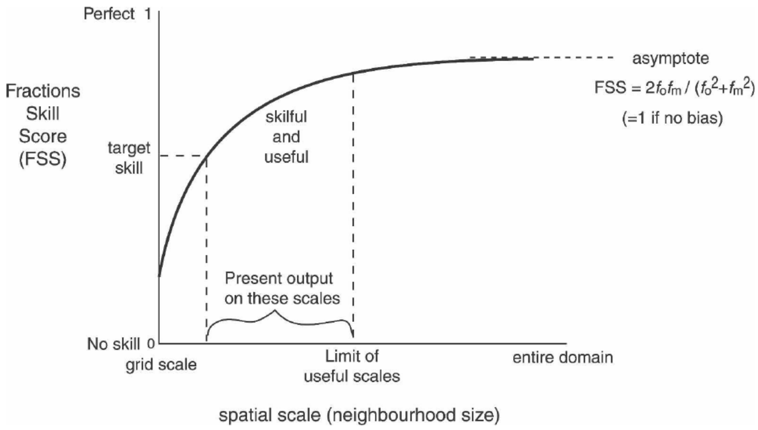

Figure 5.4: Schematic graph of FSS skill against spatial scale. f_0 is the fraction of observed points exceeding the threshold over the domain. f_m is similar to f_0 but for the model. Taken from Roberts and Lean (2008).

a) Select a threshold for the forecast and verification field where the forecast field has to be projected to the verification field and create a boolean matrix.

b) Compare the neighbourhood of each forecast grid point to the neighbourhood of the verification grid point using a ratio of grid points exceeding the threshold within the neighbourhood.

c) Repeat the above step while enlarging the neighbourhood size until the entire domain is compared. This aids in the comparison of how forecast varies with neighbourhood size.

d) Identify the smallest neighbourhood size that provides a sufficiently skillful forecast. Figure 5.4 taken from Roberts and Lean (2008) describes this bullet aptly.

FSS tends to 1 when the entire domain is averaged. According to Roberts and Lean (2008), a skillful spatial scale is given by $FSS > 0.5 + \frac{f_q}{2}$, where f_q is the observed fractional quantity (e.g. rainfall) coverage over the domain.

Chapter 6

Case Selection

This chapter presents the results obtained after the application of the analysis method described in section 5.2.1. For purposes of this work, only three cases were chosen. The cases considered were such that they represented at least a distinct homogeneous region in precipitation. These regions are defined in Indeje et al. (2000). The dates were chosen from TRMM and Gauge 24-hour accumulated precipitation between 0600–0600 UTC (A06) based on pixel and gauge exceedances. The routine employed searched for the largest precipitation object based on the eight neighbouring and touching pixels based on the Queen's case contiguity (Lloyd, 2010) within the 1998–2014 period. The most ideal coinciding dates between TRMM and gauge were, thereafter, selected based on the highest number of TRMM pixels exceeding the 98^{th} percentile and the highest number of gauge stations exceeding the 98^{th} and (where this high percentile was unattainable) the 80^{th} percentile. Due to vastness of the regions considered and the limited number of gauges per region, TRMM A06 was accorded higher preference in case identification. An example is the Lowlands and the Central Highlands cases where, notwithstanding the few (or zero) number of gauges that surpassed the 98^{th} percentile in climatology, the cases were selected because of the spatial size of contiguous pixels identified from TRMM A06 since at least 90% of the gauges had already surpassed the 80^{th} percentile in climatology.

Table 6.1: *Chosen coinciding dates between TRMM and Gauge based on the largest precipitation object defined as the maximum number of connected pixels whose A06 exceeded the 98^{th} percentile (**P>98**) and the maximum number of gauges whose A06 exceeded the 98^{th} percentile (**S>98**). Where this percentile was unattainable for the gauges, the percentile was relaxed to 80^{th} (**S>80**). **nP** and **nS** denotes the maximum number of TRMM pixels and gauges within the geographical boundary of a region respectively. Percentiles are computed within the period 1998-2014 and only those days whose precipitation was at least 1 mm were considered.*

	Case	**nP**	**P>98**	**nS**	**S>98**	**S>80**
Coast	2007-05-14	75	42	6	4	5
Lowlands	2011-10-29	328	87	6	1	5
Central	2012-12-29	134	59	11	2	6

For the Coastal Lowlands, 42 pixels from TRMM A06 were found to have been contiguous on 14 May 2007 representing a single precipitation object covering 56% of the region. At the same time, four gauge stations within the region were found to have recorded precipitation above the 98th percentile within the period 1998-2014. Lowering the percentile to 80th had the effect of adding one more station to the former four identified at 98th. Thus, five stations surpassed the 80th percentile. For the Lowlands, the TRMM A06 exceeding the 98th percentile was such that the largest precipitation object was characterised by 87 contiguous TRMM pixels representing about 26% of the entire geographical area on 29 Oct. 2011. Incidentally, only one gauge station had its A06 greater than the 98th percentile during this selected date. However when the percentile was relaxed to 80th, four more stations attained extreme status. A similar case was found for the Central Highlands whose selected date of 29 Dec. 2012 was such that the largest precipitation object had 59 out of 134 pixels representing about 44% of the geographical boundary. For this case however, two gauge stations had their A06 exceed the 98th percentile. Nevertheless, when the percentile was lowered to 80th, six stations were found to have their A06 exceed this threshold and therefore extreme by definition.

Figure 6.1 shows the most spatially contiguous extreme precipitation days highlighted in Table 6.1 for each region determined from TRMM A06 product. The chapters that follow diagnose extensively the selected cases as described in chapter 5.

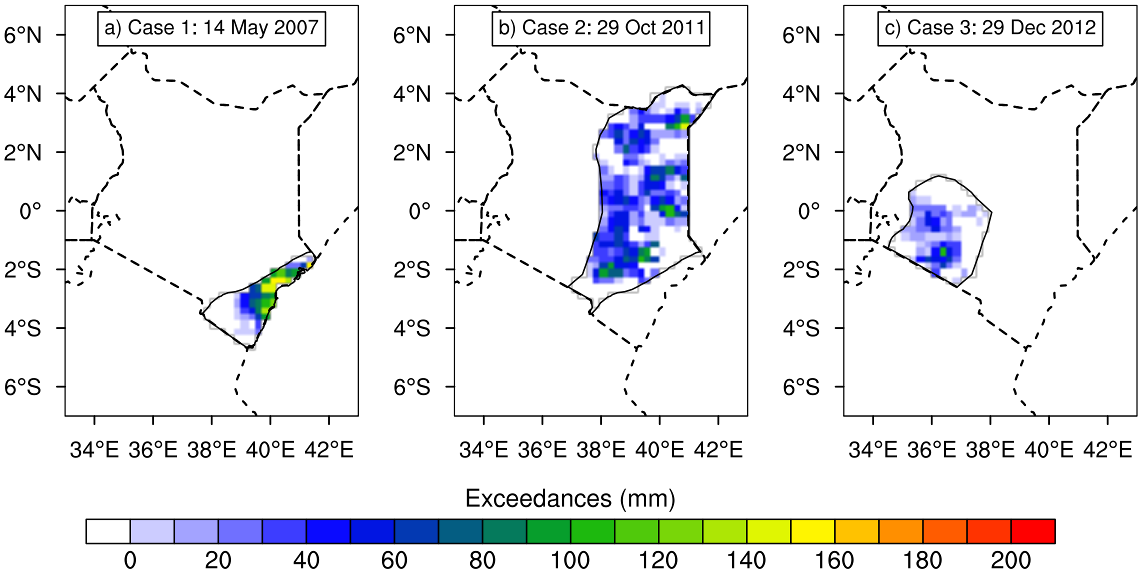

__Figure 6.1:__ Contiguity of the three selected events. Colors show TRMM A06 exceedances from the 98th percentile for a) 14 May 2007, b) 29 Oct. 2011 and c) 29 Dec. 2012 for the Coastal Lowlands, Lowlands and Central Highlands respectively. Black solid line demarcates the regions of study namely, a) Coastal Lowlands, b) Lowlands and c) Central Highlands. Only A06 >= 1 mm used in computation of exceedances. Notice that exceedances outside each demarcated region are masked.

Chapter 7

Case 1: Coastal Lowlands 12–14 May 2007

This chapter presents the results for the analysis of the extreme precipitation event that occurred on 14 May 2007 and diagnoses its possible causes. The results are arranged systematically by first documenting the magnitude and strength of the system followed by a documentation of the large-scale influences and thermodynamics that promoted and sustained the event. Results from numerical simulation using the ICON model over the Coastal Lowlands are discussed in later subsections.

7.1 Case overview from gauge and TRMM data

Torrential rains exceeding the 98th percentile from both TRMM and gauge observations in the period 1998–2014 hit the coastal strip of Kenya between 06 UTC 13 May and 06 UTC 14 May, 2007. The event was significant due to its widespread nature as well as on the amount of precipitation received. According to a Red Cross report published online on their ReliefWeb[1], close to 30,000 people were either directly or indirectly affected by the flash floods along the towns of Mombasa, Malindi, Kilifi, Witu, Mpeketoni, Kipini, and Garsen which had lasted for four continuous weeks with tens of deaths recorded and families displaced. The event brought about sanitation problems leading to emergence of waterborne diseases, severe damage to infrastructure, schools, farmlands, destruction of livelihoods as thousands of houses were submerged killing people directly or indirectly through starvation and lack of shelter.

Rain-gauges across the Coastal Lowlands of Kenya as well as satellite-based observational platforms (in this case TRMM) recorded above normal values of A06 with respect to 1998–2014 climatology. Just to illustrate, A06 of between 70 and 150 mmday^{-1} were recorded in four out of six Coastal Lowlands rain-gauges with one station (Malindi meteorological station) recording the highest amount amongst all the other rain-gauges at 153.4 mmday^{-1} representing 99.94th percentile exceedance of its daily climatological rainfall as shown in Table 7.1. Ordinarily, the mean[2] amount of rainfall in this town during this day is about 9.3 mmday^{-1}. Indeed, four Coastal Lowlands stations showed a climatological mean of between 9 and 11 mm while their records for this date were between 70 and 160

---

[1] This is an online leading humanitarian information source on global crises and disasters within the United Nations office for the Coordination of Humanitarian Affairs (OCHA).

[2] Calculated by taking 10 days centred on the event

mm. The violin[3] plot in figure 7.1 shows the extremity of A06 vis-à-vis climatology. A06 in most stations exceeded the 98th percentile. Although Voi meteorological station located further inland did register above normal rains with respect to climatology, the amount on this day was not as appreciable compared to stations located along the coastline. The station, though demarcated as a Coastal Lowlands station, usually exhibits characteristics of an inland lowland station. A possible explanation for this behaviour is that advection of moist air from the neighbouring Indian Ocean onshore precipitates much earlier over areas adjacent to the Indian Ocean further denying inland stations sufficient moisture for convection. The fact that all *in-situ* and satellite-based observations agreed in terms of the strength of the event against their climatology, including observational precipitation values higher than at least the 95th percentile, was further proof of the severity of the event.

Table 7.1: *A06 statistics for both TRMM (T) and Gauge (G) on 14 May 2007 showing their mean value (Tmean and Gmean) and the corresponding percentiles exceeded (Tpex and Gpex) between 1998 and 2014 over the Coastal Lowlands. The TRMM A06 is the 9-pixel mean value around a rain-gauge station. The mean is calculated as the average value for all years considering ten days pivoted on the event. Percentiles are calculated for all days with precipitation where a rainy day had at least 1 mm of A06.*

Station	T (mm)	Tmean (mm)	Tpex	G (mm)	Gmean (mm)	Gpex
Lamu	151.47	6.00	99.89	28.60	10.4	88.47
Voi	63.23	2.00	99.94	12.50	0.6	73.44
Msabaha	159.63	6.60	99.99	135.30	9.4	99.99
Malindi	171.79	6.10	99.99	153.40	9.3	99.94
Mtwapa	106.43	5.90	99.95	102.70	10.7	99.31
Mombasa	88.77	6.20	99.91	72.50	7.3	98.84

The 9-pixel A06 mean for TRMM showed a similar pattern despite the data set tending to overestimate precipitation. Table 7.1 shows that all 9-pixel TRMM A06 means indeed exceeded the 99th percentile while all gauges except one exceeded the 80th percentile with all the stations along the coastline apart from one (Lamu meteorological station) exceeding the 98th percentile. It is important to note that gauge and TRMM observations appeared to be in phase in representing the case though TRMM tended to make an overestimation compared to the gauges as shown in figure 7.2a. However, since TRMM relies heavily on a multi-assembly of level 2 TRMM datasets described in section 5.1.2, the irregularity of overpasses[4] caused by the limited number of TRMM space vehicles can stifle the analysis the much needed microwave data that usually enriches the output level 3 product after preprocessing. It is deduced that TRMM A06 for this date was almost the highest between 1998 and 2014 within a ten-day window centered around the event date (figure 7.3a). In additional to the magnitude of the event being way above average, it was also observed that the A06 from TRMM was contiguous with at least 56% of connected pixels[5] (or 42 out of

---

[3] A modified form of a boxplot showing distribution of data e.g. Azarian et al. (2018)

[4] These are the overhead flights for polar-orbiting satellites like TRMM which scan the ground beneath them by sending signals and measuring the returned echoes.

[5] Queen's case contiguity that demands that 8 pixels must neighbour the cell in question (Lloyd, 2010).

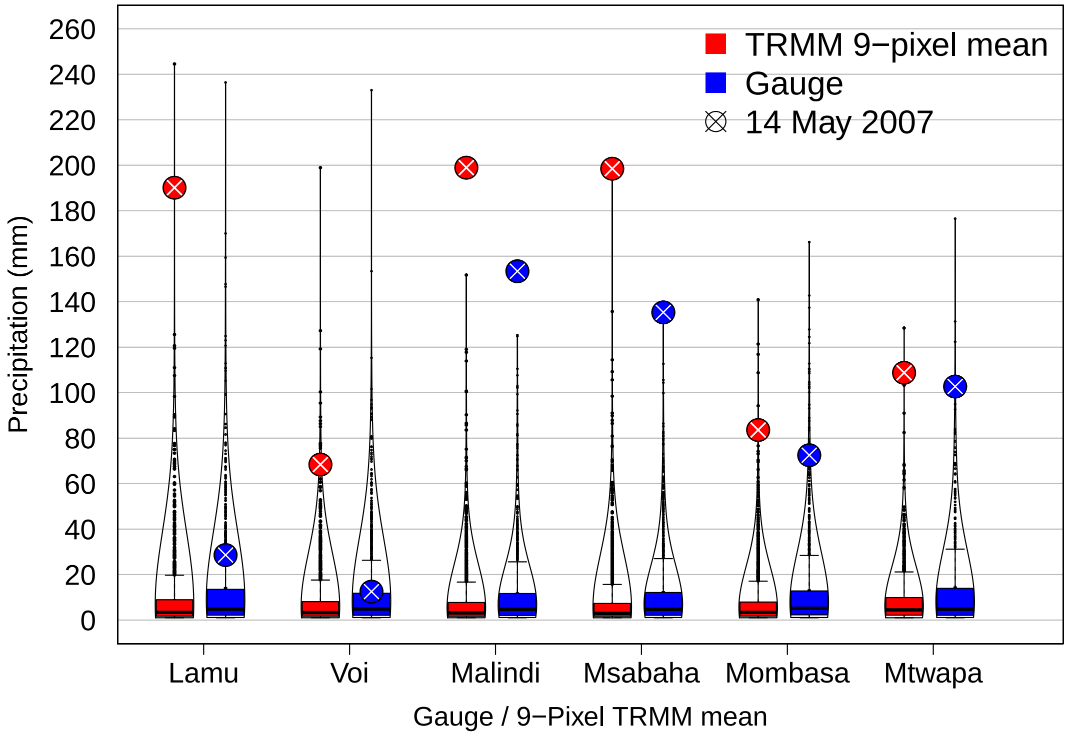

Figure 7.1: *A violin plot showing extremity of the event within the period between 01 Jan. 1998 and 31 Dec. 2014 for TRMM3B42 product aggregated to daily between 0600 to 0600 UTC (to correspond with rain gauge observational norm; shown in red) and a similar distribution but for rain gauges over the Coastal Lowlands (shown in blue). Markers show the event of 14 May 2007 when the contiguous extreme event was recorded. TRMM aggregation was based on the 9-pixel mean surrounding each station. Only days with rainfall greater than 1mm within the climatology are considered.*

75 connected cells, Table 6.1) surpassing the 98th percentile within the Coastal Lowlands. Agreement scores on pixel to gauge between TRMM and rain-gauge stations throughout Kenya for the period 1998 - 2014 can be found under appendix A.2.

7.2 24-hour accumulated precipitation between 0600–0600 UTC fields from ERAI and ERA5

Representation of the A06 totals was equally assessed using the ECMWF precipitation forecast fields. This endeavour was deemed necessary to ascertain the plausibility of the model in diagnosing evolution of the event translating to convection and subsequent precipitation. The ECMWF fields are always initialized at 0000 and 1200 UTC everyday. Forecasts are then made every hour (for ERA5) and every six hours (for ERAI). Analysis of both reanalyses outputs showed that precipitation over the coastline tending offshore was substantial - underestimation notwithstanding. Highest values recorded by ERAI over the Coastal Lowlands were in the range of 20 to 50 mm which was similar to the observations made from ERA5 data as shown in figure 7.2b and 7.2c. ERA5 however, produced intense precipitation of comparable magnitude to TRMM towards the northern part just outside the Coastal Lowlands, a situation that was absent in ERAI.

However, the higher resolution ERA5 helps to bring out the details on the distribution of precipitation which is otherwise averaged out by ERAI. The smoothed fields in ERAI as compared to ERA5 might introduce inherent problems especially over the region of study

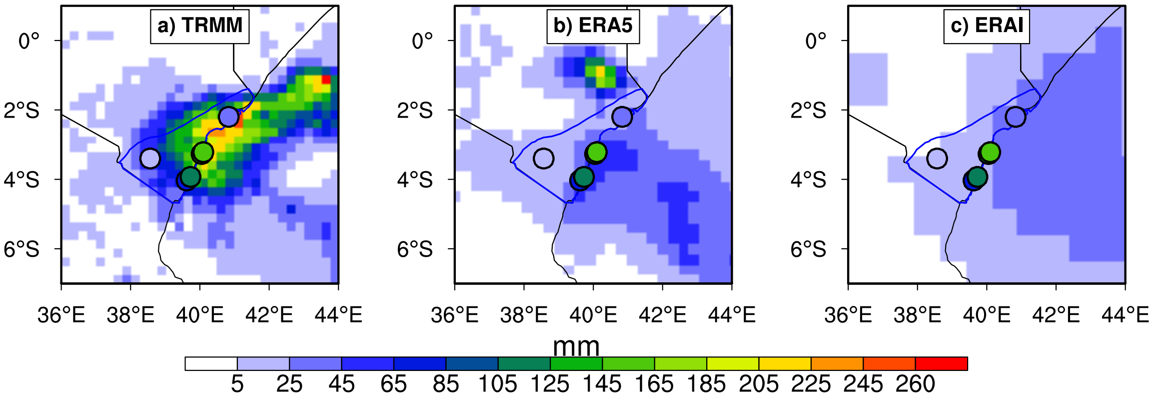

Figure 7.2: Spatial distribution of A06 over the Coastal Lowlands during 14 May 2007 for a) TRMM, b) ERA5 and c) ERAI model outputs. The gauge amounts are annotated by circular markers whose color scale is the same as the one for the filled contours. The Coastal Lowlands is shown by the blue outline.

since precipitation distribution is found to vary strongly within short distances. Factors outlined in section 5.1.6 renders ERA5 the reanalyses model of choice in representing convection. It is against this backdrop that subsequent analysis was carried out using ERA5 data. Figure 7.3b and 7.3c show a spatial map of exceedances of A06 for ERA5 and ERAI respectively. Although the two model output data sets showed rainfall totals exceeding 98th and 99th percentile threshold within the boundaries of the region of study coinciding more or less to areas covered by TRMM exceedances, none of the two data sets showed the highest attainable values in the period 2000-2014 and 1979-2014 for ERA5 and ERAI respectively. The highest attainable values in climatology for both ERA5 and ERAI sets were found slightly outside and to the north of the region. Nevertheless, these extreme precipitation exceedances from ERA5 model outputs - which to a large extent were found to coincide with TRMM exceedances - provide justification to use the underlying reanalyses fields for subsequent dynamical analysis.

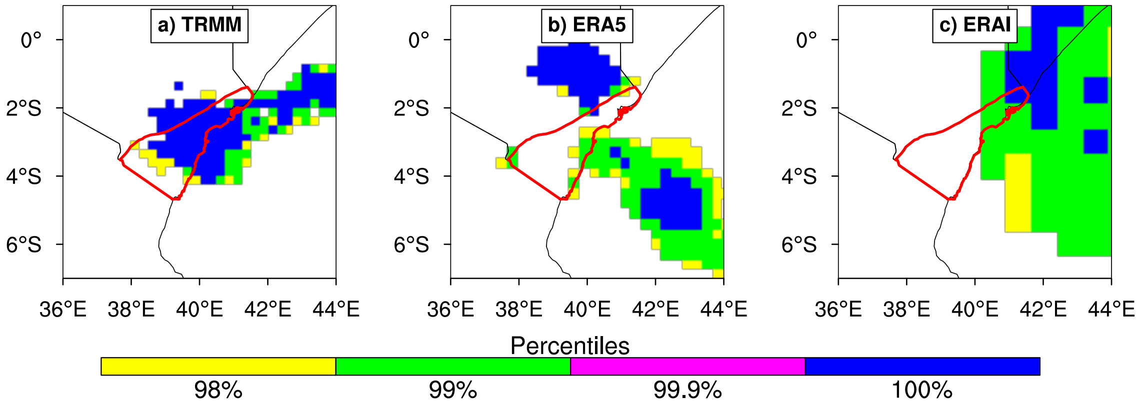

Figure 7.3: Various percentile thresholds, namely, 98, 99, 99.9 and 100% equalled or exceeded by A06 during 14 May 2007 for a) TRMM, b) ERA5 and c) ERAI. The percentiles are calculated based on a 20-day window period centered around the event date of 14 May 2007. Climatology years are 1998-2014, 2000-2014, and 1979-2014 for TRMM, ERA5 and ERAI model outputs respectively. Red outline demarcates the Coastal Lowlands.

7.3 Sub-daily evolution of the event

The preceding section presents an overview of the magnitude of the event in terms of A06 without showing how the event evolved. This section is dedicated to presenting results from sub-daily evolution of the event spatially and temporally. Since TRMM, CMORPH, SEVIRI and METAR reports have temporal resolutions higher than 24 hours, they were deployed to investigate the sub-daily characteristics of the event. In addition, satellite overpasses of TRMM, AMSU/MHS and A-train (CALIPSO and CloudSat) have been utilised as well.

Hours leading up to the event on 14 May 2007 reflected an active troposphere. Figure 7.4 shows evolution of the event between 06 UTC 13 May to 06 UTC 14 May 2007. On average, moderate to deep convective clouds were found to characterise the troposphere intermittently between 06 UTC 13 May and 06 UTC 14 May 2007. Note that low SEVIRI Infrared brightness temperatures at 10.8μ (BT) are a proxy for deep convection as they infer the height of a cloud. Shallow to moderate convection was found to develop between 06–15 UTC 13 May where BT gradually decreased from about 250 K to just below 240 K[6]. This was also reflected in the 3-hourly accumulated precipitation from CMORPH and TRMM where precipitation gradually increased on average between 09 and 12 UTC 13 May. A TRMM-2A12 overpass recorded the initial stages of the event at around 0542 UTC 13 May showing moderate to heavy showers with the northern part of the Coastal Lowlands reporting showers of between 4 and 7mm as shown in figure 7.5a. An A-train overpass between 1104 UTC and 1117 UTC May 13 (polar orbital path shown in figure 7.7a) pointed to a developing convective system. The vertical depth of the system during this time when A-train satellites scanned the region was about 15 Km. The depth was characterised primarily by cirrus clouds between 14 and 15 Km above ground and a relatively deep convective system between 5 and 14 Km in the vertical captured by CALIPSO lidar as shown in figure 7.7b. The rest of the vertical extent appeared transparent to the lidar beam with no much activity below 5 Km. However, CloudSat - a twin sister of CALIPSO - reflected a brightband[7] between 4 and 7 Km above ground as shown in figure 7.7c. A brightband is usually a clear reflection of stratiform precipitation as argued by Houze et al. (2015).

Between 15–18 UTC, the moderately deep clouds dissipated as BT rose to about 260 K. Formation of new cloud cells ensued after the dissipation of the former, but this time, at a faster rate between 18 UTC and midnight. BT went to as low as 235 K at 00 UTC reflecting a tentatively deep system. During this period, an AMSU-B instrument overflew the Coastal Lowlands. The 150 GHz microwave channel of AMSU-B reported brightness temperatures of as low as 160 K near the center of the system less than an average of 10 miles off the coastline as shown in figure 7.5b. At these temperatures, the microwave channel interpretation is a deep convection laden with hydrometeors due to a reduction of brightness temperatures by scattering of large ice particles e.g. Redl et al. (2015). This was also the window period when precipitation peaked to reach highs of 23 mm in 3 hours between 18–21 UTC as reflected by the spatially-averaged TRMM precipitation in figure 7.4. Within the same window period, CMORPH showed a somewhat similar precipitation signal with the highest amount of 18 mm in three hours recorded at just about midnight.

Availability of a METAR report at the Moi International Airport in Mombasa as-

---

[6] BT brightness temperatures below this value reflect deep convection e.g. Rempel et al. (2017); Feidas and Giannakos (2012); Tobin et al. (2012)

[7] A layer characterised by melting of ice and snow

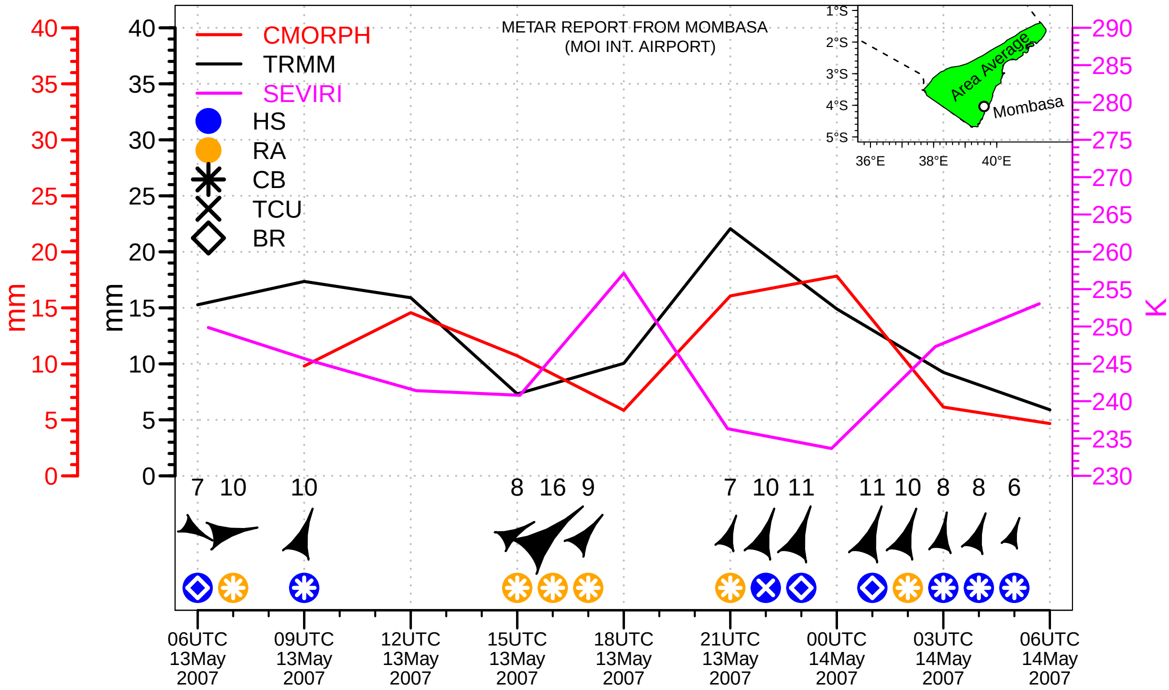

Figure 7.4: *Three-hourly evolution of precipitation and convection between 06UTC 13 May to 06 UTC 14 May 2007. Shown are the spatially averaged precipitation from CMORPH (red, mm) and TRMM (black, mm) as well as the spatial mean of BT from SEVIRI (pink, Kelvin). Symbols represent the METAR report for Moi international airport, Mombasa between 13 and 14 May 2007. The Key is as follows: HS: Heavy showers, RA: Moderate to heavy rain, CB: Cumulonimbus clouds, TCU: Towering cumulus clouds, BR: Broken clouds. Arrow heads represent wind vectors which show wind direction from the true north while annotated numbers are the wind speeds in m s^{-1}. Blue region in the inset map shows the Coastal Lowlands - the area where the spatial averaging was done. Geographical location of the Moi International Airport, Mombasa where METAR report was available is shown by a ring in the inset map.*

certained the situation leading to the event of 14 May 2007 as reported by other data sources. Symbols in figure 7.4 represent the evolution of weather as reported at the airport at irregular hourly intervals. The METAR report differed slightly on sub-daily scale with the satellite-based products because, the latter is spatially averaged over the entire Coastal Lowlands with the bulk of severe weather located towards the north-eastern part whereas the station whose METAR report was analysed here is located towards the south-western part of the region as shown in the inset map of figure 7.4. Nevertheless, the station reported intermittent heavy showers from broken clouds in the early hours of 13 May alternating with moderate to heavy rain with towering cumulus clouds. TRMM and CMORPH also showed signs of moderate rains during these dawn hours too. The winds were predominantly westerly between 06 UTC and 08 UTC but later turned south-westerly throughout the day leading to the morning of 14 May 2007. The wind speeds were moderate during the morning hours rising to a maximum of about 10 m s^{-1} at 09 UTC 13 May. There were no METAR records during the mid-morning hours (10 - 14 UTC). However, moderate to heavy precipitation was reported over the station between 15 – 18 UTC even though this is the window period when there was not much activity as observed from the satellite-based products namely, CMORPH, TRMM and SEVIRI. Wind speeds were the highest here compared to the rest of the day ranging between 8 and 16m s^{-1}. Even though no METAR reports were available between 18 – 20 UTC, the available reports at 21 UTC confirms the occurrence of a heavy storm alternating with showery convection. Towering cumulus and broken clouds were reported during the late hours of the night going into midnight.

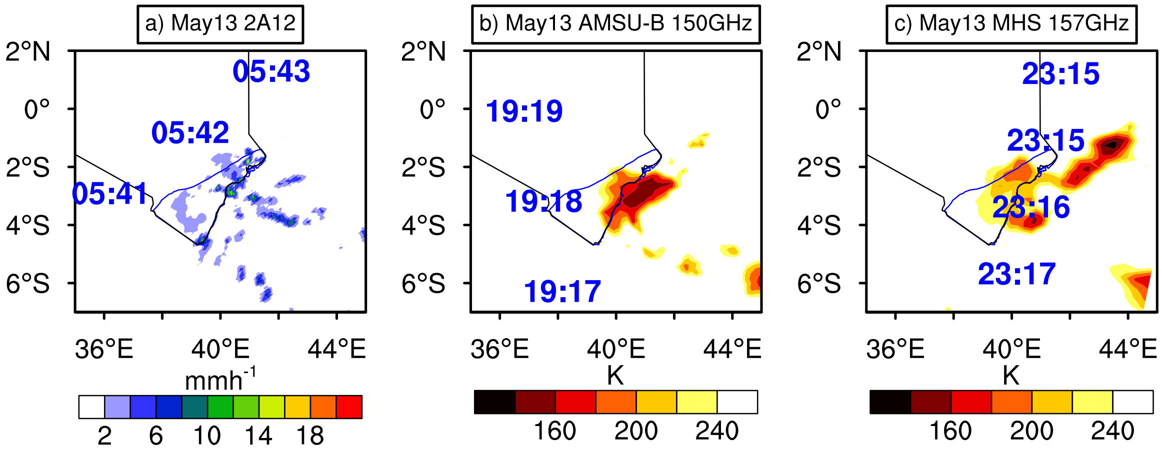

Figure 7.5: Selected overpasses of TRMM level 2 product (2A12), AMSU-B and MHS instruments. a) is the surface precipitation rate from TRMM 2A12 product at 0542 UTC, b) shows BT at the microwave channel of 150GHz from the AMSU-B instrument at 1918 UTC while c) depicts BT at 157GHz from the MHS instrument at 2315 UTC. Annotated numbers show the actual time when the overpass was flying over the Coastal Lowlands.)

Indeed, 15-min BT loops over the Coastal Lowlands (only a few selected images from the loops are listed here) showed shallow clouds beginning to form offshore at 18 UTC 12 May 2007 (figure 7.6a). The shallow clouds intensified as they moved onshore and became a moderate twin system approaching the shore 6 hours later (figure 7.6b). This dual system was already over the region at 0415 UTC (figure 7.6c) and had even shifted a few hundred miles inland at 1515 UTC. During this time, a deep system was already offshore a few kilometers from the mainland while another fully-developed system was trailing it further offshore (figure 7.6d). The CLAAS algorithm confirmed the presence of an already deep system during this hour some miles offshore (stippling in figure 7.6d). The deep system observed further offshore at 1515 UTC rapidly shifted onshore towards the Kenyan coastline and enhanced the intensity of the already moderately deep system near the coastline and together created an even deeper system with cloud top temperatures below 200 K. This was also the period when the region a few miles offshore and over a wide area was characterised by overshooting towers of convection whose cloud top temperatures were in the order of 180 to 190 K (figure 7.6e).

In fact, the same convective organisation was reported as well by the 150 GHz AMSU-B microwave channel overpass at around 1918 UTC (figure 7.5b). This deep[8] system is hypothesized to have resulted to the heavy precipitation episode between 18 UTC 13 May and midnight as has been shown previously by the spatially averaged TRMM and CMORPH precipitation (figure 7.4). The deep system was then observed to retreat offshore towards the Somali coast (figure 7.6f) where overshooting towers of convection as well as the low brightness temperatures were observed to retreat offshore towards the coast of Somalia. Indeed, a 157 GHz microwave channel of the MHS at 2315 UTC showed the leading edge of the system retreating offshore towards the Somali coast while part of the system trailed over the northern part of the Coastal Lowlands contributing to enhanced precipitation as reported by TRMM and CMORPH between 21 UTC and midnight. The system eventually dissipated as it encroached further into the Indian Ocean as observed

---

[8] This is inferred from the low BT and CLAAS algorithm on cloud types. The lower the temperatures, the higher is the cloud top and hence the deeper the system. CLAAS algorithm has been implemented by Stengel et al. (2014).

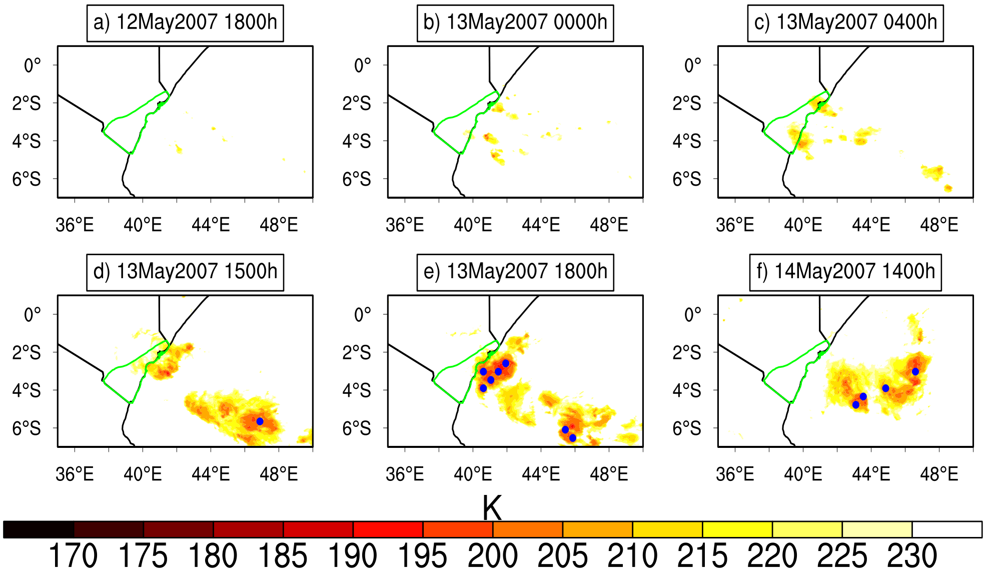

Figure 7.6: *Spatial evolution of convection from SEVIRI BT (filled contours, K) and cloud type (blue stipples, no units) over the Coastal Lowlands for selected hours namely a) 1800 UTC 12 May b) 0000 UTC 13 May, c) 0415 UTC 13 May, d) 1500 UTC 13 May, e) 1800 UTC 13 May and f) 1445 UTC 14 May. BT above 230 K have been suppressed while only the* ***overshooting convection*** *cloud type from the CLAAS algorithm has been rendered to emphasize deep convective areas. (Full 15-min IR brightness temperature loops between 0000 UTC 12 May 2007 to 2345 UTC 14 May 2007 can be accessed at:* `https://drive.google.com/file/d/1DkRmCImAvk2Fz674fQUliFdHJkbKiOiY/view?usp=sharing`*).*

from the 15-min SEVIRI loops (not shown).

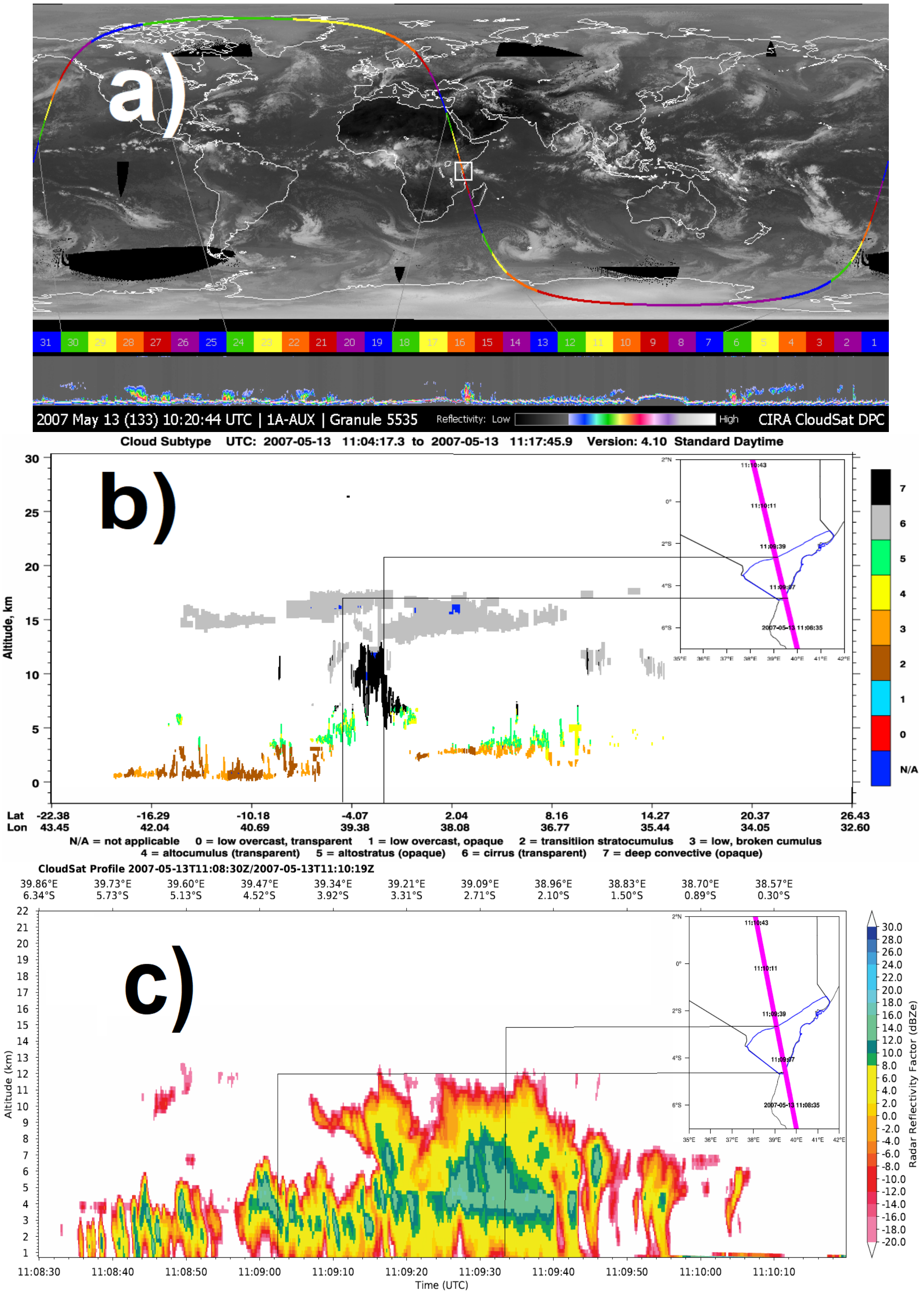

Figure 7.7: *a) shows the A-train polar-orbital path (available on cloudSat website). The spacecraft was overhead the region of study at 1110 UTC May 13 2007 (white box). b) shows the Cloud subtype derived from the vertical feature mask of CALIPSO Lidar (image url:* `https://www-calipso.larc.nasa.gov/products/lidar/browse_images/show_date.php?s=production&v=V3-01&browse_date=2007-05-13` *) and c) shows Radar reflectivity (dBze) derived from the* CloudSat *Cloud Profiling Radar.*

7.4 Synoptic and dynamic development

This subsection presents results on the investigation of the underlying dynamics and synoptic evolution of the atmosphere prior to the occurrence of the event.

7.4.1 Tropical waves

The event is hypothesized to have either been triggered or enhanced by interaction amongst a couple of tropical waves. The tropical waves whose influence was investigated included the Madden Julian Oscillations (MJO), Kelvin waves (Kelvin), Equatorial Rossby waves (ER) and Tropical Depressions (TD). These waves were filtered based on Wheeler and Kiladis (1999) wave-number frequency domain concept (figure 7.8). It is evident from figure 7.8 that between about 12 and 13 May 2007, an eastward propagating Kelvin wave was superposed on a westward propagating equatorial Rossby wave. The superposition may have been responsible for the slight drop in pressure creating a temporary trough between 06 UTC 12May and 04 UTC 13May. Apart from the semi-diurnal tidal wave in

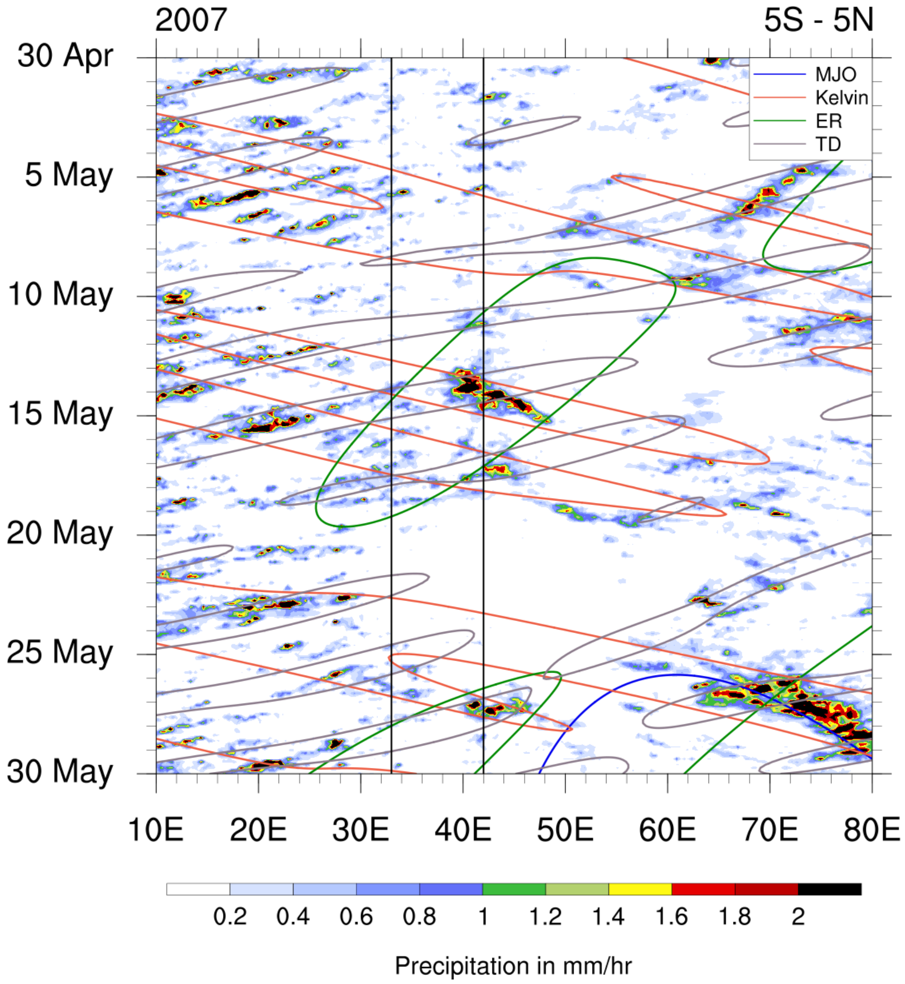

Figure 7.8: *A hovmöller diagram of TRMM daily precipitation totals between 30 Apr. and 30 May 2007 averaged between 5°S - 5°N latitude and confined to within 10°E - 80°E longitude. The event center is enclosed within the two vertical lines and between 12 and 14 May 2007. Filled contours are precipitation totals (in mm) while line contours depict tropical waves namely, MJO, Kelvin, equatorial Rossby (ER) waves and tropical depressions (TD). The diagram was created after application of the wave-number frequency domain concept from Wheeler and Kiladis (1999) using a routine written by Andreas Schlütter (IMK-TRO).*

mean sea level pressure, it can be observed from figure 7.9, that the lowest MSLP values were reported at between 07 UTC 12 May and 12 UTC 13 May. The superposition of the Kelvin and equatorial Rossby wave initiating a tropical disturbance and the eventual drop in pressure is hypothesized to have triggered a westward moving tropical disturbance over the Indian Ocean between 12 and 13 May.

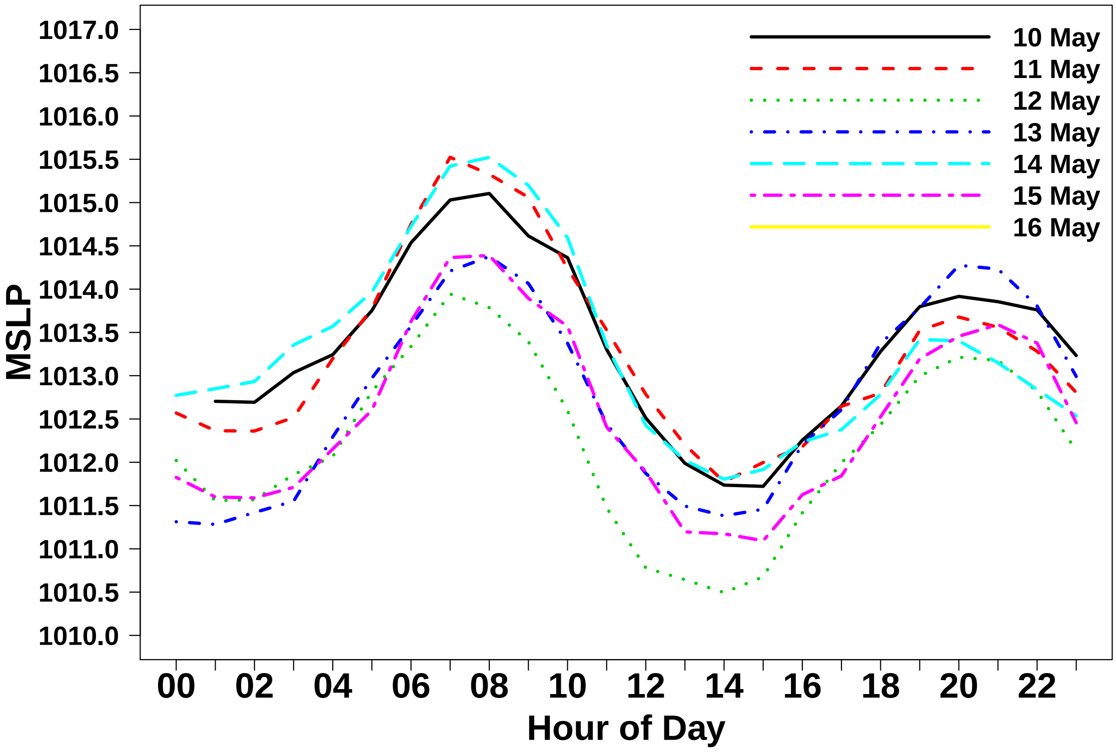

Figure 7.9: *Hourly evolution of ERA5 Mean Sea Level Pressure (MSLP; hPa) in a 7-day window pivoted at the event center on 13 May 2007. MSLP is averaged over the spatial box, 38°E - 45°E and 6°S - 1.5°S over the Coastal Lowlands.*

7.4.2 Wind convergence and relative vorticity

The weak surface low on 12 May over the Coastal Lowlands caused by tropical wave superposition as has been shown in section 7.4.1 may have resulted in the acceleration of low-level winds onshore between 12 and 13 May 2007. Figures 7.15d, 7.15e, and 7.15f shows the 850 hPa wind field at 12 UTC on 12th, 13th and 14th of May oriented onshore and towards the Coastal Lowlands of Kenya at speeds in the order of 10 - 20 m s^{-1}. The wind speeds increased from about 10 m s^{-1} on the 11th to about 20 m s^{-1} on the 12th and maintained this magnitude until the 14th May. Wind divergence characterised the region from 1000 to the 850 hPa level just before 12 UTC 11 May. However, between 12 UTC 11 May to 00 UTC 14 May, the lower levels were characterised by convergence whose intensity ranged between -0.4 and -0.8 x $10^{-5}s^{-1}$ (figure 7.10a). The highest intensities of convergence occurred in the late evening hours of 12 May all the way to the early morning hours of 13 May. This low level convergence was observed to characterise the entire middle troposphere up to the 500 hPa level where it weakened. Beyond this level, the atmosphere was characterised by divergence. In terms of the evolution of the vertical distribution of relative vorticity, the lower levels throughout the 7 days centered around the event were found to have been very active. Going by the vorticity equation, the relative vorticity may have been strengthened due to stretching brought about by the low-level convergence (figure 7.10a). Between 11th and 12th May at 00 UTC, a weak vortex of the order of -0.5 x $10^{-5}s^{-1}$ characterised the lower levels with levels between 850 and 500 hPa reporting a stronger vortex maximizing at 700 hPa with values of more than -1.5 x $10^{-5}s^{-1}$. It is noted that vortices in regions to the south of the equator are said to be cyclonic if relative vorticity is negative. Thus, between 1000 and 500 hPa and within the 7-day window centered on 13 May, relative vorticity values reflected a very active middle troposphere. The maximum intensity in relative vorticity reported values larger than -2 x $10^{-5}s^{-1}$ observed just before the event at 12 UTC May 13 between 850 and 700 hPa levels. It is speculated that this strong mid-level vortex prior to the extreme event on May 14 may have instigated intense upward motion from the lower levels. Beyond the 500 hPa level, a major reversal of the phenomenon witnessed within the lower levels emerged. The cyclonic circulation in the lower levels was replaced by an anticyclonic circulation between 400 and 250 hPa levels. This upper level divergence supported the earlier observation of the existence of tropical wave disturbances. The growth of relative vorticity was observed to evolve from the lower troposphere, through the mid-troposphere then followed by the eventual dissipation beyond the mid-level altitudes. This vortex benefited substantially from a relatively strong wind speed shear between the upper and lower levels.

7.4.3 Vertical velocity and wind shear

The weak vortex discussed in subsection 7.4.2 may have been aided by a vertical speed shear of the wind between the lower and upper levels. To quantify the effect of vertical shear to the formation of the vortex, a comparison between a deep layer shear (850 - 200 hPa) and a mid layer (850 - 500 hPa) shear was made. While it is known that a very strong vertical wind shear serves to disorganize and eventually destroy a vortex in a cyclone, a relatively moderate vertical wind shear maybe helpful in the formation of a weak to moderate vortex aiding the sustenance of a convective system. This is mainly achieved by virtue of the upward and the downward motion being separated from one another by the intense upper level winds in a manner that ensures no degradation of the upward component. Figure 7.10c shows the vertical wind shear for the two layers mentioned above. Just before the event, the vertical shear in both the deep and the mid layer were observed to be relatively weak but after 00 UTC 12 May, both shears were found to be monotonically increasing with the deep layer shear increasing more rapidly than the mid layer one. The mid layer shear (which should affect any vortex forming below 500 hPa level) was found to increase gradually between 00 UTC 12 May and 00 UTC 13 May. This gradual increase is speculated to have provided a conducive environment for the vortex to develop. Beyond 13 May, both shears shot up drastically with the deep layer shear shooting to values in the order of 0.7 x $10^{-3}s^{-1}$ between 00 UTC 13 May and 12 UTC the same day. The vertical shear later subsided beyond 12 UTC 13 May in a consistent fashion with the dissipation of the event.

The low-level convergence described in subsection 7.4.2 may have had an impact on upward motions responsible for the heavy precipitation reported on 14 May. Figure 7.10b shows the evolution of ω between 00 UTC May 11 and 00 UTC May 15. Consistent with the results on convergence, wind shear and vorticity, ω was positive (implying downdrafts or downward motion) just before 00 UTC 12 May. Beyond this time, the troposphere was characterised by upward motion until 00 UTC 14 May. The upward motion was found to reach the 200 hPa level and possibly beyond. The vertical motion in the lower levels was strongest between 00 UTC 13 May and 00 UTC 14 May. This ascending motion was found to increase in magnitude beyond the mid-tropospheric levels (500 hPa) to the top of the atmosphere. During the same window period, equivalent potential temperature was found to decrease with height from values of about 340 K within the 1000–850 hPa layer to 335K just about the 500 hPa mark (shaded contours on figure 7.10b). Instability is discussed in subsequent subsections.

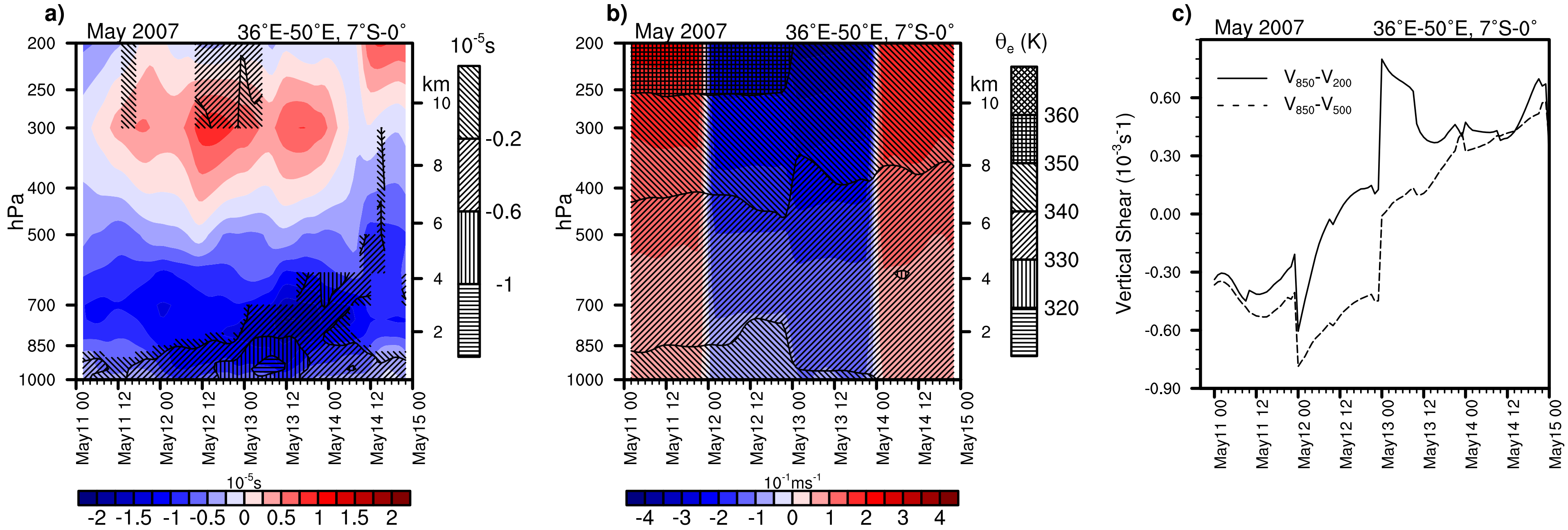

Figure 7.10: ***a:*** *Evolution of the vertical distribution of relative vorticity (filled colors; $10^{-5}s^{-1}$) and wind convergence (shaded contours, $10^{-5}s^{-1}$ - divergence masked) over the Coastal Lowlands averaged between 36° - 50°E, 7°S - 0° two days before and 1 day after the event of 14 May 2007.* ***b:*** *Same as* ***a*** *but for the vertical distribution of omega (filled colors; $10^{-1}m\ s^{-1}$) and equivalent potential temperature (shaded contours; K).* ***c:*** *Same as* ***a*** *but for the vertical shear of wind ($10^{-3}s^{-1}$) in a mid layer (850 and 500 hPa) and a deep layer (850 and 200 hPa).*

7.4.4 Moisture flux and convergence

Moisture was advected to the Coastal Lowlands across the western equatorial Indian Ocean by a moderately strong and persistent moisture flux between the surface (1000 hPa) and the mid-levels. Figure 7.11a to 7.11c illustrates the transport of moisture and its eventual convergence over the region. The moisture flux was found to converge onshore just before hitting the coastline. Convergence of moisture flux was less pronounced during the event onset at 00 UTC 12 May but picked up significantly so that by 00 UTC 13 May, the northern part of the Coastal Lowlands and the Indian Ocean waters next to the East African mainland was a moisture convergence zone. By the time the event became pronounced on 00 UTC 14 May, the moisture convergence had already produced towering cumulonimbus clouds with BT over the northern region and towards the Somali coast reaching lows of 230 K (dot stippling in figure 7.11c).

The wind vectors at low levels (850 hPa) and the moisture fluxes were found to have a similar orientation as they approached the Coastal Lowlands where convergence took place within the region and divergence beyond. The moisture flux and its convergence contributed to high amounts of precipitable water in a column. The highest values of precipitable water in the order of 70 to 75 mmday^{-1} were found to characterise the northern region of the Coastal Lowlands where convergence was the most marked within the duration of the event peaking at 00 UTC 13 and 14 May. Indeed, the entire region was covered by high values of precipitable water to the extent that within the 2000-2018 ERA5 climatology, the values near the southern part of the region had surpassed the 98th percentile (meshed stippling in figure 7.11b and 7.11c).

It is speculated that the deep convection was promoted by moisture flux (whose orientation was orthogonal to the coastline) into the region and the consequential moisture convergence within the troposphere. The moisture flux convergence was most pronounced along the coastline and towards the northern part of the Coastal Lowlands. This implied that frictional convergence with the coastline could have played a larger role as opposed to directional[9] convergence. The onshore winds blew over a relatively warm ocean with SSTs over the neighbouring Indian Ocean reaching highs of between 28 and 29°C (figures 7.15d to 7.15f). As such, advection of high θ_e-air was almost certain. The highest values of θ_e at 850 hPa were over the neighbouring western equatorial Indian Ocean during 12th of May and remained relatively high for the next two days (figures 7.15d – 7.15f). With the wind vector oriented towards the Coastal Lowlands, advection of warm moist air onshore ensued. The accumulation of high θ_e-air in a column through convergence resulted in an eventual build-up of instability inferred from the negative θ_e gradient just before the event as shown in figure 7.10b.

---

[9] winds meet over a wide area to initiate convergence

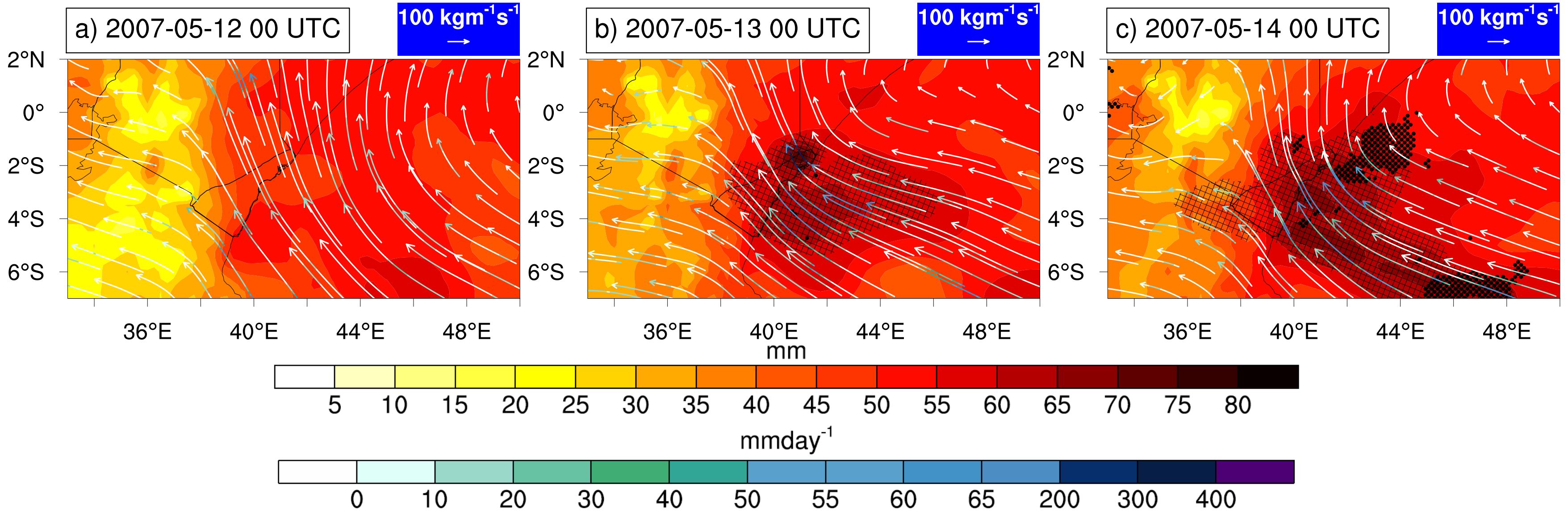

Figure 7.11: *a-c: Evolution of total precipitable water (filled contours, mm) over the Coastal Lowlands at 00 UTC on 12, 13 and 14 May 2007. Overlaid is the vertically integrated moisture flux (vector; kgm^{-1}s^{-1}) and its convergence (vector color; mmday^{-1}). Divergence of moisture flux has been suppressed. Dot stipples indicate areas of deep convection from BT (BT < 230 K). Meshed stipples show exceedances of total precipitable water from the 98th percentile during the 2000-2018 period.*

7.4.5 Moisture trajectory analysis using LAGRANTO

In this section, results obtained after examination of backward trajectories of moisture using the Lagrangian trajectory analysis tool highlighted in section 5.2.7 are presented. u and v wind components at various pressure levels were used as forcings to the Lagranto tool. The main variable of choice identified to emphasize moisture advection was specific humidity. The analysis was done to identify source regions of moisture as well as the physical mechanisms which led to the release of latent heat once moisture arrived at the Coastal Lowlands within the lower levels. Backward trajectories were started from 10 levels namely, 500, 550, 600, 650, 700, 750, 800, 850, 900 and 950 hPa. The analysis showed that 4-5 days prior to the event, air from higher levels sunk over the Mascarene high located within the western-central equatorial Indian Ocean. Once reaching the lower levels (between 900-800 hPa), the air became persistently south-easterly heading towards the region of interest as shown in figure 7.12a. Once the air hit the coast, it was forced to rise by factors speculated in section 7.4.4. Of important to note is the fact that all trajectories from all starting levels sunk at the Mascarene high 4 - 5 days prior to the extreme event and rose near the grid point, 40°E-3°S chosen based on the amount of precipitation received. In terms of moisture uptake along the trajectory, all backward trajectories showed that specific humidity was picked along the track within the lower levels (between 1000 - 800 hPa) and especially over the region between 70° - 40°E. Figure 7.12b which is an example of a backward trajectory that was started at 500 hPa to trace specific humidity, corroborates the theory of vertically rising air parcels near the said grid-point. Figure 7.13 shows the $T-\theta$ curves whose explanation is elucidated in section 5.2.7.1. Only three starting levels were chosen namely 500, 750 and 900 hPa. Consistent with the trajectories in figure 7.12a, five days (120 hours) prior to the event, the region just above the Mascarene high was

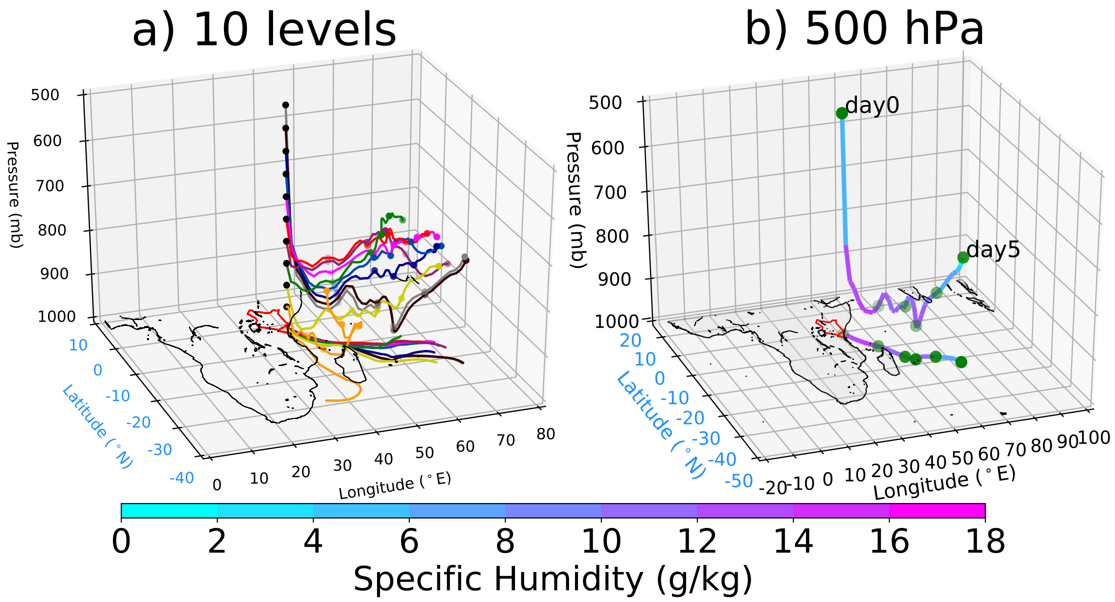

Figure 7.12: ***a)*** *Three dimensional 5-day backward Lagranto trajectories showing air mass sources for various starting levels using ERA5 model data over the Coastal Lowlands initialized at 06 UTC 14 May 2007. The starting levels are namely, 500, 550, 600, 650, 700, 750, 800, 850, 900, and 950 hPa shown by grey, darkbrown, darkblue, blue, magenta, red, purple, green, yellow, and orange lines respectively. The color markers indicate every day lapsed. Black markers represent the initial grid point namely 40°E, 3°S.* ***b)*** *Specific humidity traced along the backward trajectory starting from the 500 hPa level. Notice that the trajectory in* ***b)*** *is mapped onto the surface too, using the same color configuration.*

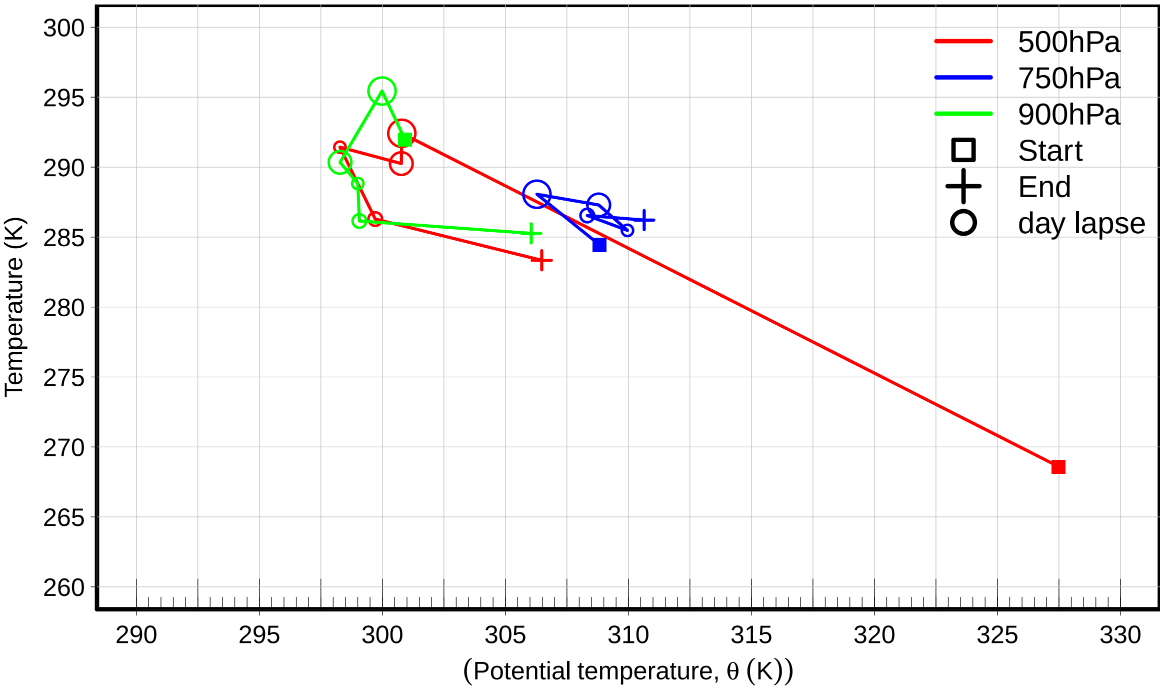

Figure 7.13: *Temperature-Potential temperature ($T - \theta$) curves showing the evolution of T and θ each day for 5 days since the beginning of the backward trajectory at 06 UTC 14 May 2007 (shown by the diamond marker) until the end of the trajectory 5 days later (shown by the cross marker). Rings indicate every day lapsed and their size diminish further away from the event every 24 hours. The starting levels are 500, 750 and 900 hPa and each curve represents a specific starting level of the trajectory.*

characterised by sinking motion and a near adiabatic compression. This is evident from figure 7.13 which shows subsidence (adiabatic compression associated with warming air) accompanied with diabatic[10] cooling (θ decreasing and T increasing). This corresponded to the moment when the air parcels sunk over the Mascarene anticyclone.

Between 96 and 72 hours prior to the event, the subsidence continued accompanied by a sharp temperature increase implying a strong descent while undergoing a more or less adiabatic warming (with θ almost constant). Between 48 and 72 hours corresponding to the time window when the wind field was predominantly south-easterly, the air parcels underwent both diabatic warming (increase in θ) either due to radiative warming or absorption of sensible heat fluxes from the ocean and adiabatic warming (increase in T). At this stage, it was difficult to infer any upward or downward motion. However, a glance at figure 7.12 indicates that during this specific period, the air parcels sunk slightly over the western equatorial Indian Ocean. This indicated that the increase in T caused by compression as a result of subsidence far outweighed radiative heating (which increases θ) causing the parcels to sink. During the last 24 hours before the event, T and θ decreased and increased respectively which is a phenomenon associated with lifting. Almost all the backward trajectories (10 levels between 500 and 950 hPa) were similar in terms of general structure. These vertically rising air parcels contributed significantly to the strong ascents observed in the vertical velocity plot shown in figure 7.10b.

---

[10] Heat changes triggered by radiative processes, subgrid-scale turbulent fluxes within the boundary layer and the release of latent heat due to phase changes in clouds (Zschenderlein et al., 2018).

7.4.6 Analysis of atmospheric instability

As indicated before, the trigger mechanism to the extreme convection may have been a Kelvin-equatorial Rossby wave superposition (figure 7.8) causing upper level divergence (figure 7.10a). The convection enhanced through advection of moisture and the resulting moisture convergence (figure 7.11a-c). Indeed, using ERA5 vertical profile variables of temperature and relative humidity, it was demonstrated that a warm air parcel from the surface required just a slight push to get lifted to the level of free convection which was observed to be as low as 980 hPa (figure 7.14). The atmosphere was nevertheless very moist with the two curves, namely the environmental temperature and dew-point being relatively close to each other throughout the column. The sounding revealed an already raining atmosphere based on the moist column between the surface and 200 hPa level. It appeared that ERA5 had started raining early over this grid point as a response to, presumably, daytime heating at 12 UTC. Calculated value of convective inhibition for this ERA5-based sounding was not different from zero implying that frictional convergence

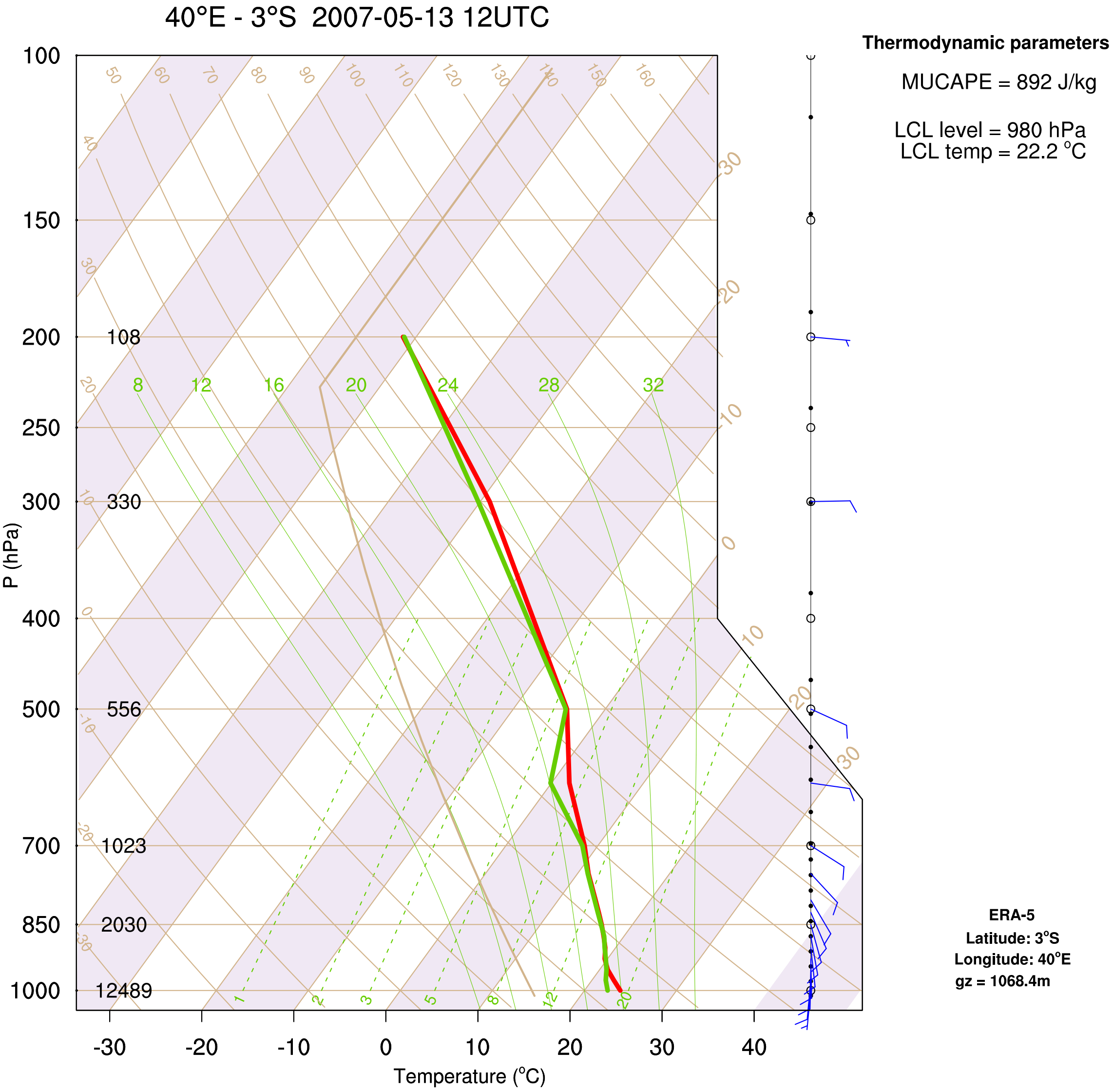

Figure 7.14: SkewT-logP plot taken from ERA5 model data at grid point 40°E - 3°S during 12 UTC 13 May 2007 over the Coastal Lowlands. The bold green line is the dew-point while the red line is environmental temperature.

could have been enough to trigger lifting to LFC. CAPE for the most unstable layer was found to average about 892 JKg^{-1} over the grid point where the sounding was taken. This value was relatively moderate. Analysis of ERA5-based CAPE between 12 and 14 May revealed a seemingly weaker influence to convection as the values were less than 800 J/Kg (figure 7.15a to c). However, further analysis of anomalies of CAPE within the period 1979–2018 indicated that ERA5 has a relatively low CAPE bias over this region and that moderate values of CAPE as found here are indeed associated with extreme precipitation within ERA5's own climatology. From figure 7.15b, it can be speculated that there was advection of CAPE from the neighbouring Indian Ocean though much of the advected CAPE did not reach the shore. Relative humidity for most of the three days analysed was well beyond 80% implying that there was sufficient moisture to trigger convection (figure 7.15a-c). Much of the relative humidity was speculated to have been as a result of evaporation from the neighbouring Indian Ocean (whose SSTs were higher than 28°C) and the eventual advection onshore. Analysis of conditional instability using Yang et al. (2015) method (figure 7.16) showed that the entire Coastal Lowlands was conditionally unstable throughout the three-day period centered on 13 May 2007. The gradient of conditional instability between the eastern and western parts next to the Coastal Lowlands was strong peaking to its highest value on the 13 May (Figure 7.16a to c).

Thus, the conditions were right for the formation of towering cumulus and cumulonimbus clouds. Spatially averaged conditional instability indices between 00 UTC 12 May and 00 UTC 14 May (figure 7.16d) showed that the conditional instability was positive throughout the three day period. Just as Yang et al. (2015) observed in their study on east African precipitation variability on annual cycles, the conditional instability was in phase with the surface moist static energy with the latter being two to three times stronger than the saturated moist static energy at 700 hPa. It was also found to be in phase with precipitation (red curve in figure 7.16d) leading the latter by about 2 to 4 hours. The stability analysis also showed that after the towering clouds rained out (as shown by the high amount of precipitation at about 12 UTC 13 May), the stability of the atmosphere weakened between 12 UTC 13 May and midnight. The reduction in moist static energy at the surface (blue curve, figure 7.16d) triggered a corresponding decrease in precipitation amount. However, since the stability never went to below zero, conclusion can be drawn that there were factors that contributed to the atmosphere remaining either weakly or strongly unstable. Some of the factors include the perpetual advection of high - θ_e air from the Indian Ocean as demonstrated in figure 7.15d-e.

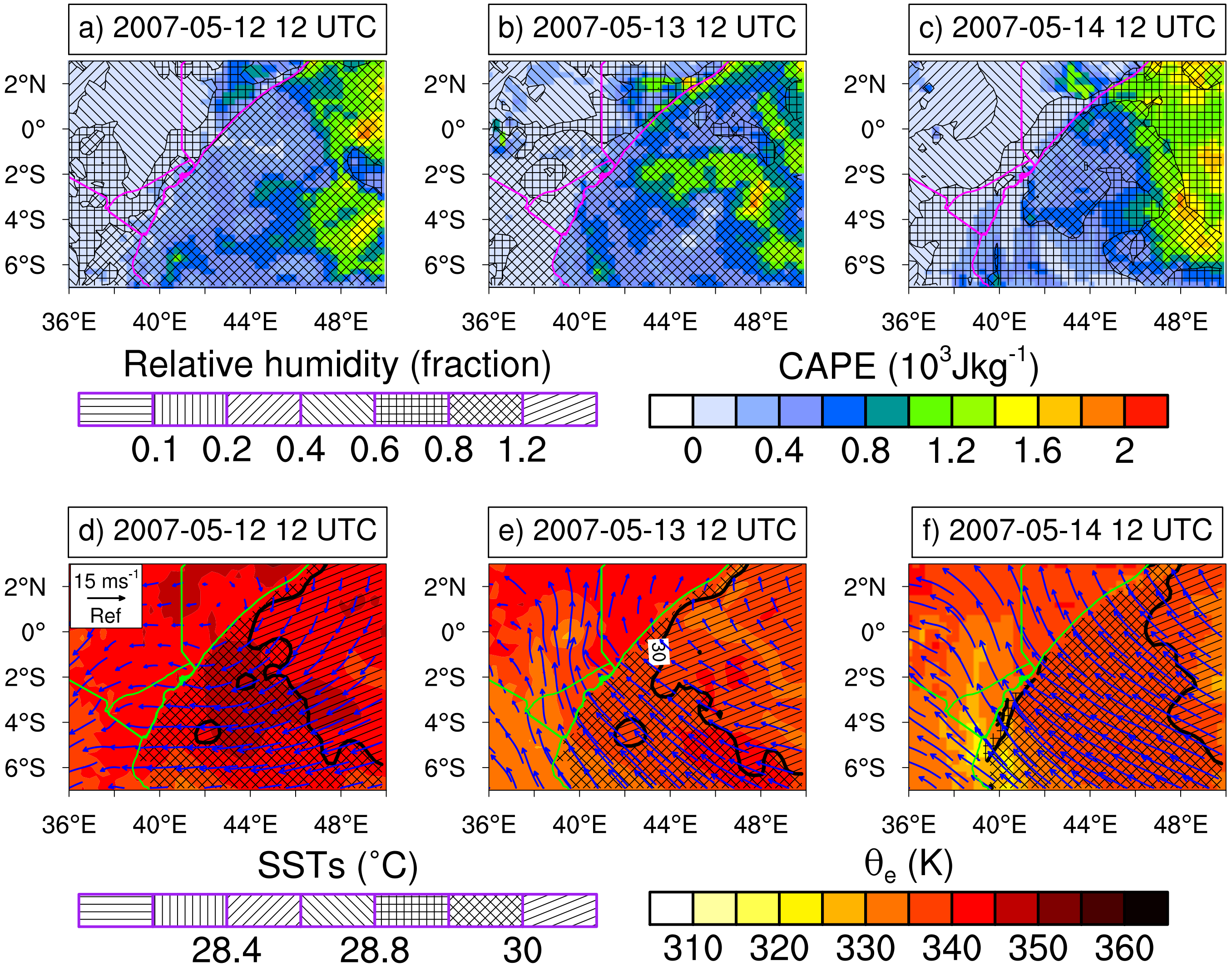

Figure 7.15: ***a-c:*** *Evolution of ERA5 Convective Available Potential Energy (filled contours; 10^{-3} Jkg^{-1}) and relative humidity (shaded contours; no units) at 12 UTC between 12 and 14 May 2007.* ***d-f:*** *Evolution of 850 hPa level equivalent potential temperature, θ_e (filled contours; K) and sea surface temperatures (shaded contours; K) with 850 hPa wind field overlaid on the contours.*

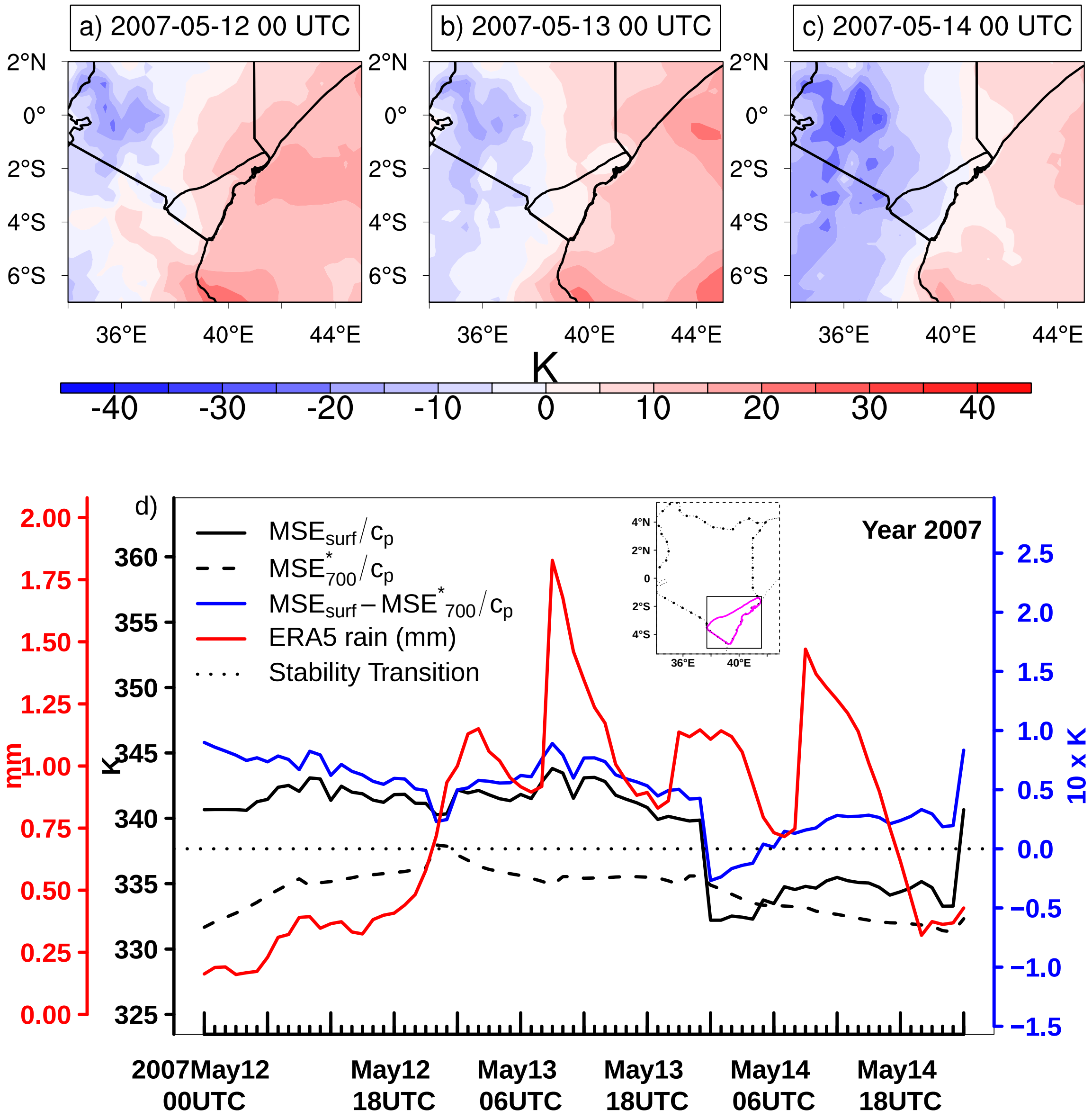

Figure 7.16: Top panel (a-c): *24-hour spatial evolution of conditional instability between 00 UTC 12 May and 00 UTC 14 May over the Coastal Lowlands.* ***Bottom Panel (d):*** *Hourly evolution of spatially averaged conditional instability (blue curve) between 00 UTC 12 and 00 UTC 14 May 2007. Also shown is the MSE at 2m above the surface (black curve) and the saturated MSE at 700 hPa level (black dotted curve). The red curve is the evolution of spatially averaged hourly precipitation. Stability transition curve shown with black dots is the line that separates stable and unstable air. All data are derived from the ERA5 forecast model and averaged spatially within the rainiest spatial domain of 38°-42°E and 5°S-1.5°S (Spatial box shown in the inset map).*

7.5 Results from ICON simulation of the Coastal Lowlands case

This section presents results from simulation of precipitation using the ICON model. The questions addressed in this section are whether the aforementioned model could give comparable results to those from observations. Section 7.5.1 explores the plausibility of the model in simulating the A06 on 2007 May 14 subjectively while section 7.5.3 evaluates the performance of the model objectively. Section 7.5.4 evaluates the performance of the model in simulating CTT.

7.5.1 Simulation of the 24-hour accumulated precipitation between 0600–0600 UTC (A06)

Results from the nested ICON model simulation for the A06 of 14 May 2007 are presented here. As had been discussed before under data and methods section in chapter 5, the low density of gauge network over the region necessitated pegging further evaluation of ICON model performance to TRMM rainfall records. Initialization was done at 12 UTC May 12, 18 UTC May 12, 00 UTC May 13 and 06 UTC May 13 as shown in figure 7.17(b-e). It can be subjectively argued that the model seemed to perform reasonably well in capturing the extreme precipitation event and especially along the coastline when initialization was centred at 12 and 18 UTC May 12 2007. The performance of the model towards the interior parts of the Coastal Lowlands was poorer compared to representation in regions offshore. Compared to TRMM, structure of the precipitation in the model appeared to be in form of convective cells which usually develop in a synoptically forced environment as opposed to spatially larger precipitation objects associated with propagating mesocale convective systems or squall lines[11]. The 12 UTC initialization (figure 7.17b) produced very intense but isolated cells of convective precipitation along the coastline. Later simulations tended to displace the center of mass of total precipitation offshore. It can be argued that due to the high resolution of the model, the tendency to produce very deep but isolated convective cells is not uncommon (Woodhams et al., 2018). Compared to the rain-gauges, the model produced enhanced precipitation. As an example, model grid points close to Mombasa meteorological station tended to produce A06 amounts ranging from 240 to 300 mm for 12 and 18 UTC initializations while the amount reported at the rain gauge station was less

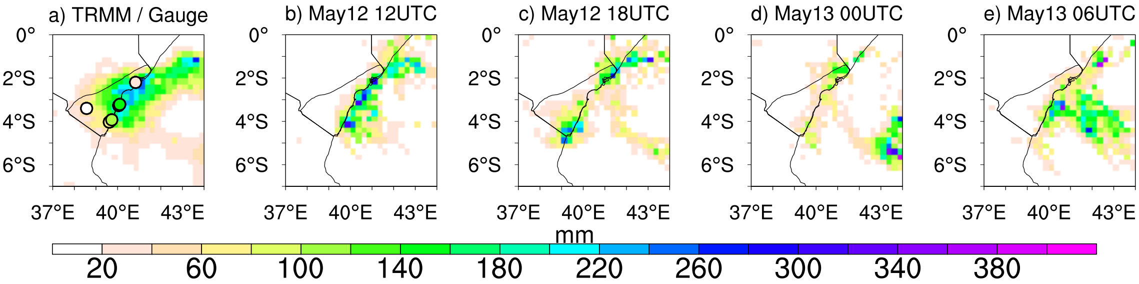

***Figure 7.17: a:** A06 of gauge overlaid on TRMM. **b to e:** A06 from ICON nested simulations forced by ERAI and initialized at 12 UTC May 12, 18 UTC May 12, 00 UTC May13 and 06 UTC May13 respectively over the Coastal Lowlands.*

---

[11] Lines of thunderstorms where inflow and outflow is well organized and stable fuelled by CAPE and low-level wind shear

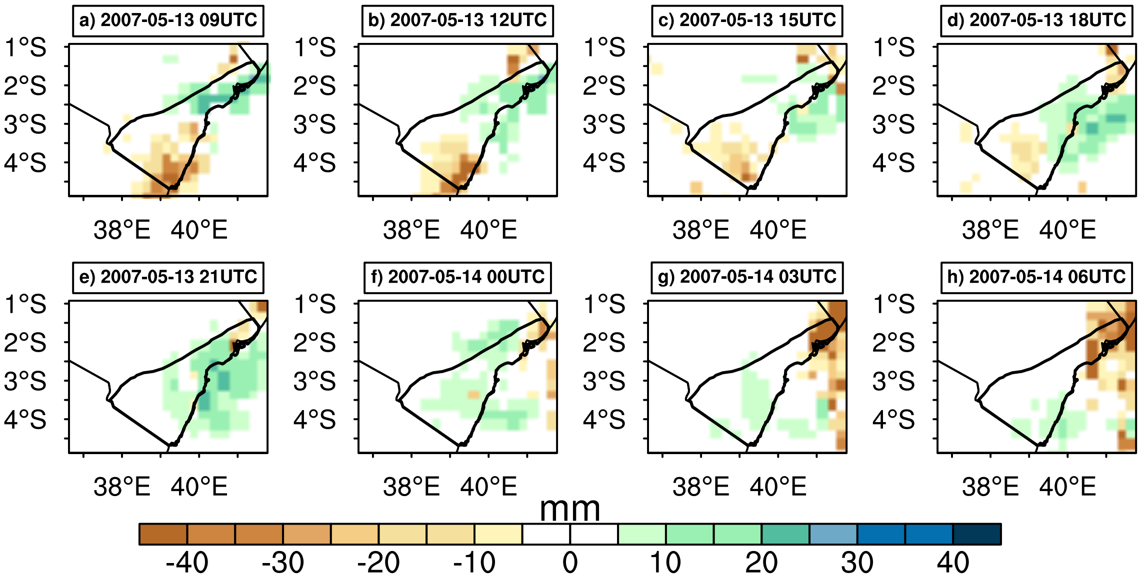

Figure 7.18: Evolution of the difference between TRMM and ICON (calculated as icon − trmm) between 09 UTC 13 May and 06 UTC 14 May, 2007 corresponding to the time window that informs the A06 in figure 7.17a. Plots based on the 18 UTC May 13 initialization over the Coastal Lowlands.

than 80 mm. Section 7.5.3 provides a more objective evaluation of the performance of the model based on the Structure-Amplitude-Location (SAL) technique introduced by Wernli et al. (2008).

7.5.2 Perspective of the model on sub-daily precipitation evolution

The model struggled to simulated the observed precipitation on a sub-daily scale. During the initial stages of the day after initialization (18 UTC May 13 initialization), the difference between TRMM and ICON was not as large as it was in the last few hours making up the A06. As can be seen from figure 7.18a centred on 09 UTC May 13, apart from the positive bias of the model tending to produce higher amounts of precipitation towards the northern part of the Coastal Lowlands, the model precipitation was more or less comparable to TRMM with reported differences of between 0 and 20 mm. This scenario was replicated in the next six hours until 15 UTC. At 18 UTC, the model tended to produce enhanced rainfall just offshore while producing suppressed rainfall towards the south-western and north-eastern parts of the region. At 21 UTC May 13 (Time of the most enhanced precipitation), the model produced more rain than TRMM almost throughout the region. At later stages of the night, the model produced depressed precipitation compared to TRMM with the model underestimating precipitation towards the north-eastern parts of the region. Over these parts, negative biases in the order of 80 mm were reported. Thus, the model can be said to have performed worse on a sub-daily scale than on a daily scale for isolated convection but much better performance realized when convection was enhanced and much organized as the situation on 21 UTC May 13 revealed. The description of model performance here is based on an "eye-ball" method which tends to be subjective. Consequently, section 7.5.3.2 analyses ICON performance on a sub-daily scale more objectively.

7.5.3 Spatial evaluation of model skill in representation of precipitation

In order to make TRMM observations and those from the ICON output comparable, the output *namelist*[12] from ICON model had to be adjusted to allow for a cubic interpolation so as to include a precipitation output that maps exactly to the time and space dimensions of TRMM.

7.5.3.1 Skill evaluation for the 24-hour accumulated precipitation between 0600–0600 UTC (A06)

We now turn to model skill evaluation in capturing A06. As discussed in the data and methods part (section 5.3.3) the SAL method - which is sensitive to the physical nature of a precipitation event (Wernli et al., 2008) - was used to assess the skill of the ICON model. Figure 7.19 shows the SAL scores for the A06 of the model initialized at four different times of day namely, 12 UTC 12 May, 18 UTC 12 May, 00 UTC 13 May and 06 UTC 13 May. The 00 UTC 13 May initialization tended to underestimate the overall amplitude of precipitation with a score of about -0.9. Figure 7.17d shows that the magnitude of precipitation as a result of the 00 UTC initialization was in fact underestimated within the boundaries of the region. Only the north-eastern part of the region showed appreciable amounts of precipitation of betwen 100 and 140 mm while over other areas, the model produced suppressed precipitation. In terms of the structure of the precipitation, the A06 output from the 00 UTC initialization was negative with S-value of

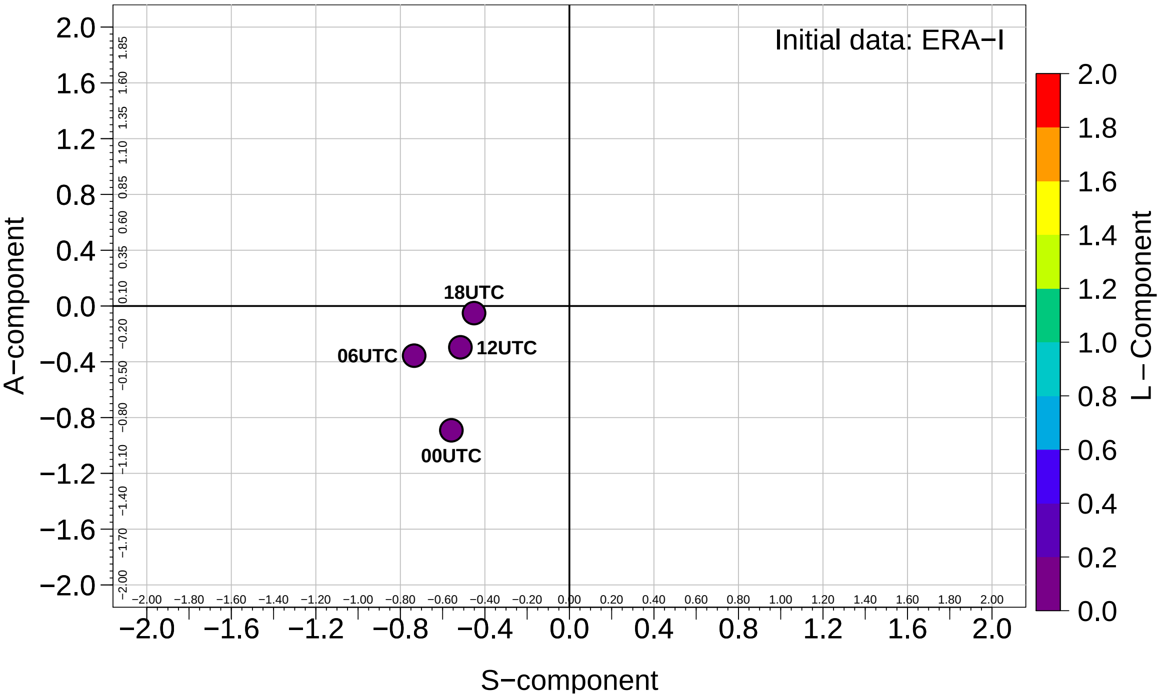

Figure 7.19: SAL diagram for the A06 forecasts from the ICON model over the Coastal Lowlands at three different initialization times namely, 12, 18, 00, and 06 UTC May 12 - 13, 2007. ICON model was initialized using ERAI. Every dot shows the value of the three components of SAL with the location component shown by color. TRMM data was used as the verification field.

---

[12] The adjustable variables in the ICON model to serve the purposes of a certain simulation experiment e.g. switching off a convection scheme

about -0.5. A negative value of S is a strong indicator of a forecast that is less organized (too flat or scattered precipitation) than observed. The L-component value (L < 0.01) for this initialization showed that the forecast was not further away from the center of mass of the observed event. Figure 7.17d confirms that the isolated cells of convection were still within the region of event occurrence. For the 06 UTC initialization, the model output of A06 was such that A, S and L values of the model were -0.4, -0.7 and 0.083 respectively. This implied an overall underestimation of overall precipitation, isolated convection but no-shift in the location of the event. Figure 7.17e shows this scenario. It is evident from the figure that much of the precipitation is shifted offshore away from the region and only isolated pixels of convection remain over the mainland. The only two initializations that showed some degree of adequate skill in estimating the observed A06 are the 12 and 18 UTC initializations. Although both initializations tended to underestimate the amplitude of A06, the amplitude of the 18 UTC initialization was not too far from zero (A = 0.03) with a less significant location bias (L = 0.05). However, both initializations (12 and 18 UTC) failed to capture adequately the structure of precipitation reporting S-values of -0.45 and -0.50 implying more isolated precipitation than TRMM. This, however, can be the case for a convection-permitting model with such a high resolution (3.25 Km in the innermost nest). Contrasting the 12 and 18 UTC actual precipitation values in figure 7.17b and 7.17c using the "eye-ball" subjective method, this narrative was conspicuous. The two initializations produced comparable precipitation values along the coastline from south to north (hence the small magnitude of A) but failed to capture precipitation in the interior parts observed in TRMM (and hence the higher negative value of S). However, the location of the precipitation object was observed to be over the same area as that observed in TRMM.

7.5.3.2 Sub-daily evaluation of model skill

On the sub-daily scale (3-hourly scale), the skill of the model in simulating precipitation was remarkably different from the skill in estimating A06. It should be noted that since the major focus of the simulation is on the total precipitation between 06 UTC 13 May to 06 UTC 14 May 2007, only the simulation that showed the best skill in section 7.5.3.1 is chosen so as to identify the trends of precipitation on higher temporal scale. Thus, only results from the model output initialized at 18 UTC are shown here. Figure 7.20 shows the SAL statistics of all the 3-hourly precipitation estimates from ICON. In total, there were 16 time-steps from 18 UTC 12 May to 15 UTC 14 May. These time-steps were used to generate the various statistics complementing SAL, namely, the mean, median and the 1st and 3rd quartiles (Q_1 and Q_3) and the eventual calculation of the interquartile range ($Q_3 - Q_1$). The performance of the model on sub-daily scale was remarkably poor. Using the assessment of skill given by Wernli et al. (2008), it is apparent that the model overestimated the domain averaged precipitation by a factor ranging from 1.5 to 3 while underestimating the overall size and shape (structure). In fact, the model failed completely to capture the structure of the precipitation objects within the domain as S-values ranged between -0.6 to -1.6, an indicator of too peaked or isolated precipitation events or a combination of both. And in terms of location, a similar situation was found. The model failed to locate the center of mass of the system. With L-values ranging from 0.2 to over 0.8, the location of the center of mass of the object in the model was too far away from the center of mass of the verification field. Perhaps with model tuning strategies coupled with a higher quality verification field (TRMM products may be laden with bias related to satellite's view of a system or (mis)interpretation of backscatter as well as time-limited

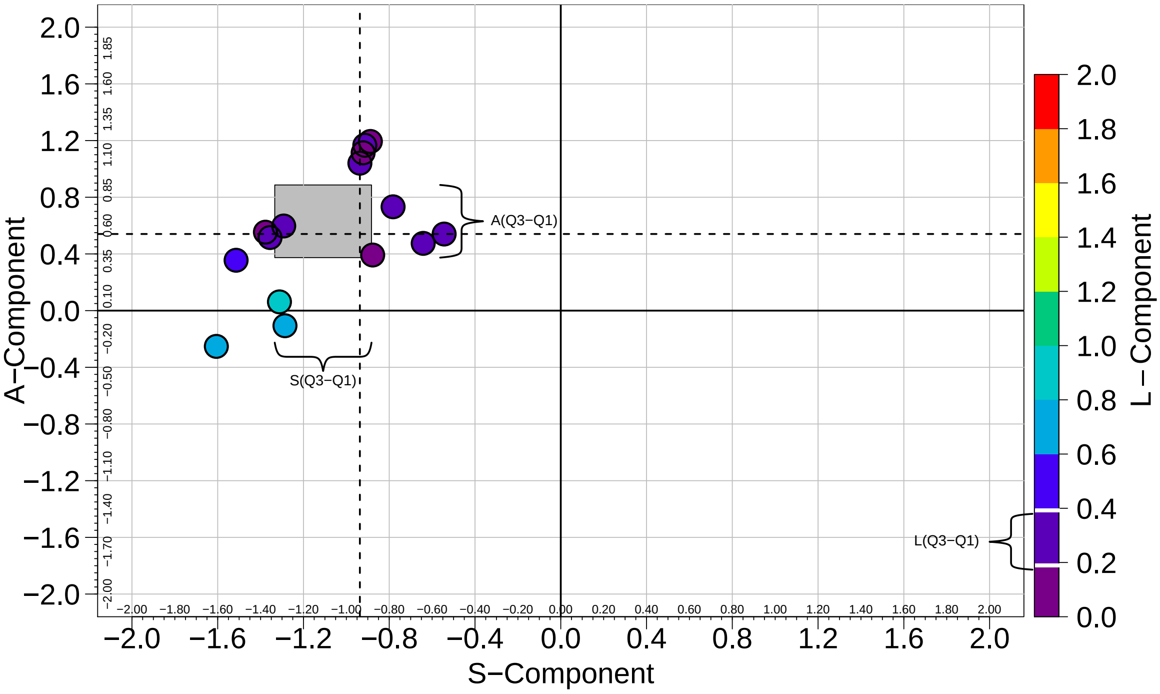

Figure 7.20: *SAL diagram for the three-houly ICON model outputs initialized at 18 UTC over the Coastal Lowlands. Every dot shows the value of the three components of SAL at a particular 3-hour interval since initialization. The L-component is shown by color. Median values of the S and A components are shown as dashed lines, while the gray box extends from the 25th to the 75th percentile of the distribution of S and A annotated as* $S(Q_3 - Q_1)$ *and* $A(Q_3 - Q_1)$ *respectively. The corresponding interquartile range of the L-component is shown by the two white dashes on the color scale and annotated as* $L(Q_3 - Q_1)$.

microwave overpasses), the model could perform much better.

7.5.4 Evaluation of simulated cloud top temperatures

Simulated CTT from the ICON model were compared with BT on a sub-daily scale of 15 min. Loops were created covering the period between 0615h 13May and 0600h 14May 2007. Only five timesteps of the loops are shown here (figure 7.21). The results were not promising either as the model tended to created patches of isolated clouds outside the region of interest contrary to what was observed by SEVIRI instruments. The temperatures were also found to be higher than those observed from SEVIRI. As can be observed from figure 7.21, it is evidently clear that even during the periods of strongest convection (between 1800 and 2200h, 13May 2007), the model struggled to capture the organised and relatively deep cloud system observed in SEVIRI. At 1815 UTC for example, figure 7.21a shows a deep system over the western equatorial Indian Ocean that moved onshore covering a relatively large area with the biggest chunk of the cloud system hovering over the neighbouring western equatorial Indian Ocean. In contrast, the corresponding figure in the lower panel shows that the model failed to simulate these system adequately as most of the clouds produced by the model had temperatures above 240 K[13]. The few low temperature clouds produced by the model were displaced towards the Somali coast. A similar scenario was observed at 1915h, 2015h, 2115h and 2215 in figures 7.21b, 7.21c, 7.21d and 7.21e respectively.

---

[13] Notice that temperatures above 240 K have been masked to emphasize deep clouds,e.g. Rempel et al. (2017); Feidas and Giannakos (2012); Tobin et al. (2012)

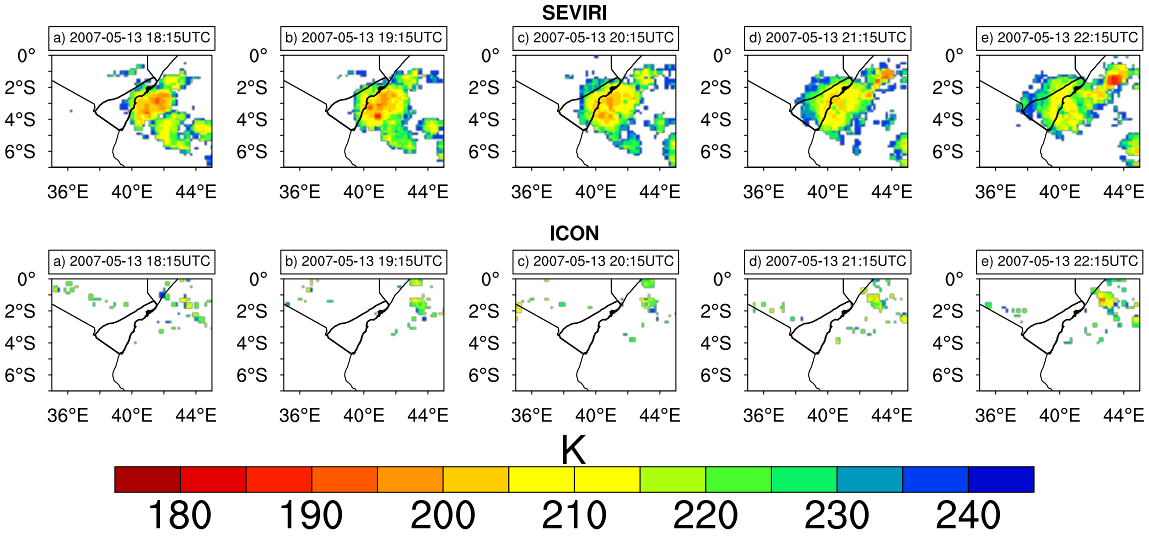

Figure 7.21: *Top panel (a-e): Selected frames of 15-min BT at 1815, 1915, 2015, 2115 and 2215 UTC 13 May 2018. Bottom panel (a-e): Same as top panel but for the simulated cloud top temperatures from the ICON model initialized at 18 UTC. Temperatures above 240 K have been masked.*

Indeed, objective analysis of the skill of the model in simulating these cloud tops was done using the FSS discussed in section 5.3.3.2 and grid point to grid point pearson product-moment correlation analysis between 1815h 12May and 0500h 14 May, 2007. The skill was evaluated within the spatial grid box 35°-43°E and 6°S-1°N. Figure 7.22 shows the results obtained after the application of these two methods. Only results for the period of deepest convection are shown (1500h to 2300h May 13, 2007). It was deduced that the model could not adequately reproduce the observed BT with the adopted model configuration and initial data as all the FSS scores were below 0.5 for distances less than 100 Km. Since FSS skill usually increases with spatial scale, Roberts and Lean (2008) recommends that for a high resolution model with a spatial resolution of 4 Km and less, it would be a waste of resources to insist on skill evaluation for larger spatial scales (for example evaluating skill at scales of over 100 Km when running a 1 Km model) since the information content of the forecasts is limited by the additional smoothing. Thus a compromise has to be reached as to which spatial scale is reasonable for skill evaluation. It is against this backdrop that a value of 0.5 over a spatial scale of at most 50 Km is adopted below which the model skill is considered inadequate. None of the FSS curves produced between 1500 and 2300 UTC reached this threshold for scales less than 50 Km. Therefore, with this fixed skill threshold in mind, it was concluded that the ICON model could not reproduce the observed brightness temperatures over the domain at its hitherto configuration and initial conditions. Grid point to grid point correlation was also performed between the observed and the forecasts. This is however not a preferred statistic to evaluate the spatial skill of a model due to the double penalty problem e.g. Roberts and Lean (2008); Wernli H. and Sprenger M. (2018) among others. A linear correlation map was, nevertheless, produced (figure 7.22). Over the region, the correlation was poorer than over the neighbouring Indian Ocean, with some parts reporting negative correlation. This random nature of high negative/positive correlation is a further pointer to the inability of the current model set-up to simulate adequately the cloud-top temperatures.

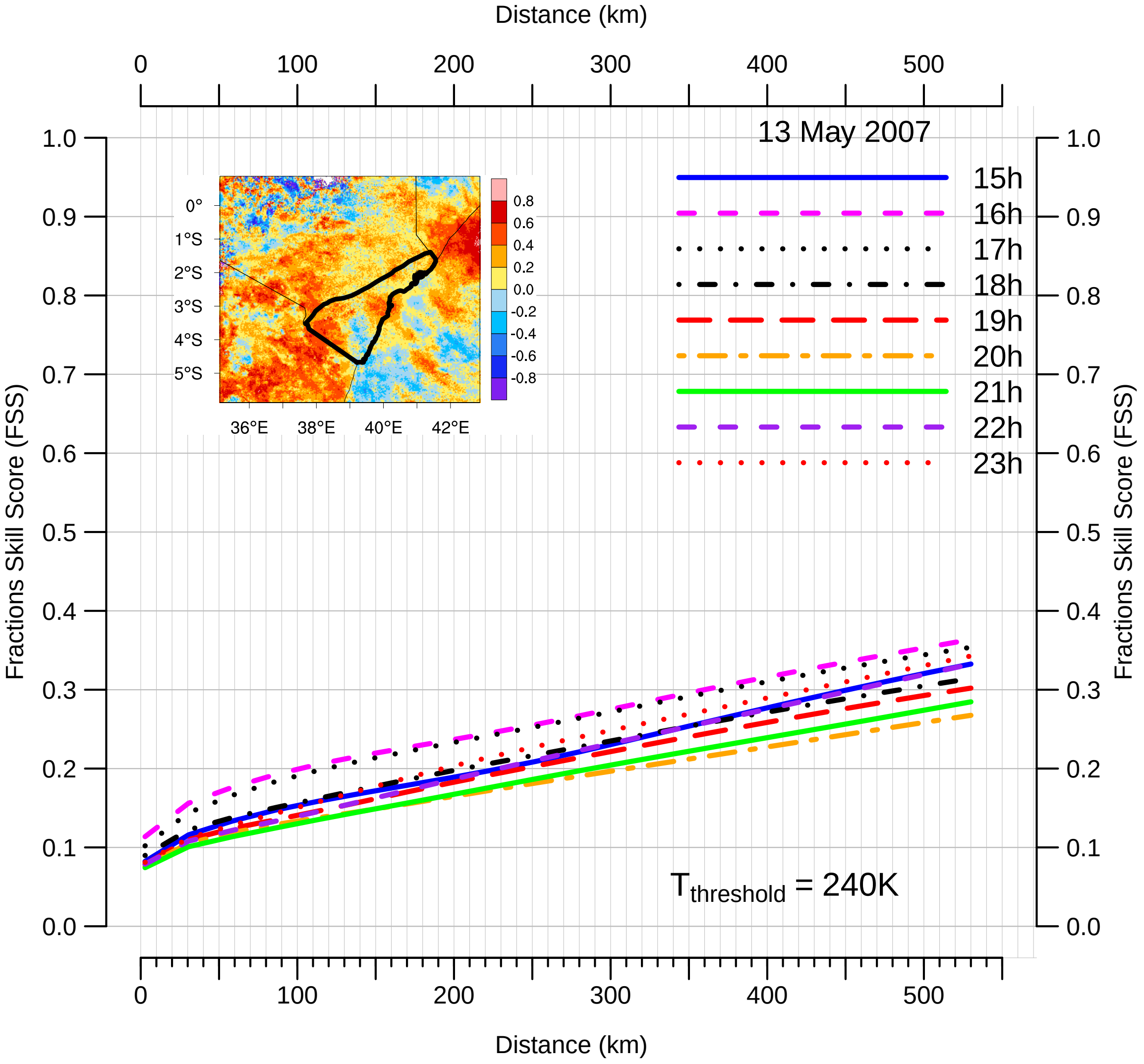

Figure 7.22: Fractions Skill Score (FSS) and grid-point based correlation coefficient between BT and ICON model simulated cloud top temperatures (CTT) initialized at 18 UTC over the Coastal Lowlands using ERAI reanalysis datasets. Shown are FSS curves during the most intense convection (between 1500–2300 UTC 13 May, 2007). Temperatures below 240 K are deemed to be representative of deep convection to which the binary fields of FSS are defined. Inset plot is the linear correlation coefficient map between the observed (BT) and the forecasts (ICON simulated cloud-top temperatures) between 1815 UTC 13 May and 0500 UTC 14 May, 2007.

7.6 ICON simulation using ERA5 as initial data

A similar simulation as in section 7.5 was also undertaken using ERA5 reanalysis as initial data in an attempt to seek for a better representation of the case. However, the results were not significantly different from those obtained with ERAI initialization. Contrastingly, all initialization times using ERA5, namely 12 UTC 12 May, 18 UTC 12 May and 00 UTC 13 May 2007 for A06 were found to produce scattered precipitation along the coastline ($S < 0$) with a corresponding enhancement in total precipitation ($A > 0$) throughout the region (figures not shown). The most representative simulation among the three attempted initialization times for the A06 precipitation was the one initialized at 12 UTC 12 May. Just like in the case of A06, application of SAL to the sub-daily (3-hourly) precipitation objects reflected too much scattered precipitation with enhanced magnitude compared to the TRMM observations. Application of FSS was also done to the ERA5-

forced simulation of Cloud Top Temperatures (CTT). The results were such that there was too weak a relationship with BT even when the number of grid spaces were increased to beyond 50 Km (which was the most ideal distance chosen for this simulation whose inner nest had a resolution of 3.25 Km). The conclusion drawn was that initialization of the ICON model using the more robust ERA5 reanalysis as initial data to the nested simulation for the Coastal Lowlands case on 14 May 2007 did not improve the results obtained from the simulation of the case using ERAI-forced simulation.

7.7 Summary and Conclusions

This chapter examined the extreme precipitation event that occurred over the Coastal Lowlands of Kenya on 14 May 2007. The date was identified based on the most contiguous areas of precipitation exceeding the 98$^{\text{th}}$ percentile threshold in observations. The event appears to have either been ignited or amplified by a superposition of an eastward propagating Kelvin wave and an equatorial Rossby wave resulting in a drop in pressure near the surface and divergence aloft. The resulting low induced strong onshore winds to the region where frictional convergence ensued. This caused uplift of high θ_e-air to the level of free convection. A persistent moisture flux between surface and the mid-levels advected moisture from the nearby anomalously warm western equatorial Indian Ocean to the region leading to significant increases in precipitable water levels in a column. Lagrangian analysis showed that the source of moisture was over the western equatorial Indian Ocean where upper level winds sunk over the Mascarene high taking a south-easterly orientation to the region releasing latent heat once forced to ascend over the region. The region was found to be conditionally unstable with moist unsaturated air lying within the lower levels. Since ERA5 reanalysis model has a low CAPE bias in its climatology compared to upper air in situ observations, the relatively moderate amounts of CAPE could have been higher since the rains appeared to be preceded by high amounts of CAPE with a few hours lag. Representation of accumulated precipitation between 06 and 06 UTC by the ICON model fell short of expectations with the model capturing the location of the event but failing to reproduce the structure and the amplitude. The model produced too isolated convective cells of precipitation while overestimating precipitation where the isolated cells reported precipitation of a higher magnitude than observations. The model also fell short in reproducing cloud top temperatures by producing too warm clouds with a noisy pattern.

It is concluded that ERA5 is an adequate reanalysis model for diagnosis of large-scale systems but misses out on the local to mesoscale processes. The reanalysis model was able to show that the extreme precipitation event on 14 May 2007 was a synoptically-forced one benefiting from a superposition of tropical waves initiating a westward moving tropical disturbance and creating a low that saw the acceleration of winds towards the region where, due to frictional convergence caused by coastal friction, saw the rising of air to the level of free convection. The anomalously warm waters of the neighbouring Indian Ocean provided the impetus in terms of availing high θ_e-air that promoted a steep instability scenario triggering the formation of cumulus towers that eventually produced highly localised extreme precipitation. The slight low pressure system, moisture flux and its convergence helped sustain the system for a longer period. Representation of the event in the convective-permitting nested set-up of ICON was not adequate probably because of a lack of a large network of upper-air data platforms that would have gone a long way into enriching data assimilation tasks at ECMWF since the latter was used to force the model. Perhaps a more representative initial data would help the model evolve and produce realistic and more accurate forecasts although in some instances, the model can be so bad that it loses this advantage over the first 24 hours. However, these initial results should be treated as a stepping stone for future endeavours in the adoption of the ICON model in simulating weather and climate extremes over the region as a complement to the existing regional numerical models.

Chapter 8

Case 2: Lowlands 27 – 29 October 2011

8.1 Event description and impacts

The extreme precipitation event of 29 Oct. 2011 was embedded within the short rains season which occur during the months of Oct. to Dec.

Not much could be found in the literature documenting this event. However, the Disaster Relief Emergency Fund (DREF) noted that the short rains of 2011 were characterized by heavy rainfall and storms in various parts of the country with the Lowlands region being the most affected. The Kenya Red Cross Society (KRCS) estimated that at least 25 people had lost their lives in flood-related incidents and approximately 15,045 households (91,692 people) had been displaced from their homes. Indeed, the Lowlands was the most affected by the floods with the districts of Isiolo, Marsabit and Moyale bearing the biggest brunt. More than 4,000 households were affected with approximately 2,152 households suffering severe losses in terms of property and body injuries. Livestock, which is the main economic mainstay of the majority of households over the northern part of Kenya suffered greatly as they transitioned from the previous protracted drought. The enhanced rains triggered major humanitarian difficulties as the existing poor infrastructure was easily destroyed by the torrential rains.

According to a United Nations High Commissioner for Refugees (UNHCR) report published online on 15th Nov. 2011, the Dadaab refugee camp in Wajir county suffered a major health crisis. The report documented about 60 cases of cholera outbreaks and other waterborne diseases leading to fatalities as personnel responsible for provision of medical services were hampered from accessing the area due to heavy flooding. The flash floods were not only unique to Kenya but affected the southern region of Ethiopia, a neighbouring country, where an airstrip in Dollo Ado was hit by flooding and remained out of service for about four days.

Nicholson (2016) opined that the strong easterly anomalies prevailed during this flood event as explained by figure 3.5. However, a marked contrast occurred in the winds in the Turkana Channel, which were very strong in Nov. 2010 but very weak in Nov. 2011 amplifying the effect of the large-scale factors governing rainfall over eastern Africa.

8.2 24-hour accumulated precipitation between 0600–0600 UTC on 29 October 2011

24-hour accumulated precipitation between 0600–0600 UTC (A06) reported on 29 Oct. 2011 was found to have been much higher than climatology. Marsabit rain-gauge station located towards the northern part of the region received 106.7 mm of rainfall in 24 hours (figure 8.1a read together with figure 2.1), the highest amount among all the stations considered. It was only in four (nine) other times that a value equal or larger than this was reported by the Marsabit rain-gauge instrument in the 1998–2014 (1985–2014) climatology. Since the methodology here required contiguity for gauge stations as well as for TRMM pixels, those other instances when higher values were reported in Marsabit were not considered as they were not buttressed by extreme precipitation elsewhere within the region. Other rain-gauge stations reported much lower values but the amounts were appreciable enough to exceed the 95th percentile in A06 for this date between 1998 and 2014.

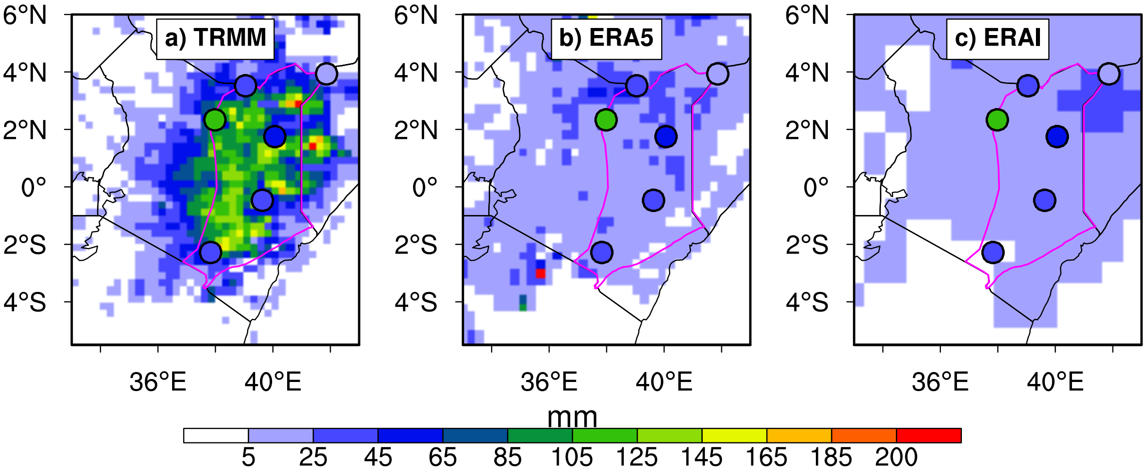

Figure 8.1: Spatial distribution of A06 over the Lowlands during 29 Oct. 2011 for a) TRMM, b) ERA5 and c) ERAI model ouputs. Corresponding rain-gauge observations are shown as markers.

Stations within the Lowlands report low amounts of rainfall annually compared to stations located within the highlands, Lake Victoria basin and along the coastline. For example, the 1985–2014 climatological period showed that Mandera meteorological station received an average of 282 mm of rainfall annually while the highest annual amount was reported by Marsabit meteorological station at an average of 703 mm (figure 2.1 for the station locations). For the date in question, the gauge station with the highest mean precipitation amongst all the Lowlands stations used in this study was Makindu at 13.2 mm (Mean calculated as the 21 days centred on the day and month for between 1998 – 2014). These non-coherent properties of gauge stations over this region are rampant across several years. The convective nature of rainfall over this vast region renders it a candidate for highly localised precipitation.

To underpin this localisation property of precipitation over this region, figures 8.2a–8.2f demonstrates precipitation incoherence over the region. A date in each panel was chosen when at least one of the rain-gauge stations in the Lowlands reported A06 that surpassed its 99.5th percentile within the 1998–2014 climatology. Figure 8.2f shows a highly localised event where only Makindu rain-gauge station (marked with an ×) reported A06 that surpassed the 99.5th percentile while the rest of the stations reported barely any

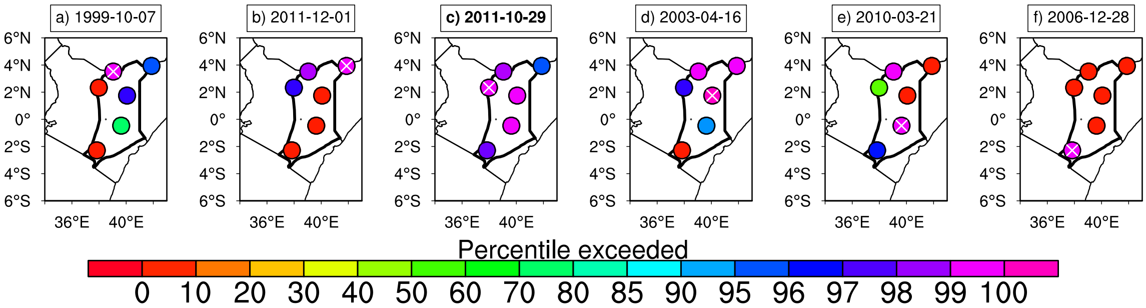

Figure 8.2: *Percentile exceeded across randomly chosen dates within the Lowlands when a single station (marked ×) reported a precipitation value greater than its 99.5th percentile within the period 1998-2014. (Only values >= 0.1mm passed to the Empirical Cumulative Distribution Function (ECDF) function.)*

precipitation. Spatial rainfall incoherence exists too over this region. For example, figure 8.2b shows three stations over the northern part of the region reporting extreme precipitation with little or no rains over the southern part of the region. During some instances, coherence is observed. For example figures 8.2a, 8.2c (which is the reference date for this study) and 8.2d, where at least more than half of the stations reported appreciable amounts of rainfall. It should be noted that coherence based on a majority of rain-gauges reporting appreciable A06 values is not entirely devoid of peculiarities. A case in point is 07 Oct. 1999 shown in figure 8.2a where Marsabit gauge station which neighbours Moyale has little or no rains. Therefore, the term "homogeneous zone" is used with caution bearing in mind this heterogeneous precipitation property. In any case, the term was used by Indeje et al. (2000) in their study using monthly precipitation records.

TRMM-3B42 blended precipitation product reported a contiguous A06 object on 29th Oct. 2011 (figure 8.1a). The precipitation object was locked within the Lowlands boundary with the rainiest part located further to the east. A sharp contrast emerged among gauges, TRMM and ECMWF reanalysis outputs. First and foremost, ERAI produced relatively higher amounts of precipitation towards the north-eastern part of the region than over other areas (figure 8.1c). Maximum precipitation object from ERA5 was shifted westward relative to ERAI though remaining over to the north of the region with smaller isolated cells of convection distributed randomly across the country and beyond (figure 8.1b). None of the A06 object from ERA5 mimicked the corresponding TRMM object. Sharp differences were evident too between precipitation reported by gauges and that produced by the reanalyses model. The model tended to underestimate extreme precipitation by a factor of about five (like is the case for Marsabit station) but producing relatively reasonable values across the rest of the region when the event was not as extreme. It can therefore be concluded that the model performed well in producing non-extreme precipitation values but poorer in representing highly intense precipitation systems.

8.3 Event extremity against climatology

This section examines the extremity and contiguity of the precipitation event of 29 Oct. 2011 relative to the climatological period, 1998–2014, from both rain-gauges and TRMM. A summary of extreme precipitation statistics for both data sets is given in Table 8.1. In general, all the stations except one surpassed the 98th percentile in climatology with two stations surpassing the 99.5th percentile within the TRMM period. The mean precipitation rates for the stations were comparable to one another even though TRMM

Table 8.1: *A06 statistics on 29 Oct. 2011 for both Gauges and TRMM illustrating their mean values (Gmean and TMean) and the percentiles exceeded (GExceed and TExceed) respectively between 1998 and 2014 over the Lowlands. TRMM A06 is the 9-pixel mean around a gauge station.*

Station	Gauge (mm)	TRMM (mm)	Gmean (mm)	Tmean (mm)	GExceed (%)	TExceed (%)
Moyale	22.20	49.30	8.80	7.90	98	99.99
Mandera	7.80	14.40	11.60	10.2	95	99.99
Marsabit	106.70	72.20	11.90	9.1	99.5	99.99
Wajir	45.10	100.90	11.60	10.6	99.5	99.99
Garissa	35.20	83.50	10.60	9.1	99	99.99
Makindu	24.00	88.30	13.20	10.3	98	99.99

tended to overestimate average precipitation by a factor of seven. The severity of the event during this date cannot be overstated given that all stations reported enhanced rains and their extremity ascertained through the application of percentile-based statistics.

The violin plot in figure 8.3 shows the overestimation of precipitation by TRMM while the gauges, though showing above normal precipitation, did not report their highest precipitation magnitude on record. Mandera meteorological station located at the far flung corner of the Kenyan map (figure 2.1 and Table A.1) reported an amount that was less than its climatological mean for this day. TRMM precipitation totals underpinned this low A06 value reporting a meagre 14.40 mm which is the average for this station. Compared to the amounts of precipitation that TRMM reported for other Lowlands stations, this amount was significantly lower. It was apparent that this particular area was not fully affected by the system that brought heavy rains to the rest of the Lowlands.

Indeed, the 2°x2° space-averaged IR brightness temperatures from SEVIRI showed that the space within this grid box was not as cold compared to other grid boxes surrounding other rain-gauge stations within the Lowlands. Figure 8.6c shows that IR brightness temperatures from SEVIRI hardly went below 240 K. This buttresses the findings of section 8.2 about localised precipitation in this vast homogeneous rainfall region.

In terms of the extremity of the event relative to climatology, TRMM produced its maximum precipitation amount on record within the region and its surroundings with the center of mass of the highest percentile exceeded within the TRMM period located slightly to the northern part of the region as shown in figure 8.4a. The precipitation maxima was observed to be fairly coherent. Though the gauge stations did not reflect this scenario for reasons elucidated before, availability of TRMM precipitation data alleviates this problem by virtue of its wider spatial coverage and relatively high resolution. It is a more robust product compared to other alternative data sources. The center of mass of the precipitation as reported by TRMM was found to cover the area around Marsabit (whose rainfall was the highest among all the stations considered) and was absent around Mandera (the station that did not report appreciable amounts of precipitation).

To re-emphasize the tendency of ERA products in underestimating precipitation over the region, figure 8.4b and 8.4c show that within the climatological period of 2000 – 2018 and 1979 – 2018, ERA products produced extremely low amounts of precipitation

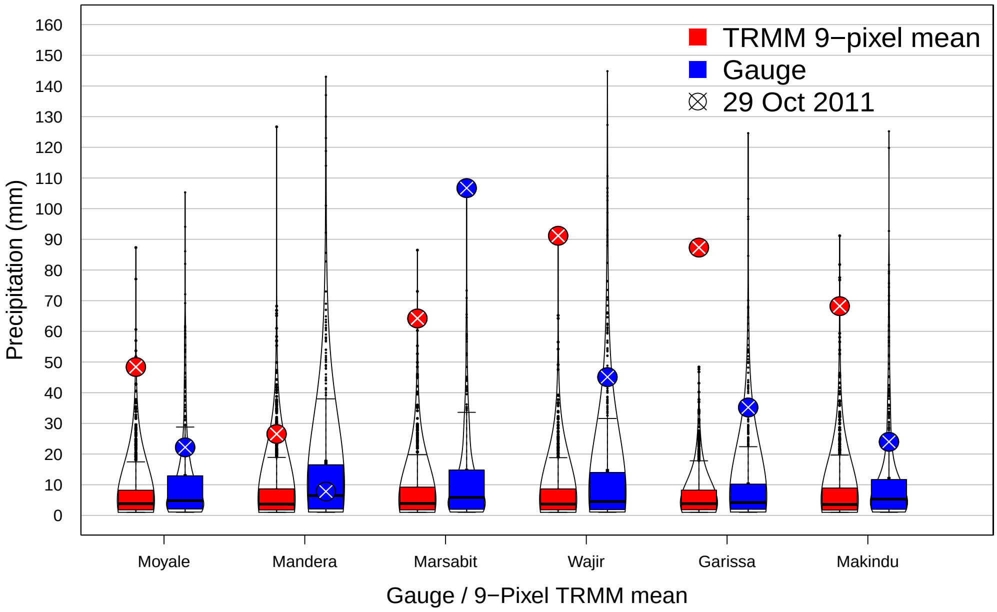

Figure 8.3: *A violin plot showing extremity of the event within the period between 01 Jan. 1998 and 31 Dec. 2014 for A06 TRMM3B42 (A06 to correspond with rain gauge observational norm; shown in red) and a similar distribution but for rain gauges over the Lowlands between 01 Jan. 1983 and 31 Dec. 2014 (shown in blue). Markers show the event of 29 Oct. 2011 when the contiguous extreme event was recorded. TRMM aggregation is based on the 9-pixel mean surrounding each station.*

compared to gauges and TRMM on 29 Oct. 2011. However, from the climatology of the model, this A06 was the highest on record for this day (considering 10 days centred on this date). ERA5 model showed that over to the northern part of the region where it produced the highest amounts of precipitation on record, the values were at their highest as they corresponded to the 100th percentile. For ERAI, the precipitation amount produced during this day surpassed its 99th percentile in climatology. The contrast between the two model outputs is again the spatial shift in percentile where the latter tended to maximise its precipitation over the north-eastern part of the region and the former within the north-central part. Though none of the ERA-model outputs produced coherent precipitation across the entire region as observed by TRMM, their ability to simulate the magnitude of the event towards the north of the region is appreciated and subsequent sections shall strive to reveal the possible causes using various ERA5 model output variables. It was beneficial to this study that ERA5 renalysis model produced extreme precipitation with respect to its climatology since that justified examination of various dynamical variables whose evolution could reveal the scale of the system including its thermodynamic characteristics.

8.4 Sub-daily characteristics of the event

The event was observed to have been a long-lived synoptic system between 27 and 29 Oct. 2011. Inspection of BT loops between the two dates pointed to a system that emerged from western Uganda with smaller convective cells developing from southern Ethiopia, enhanced by an intense LSB emerging from the southern Somali coast to become an intense and contiguous system characterised by BT<220 K. This system was observed to remain stationary over the Lowlands with a subtle westward propagation. The system eventually grew with time to become a huge cloud cluster that is attributed to the heavy

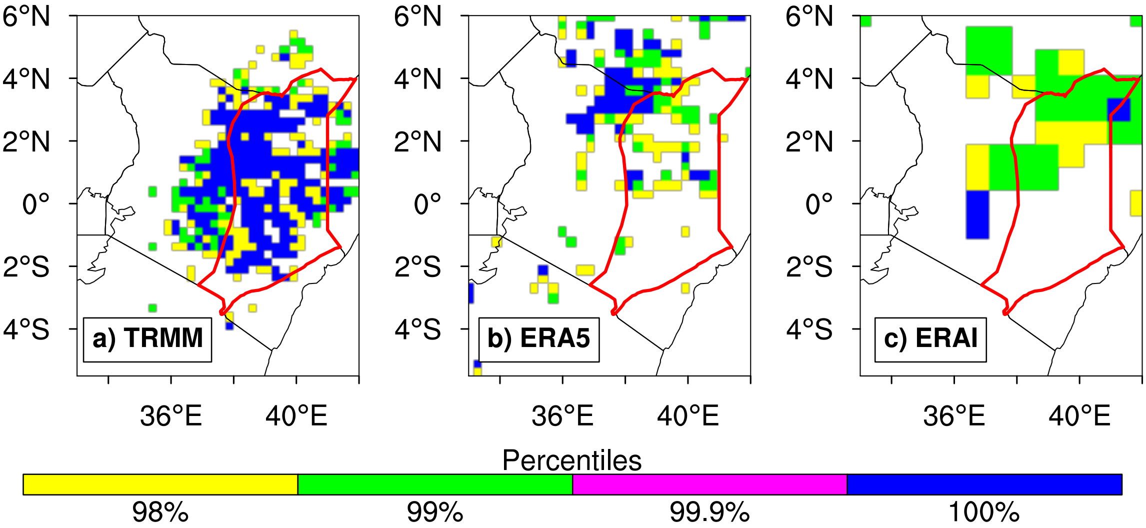

__Figure 8.4:__ Various percentile thresholds, namely, 98, 99, 99.9 and 100th equalled or exceeded by precipitation during 29 Oct. 2011 by a) TRMM, b) ERA5 and c) ERAI. The percentiles are calculated based on a 20-day window period centered around the event date of 29 Oct. 2011. Climatology years are 1998-2014, 2000-2014 and 1979-2014 for TRMM, ERA5 and ERAI model outputs respectively.

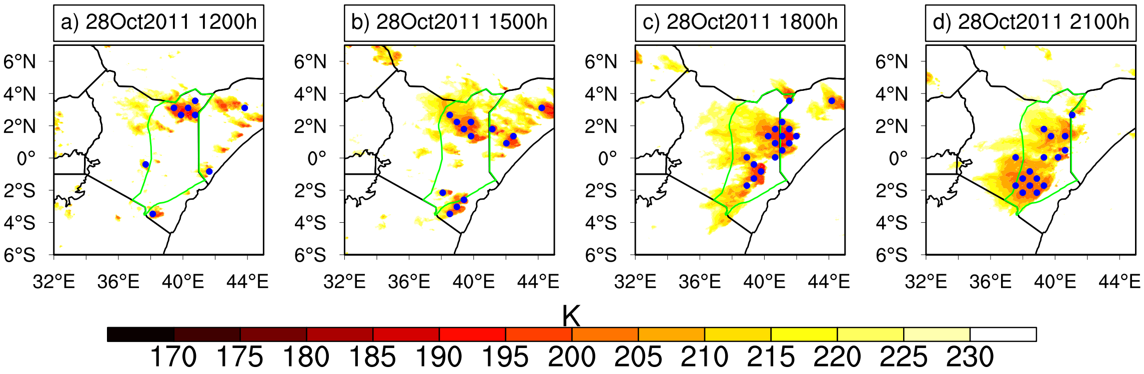

__Figure 8.5:__ Evolution of IR brightness temperatures from SEVIRI (filled contours; K) and overshooting towers from the CLAAS algorithm (dot stipples; no units) on a 3-hourly interval between 1200 and 2100h 28 Oct. 2011 (IR temperatures > 230 K are masked to highlight deep convection). Full 15-min IR Brightness temperature loops between 00 UTC 27 Oct. 2011 and 03 UTC 29 Oct. 2011 can be found under the link: `https://drive.google.com/file/d/1EzMCpRzkW1yfUAMZ-NTqGRltQf5o0A2Z/view?usp=sharing`

precipitation that characterised the Lowlands between 28 and 29 Oct. 2011. Interestingly, the evolution of the event on 28 Oct. was similar to the evolution on 27 Oct. in terms of cold cloud development in an outstanding diurnal cycle that contributed to the heavy rains observed on both days over the region. A summary of the evolution of the event as observed especially from SEVIRI infrared brightness temperatures between 27 and 29 Oct. is provided in Table 8.2.

Table 8.2: *A summary table for the sub-daily evolution of convection and precipitation over the Lowlands between 27 and 29 Oct. 2011*

Day	Time (UTC)	Activities
27-Oct.	0900 – 1300	A weak convective system emanates from the western side of the Lowlands and spreads North – South (N–S) covering N. Tanzania, W. Kenya and S. Sudan as it propagates slowly eastward. An intense LSB with BT<200 K at the center develops over southern Somali coast propagating westward. Rains between 0–5 mm in 3 hrs reported by TRMM, CMORPH and ERA5 over southern and central parts of the Lowlands.
	1300 – 1600	The LSB propagates westward towards the northern part of the Lowlands and becomes stationary. Cells of convection emerge from the southern part of the Lowlands. Moderate to heavy rains reported across all station's 2° × 2° spatial box (figure 8.6).
	1600 – 1815	The LSB system weakens and spreads towards the central parts of the Lowlands and western Somalia too. Convective cells emerge from southern flank of the Lowlands and intensify with BT<200 K. Rains between 0–5 mm in 3 hrs over Makindu lying to the south of the region.
	1815 – 0000	The convective system moves westward and weakens over the western highlands.
28-Oct.	0000 – 0530	The system continues to dissipate as it moves north-westward towards S. Sudan and disappears.
	0530 – 0945	New convective cells with BT<200 K emerge from within the central parts of the northern Lowlands propagating westward.
	0945 – 1045	The cells grow into a large cloud cluster over the northern Lowlands with enhancement coming from the southern Somali coast as a new LSB develops. Overshooting towers of convection from CLAAS emerge randomly across the region with the northern part of the Lowlands experiencing the deepest cloud clusters (figure 8.5).
	1045 – 1815	The LSB grows in size to become a deep convective system spread over the entire Lowlands and western Somalia. The system is observe to split into three large convective systems covering the entire Lowlands and characterised by overshooting convection.
	1815 – 2000	This was the period of the most intense intense convection. Convective system remains stationary and splits into two large systems with BT<200 K. Overshooting towers of convection reported over a wide area. Heavy rains across the entire Lowlands of between 10 – 30 mm in 3 hrs reported in TRMM and CMORPH. Southern and eastern parts receive the highest amounts at 30 mm.
	2000 – 2345	The deep system weakens in intensity with BT of between 210 – 230 K propagating westward and spreading over large area. Rains are suppressed.
29-Oct.	0000 – 0615	Dissipation period as the system continues to move westward and dies off afterwards.

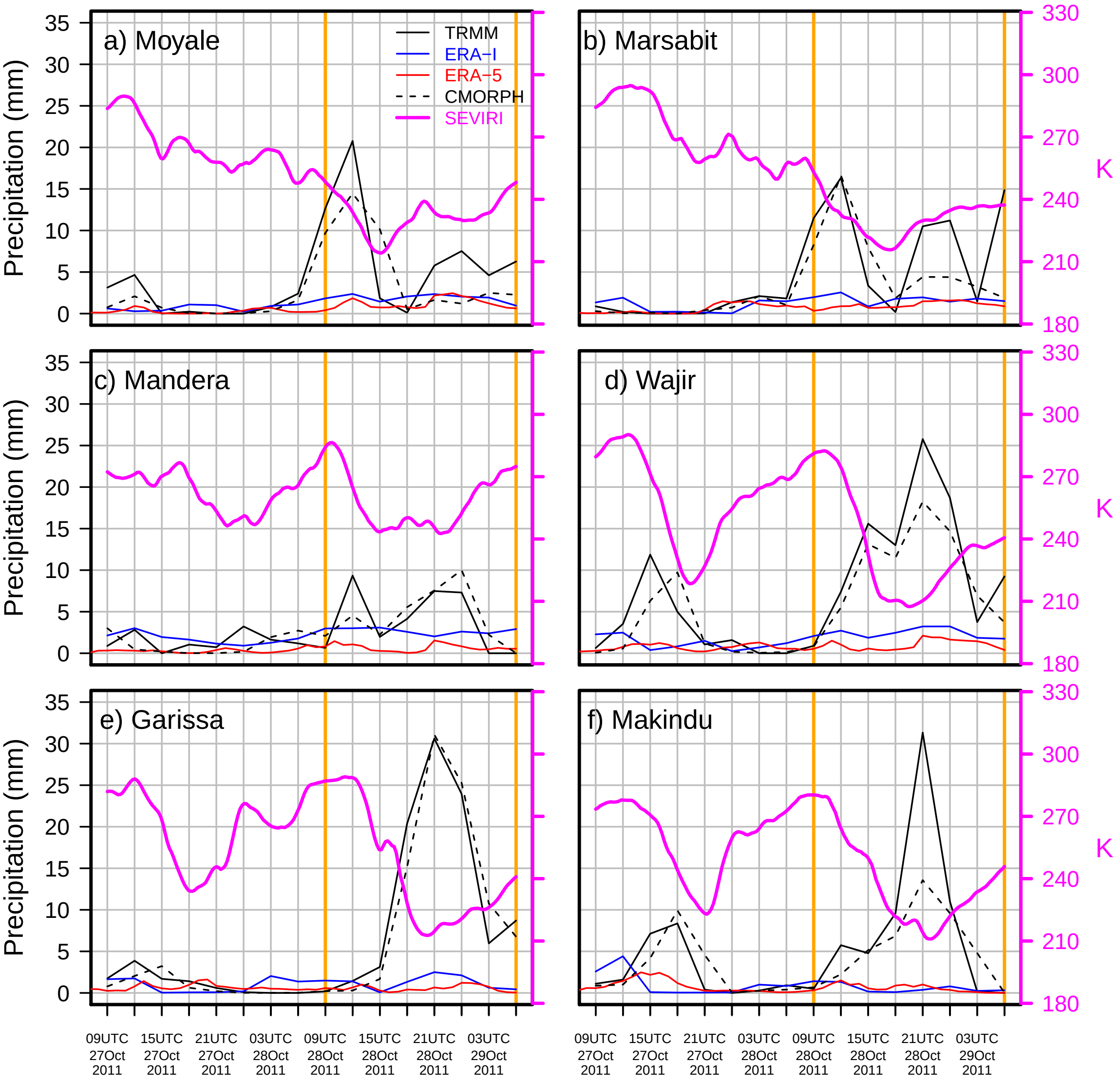

Figure 8.6: *Evolution of convection and precipitation within a 2°x2° spatially averaged grid box surrounding each rain-gauge station over the Lowlands namely a) Moyale, b) Marsabit, c) Mandera, d) Wajir, e) Garissa and f) Makindu (For locations on map, (figure 2.1). Data sources are namely, TRMM, CMORPH, SEVIRI and ECMWF model outputs of ERAI and ERA5 on a three-hourly interval between 09 and 06 UTC Oct. 27-29, 2011. Precipitation data (mm) from all sources were accumulated to three-hours where possible while BT are made every 15 seconds. The vertical lines in orange color indicate the 06 to 06 UTC time window which contributed to the accumulated precipitation for 29th Oct. 2011.*

8.5 Synoptic development

8.5.1 Tropical waves

A superposition between an eastward propagating Kelvin wave and an equatorial Rossby wave may have triggered a TD between 25 and 28 Oct. 2011 (figure 8.7). Indeed, the event was found to have been trapped within an eastward propagating convectively coupled tropical wave and benefited immensely from an interaction between the wave and an enhanced LSB (figure D.1) The two figures demonstrate that the event was clearly embedded within convectively coupled Kelvin waves propagating from west Africa.

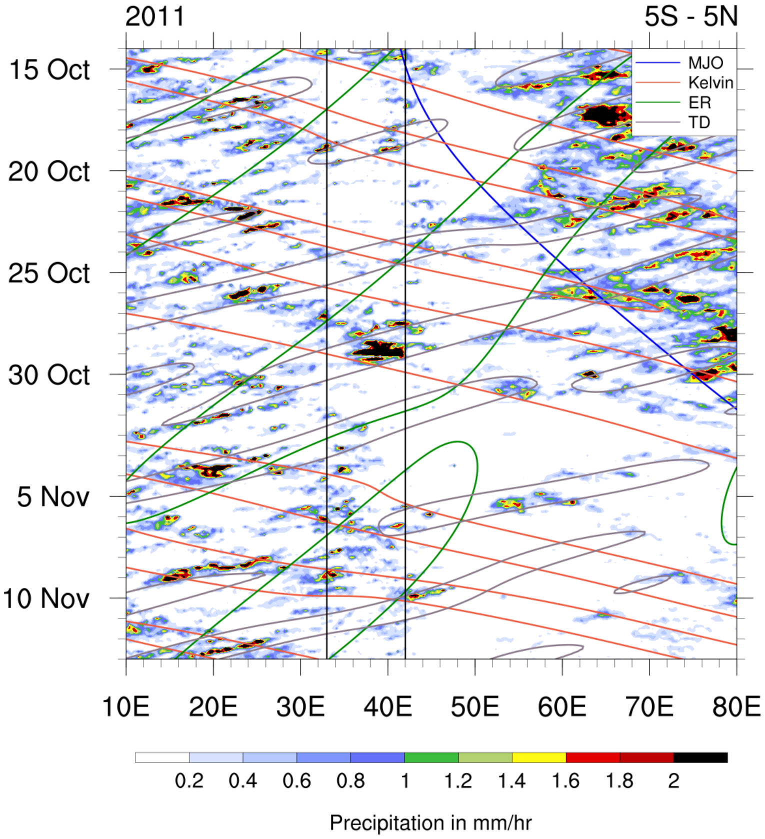

Figure 8.7: *A hovmöller diagram of TRMM daily precipitation totals between 15 Oct.–15 Nov. 2011 averaged between 5°S–5°N latitude and confined to within 10°–80°E longitude. The event center is enclosed within 33°–42°E in space and between 27–29 Oct. 2011. Filled contours are precipitation totals (in mm) while line contours depict tropical waves namely, MJO, Kelvin, equatorial Rossby (ER) waves and tropical depressions (TD). The diagram was created after application of the wave-number frequency domain concept from Wheeler and Kiladis (1999) using a routine written by Andreas Schlütter (IMK-TRO).*

No discernible convectively coupled Kelvin wave propagation was detected towards the east of 50°E, a situation affirmed by BT loops where cold clouds were absent over the western equatorial Indian Ocean. To underpin further the presence of a disturbance especially during the first phase of the convective system that was active between 27 and 28 Oct., a slight MSLP drop was registered on 26 Oct. 2011 between 00 and 13 UTC over the Lowlands. The spatial average was done in such a way as to include the neighbouring western equatorial Indian Ocean where the event was observed to have intensified under an enhanced LSB. A 24-hr evolution of MSLP and its tendency between 26 Oct. and 01 Nov. 2011 was examined in a bid to identify any drop in pressure that might have initiated the precipitation system through mass convergence. It is evident that a drop in pressure of approximately 2 hPa day^{-1} was reported during the morning hours of 26 Oct. This drop was highest at 00 UTC and weakest at 16 UTC 27 Oct. onward (figure 8.8). The drop might have been responsible for the convective regime observed during the first phase of the system observed from BT loops on 27 Oct. between 08–19 UTC. The period of calm weather observed from the loops between 20 UTC 27 Oct. and 11 UTC 28 Oct. was also observed from the pressure tendency. The second phase of extreme convection witnessed from the BT loops between 12 and 21 UTC was not observed on the pressure tendency plot between 28 and 29 Oct. as the model tended to reflect a sharp drop in MSLP much later on 29 and 30 Oct. 2011 when the event had already dissipated.

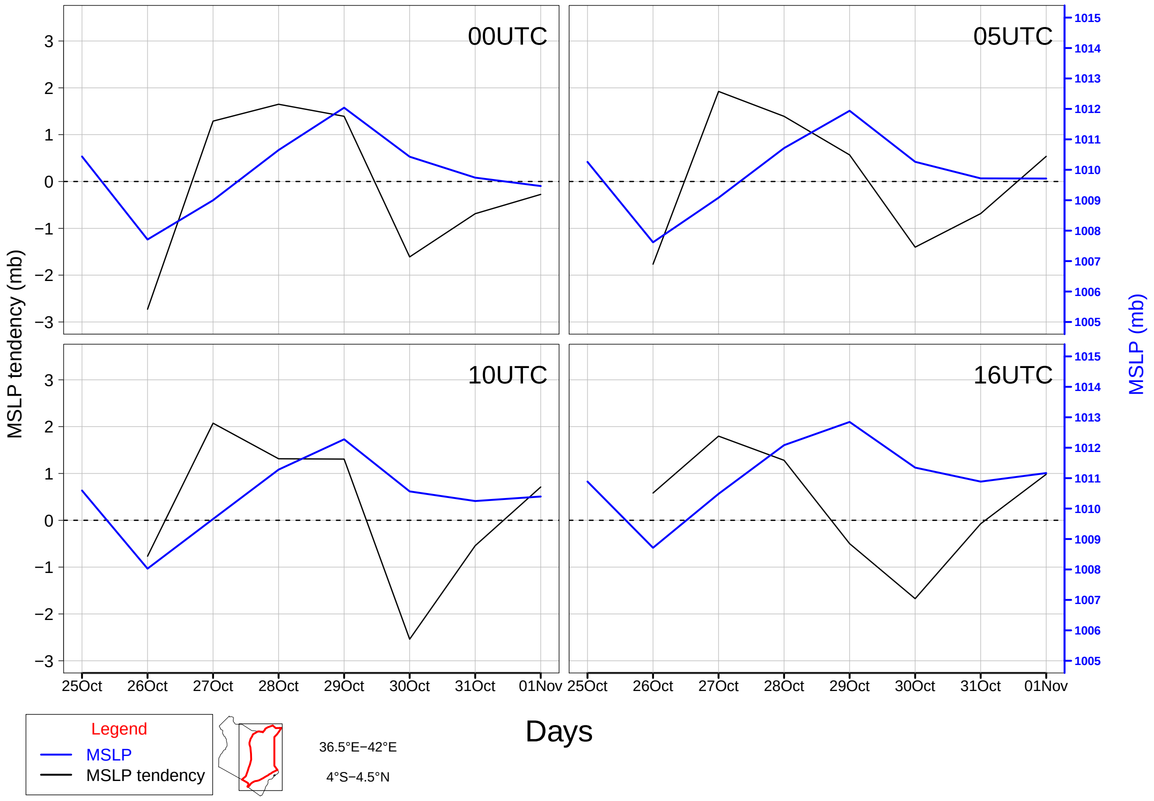

Figure 8.8: 24-hour evolution of ERA5 MSLP (blue curve) and its tendency, ρ (black curve, calculated as $\rho_{t_o} - \rho_{t_o-24}$ where t_o is hour of day) between 26 Oct. and 01 Nov., 2011 and averaged between 35°E-45°E and 5°S-5°N. Only 4 times of day are shown namely 00, 05, 10, 16 UTC. (spatially averaged region is shown at the bottom of the main figure.)

8.5.2 Wind convergence, relative vorticity and vertical wind shear

During the first phase of the event that took place between 25 and 26 Oct. 2011, the depression discussed in section 8.5.1 triggered widespread wind convergence over the Lowlands (figure 8.9a and 8.9d). Loops of 850 hPa winds (see the link under figure 8.11) pointed to a persistent low-level flow of north-westerlies and north-easterlies over the east African region with speed convergence observed over the Ethiopian highlands, the Kenyan highlands as well as over the lake basin. This convergence was presumably associated with the observed convection and precipitation over the lake basin and some parts of southern Lowlands as well as over the north-eastern Lowlands between 26 and 27 Oct. 2011 (BT loops under the link in figure 8.5 read together with Table 8.2). The continued flow of westerlies across the east African region on 26 Oct. and the incoming low-level flow from the northern part of the western equatorial Indian Ocean was responsible for the lifting of air parcels through both directional and speed convergence. This widespread convergence was responsible for the first phase of precipitation regime witnessed on 27 Oct. 2011 between 1000–1530 UTC (Table 8.2). Indeed, the period between 18 UTC Oct. 26 and 15 UTC Oct. 28 was on average characterised by convergence in the lower levels up to the 700 hPa level. Over the region to the north of the equator (figure 8.9a), the vertical extent of convergence increased with time from the surface to about 500 hPa level between 00 UTC Oct. 26 and 00 UTC 29 Oct.

Over the region to the south of the equator (figure 8.9d), the vertical extent of convergence was somewhat deeper than over the northern part growing upto the 700 hPa level especially during the first phase of convection. However, convergence beyond the 700 hPa was short-lived over the south with only a few hours (12 UTC Oct. 28 – 12 UTC Oct. 29) when convergence was deeper compared to over the northern part where deep convergence persisted for a longer duration beginning at 12 UTC 27 Oct. to 18 UTC 29 Oct. This might explain why the ERA5 model produced more precipitation towards the northern part of the region than to the south.

Going by the rule of thumb that positive (negative) relative vorticity in the northern (southern) hemisphere implies convergence (divergence) over an area (Kutty and Gohil, 2017), cyclonic flow characterised the Lowlands between 700 and 400 hPa throughout the two precipitation phases intensifying and taking place over a deeper vertical column between 12 UTC 28 Oct. and 12 UTC 29 Oct. This was in phase with ERA5 (figure 8.12) where precipitation was observed later after 28 Oct. 2011. Indeed, as time progressed, the intensity of cyclonic flow between the surface and about 850 hPa level increased dramatically between 00 UTC 28 Oct. 2011 and 00 UTC 31 Oct. 2011. This promoted the ascent of air through a column triggering the release of latent heat and producing intense precipitation.

Inspection of vertical motion between 25–31 Oct. indicated that the first and second phases of convection (27 and 28 Oct. 2011) were characterised by strong vertical motion. The first phase experienced weaker ascent of air of between -0.5 and -1×10^{-1}m s^{-1} in the lower levels up to the 700 hPa level followed by a time window of downward motion between 00 UTC 26 Oct. and 00 UTC 27 Oct. The second phase that occurred beyond 00 UTC 27 Oct. was characterised initially by a strong ascent whose speed was in the range of -0.5 to -1×10^{-1}m s^{-1} in the lower layers up to the 700 hPa level between 00 UTC 27 and 00 UTC 28 and eventually by the strongest upward motion beyond 00 UTC Oct. 28 in the range of -4 to -5×10^{-1}m s^{-1} in the upper layers of the atmosphere (figure 8.9b and 8.9e). This corresponded to the time window when ERA5 hourly precipitation was the highest.

During this time window of intense vertical motion, potential instability intensified too, as equivalent potential temperature, θ_e decreased rapidly with height. Within the 850–1000 hPa layer, $\frac{\partial \theta_e}{\partial p}$ was as large as 15K per 150 hPa (or 0.1KhPa^{-1}). This instability was more pronounced over the northern part of the region compared to the south (figure 8.9b and 8.9e). Vertical speed shear in the horizontal wind especially in the deep layer (850 – 200 hPa level) was found to intensify with time and especially during the time window of the most intense convection (figure 8.9c and 8.9f). A quick interpretation would be that this deep layer shear was beneficial in terms of separation of the upward motion from the downward motion by pushing the anvil ahead as a result of increased upper level wind speeds. This ensures that the downward motion does not degrade the momentum of the upward motion and as such, assists the system to propagate in a line like in an MCS or a squall line. However, since the BT loops did not indicate a systematic and organised movement of cloud clusters, it was concluded that shear (both deep and mid layer) did not play a major role in either sustaining or intensifying the system.

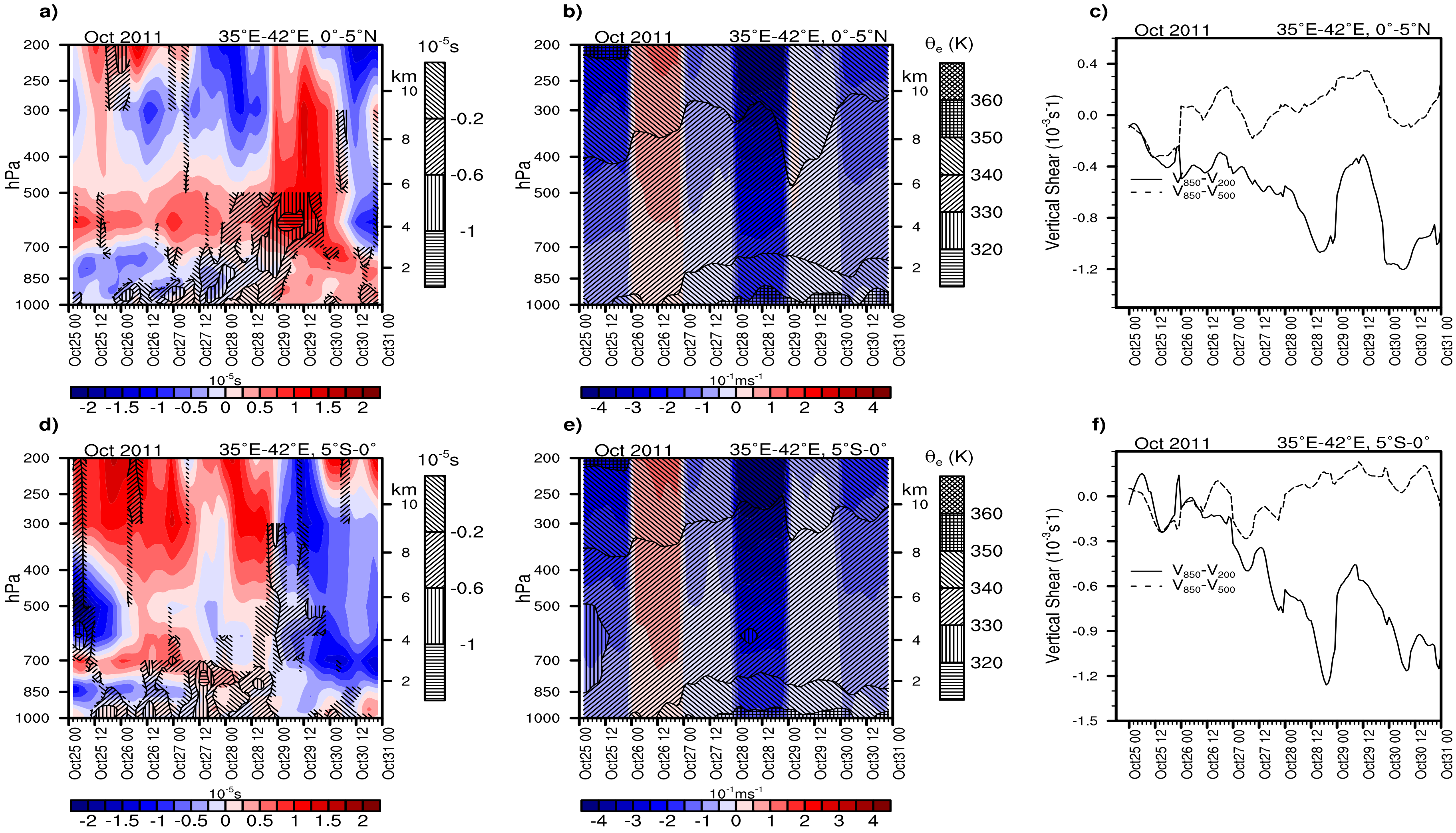

Figure 8.9: ***a*** *and* ***d****: Evolution of the vertical distribution of relative vorticity (filled colors; $10^{-5}s^{-1}$) and wind convergence (shaded contours, $10^{-5}s^{-1}$; Divergence is masked) over the Lowlands averaged between 35°–42°E, 0°–5°N for* ***a*** *(North of the equator) and between 35°E–42°E and 0°–5°S for* ***d*** *(south of the equator) three days before and two days after the event of 29 Oct. 2011.* ***b*** *and* ***e****: Same as* ***a*** *and* ***d*** *but for the vertical distribution of omega (filled colors; $10^{-3}m\ s^{-1}$) and equivalent potential temperature (shaded contours; K).* ***c*** *and* ***f****: Same as* ***a*** *and* ***d*** *but for the vertical shear of wind ($10^{-3}s^{-1}$) in a mid layer (850 and 500 hPa) and a deep layer (850 and 200 hPa).*

8.5.3 Moisture transport and conditional instability

Moisture was transported to the region by a steady northeasterly flow that was complemented at the southern Somali coastline by a southerly flow from the nearby western equatorial Indian Ocean (figure 8.10a–8.10c). Highest amount of total column water was found along the Somali coastline throughout the evolution of the event (figure 8.10a–8.10c). The high SSTs (>28°C) over this region provided sufficient moisture through evaporation that was advected onshore (figure 8.11d to 8.11f). In a subsequent section of this chapter (section 8.5.5), it was found that moisture was collected along a trajectory across the northern part of western equatorial Indian Ocean and released over the region. It is hypothesized that based on moisture flux and its convergence alone, advection of moisture from the northern end of the western equatorial Indian Ocean contributed immensely to the high amounts of relative humidity which averaged over 90% as well as CAPE over the region (figure 8.11a–8.11c). Over the southern ends of the western equatorial Indian Ocean, depressed amounts of precipitable water (<30 mmday^{-1}) were reported implying that the south-easterlies might not have acquired sufficient moisture compared to the north-easterlies. Moisture convergence over the region was most pronounced during the evening and night hours of Oct. 28 and in the morning of 29 Oct. 2011, averaging about 50 – 60 mmday^{-1} with precipitable water amounts of a similar magnitude. In fact, exceedances of total column water from the 98th percentile within the 1979–2018 climatology characterised the central to northern parts of the lowlands region. (figure 8.10b and 8.10c). These parts were, as a matter of fact, observed to have been associated with extreme precipitation amounts in ERA5 (figure 8.4). During the same time, overshooting convection inferred from BT<230 K covered the central parts of the region reflecting deep convection that produced the heavy precipitation.

Convective Available Potential Energy during the two phases of the event was moderate ranging between 1200 – 2000 Jkg^{-1}. During the first phase on 27 Oct., high amounts of CAPE were confined towards the north-eastern part of east Africa. The absence of sufficiently high CAPE over the region (<1500 Jkg^{-1}) during this phase could have been the reason why ERA5 model struggled to capture the magnitude of the event in terms of total precipitation output as observed in TRMM. However, the moderate values of CAPE ranging from 1000 to 2000 Jkg^{-1} could have resulted in the low values of precipitation output from the ERA5 model (figure 8.11a and 8.11b). Anomalies within the 1979–2018 period showed that values of CAPE in ERA5 model are usually low and therefore, values of over 1200 Jkg-1 are actually high relative to CAPE's own climate (figure 8.14). The figure indeed showed that high amounts of precipitation were preceded by a corresponding high amount of CAPE in relation to its own climatology. At the same time, the presence of high amounts of relative humidity throughout the region ranging from 90 to 100% (figures 8.11a–8.11c) pointed to an atmosphere that was in a state of instability that required a trigger mechanism for it to be released.

Equivalent potential temperature at 850 hPa level was the highest over the northern part of the Lowlands and appeared to be advected within a westerly wind regime (figure 8.11e and 8.11c). In fact, θ_e was found to decrease with height especially between 1000–700 hPa levels (figure 8.9b and 8.9e). A strong dipole mode in conditional instability was evident throughout the three days considered where the region lying to the western side of the Lowlands was highly stable compared to the eastern side (figure 8.12a–8.12c). The area within the Lowlands boundary was unstable with instability increasing towards the neighbouring Indian Ocean. This meant that throughout the three days, the atmosphere was in the right state to allow convection once a trigger mechanism (that would aid in

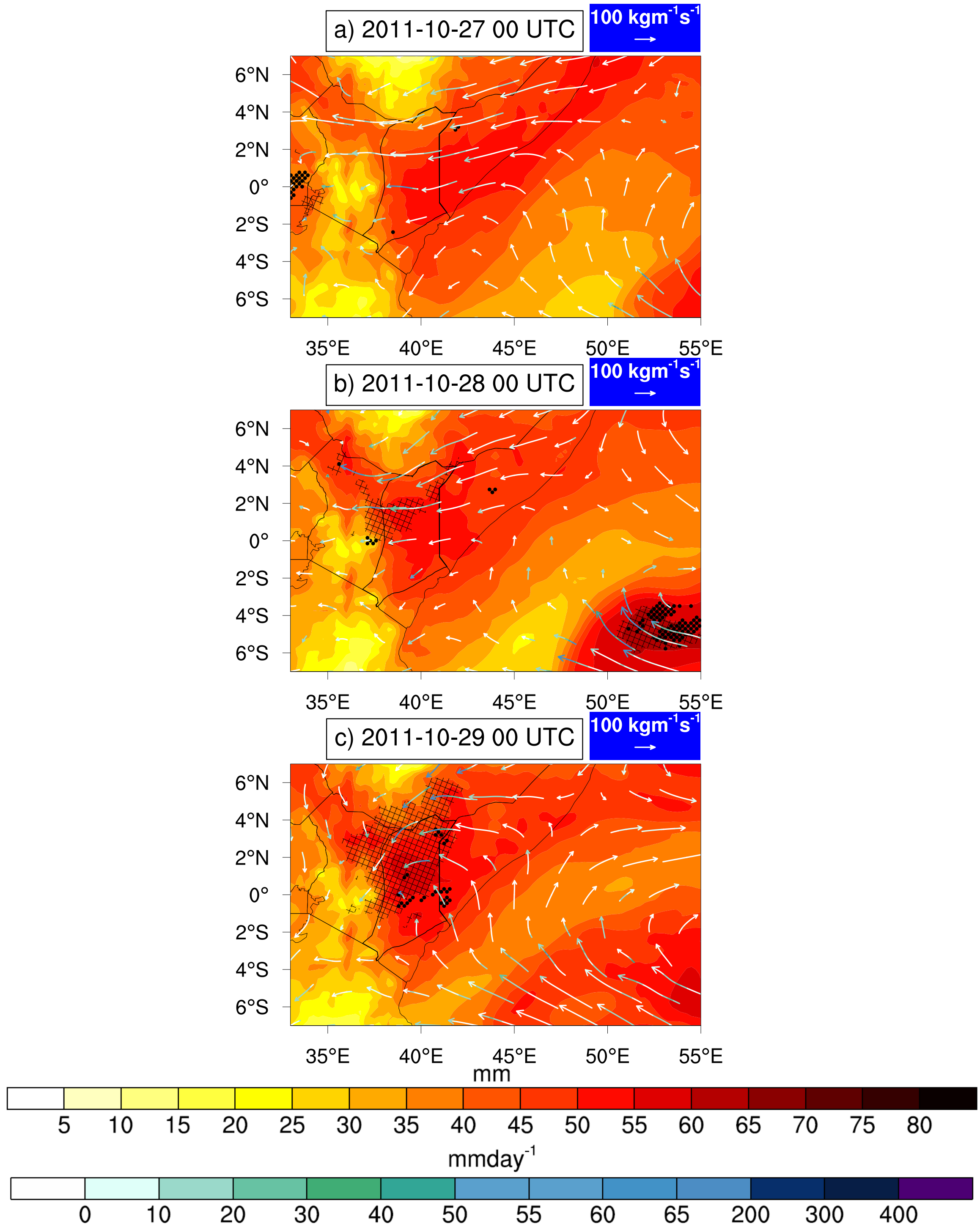

Figure 8.10: *a-c: Evolution of total precipitable water (filled contours; mm) over the Lowlands at 00 UTC on 27, 28 and 29 Oct. 2011. Overlaid is the vertically integrated moisture flux (vector; kgm*$^{-1}$*s*$^{-1}$*) and its convergence (vector color; mmday*$^{-1}$*). Divergence of moisture flux has been suppressed. Dot stipples indicate areas of deep convection from SEVIRI IR brightness temperatures (T < 230 K). Meshed stipples show exceedances of total precipitable water from the 98th percentile during the 2000-2018 period.*

lifting the underlying warm and moist air parcels to the LFC) became available. In fact, the MSE at the surface and the conditional instability peaked substantially between 28 Oct. at 06 UTC and 18 UTC. ERA5 hourly precipitation forecasts were found to be in phase with conditional instability lagging it by a few hours. However, during 28 Oct. at

22 UTC, a steep positive jump in ERA5 precipitation forecast was not accompanied by a corresponding increase in conditional instability though it was still positive (figure 8.12d)). It was speculated that convective instability observed between 12 UTC 28 Oct. and 00 UTC 29 Oct. by virtue of a decreasing θ_e could explain why ERA5 produced the rains.

A strong trigger mechanism must have been available to cause the ascent of moist air parcels to the LFC. Consequently, inspection of wind flow at the 850 hPa level indicated a strong speed and directional convergence between 18–21 UTC 28 Oct. This might have been the trigger mechanism that was responsible for vertical ascent of air parcels and the subsequent heavy precipitation (documentary material linked in figure 8.11). In a bid to understand further the extent of instability, ERA5 pressure level output data was used to make an atmospheric sounding. The rainiest grid point (40.7°E, 0.1°S) at 15 UTC 28 Oct. 2011 was chosen to vertically probe the atmosphere above it. The probe was centred on 12 UTC, 3 hours earlier. It was found that the atmosphere was indeed stable for unsaturated air parcels but unstable for saturated parcels (essentially conditional instability). The Lifting Condensation Level (LCL) and LFC were low at 903 and 900 hPa respectively (figure 8.13). This implied that not much effort was required to neutralize the CIN and trigger a lift of moist air parcels to the LFC. The parcel path over this rainiest grid point lied to the right of the environmental temperature along a deep stretch that went beyond the 200 hPa level creating the most unstable layer CAPE of about 2262 $\mathrm{Jkg^{-1}}$. Mid to higher levels were found to be very dry with lower levels being very moist a situation that could promote convective overturning in the effect that the stable lower layer is lifted.

8.5.4 Anomalies of ERA5 dynamical variables

Evolution of anomalies of ERA5 dynamical variables were further investigated to reveal the dynamical peculiarity of the event (figure 8.14). Temperature was found to have been below normal throughout the period between 27 and 29 Oct. 2011. As expected, after the intense rains at 12 UTC 27 Oct. and 21 UTC 28 Oct. respectively , the atmosphere was much cooler than average by about 4°C. This is due to the tendency of precipitation to cool the atmosphere. Dew point temperature was above normal and the anomaly preceding precipitation was even higher. In terms of moisture in the atmosphere, the RH was found to be way above normal either and increased substantially after every rain-out. This presence of anomalous humidity values played a key role in sustaining the event. Vertical integral of convergence of moisture flux in a column was found to be anomalously high as well especially during the period of intense precipitation explaining why the atmosphere was very humid. Indeed, the convergence of moisture flux contributed to high amounts of precipitable water in a column. Anomalies of precipitable water were found to be highly positive and increased just before the period of most intense convection. As mentioned in the preceding section, CAPE values were moderate. Surprisingly, these values were found to have been the highest within the period 1979–2018. Indeed, CAPE anomalies were highly positive throughout the evolution of the event. The abundance of low-level moisture might have been the reason for this anomalous CAPE amounts. Temperature at 500 hPa over the tropics has a high impact on CAPE. Decreasing θ_e^* at 500 hPa has the impact of increasing CAPE as it enlarges the area under the curve between the parcel path θ_e^* on a pressure - temperature curve. This was, however, not examined for this case but forms the basis for future advancement of this work.

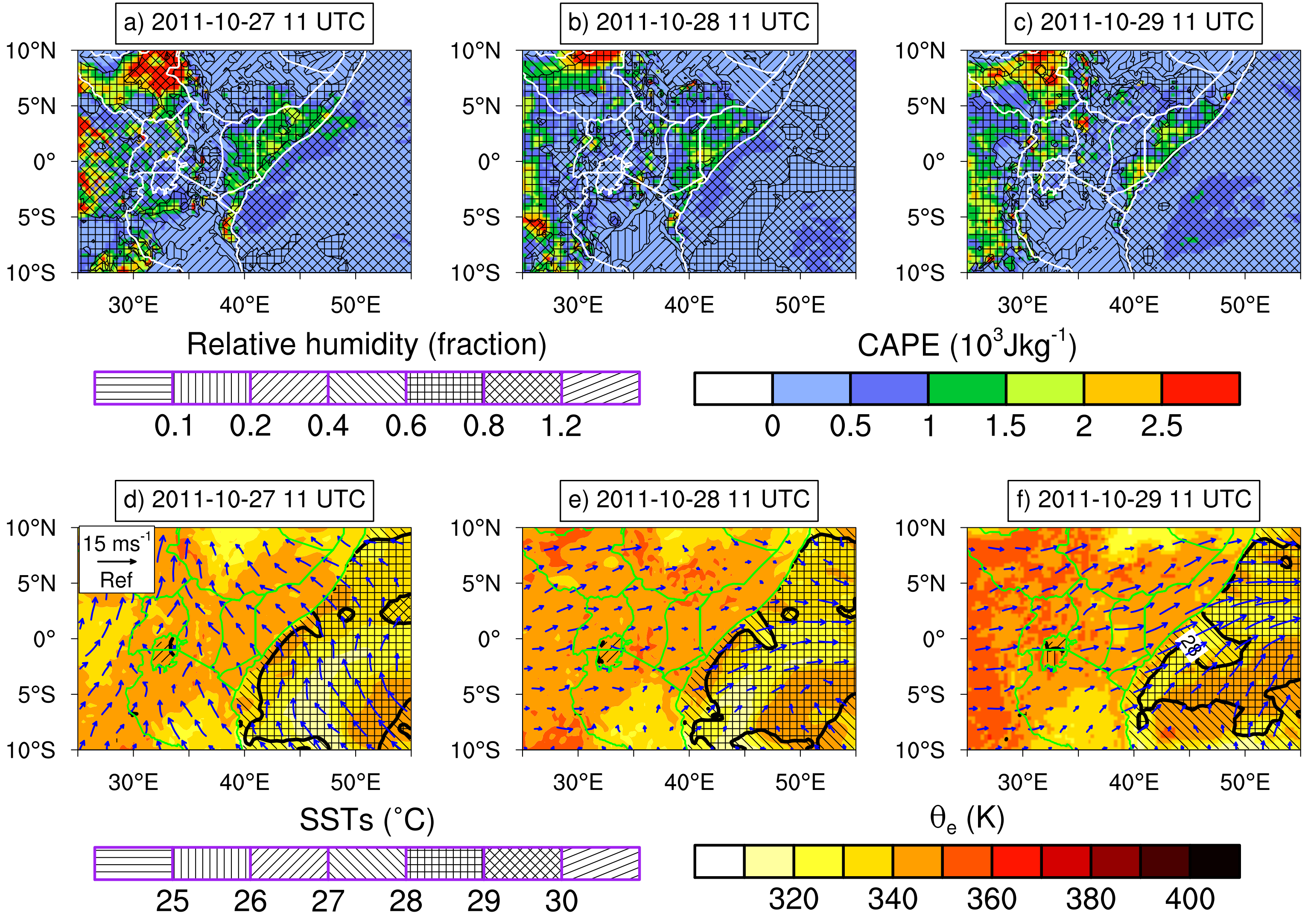

Figure 8.11: *(a-c): Evolution of ERA5 Convective Available Potential Energy (filled contours; 10^{-3} Jkg^{-1}) and relative humidity (shaded contours; no units) at 12 UTC between 27 and 29 Oct. 2011. (d-f): Evolution of 850hPa level equivalent potential temperature, θ_e (filled contours; K) and sea surface temperatures (shaded contours; K) with 850 hPa wind field overlaid on the contours. Loops of 850 hPa winds between 25 and 29 Oct. on an hourly interval can be accessed here:* `https://drive.google.com/file/d/1FCVYHLdALgrQqD0OnMAqCFZNE-goA_gT/view?usp=sharing`

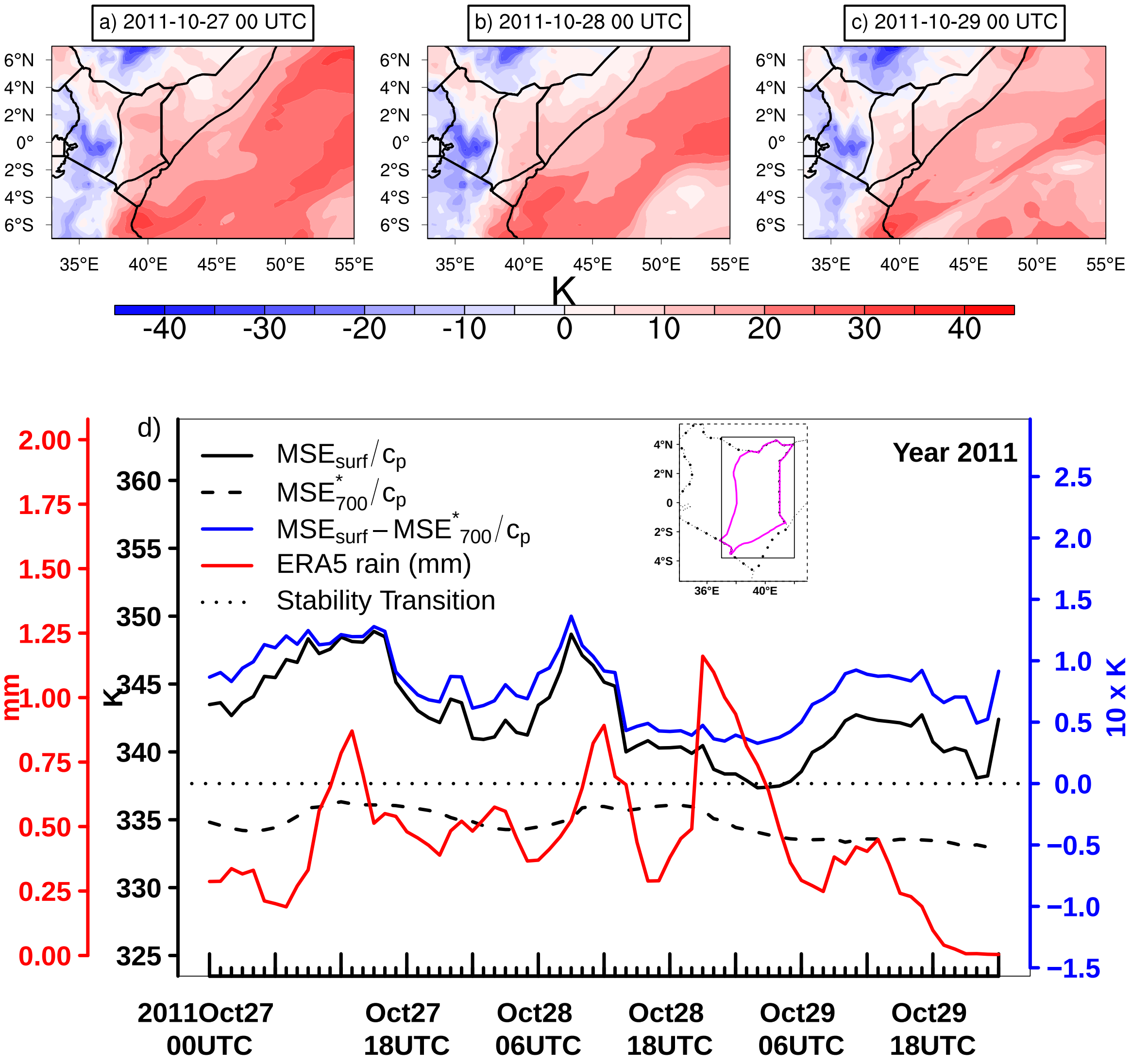

Figure 8.12: ***Top panel (a-c):*** *24-hour spatial evolution of conditional instability ($mse_{surface} - mse_{700}$) between 00 UTC 27 Oct. and 00 UTC 29 Oct. 2011 over the Lowlands.* ***Bottom Panel (d):*** *Hourly evolution of spatially averaged conditional instability (blue curve) between 00 UTC 27 and 00 UTC 29 Oct. 2011. Also shown is the MSE at 2m above the surface (black curve) and the saturated MSE at 700mb level (black curve with dashes). The red curve is the evolution of spatially averaged hourly precipitation. The dotted black curve shows the stability transition which is the line above which the atmosphere is conditionally unstable and below which it is conditionally stable. All data are derived from the ERA5 forecast model and averaged spatially within the rainiest spatial domain of 37°-42°E and 3.8°S-4.5°N (Spatial box shown in the inset map).*

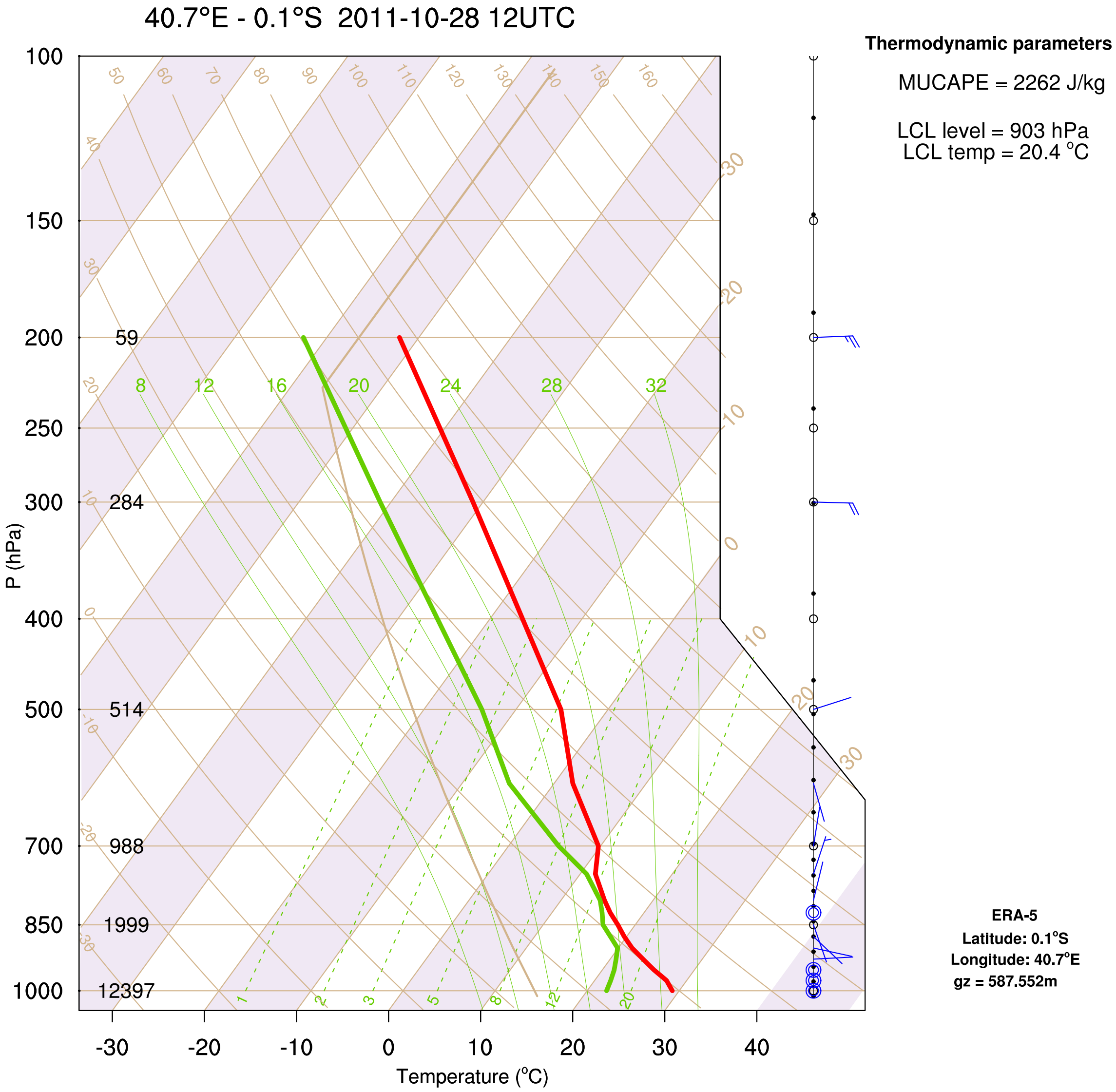

Figure 8.13: *SkewT-logP plot taken from ERA5 model data at grid point 40.7°E–0.1°S at 12 UTC 28 Oct. 2011 over the Lowlands. The bold green line is the dew-point while the red line is environmental temperature. Various stability parameters are shown at the periphery of the plot.*

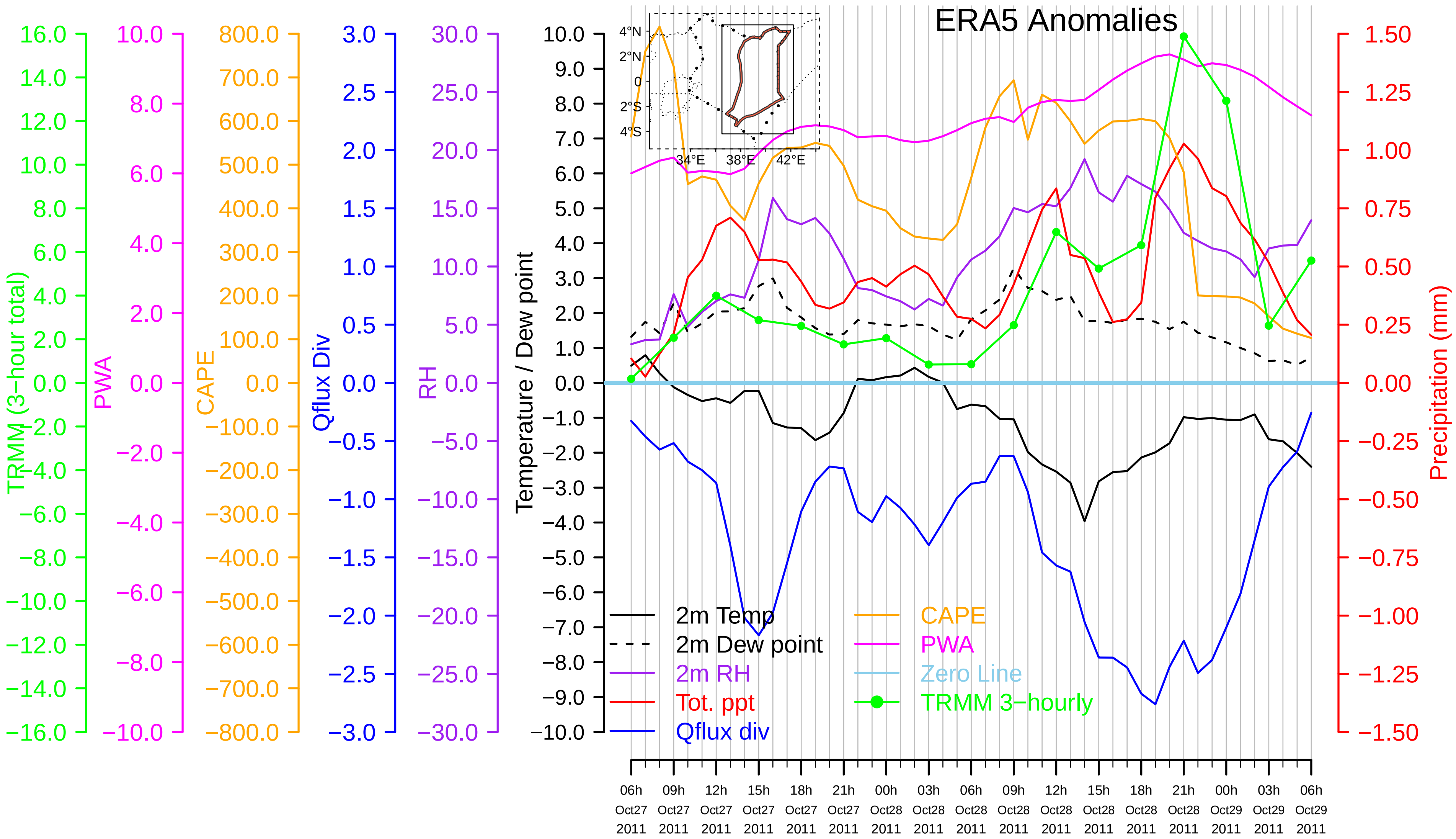

Figure 8.14: *Anomalies of various ERA5 variables namely 2-meter temperature (solid black curve), 2-meter dew-point (dashed black curve), relative humidity at 2m hPa level (purple curve), total precipitation (red curve), vertically integrated moisture flux divergence (blue curve) and Convective Available Potential Energy (CAPE; orange curve).The variables are calculated as hourly means between 26 and 30 Oct. 2011 averaged within the 1979–2018 ERA5 climatology. Note that every variable is color-coded. TRMM 3-hourly totals averaged over the Lowlands spatial domain are shown in green. The inset map shows the Lowlands over which the spatial averaging was done.*

8.5.5 Lagrangian analysis of moisture

Besides the Eulerian approach adopted in the preceding sections to investigate the factors influencing the event discussed in this chapter, a Lagrangian analysis was performed to determine the source regions and to describe the trajectory of moisture that build-up to create convection and precipitation over the Lowlands. The tool adopted for Lagrangian analysis was *LAGRANTO* described under section 5.2.7. Backward trajectories of specific humidity were analysed since the day of event (specifically at 06 UTC 28 Oct. 2011) to the last five days. Ten pressure levels namely 500, 550, 600, 650, 700, 750, 800, 850, 900, and 950 hPa were used as starting levels to initialize the tool from the rainiest grid point (39.5°E–3°N). All backward trajectories indicated that the air mass region was the Arabian sea five days prior (figure 8.15a and 8.15b). The trajectories took a north-easterly orientation across the northern section of the western equatorial Indian Ocean, cruised through southern Somalia and ascended drastically over the region on 29 Oct. 2011. Moisture uptake took place along the trajectory within the lower levels and especially over the oceanic regions. Since SSTs were high during this period (>28°C, figure 8.11d to 8.11f), the flow field presumably benefited from evaporated oceanic water along the flow with the air undergoing expansion as it ascended over the region eventually releasing latent heat of condensation aiding the intensification of the event.

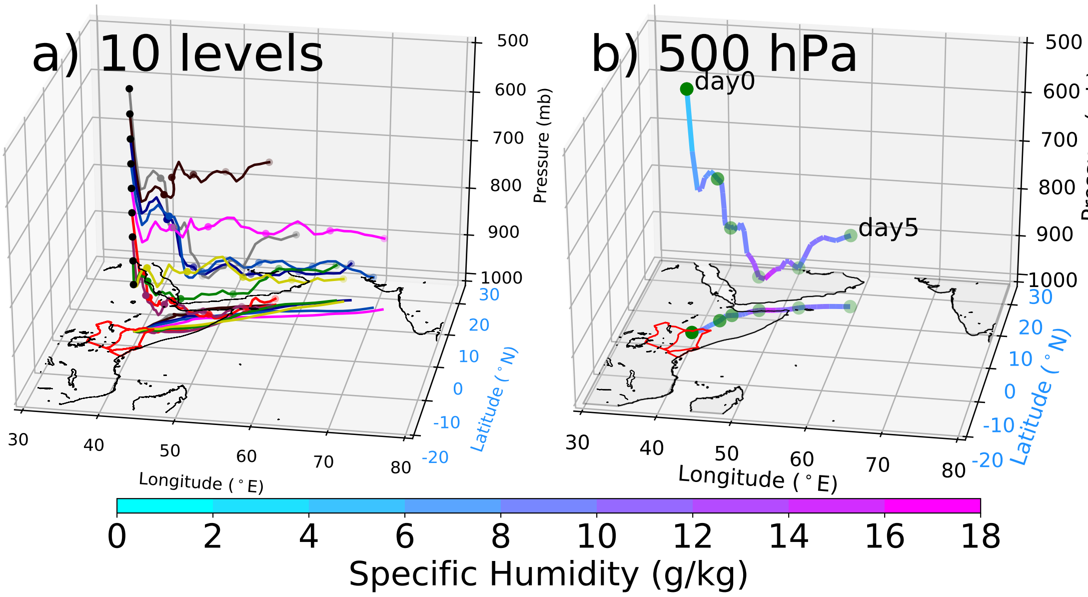

Figure 8.15: ***a)*** *Three dimensional 5-day backward Lagranto trajectories showing air mass sources for various starting levels using ERA5 model data over the Lowlands initialized at 06 UTC 29 Oct. 2011. The starting levels are namely, 500, 550, 600, 650, 700, 750, 800, 850, 900, and 950 hPa shown by grey, darkbrown, darkblue, blue, magenta, red, purple, green, yellow, and orange lines respectively. The color markers indicate every day lapsed. Black markers represent the initial grid point namely 39.5°E, 3°N.* ***b)*** *Specific humidity traced along the backward trajectory starting from the 500hPa level. Notice that the trajectory in* ***b)*** *is mapped onto the surface too using the same color configuration.*

Figure 8.16 demonstrates the physical mechanisms that air parcels started from different levels in Lagranto underwent before being released over the region. The air parcels started at lower levels (950–850 hPa) and arriving at the rainiest grid point initially underwent diabatic cooling while decreasing their temperature 120 hours prior to the event. No immediate conclusion could be made regarding their upward or downward motion. Diabatic cooling is usually caused by air parcels losing infrared radiation to the atmosphere or through evaporation. This eventually caused the air parcels to cool down. 96 to 72 hours prior to the event, the air parcels at these levels underwent expansion since they had their temperature decrease as potential temperature increased. This can only be explained by lifting. 48 hours prior, the parcels underwent adiabatic cooling caused by lifting while 24 hours prior, the parcels lost energy through radiational cooling while keeping their temperature constant.

For the parcels started from mid-levels (800 – 600 hPa), they initially underwent diabatic warming with their temperature increasing implying that the parcels warmed radiatively along their trajectory. 96 hours before the event, these parcels underwent diabatic cooling by losing infrared radiation to space while decreasing in temperature. Finally, for the parcels started at 500 hPa level, they initially experienced compression by virtue of increasing T and decreasing θ, a phenomenon that can only be explained by subsidence. Diabatic cooling by loss of infrared radiation with a constant temperature characterised these parcels 96 hours prior to the event before experiencing expansion throughout the rest of their path explicable only by lifting. All these physical mechanisms can be ascertained by examining figure 8.15.

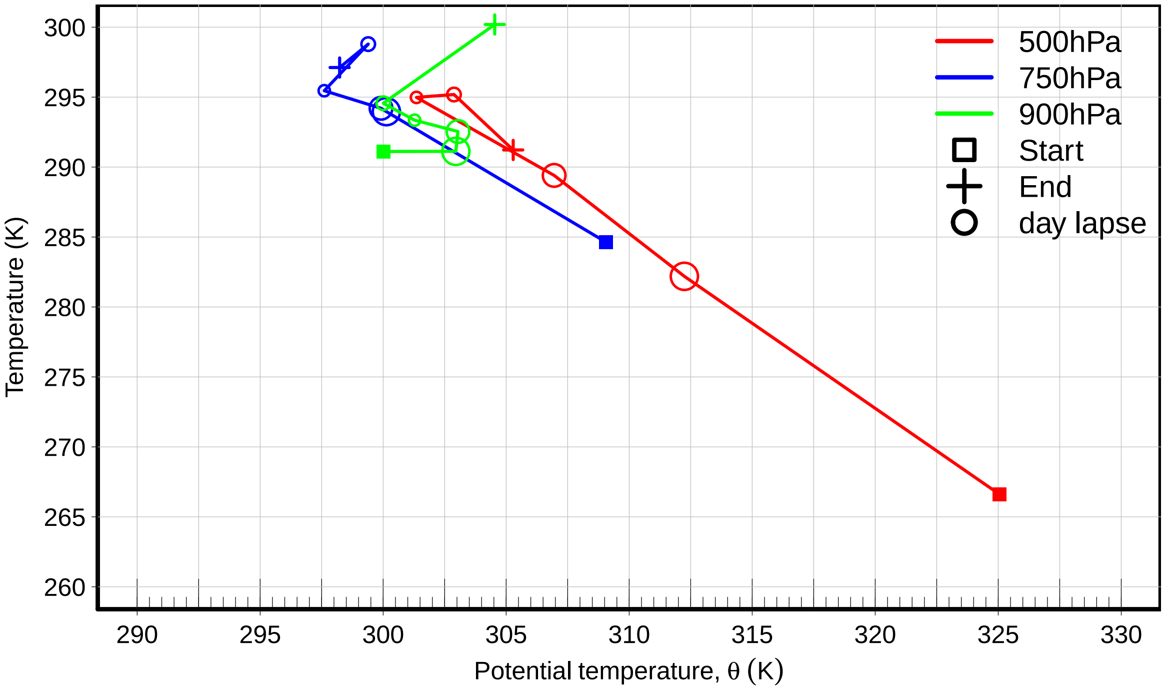

Figure 8.16: *Temperature-Potential temperature curves ($T - \theta$ curves) showing the evolution of T and θ each day for 5 days since the beginning of the backward trajectory at 06 UTC 29 Oct. 2011 (shown by the diamond marker) until the end of the trajectory 5 days later (shown by the cross marker). Rings indicate every day lapsed and their size diminish further away from the event every 24 hours. The starting levels are 500, 750 and 900hPa and each curve represents a specific starting level of the trajectory.*

The eventual rising of air parcels near the region of interest was vital in promoting the release of latent heat that was necessary to fuel the ensuing belated[1] extreme convection.

---

[1] belated since it occurred far later than precipitation observed in TRMM

8.6 ICON simulations

This section presents results from the simulation of daily (A06) and sub-daily precipitation totals by ICON. Sub-daily precipitation denote the three-hourly precipitation as observed in TRMM since the initialization of the model. Each of these temporal scales has two components. The first component evaluates the skill through a subjective *'eye-ball'* view between observations (TRMM and gauges) against the ICON simulated precipitation totals while the second component makes an objective evaluation of model skill using statistical methods elucidated in chapter 5.

8.6.1 Simulation of the 24-hour accumulated precipitation between 0600–0600 UTC (A06)

The model struggled to mimick the extreme precipitation event on 29 Oct. 2011. For the 12 UTC initialization (figure 8.17b), the model produced random and isolated convective cells especially to the west of the Lowlands with intense cells within the central parts. This ERAI-driven simulation produced patterns to the eastern side of the region which were to some extent similar to observations though less intense. The shape of the entire precipitation structure for this initialization time was subjectively poor as vast parts of the region were characterised by little to no cells of convection. For the 18 UTC initialization (figure 8.17c), the model produced a more improved precipitation pattern with the deepest cells confined within the eastern side of the region. The strength of the model output was in its simulation of the event towards the Somali coast where the convective cells nearly matched the structure of the event as observed from TRMM. It is noted that both the 12 and 18 UTC initializations failed to reproduce the high precipitation totals over Marsabit where the local meteorological station produced A06 of about 106.7 mm. Specifically, the model could hardly produce any precipitation over the region. For the 00 UTC initialization (figure 8.17d), the model was poor though producing a realistic precipitation object within the central parts of the region. The precipitation structure to the east of the region for this initialization was realistic in terms of structure. The model produced some amounts of precipitation over Marsabit. In general, ICON output did not capture the overall pattern of the precipitation object even when the number of levels were increased from 70 to 100 and forced with the various initial data (ERAI and IFS).

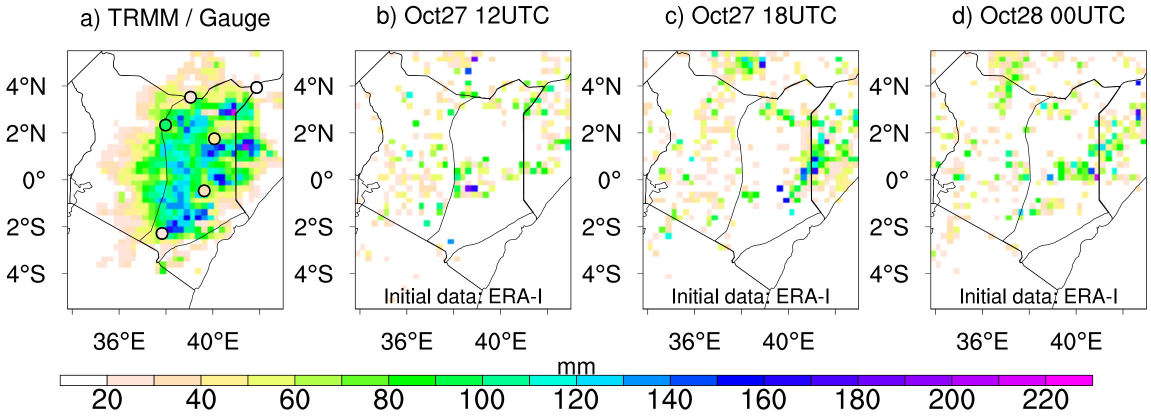

Figure 8.17: A06 for ***a:*** *Gauges (markers) overlaid on TRMM (filled contours).* ***b–d:*** *ICON simulated precipitation initialized at 12 UTC 27 Oct., 18 UTC 27 Oct., and 00 UTC 28 Oct. respectively using ERAI.*

8.6.1.1 Skill evaluation of the 24-hour accumulated precipitation between 0600–0600 UTC (A06)

In this section, results from the spatial evaluation of A06 on 29 Oct. 2011 are presented. It was found that all the attempted initializations namely, 12, 18 and 00 UTC were remarkably poor with SAL values indicating poor skill (figure 8.18a). It was clear that the location of the event was better forecast than its amplitude and structure with the model locating the precipitation object with more skill for all the initialization times adopted. The model underestimated precipitation by a factor of more than 3 ($A < -1$) while producing too small and isolated convective elements (large negative values of S) at all times of initialization. Thus, it is concluded that the ICON model performed poorly in reproducing A06. For the purposes of the next sections, the 18 UTC initialization was adopted to evaluate sub-daily characteristics of the event as it was the best simulation in the circumstances, that attempted to reproduce the structure observed in TRMM.

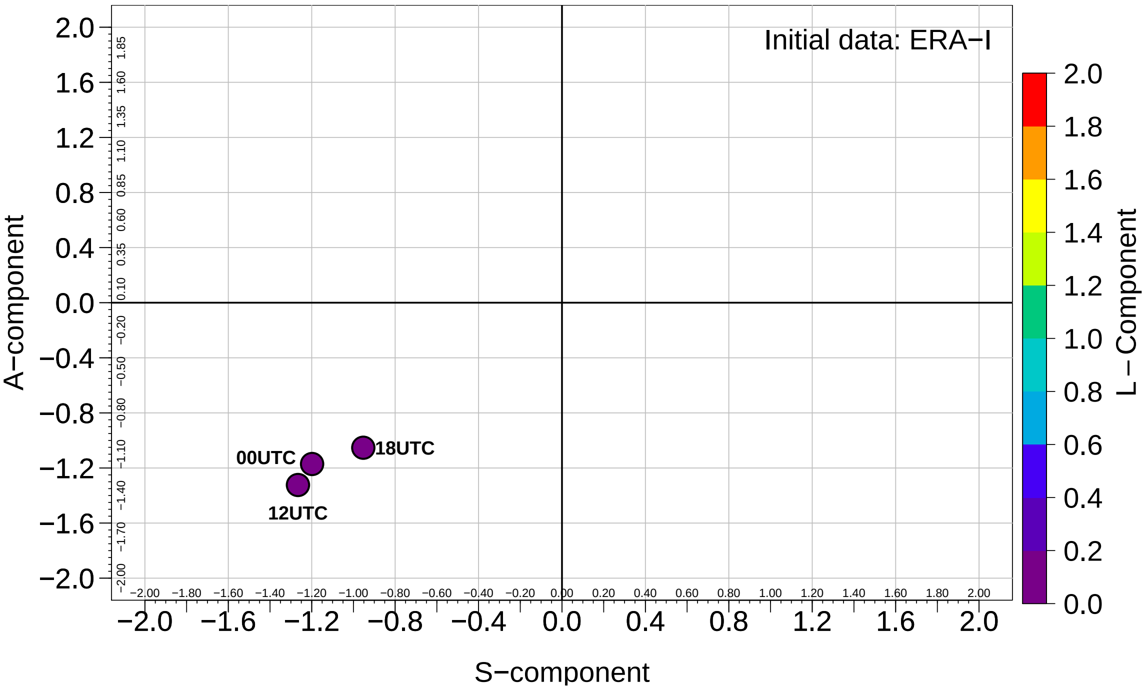

Figure 8.18: SAL diagram for A06 forecasts from the ERA-interim forced ICON model at three different initialization times namely, 12 UTC, 18 UTC 27 Oct. and 00 UTC 28 Oct. 2011. Every dot shows the value of the three components of SAL with the location component shown by color. TRMM data was used as the verification field.

8.6.2 Sub-daily precipitation

Results from the evolution of the 18 UTC initialized ICON model forced by ERAI are presented here. Differences between three-hourly TRMM and ICON model precipitation outputs showed as expected that the model underestimated precipitation. Lowest grid point to grid point differences between the observations and ICON were found during the time window when there was little or no precipitation in TRMM especially at 09 UTC 28 Oct. (figure 8.19a). However, as time evolved and more precipitation was reported, the differences began to emerge with obvious underestimation of precipitation by ICON over the northern parts of the region becoming conspicuous especially during the time windows

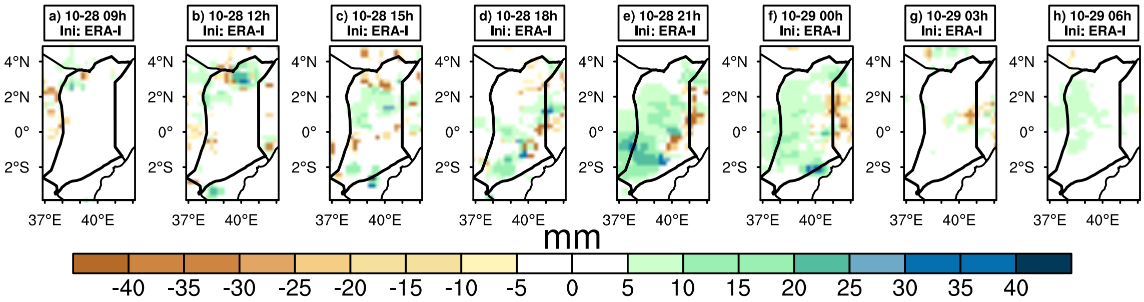

Figure 8.19: a–h: *Sub-daily evolution of the difference between TRMM and ICON ($trmm - icon$) between 28 Oct. 09h and 29 Oct. 06h for the 18 UTC initialization and initialized by ERAI.*

of well organised and intense convection (figure 8.19c to 8.19e). The spontaneous negative differences that emerged during the evolution was caused by the popping up of convection within the model while no corresponding observations were made from TRMM.

8.6.2.1 Skill evaluation on sub-daily precipitation

In this section, results obtained after the application of the SAL evaluation method are presented. The method was applied to the three-hourly ICON model precipitation

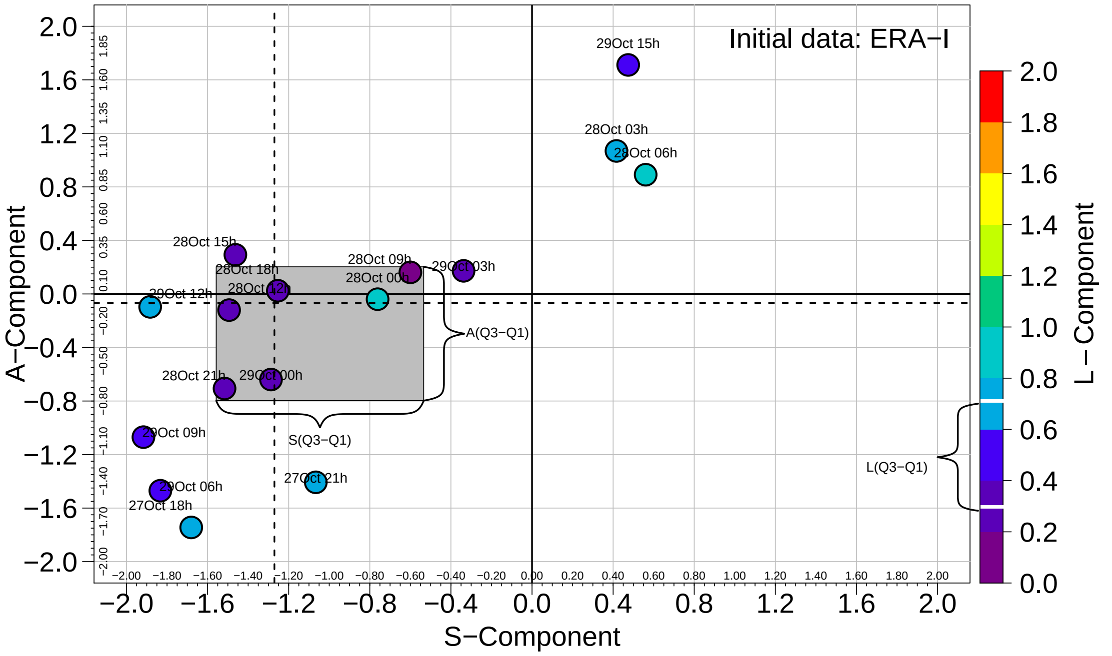

Figure 8.20: *SAL diagram for ICON model outputs at three-hourly interval initialized at 18 UTC. Every dot shows the value of the three components of SAL at a particular three-hour interval since initialization. The L-component is shown by color. Median values of the S and A components are shown as dashed lines while the gray box extends from the 25th to the 75th percentile of the distribution of S and A and annotated on the diagram as $S(Q_3 - Q_1)$ and $A(Q_3 - Q_1)$ respectively. The corresponding interquartile range of the L-component is shown by the two white dashes on the color scale and annotated as $L(Q_3 - Q_1)$. Notice that the individual hours of the day are annotated.*

outputs. The SAL scores indicated that the model was poor in reproducing sub-daily precipitation totals too. The overall magnitude of precipitation compare better to the verification field (TRMM) especially during the time window of intense precipitation (between 15 and 00 UTC 29 Oct.) than during the other time windows when precipitation was isolated, the magnitude of precipitation was either overestimated just before the event or underestimated during other instances. In fact, during the first phase of precipitation evolution, the overall magnitude of precipitation was underestimated especially at 18 and 21 UTC 27 Oct. The overall median value of the A-component showed that the magnitude of the individual three-hourly events produced by ICON were skillful though tending towards underestimating precipitation (figure 8.20). The structure of the event was such that during the period of the most intense convection, the model produced too many isolated convective cells inferred from S<0. Indeed, the structure of precipitation during this period of most intense convection was confined within the interquartile range of S with the median value reflecting too much scattered rain (figure 8.20). Sub-daily precipitation events outside the period of the storm were either too organised (positive value of S) as happened just before the event on 03 and 06 UTC 28 Oct. or were too scattered (after 29 Oct.).

8.6.3 Simulated cloud top temperatures

In this subsection, results obtained after comparing evolution of convection from SEVIRI IR temperatures and cloud top temperatures from ICON are presented. The initialization performed at 18 UTC 27 Oct. 2011 was again adopted. The experiment found that the model performed relatively better in simulating cloud top temperatures than in reproducing precipitation. Temperatures over the central parts of the region were relatively well replicated especially during the period of the most intense storm (figure 8.21f–8.21j). On 1800h for example (figure 8.21a and 8.21f), the model output of cloud top temperatures reproduced the system observed from BT near the border with Somalia even though at a lesser intense magnitude (warmer cloud tops than observed). However, the model failed to replicate the relatively warm clouds observed over Mandera meteorological

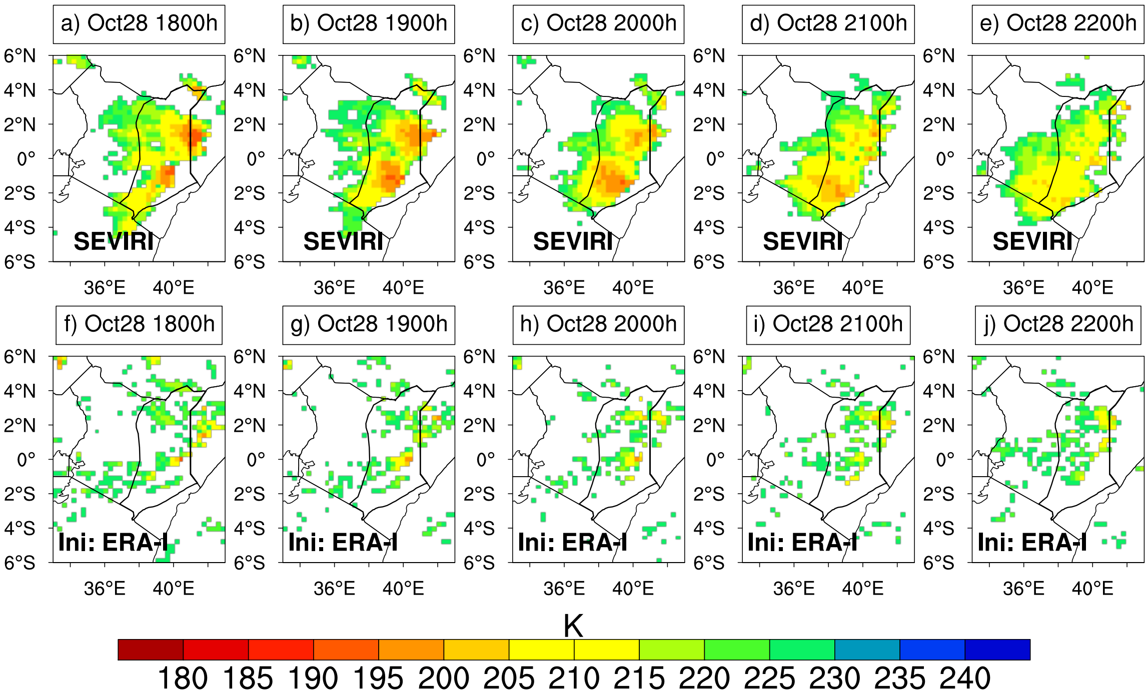

Figure 8.21: *Evolution of cloud-top temperatures over the Lowlands between 18 and 22 UTC 28 Oct. 2011.* ***a–e*** *are the SEVIRI IR brightness temperatures while* ***f–j*** *are the simulated cloud top temperatures from ICON. Initialization at 18 UTC 27 Oct. was chosen.*

station. The model also produced too warm clouds over the central parts of the region where BT reported relatively warmer cloud tops. Observations at 19, 20, 21 and 22 UTC were such that the model produced organised systems which were somewhat smaller in size and relatively warmer compared to BT.

8.6.3.1 Evaluation of cloud top temperatures

Objective evaluation of model skill in simulating cloud top temperatures over the Lowlands during the period 1815 UTC 27 Oct. 2011–12 UTC 29 Oct. 2011 underpinned the subjective *eye-ball view* assessment under section 8.6.3. The Fractions Skill Score

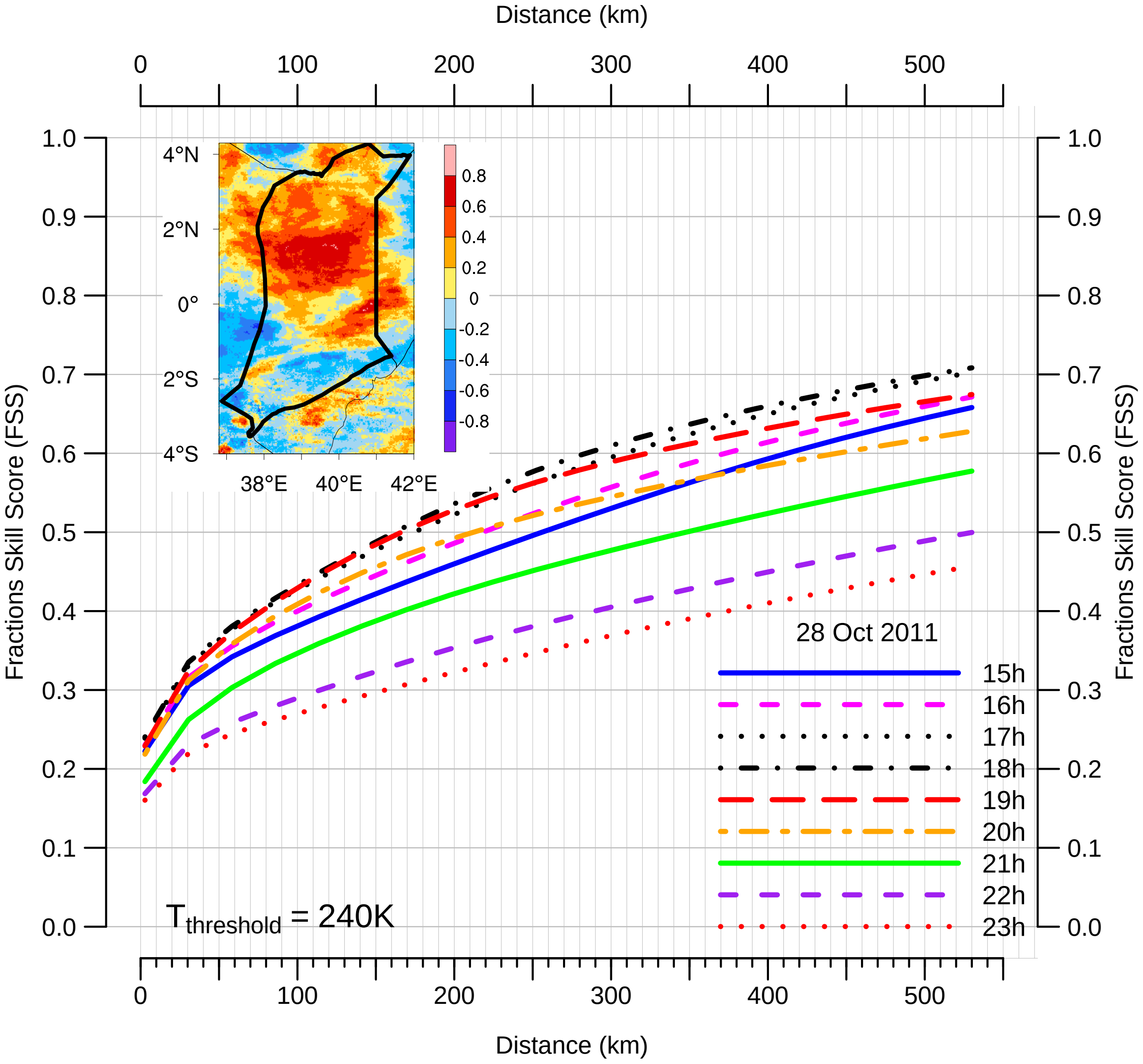

Figure 8.22: Fractions Skill Score (FSS) and grid-point based correlation coefficient between SEVIRI IR brightness temperatures and ICON model simulated cloud top temperatures (CTT) initialized at 18 UTC using ERAI reanalysis datasets. Shown are FSS curves during the most intense convection (between 15–23 UTC 28 Oct., 2011). Temperatures below 240 K are deemed to be representative of deep convection to which the binary fields of FSS are defined. Inset plot is the linear correlation coefficient map between the observed (SEVIRI IR temperatures) and the forecasts (ICON simulated cloud-top temperatures) between 18 UTC 27 Oct.–12 UTC 29 Oct. 2011.

(FSS) was calculated within the spatial grid box 36.8°-42°E and 4°S-4°N (inset plot in figure 8.22) where the threshold of 240 K was used to demarcate the intense convection contour. This threshold was later used to create the binary fields for both observed and forecast fields necessary as inputs during the calculation of FSS. As mentioned in a separate section in this thesis, the 240 K contour threshold for intense convection has been adopted in other studies to highlight deep convection e.g. Rempel et al. (2017); Feidas and Giannakos (2012); Tobin et al. (2012). FSS was calculated for the duration of the most intense convection (15–21 UTC 28 Oct., 2011).

Consistent with the *eye-ball* observations made under section 8.6.3, FSS skill during the time window of the most intense storms was better especially when the spatial scale (distance, n), was increased. FSS scores were found to increase asymptotically although the frequency of observations and forecast (f_0 and f_m) differed. This difference, quantified by a bias score known as Asymptotic Fractions Skill Score (AFSS) (formulation in Roberts and Lean (2008)) was such that FSS score never went beyond 0.7 even for the largest spatial scale (figure 8.22). If a FSS value of 0.5 could be taken as the $fss_{uniform}$ below which the skill should be treated as poor e.g. Roberts and Lean (2008), then, a spatial scale of 200 Km from the center of mass should be taken as the smallest spatial scale at which the ICON model output fulfills the desires of an adequate forecast. However, given that the region considered is rather small and bearing in mind the fact that the model is run on a high resolution of 3.25 Km, a spatial scale of 200 Km is said to be undesirable in evaluating the spatial skill. The author, therefore, found it relatively difficult to tolerate spatial scales larger than 50 Km when using such a high resolution model. The verdict, therefore, is that the model in its current set-up could not inspire much confidence in simulating cloud-top temperatures observed in BT. However, the findings here should inspire future endeavours in model fine-tuning and use of alternative and more robust initial data in a bid to obtain an improved result. After linear correlation was performed between BT temperatures and the simulated cloud-top temperatures for the entire simulation period (1815 UTC 27 Oct.–12 UTC 29 Oct.), the correlation scores were found to be high and significant especially over the northern part of the Lowlands which was certainly affected by the most intense convection (inset map in figure 8.22). However, linear correlation does not quantify the magnitude of both fields and only considers the relative responses of one variable against the other. It is therefore an unsatisfactory way of evaluating skill especially when value matching is desired. Nevertheless, this relationship demonstrates that even though a model might struggle to adequately predict precipitation, it may very well reproduce the evolution of convection by simulating cold cloud tops which are in many instances associated with precipitation.

An IFS-forced simulation was also attempted to reproduce both precipitation and cloud top temperatures but the results were not different from the ERAI. In fact, ERAI was by far, a better initial condition than Integrated Forecast System (IFS).

8.7 Summary and conclusions

The event of 29 Oct. 2011 was found to have been extreme and contiguous within the Lowlands and within the TRMM period of 1998–2014. The chapter analysed both synoptic and mesoscale conditions that could explain how the event evolved. The ERA5 model was instrumental in performing the diagnosis although it suffered from inability to reproduce mesoscale and locally-induced events. However, it was adequate in reproducing the large-scale dynamics. A summary on how this extreme precipitation was possible can be drawn as follows:

- Large-scale dynamics suggested that the system was triggered by a Kelvin wave superposed on an equatorial Rossby wave creating a low pressure system.

- The low pressure system induced low-level winds from the north-east, north-west and south-east converging into the region.
- A developing LSB from the east African coast augmented the large-scale wave activity aiding in the sustenance of the system.
- The north-easterlies were warm and moist and advected moisture to the Lowlands from an anomalously warm ocean eventually converging over the region and contributing to high amounts of precipitable water in a column.
- The region became conditionally unstable with high amounts of moist air in the lower levels and drier air within mid to higher levels. However, challenges with ECMWF reanalysis data existed in terms of reproducibility of mesoscale instabilities as the reanalyses model exhibited difficulties in simulating locally induced convective events.
- The wind convergence may have been the mechanism that broke the barrier and delivered the unsaturated moist air to the LFC as day-time heating could not be established.
- The build-up of moderate CAPE helped to strengthen vertical motion translating to development of deep convective clouds.
- Heavy precipitation ensued that lasted for several hours.
- The ICON model forced by ERAI and IFS could not adequately reproduce this event in terms of precipitation or cloud top temperatures.

It is concluded that the extreme precipitation event of 29 Oct. 2011 was an outstanding event in terms of magnitude and contiguity within the TRMM period of 1998 – 2014. ERA5 reanalyses model struggled to reproduce the mesoscale dynamics e.g. small-scale convection and instabilities but did a better job in reproducing the synoptic evolution of winds, moisture and temperature. Perhaps the scarcity of observed data over the region might explain why the model struggled to forecast adequately the extreme precipitation event. It is therefore imperative that efforts are taken in future to enhance the spatial and temporal frequency of observations especially on upper air data that would go a long in complimenting data assimilation tasks at ECMWF. This would greatly improve future forecasts of extreme events as the reanalyses model would be better trained to make such forecasts.

Chapter 9

Case 3: Central Highlands 27–29 December 2012

This chapter presents analysis results of the extreme precipitation case of 29 Dec. 2012 over the Central Highlands of Kenya. The first section is a description of the case including an account of the impacts followed by observational evidence from different platforms both on ground and satellite. The diagnosis of the event from initial stages to maturity to dissipation follows in later sections as well as the representation of the event in the CP - ICON model.

9.1 Description and Impacts

The event took place within the short rains season of Oct. – Dec. According to a report from the International Federation of Red Cross and Red Crescent Societies (IFRC) published on 15 Jan 2013 on ReliefWeb, approximately 300,000 Swiss Francs were allocated from IFRC's Disaster Relief Emergency Fund (DREF) to support the KRCS in attending to approximately 13,000 men, women and children in western and highland zones of Kenya affected by flash floods. Those affected were especially from the slopes which are covered by little vegetation while in western Kenya, the most affected were those who lived within the Kano plains - an area that is perennially flood-prone due to the flat terrain. A total of 13 fatalities was reported. These fatalities were mainly due to mudslides which had displaced a total of 765 persons with scores reported missing. The floods triggered a humanitarian problem with those displaced requiring shelter, water supply and improved sanitation as well as provision of food relief and medical services.

According to the Kenya Meteorological Services (KMS), the rains began in early Dec. 2012 and were forecast to intensify until mid January of 2013. A report later published online by the KMS ((KMD, 2013) gave an overall assessment of the rains during the season as having been near normal since a vast majority of meteorological stations within the country were reported to have recorded between 75 and 125% of their seasonal long-term means. In spite of the overall normal assessment for the season, several meteorological stations, especially over northwestern Kenya, western and Central Highlands including Nairobi as well as those reporting from the coastal strip of Kenya recorded enhanced rains compared to climatology. Most of these coastal and highland-based stations reported seasonal rains that were more than 150% of their seasonal long-term means. Only stations located towards the north-eastern part of the country in a region referred to in this thesis as the Lowlands reported depressed rains of less than 50% of their seasonal long-term means.

In terms of the impacts, the KMD (2013) report made an argument that the rains during the season promoted a good crop performance over the agriculturally productive areas of Central and Western Highlands, improved foliage and pasture for pastoralists, increased water levels in the Seven-Folks and Turkwell hydroelectric power centres (which are the main energy production centers for the country), improved food security over the agricultural highlands and slight improvements in water resources for domestic and industrial use in various parts of the country.

9.2 24-hour accumulated precipitation

We start off by reviewing the performance of the various products, namely TRMM, ERA5 and ERAI against the rain-gauges during the day of event especially over areas where gauge data was available. Performance of TRMM against the rain-gauges was considered key in this study as the former was the best alternative where gauges were absent or not operational. Luckily, for the region under study, rain-gauges are relatively well distributed and have a relatively long and consistent record. It was found that during the day of the event, 24-hour accumulated precipitation between 0600–0600 UTC (A06) for both products (gauge and TRMM) were not only in phase spatially but relatively comparable with the latter tending to overestimate the rains by an average of 20 mm (figure 9.1a) and Table 9.1. However, for cases when localised torrential rains hit a station, TRMM tended to underestimate the amount of precipitation. Case in point is Eldoret (WMO number: 63686) and Dagoretti (WMO number: 63741) where enhanced rains of about 83 and 70 mmday^{-1} were underestimated by TRMM. One oustanding pixel in TRMM within the Central Highlands region reported A06 of more than 150 mm, a situation that was not observed by any neighbouring station (figure 9.1). ERA5 model forecasts, though inferior to TRMM in terms of spatial distribution and magnitude, generally made a good forecast for a model that relies heavily on availability of *in-situ* observations for data assimilation. Over areas where gauge stations exist, the agreement between the two datasets was reasonable. The only drawback with the ERA5 forecast was its poor skill in forecasting extreme rains. For example, over the two mentioned locations of Eldoret and Dagoretti, the enhanced rains observed in the rain-gauges were poorly reproduced

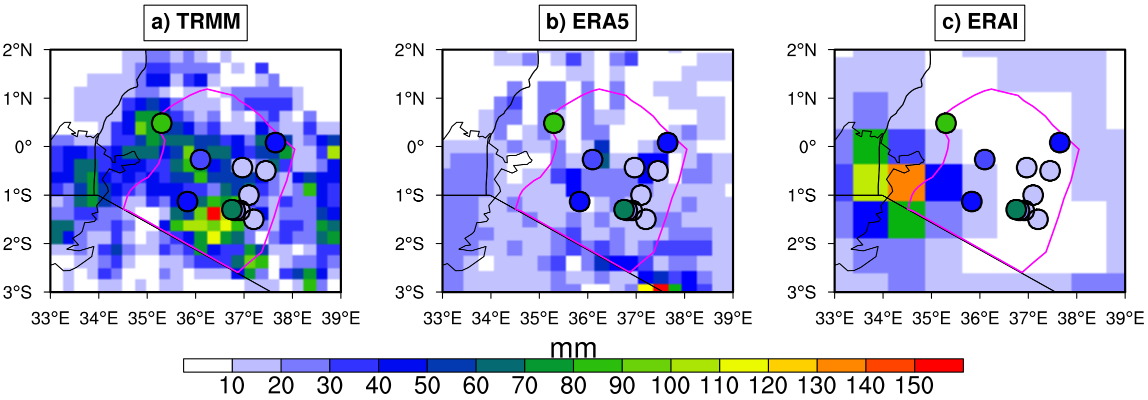

Figure 9.1: *Spatial distribution of A06 over the Central Highlands during 29 Dec. 2012 for a) TRMM, b) ERA5 and c) ERAI model outputs. The gauge amounts are annotated by circular markers whose color scale correspond to the filled contours. The Central Highlands is shown by the pink outline.*

in ERA5 where the product overwhelmingly underestimated precipitation amounts. The product also tended to spatially smooth precipitation observations giving little regard to localised precipitation. For example, over the stations to the east of the region which reported A06 of less than 30 mm, ERA5 product made forecasts to the effect that the entire eastern region was homogeneous. For instance, it made a near perfect forecast for precipitation over Meru (WMO no: 63695) but then displaced the object slightly to the south-west where it appeared to suggest that a wider region was affected by enhanced rains ultimately ignoring the localised suppressed rains observed by a total of four gauge stations located within this part of the region (figure 9.1b).

A06 forecasts from ERAI were poor. The product produced enhanced precipitation over the lake basin with almost nil observations in a vast part of the Central Highlands (figure 9.1c). Just as it was observed in preceding chapters, ERAI has a tendency to produce convection within large water bodies especially over Kenya perhaps due to day time heating. The ERA5 forecast were superior to ERAI forecasts mainly due to the reasons elucidated in section 5.1.6.

9.3 Event extremity against climatology

In this section, results from analysis of the extremity of A06 against climatology are presented. The real-time data products of gauge and TRMM as well as ERA5 and ERAI forecasts were assessed. Firstly, extremity in gauges and the TRMM 9-pixel mean A06 were analysed as TRMM data was used elsewhere in this study as a proxy for precipitation where rain-gauge data was unavailable. Results indicated that all TRMM 9-pixel mean amounts around each rain-gauge station exceeded the 99th percentile within the 1998–2014 climatological period (figure 9.1 and Table 9.2). For gauges, only one

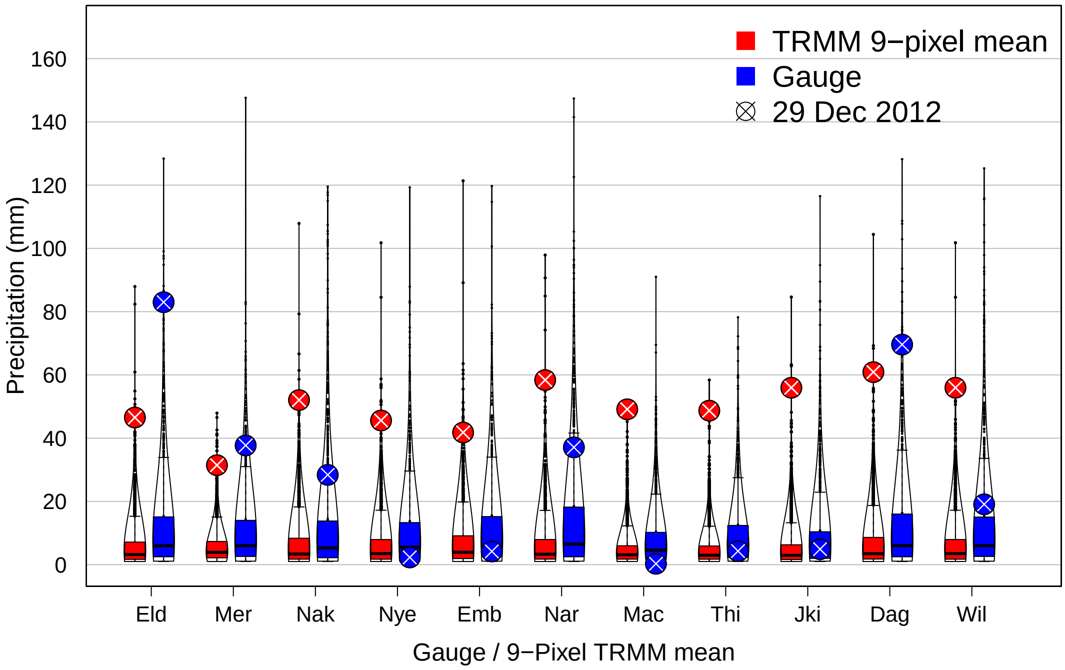

Figure 9.2: *A violin plot showing extremity of the A06 event of 29 Dec. 2012 within the climatological period 1998-2014 for TRMM and rain-gauges over the Central Highlands shown in red and blue respectively. Markers show the day of the event. TRMM aggregation is based on the A06 9-pixel mean surrounding each station. Only days with rainfall greater than 1 mm within the climatology are considered.*

gauge station (Eldoret) exceeded this threshold though six other stations exceeded the 80th percentile. For the rest of the rain-gauge stations which could not exceed the 80th percentile threshold, it was speculated that local factors could have slightly displaced the precipitation object from the rain-gauge location especially give that a nearby rain-gauge station reported enhanced rains. For example, Nyeri (WMO no. 63717) and Embu (WMO no. 63720) rain-gauge stations which are located just a few tens of kilometers from Meru rain-gauge station (WMO no. 63695) reported A06 that was less than the 50th percentile in contrast to the precipitation object over Meru station which exceeded the 90th percentile. This scenario is expected especially because, a rain-gauge measures rainfall at a point, and any slight changes in, for example wind flow, might displace a precipitating cloud. As for ERA5 forecasts, the 9-pixel mean amounts showed that within the region, precipitation amounts were not the highest on record although most pixels-means surpassed the 90th percentile (Table 9.1). However, these extreme observations were biased towards the south-eastern parts of the region. This was also observed from the spatial analysis of exceedances in figure 9.3b. As an example, the model was unable to reproduce the extreme precipitation object produced over Eldoret rain-gauge station just as TRMM had done by underestimating precipitation while producing higher values towards the south-eastern parts. As for ERAI, the 9-pixel mean amounts indicated that the model produced precipitation that surpassed the 99th percentile even for regions towards the northern part (Table 9.1). However, examination of the spatial distribution of A06 as well as the empirical cumulative distribution showed that the reanalysis model was poor in representing both the magnitude and location of the most enhanced precipitation areas with a tendency to bias precipitation over the lake region.

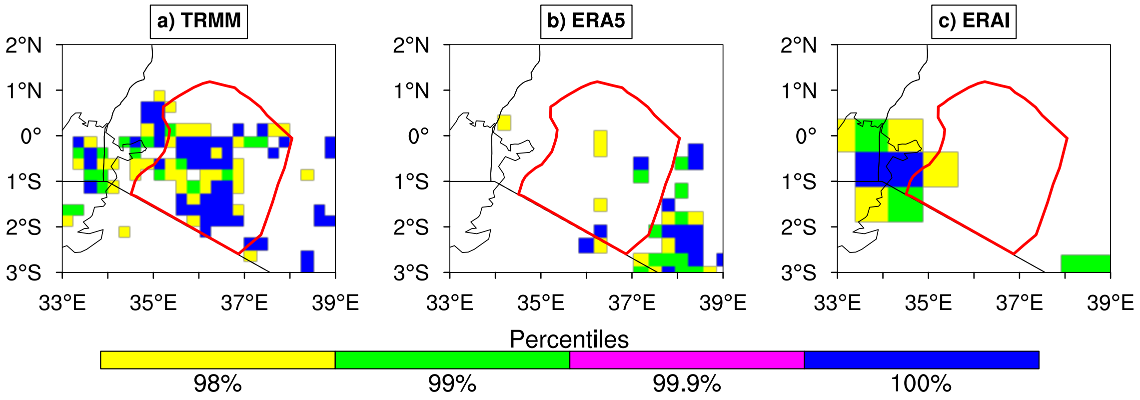

Figure 9.3: *Various percentile thresholds, namely, 98, 99, 99.9 and 100% equalled or exceeded by precipitation during 29 Dec. 2012 for a) TRMM, b) ERA5 and c) ERAI. The percentiles are calculated based on a 20-day window period pivoted at the event date. Only rainy days ($r_i >= 1$ mm) were considered. Climatology years are 1998-2014, 2000–2014, and 1979-2014 for TRMM, ERA5 and ERAI model outputs respectively. Red outline demarcates the Central Highlands.*

On a spatial scale, results showed that TRMM data surpassed the 98th percentile over an average of 70% of the Central Highlands area. Of this, more than 50% received the highest amount in climatology save for a few areas which did not but nevertheless surpassed the 99th percentile. This indicates that the precipitation amount received on this day was actually intense (figure 9.3a). The picture was however different for ERA5 and ERAI in terms of event extremity. Only a few isolated areas within the region produced the highest amounts of precipitation in climatology alternating between 98th and 99th percentile exceedances. Interestingly, just beyond the south-eastern border of the Central Highlands, ERA5 produced maximum precipitation in climatology (figure

9.3b). The slight displacement of the maxima in precipitation was speculated to be a normal occurrence for models especially over tropical regions where *in-situ* observations are scattered compare to other regions of the globe rendering data assimilation tasks at ECMWF challenging. It is to be appreciated that the spatial precipitation maxima from ERA5 reanalyses model were much more improved than those produced by ERAI (figures 9.3b and 9.3c). As observed before in the representation of A06, ERAI forecast was apparently biased towards the lake basin even when percentile-based statistics were performed. A glance at Table 9.1 shows that ERAI surpassed its 99th percentile for most of the stations. However, since the percentile is computed as an average of 9 grid points around a station, the spatial area contained by the 9-pixels is larger than in both ERA5 and TRMM due to the coarse resolution of ERAI. Thus, comparison between ERAI exceedances shown in Table 9.1 and figure 9.3c is bound to have a difference. It is for this reason that ERA5 was considered a better forecast product to conduct further diagnosis of the case.

Table 9.1: *A06 statistics for rain-gauges, TRMM, ERA5 and ERAI on 29 Dec. 2012 showing the A06 for gauge and the corresponding percentile exceedances for the period 1998–2014, the differences between each gridded product and gauge A06 (calculated as Gauge – gridded) and the corresponding percentile exceeded between 1998–2014, 2000–2017, and 1979-2017 for TRMM, ERA5 and ERAI respectively over the Central Highlands. The gridded product value is the 9-pixel mean around a rain-gauge station. Percentiles are calculated for all days with precipitation where a rainy day is defined as a day with A06 >= 1 mm.*

Gauge Observations			**9-pixel mean statistics about a gauge station**					
Gauge	**A06 (mm)**	**Percentile Exceeded**	**Difference (Gauge - gridded) (mm)**			**Percentile Exceeded**		
			TRMM	**ERA5**	**ERAI**	**TRMM**	**ERA5**	**ERAI**
Eldoret	83	99.95	36.46	71.22	65.54	99.98	75.81	99.67
Meru	37.7	91.09	6.24	27.13	31.29	97.98	93.83	92.31
Nakuru	28.4	95.94	-23.65	13.84	11.9	99.99	93.09	99.76
Nyeri	2.3	28.83	-43.3	-11.21	-10.22	99.8	95.02	99.34
Embu	4.2	44.28	-37.59	-8.5	-3.06	99.15	94.96	94.72
Narok	37.1	97.32	-21.29	20.66	17.97	99.99	95.31	99.87
Machakos	0.3	0	-48.84	-18	-8.43	99.53	98.65	97.14
Thika	4.3	40.35	-44.41	-11.99	-8.22	99.53	97.27	99.34
JKIA	4.9	46.28	-51.06	-11.7	-9.44	99.76	97.98	99.55
Dagoretti	69.6	98.97	8.71	51.29	55.26	99.91	97.98	99.55
Wilson	19.1	80.75	-36.86	2.5	4.76	99.76	97.98	99.55

9.4 Sub-daily Evolution of the event

In this section, results from the sub-daily evolution of precipitation building up to the A06 of 29 Dec. 2012 are presented. This case benefited immensely from the availability of SYNOP reports from three gauge stations namely Meru, Jomo Kenyatta International Airport and Eldoret International Airport of WMO IDs 63695, 63740, and 63688 respectively (Table 9.2). The SYNOP reports indicated convective activity beginning to emerge as early as midnight of 28 Dec. Overcast skies were reported over JKIA and Eldoret international airports accompanied by relatively calm north-easterlies at speeds of 3–5 knots. Showers characterised the skies in both locations with rainfall amounts averaging between 1.6–3 mm accumulated in the previous 24 hours. Low clouds in both locations appeared isolated at between 3 and 4 oktas. However, the clouds were of the cumulus and cumulonimbus *genus* over JKIA and Eldoret respectively. During the next three hours, the skies were relatively clear. At 0600 UTC 28 Dec., the convection apparently shifted to the east where convective activity was more enhanced than over the western and southern parts of the region. The skies over Meru were overcast with a relatively calm south-easterly flow at a speed of 2 knots. Precipitation enhanced with an accumulated amount of 37 mm in 24 hours. However, Cumulonimbus cloud genus characterised the southern part of the Central Highlands (over JKIA) while stratocumulus cloud genus characterised the skies over Meru and Eldoret (Table 9.2). Over the next six hours, relative calm prevailed in terms of wind flow over all the three locations though clouds genus was of the cumulonimbus type. At 15 UTC 28 Dec., the skies became overcast again over the southern part of the Central Highlands with a calm south-westerly flow of 3 knots reported over JKIA with a relatively high precipitation of 33 mm accumulated in the previous six hours. This was also the time window when BT reduced drastically over the region from an average of 265 to 240 K (figure 9.4). An AMSU-B overpass on 1550 UTC 28 Dec. confirmed the convective activity over the southern part of the Central Highlands where microwave temperatures of less than 200 K were reported, an indicator of hydrometeors characterising the cumulonimbus clouds (figure 9.5a). Indeed, examination of diurnal cycle of precipitation from TRMM showed that during this hour, the southern part of the region was characterised

Table 9.2: *Summary table of the diurnal characteristics of convection between 00 UTC 28 and 06 UTC 29 Dec. 2012 extracted from SYNOP reports for three land stations in Kenya namely, Meru (WMO ID = 63695), JKIA (WMO ID = 63740) and Eldoret (WMO ID = 63688) located within the Central Highlands (2.1).* ***N, D, S, R, Nh, Ct*** *denote total cloud cover (oktas), wind direction, wind speed (Kts), rain amount in mm (accumulated for the last xx hours), amount of low cloud (Oktas) and the low cloud genus type (Sc: Stratocumulus, Cb: Cumulonimbus and Cu: Cumulus.) respectively.*

	Meru (63695)						**JKIA (63740)**						**Eldoret (63688)**					
Date/time	**N**	**D**	**S**	**R**	**Nh**	**CT**	**N**	**D**	**S**	**R**	**Nh**	**CT**	**N**	**D**	**S**	**R**	**Nh**	**CT**
28 00h	-	-	-	-	1	Sc	7	20	5	3 (24h)	3	Cu	7	40	3	0.4 (6h)	4	Cb
28 03h	-	-	-	-	7	-	-	-	-	-	7	Sc	-	-	-	-	4	Sc
28 06h	7	170	2	37 (24h)	1	Sc	-	-	-	-	6	Cb	7	70	7	0.4 (24h)	3	Sc
28 09h	-	-	-	-	5	Sc	-	-	-	-	5	Cb	-	-	-	-	3	Cb
28 12h	-	-	-	-	5	Cb	-	-	-	-	6	Cb	-	-	-	-	4	Cb
28 15h	7	230	3	33 (12h)	1	Cb	-	-	-	-	7	Sc	-	-	-	-	6	Cb
28 18h	7	260	3	4 (6h)	3	Sc	-	-	-	-	7	Sc	8	0	0	31 (12h)	5	Cb
28 21h	-	-	-	-	7	-	-	-	-	-	7	Sc	-	-	-	-	5	Cb
29 00h	7	0	0	38 (24h)	4	Sc	8	360	3	5 (24h)	5	Sc	8	90	7	23 (6h)	5	Sc
29 03h	-	-	-	-	3	Sc	-	-	-	-	5	Sc	-	-	-	-	5	Sc
29 06h	-	-	-	-	5	Sc	-	-	-	-	5	Cb	8	80	3	70 (24h)	6	Sc

by precipitation amounts of between 25 mm in 3 hours (for the less intense areas) and for the most intense areas, 70 mm in 3 hours were reported (figure D.2). In fact, ERA5 forecast predicted a similar scenario for this date reporting precipitation of between 2 and 5 mmhr^{-1} but displacing the most intense precipitation object of 9 mmhr^{-1} (27 mm in 3 hours) slightly to the north of the region (figure D.3). The SYNOP reports especially over Meru indicated that this convective situation persisted for the next nine hours upto the midnight of 29 Dec. with an intermittent break on 21 UTC. This was consistent with the analysis of BT (figure 9.4 and 9.6a–g) where BT temperatures were at their lowest during these time periods. Another MHS overpass at 2345 UTC (figure 9.5b) showed clearly the spatial extent of the convective activity especially over the north eastern flank of the Central Highlands with microwave temperatures of less that 180 K characterising a wide area that covered Eldoret international airport. This possibly corroborates the high amounts of A06 reported by this rain-gauge on 29 Dec. 2012. Evidently, the period between 15 UTC 28 and 00 UTC 29 Dec. was characterised by a sudden increase in precipitation as reported by both TRMM and CMORPH (figure 9.4).

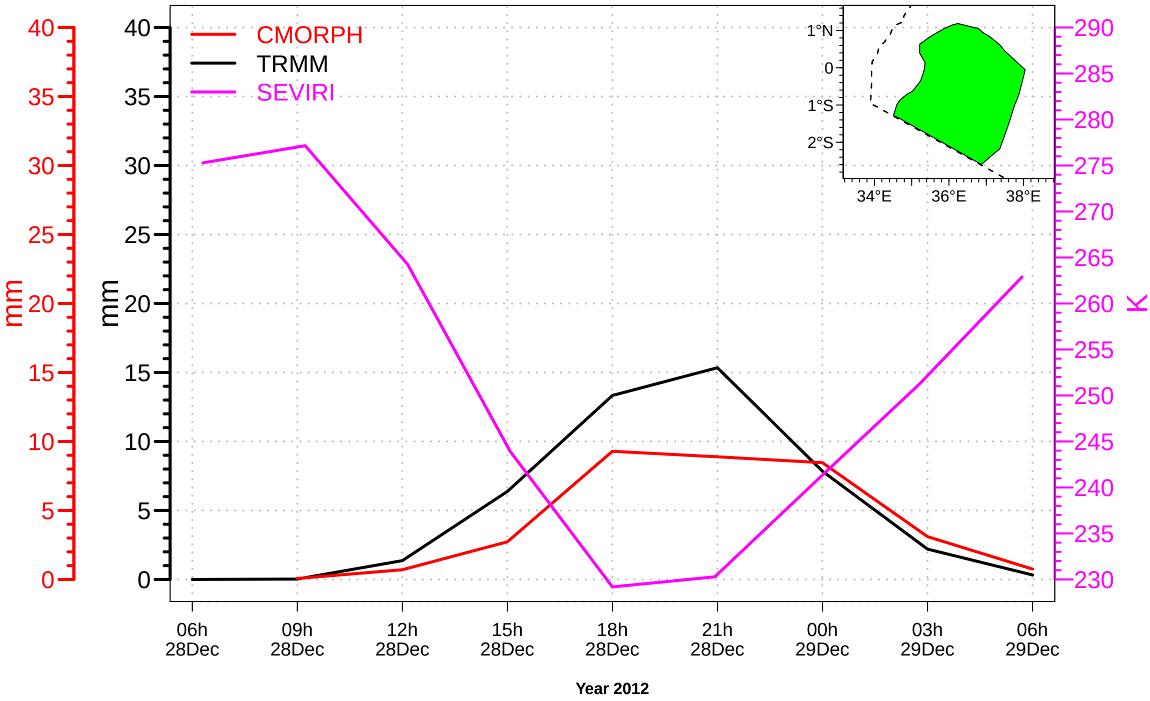

Figure 9.4: *Evolution of convection and precipitation in a three-hourly interval between 06 UTC 28 and 06 UTC 29 Dec. 2012. Both CMORPH and TRMM (red and black curves respectively) show amounts of precipitation received (in mm) while BT (pink curve) show the evolution of convection by way of cloud top temperatures (K). The Central Highlands within which the area averages were calculated is shown in the inset map (green area). For spatial maps of evolution using TRMM and ERA5 data, see figures D.2 and D.3*

Examination of BT and CLAAS cloud type loops indicated that convection began as deep isolated cells from the Kenyan coastline at 0800 UTC 28 Dec. propagating inland. Intensification began 15 minutes later when deep and organised clouds accentuated over the coastline with relatively deeper clouds beginning to emerge inland just to the western side of the Central Highlands. Two hours later, the deep clouds had stretched horizontally to extend from the coastline where they initially sprung up over the southern parts of the Lowlands just west of the Central Highlands. Isolated deep convective cells had, at this time, started to appear over the Central Highlands. This amalgamation of deep clouds (characterised by BT<190 K) continued to organise and stretch such that four hours later (at

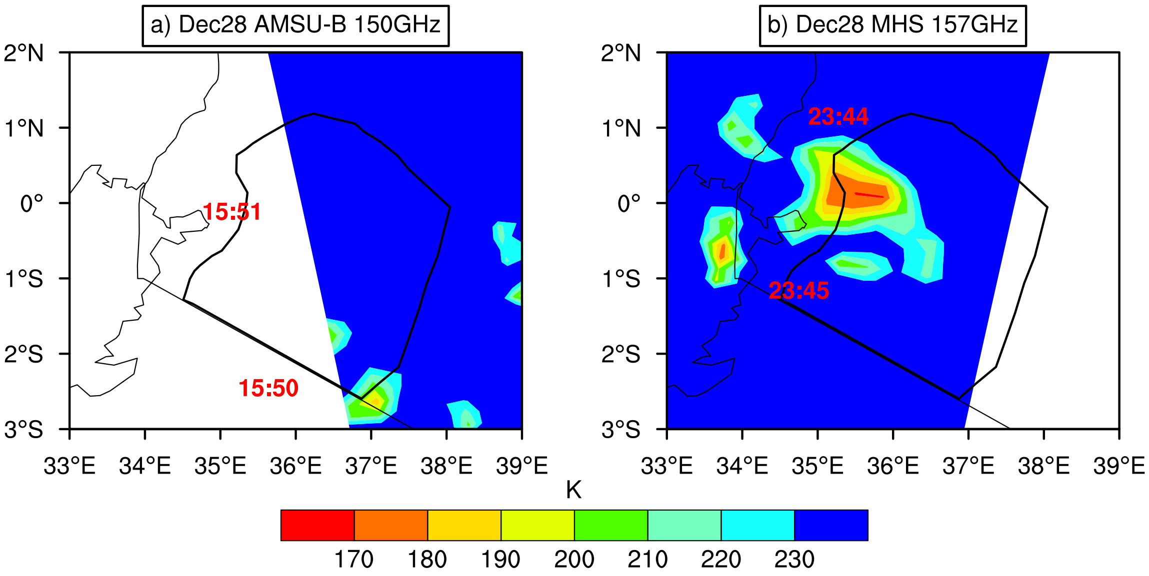

Figure 9.5: *Available AMSU-B and MHS overpasses over the Central Highlands on 28 Dec. at a) 1550 and b) 2345 UTC respectively. Annotated in red text are the actual overhead times (in UTC) when the satellites actually scanned the region.*

1400 UTC), a huge area covering the coast and southern part of the Lowlands stretching all the way to the Central Highlands and some parts of Lake and western highlands had been covered by intense deep convection. The deep system continued to evolve so that three hours later, it had propagated westward to cover the Central Highlands as it became weaker and weaker over the Coastal and southern Lowlands. Between 1530 and 2000 UTC, the system could hardly be seen over the Coastal and Lowlands areas as it had propagated north-westward to cover the entire Central Highlands stretching to the lake and Western Highlands. This can be described as the time window of the most homogeneously intense convection within the region of study (figure 9.6a–h). The system remained stationary over the region between 2000 UTC 28 Dec. and 0030 UTC 29 Dec. slightly shifting northward but still affecting a large zone over the northern side of the Central Highlands. The system decayed with time moving westward but not until 0445 UTC 29 Dec. when it became completely absent.

9.5 Synoptic development

The event was not clearly embedded within a convectively coupled tropical wave environment (see figure 9.7a) though an upper level divergence at 200 hPa gave signs of an ostensibly dry Kelvin wave (see figure 9.7b). The event could not, however, be said to have been triggered by any convectively coupled tropical wave disturbance even though a slight surface pressure drop of 0.5 mbday^{-1} was registered in almost every hour in the 24-hour analysis of surface pressure tendency between 25 and 27 Dec. (see figure 9.8). After 27 Dec., the surface pressure increased, probably after initiating the first phase of convection. Between 28 and 30 Dec. 2012, the surface pressure plummeted once again leading to the next cycle of convection. This might explain why the SYNOP reports showed intermittent rains especially between 28 and 29 Dec. 2012 in all the three locations discussed in section 9.4.

Indeed, area-averaged low-level convergence (see figure 9.9a and 9.9d) corroborated

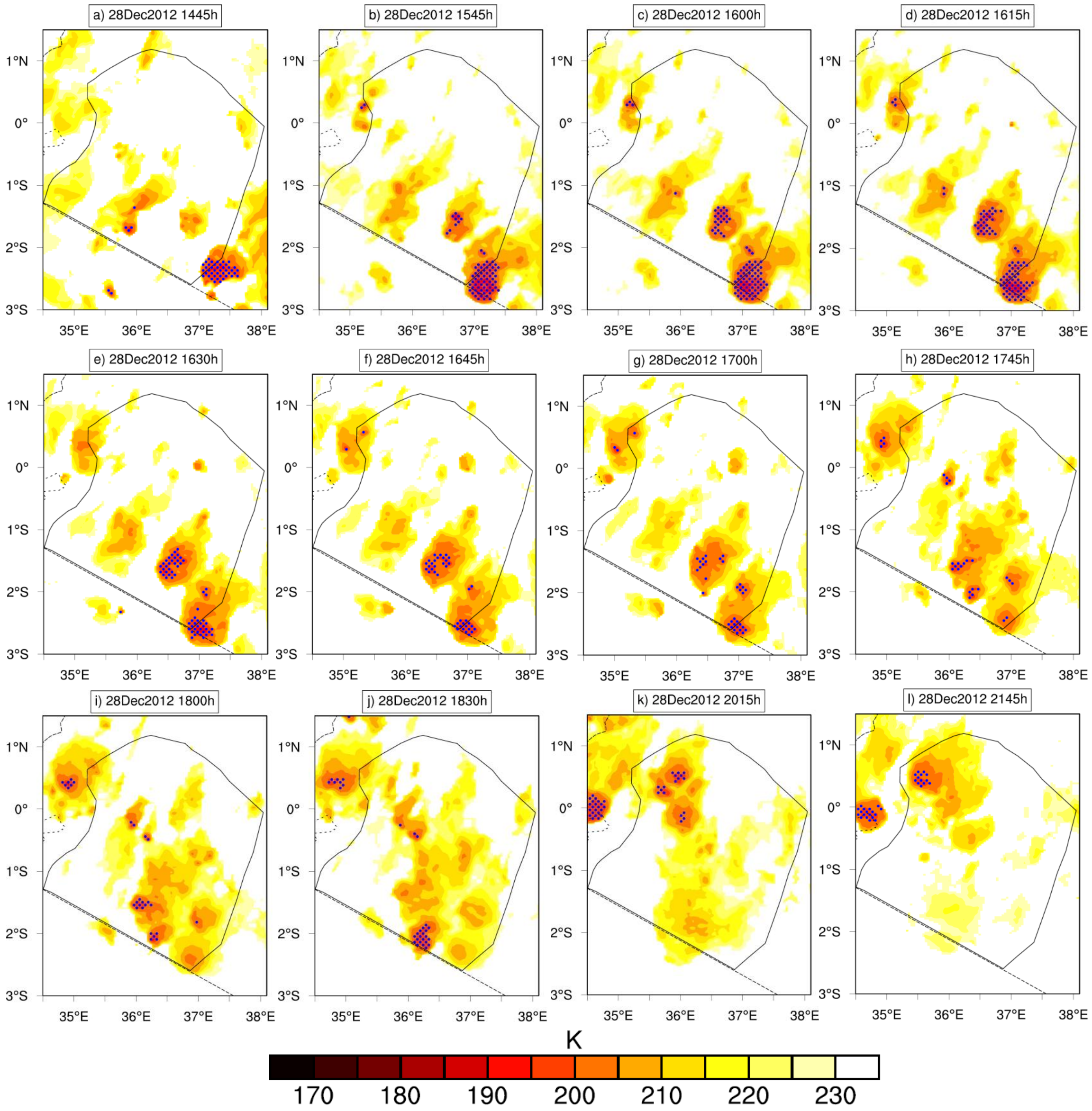

Figure 9.6: *Evolution of deep convection during the period of most intense convection on 28 Dec. 2012 during selected time intervals namely, 1445, 1545, 1600, 1615, 1630, 1645, 1700, 1745, 1800, 1830, 2015, and 2145 UTC. Colors show BT (K) where temperatures above 230 K have been suppressed to highlight deep convection. Blue stippling highlight overshooting towers of convection from the CLAAS algorithm (no units). (Full 15-min IR brightness temperature loops between 1000 UTC 28 Dec. 2012 and 0500 UTC 29 Dec. 2012 overlaid on surface pressure can be accessed at:* `https://drive.google.com/file/d/1fxwm6TcnxAPGnUgFWzVIDDBN0cF-I6-5/view`.

this situation. Relatively strong low-level convergence within the 750 – 700 hPa layer averaging between 1.5 and 0.2 x $10^{-5}s^{-1}$ characterised the region between 00–12 UTC 27 Dec. on both sides of the equator. The next six hours was characterised by relative calmness until strong convergence re-emerged at 00 UTC Dec. 28. This strong low-level convergence continued throughout the next two days until 10 UTC Dec. 30 (figures 9.9a and 9.9c).

Low-level relative vorticity (~1.2 x $10^{-5}s^{-1}$) was observed to be strongly positive over the northern hemisphere part of the region (0–1.5°N) than over the southern part (2°S–0) signalling a constructive weak vortex (see figures 9.9a and 9.9c). This is in line with the definition of the rate of change of absolute vorticity where an increase in horizontal

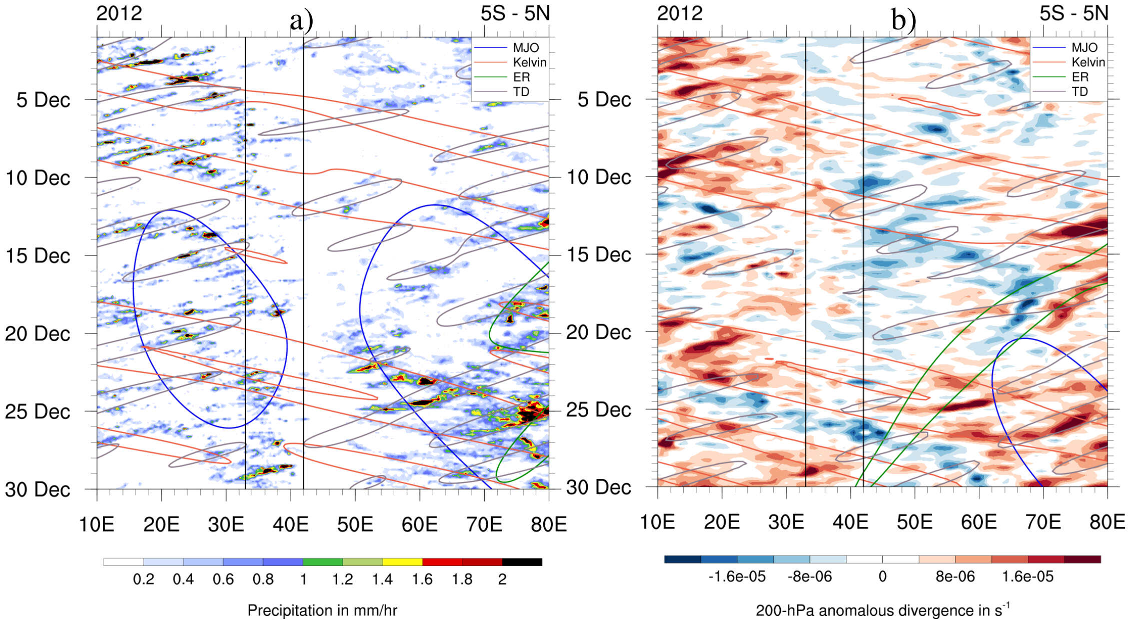

Figure 9.7: *Hovmöller diagram of a) TRMM A06 and b) ERAI 200 hPa level divergence between 01–30 Dec. 2012 averaged between 5°S - 5°N latitude and confined to within 10°E - 80°E longitude. The event center is enclosed within the two vertical lines and between 28 and 29 Dec. Filled contours are precipitation totals (in mm) while line contours depict tropical waves namely, MJO, Kelvin, equatorial Rossby (ER) waves and tropical depressions (TD). The diagram was created after application of the wave-number frequency domain concept from Wheeler and Kiladis (1999) using a routine written by Andreas Schlütter (IMK-TRO).*

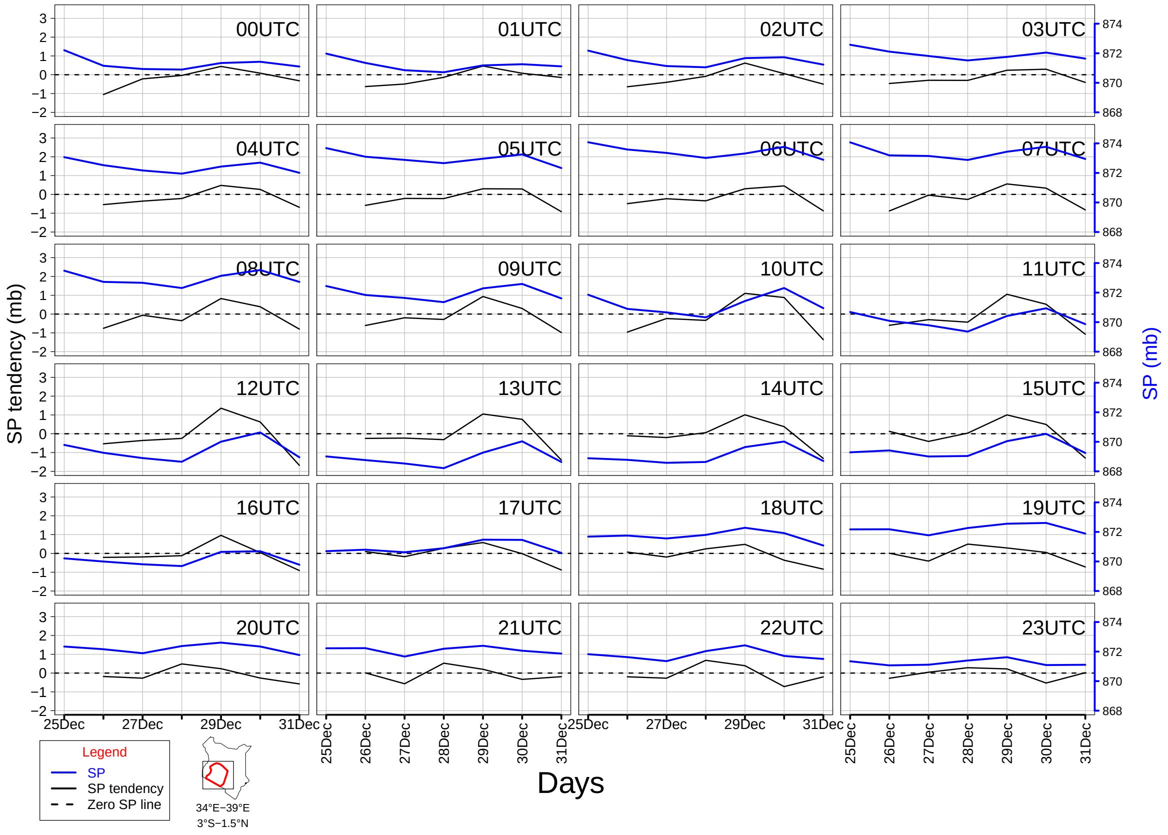

Figure 9.8: *24-hour evolution of ERA5 Surface Pressure (blue curve) and its tendency, ρ (black curve, calculated as $\rho_{t_o} - \rho_{t_o-24}$ where t_o is hour of day) between 26 and 31 Dec., 2012 and averaged between 34°E-39°E and 3°S-1.5°N. (spatially averaged region is shown at the bottom of the main figure.)*

convergence results in a strengthened relative vorticity. The rate of change of vorticity is governed by, among other factors, the stretching term or divergence (see vorticity equation in Holton and Gregory (2012)). This weak vortex was predominantly stronger during the time between 00 UTC 27 and 12 UTC 28 but alternated between weak and strong every 12 hours until 12 UTC 29 Dec.

Wind convergence was evidently in phase with this weak vortex (see shaded contours in figures 9.9a and 9.9c). Evolution of convergence and vorticity pointed to a situation where, prior to the event build-up on 28 Dec. 2012, convergence was stronger over lower levels (700–750 hPa) while divergence was more dominant over the upper levels. This scenario created a situation where mass converged over the bottom of an atmospheric column and diverged aloft promoting upward motion e.g. Kutty and Gohil (2017). Indeed, this was the situation throughout the period until 29 Dec. where vertical motion was more dominant than afterwards (see figure 9.9b and 9.9e).

Vertical motion was found to be stronger in the mid to upper levels (500–200 hPa) than in the lower levels (below 500 hPa) and intensified even further over the upper levels especially just before the event on 28 Dec. creating the deficit over the lower levels to allow for more mass to enter an atmospheric column.

Equivalent potential temperature was found to increase with height throughout the day on 27 Dec. The situation suddenly changed just before midnight of 28 Dec. when an unstable layer (θ_e decreasing with height in the lower levels) emerged. The steepest gradient of θ_e with height was reported at about 18 UTC when the unstable layer began to shrink. This situation persisted until 11 UTC 28 Dec. The decrease of θ_e with height especially within the lower levels (figures 9.9b and 9.9d) demonstrated that the atmosphere was potentially unstable.

Both deep and shallow vertical shears (750–200, 750-500 hPa) in the horizontal wind were relatively small during the advent of the event on 27th and even during the event evolution (see figure 9.9c and 9.9f). Since the deep convective system was not well organised within a line of convection, the shear did not play much of a role in the sustenance of the system and was not perused further.

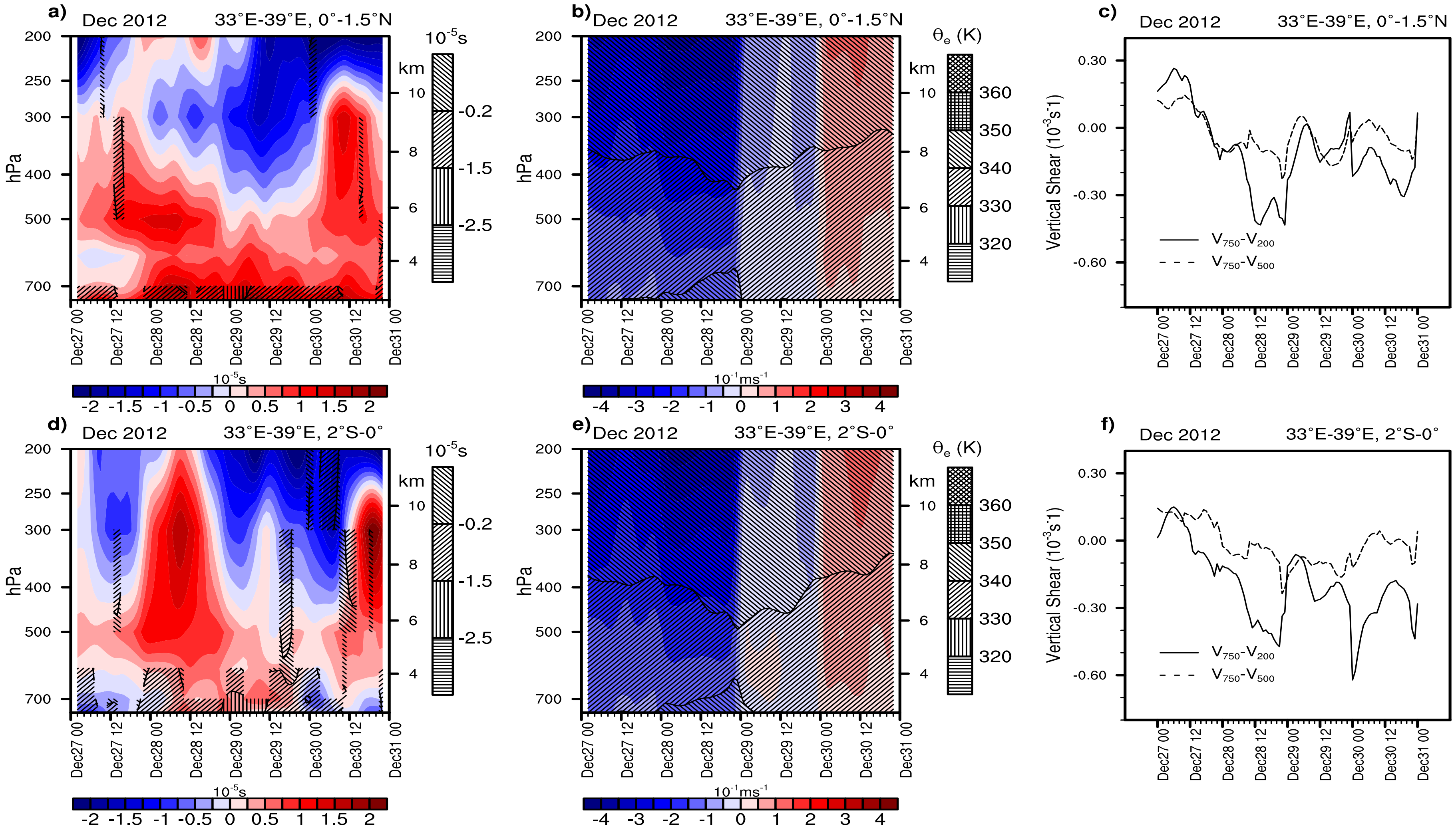

Figure 9.9: ***a*** *and* ***d****: Evolution of the vertical distribution of relative vorticity (filled colors; 10^{-5}s^{-1}) and wind convergence (shaded contours, 10^{-5}s^{-1}; Divergence is masked) over the central region averaged between 33°–39°E, 0°–1.5°N for* ***a*** *(North of the equator) and between 33°E–39°E and 0°–2°S for* ***d*** *(south of the equator) two days before and two days after the event of 29 Dec. 2012.* ***b*** *and* ***e****: Same as* ***a*** *and* ***d*** *but for the vertical distribution of omega (filled colors; 10^{-3}ms^{-1}) and equivalent potential temperature (shaded contours; K).* ***c*** *and* ***f****: Same as* ***a*** *and* ***d*** *but for the vertical shear of wind (10^{-3}s^{-1}) in a shallow layer (750 and 500 hPa) and a deep layer (750 and 200 hPa).*

9.6 Analysis of moisture variables

Analysis of ERA5 moisture variables showed that moisture was advected to the region by a north-easterly vertically integrated moisture flux (1000-200 hPa) averaging about 100 kgms^{-1} that converged over the neighbourhood of the region. The north-easterly moisture flux responsible for moisture convergence was observed to make a curvature near the Kenyan coast approaching the region from the south-east (figure 9.10a–9.10c). This flux was more rapid during the 28th and contributed to high amounts of precipitable water in a column over the southern flank of the region. The total column water was, as a matter of fact, found to have been the highest within the 1979–2018 ERA5 reanalyses period as it exceeded the 98th percentile (figure 9.10b). It built-up with time to values of approximately 60 mmday^{-1}. Coincidentally, low BT (measuring less than 230 K - a signal for deep convection) covered the entire southern area notwithstanding the slight displacement just outside the Central Highlands. This was corroborated further by TRMM and ERA5 diurnal cycle of precipitation discussed earlier in section 9.4 where enhanced rains were concentrated towards the southern part of the region.

Relative humidity was low during 27 Dec. ranging between 40 and 60% near the region but increased to between 60 and 80% on 28 and 29 Dec. (figure 9.11a – 9.11c). The convergence of moisture flux over the region is speculated to have been the cause for the increase in relative humidity. ERA5 CAPE was found to be relatively low throughout the three-day period. During 27 and 28, relatively high CAPE amounts of between 2 – 2.5 x 10^3 Jkg^{-1} were observed over the western equatorial Indian ocean region tending onshore. The CAPE advection did not reach the Central Highlands on 28 Dec. but covered the region next to the Indian Ocean. This is probably the reason why ERA5 tended to produce more rains over this region. However, on 29 Dec., highest CAPE values characterised the Central Highlands as well as the western highlands ranging from 1.5 – 2.0 JKg^{-1}. As low as these values might appear, a climatological analysis of ERA5 CAPE revealed that these values are among the highest in ERA5. Inferences from ERA5 CAPE might be misleading especially if compared to observed CAPE from, for example, an upper air sounding examining the same convective system.

Distribution of 700 hPa θ_e was such that during the 27 Dec., the highest concentrations were found over the region and towards its western flank. The situation was no different on 28 Dec. but θ_e reduced on 29 Dec. presumably after the heavy downpour. SSTs over the western equatorial Indian Ocean were high ranging between 28°C east of 50°E and higher than 30°C near the Kenyan coast. As such, evaporation took place over a wide area. Since the 700 hPa wind flow was predominantly south-easterly to easterly throughout the three days, it was presumably responsible for the advection of high θ_e-air inland from an evaporating ocean surface that aided in the moisture build-up. On the 28th, the advection of θ_e inland contributed to its build-up just to the south of the Central Highlands. Since high-θ_e is associated with more moisture, the convective situation over the Central Highlands benefited immensely from this build-up.

Examination of the vertical structure of the atmosphere during the period of most intense convection could not be adequately carried out due to lack of sounding data during this time window. Sounding data for Dagoretti Meteorological station (figure 2.1) just after the most intense convection time window, namely 2242 UTC, was available nevertheless. Surprisingly, a very saturated lower troposphere up to the 500 hPa level emerged even after the critical[1] convective period. In fact, ERA5 reanalysis data mimicked this situation

---

[1] Most intense

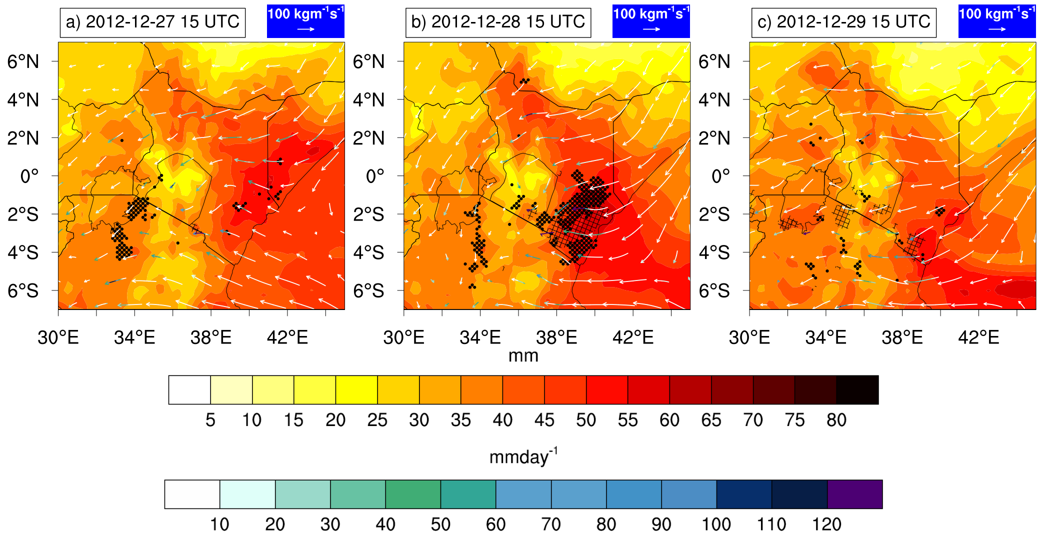

Figure 9.10: *a-c: Evolution of total precipitable water (filled contours; mm) over the Central Highlands at 15 UTC on 27, 28 and 29 Dec. 2012. Overlaid is the vertically integrated moisture flux (vector; kgm^{-1}s^{-1}) and its convergence (vector color; mmday^{-1}). Divergence of moisture flux has been suppressed. Dot stipples indicate areas of deep convection from BT<230 K. Meshed stipples show exceedances of total precipitable water from the 98th percentile during the 2000-2018 period.*

adequately well especially below 500 hPa level. The upper levels from ERA5 sounding were found to be moister than observations (figure 9.12) presumably due to the high amounts of moisture deposits from the Arabian Sea (figure 9.14). The Dagoretti upper air data appeared to have been assimilated in ERA5. The same observation was made from ERA5-initialized Lagranto trajectory (figure 9.16). Both observed and ERA5 model soundings showed a strong north easterly flow in the lower levels accompanied by a south westerly flow in the lower levels as can be seen in figure 9.12. This might explain why the troposphere remained moist and saturated even after the critical period of convection and precipitation. Radiosonde observations launched from Dagoretti meteorological station had a moistened lower troposphere with a corresponding mid-level dryness beyond 500 hPa explaining the little to no convective activity beyond this hour from TRMM and station precipitation data. That the lower atmosphere was still moist even after the rains had subsided is an indicator of a system that had evolved from a humid environment coupled with intense day heating over the highlands promoting deep convection in the absence of a wave activity.

9.7 Anomalies of dynamical variable precursors

Anomalies of seven ERA5 hourly variables (calculated as residuals from the mean ERA5 climatology i.e. 1979–2018) namely, temperature, dew-point, vertically integrated moisture flux divergence, precipitable water and precipitation were areal-averaged over the region of study (34.4 – 38.4°E and 2.6°S – 1.3°N) to determine the ability of ERA5 reanalysis model to predict the event (figure 9.14). From the figure, it is deduced that ERA5 exhibited a peculiar diurnal cycle of precipitation that maximised at 12 UTC (1500 hrs local time) over this region. Evidently, ERA5 model failed to capture this event in terms of magnitude and timing. The model is known to poorly represent local to mesoscale convection laden with high intensity precipitation e.g. MCS as well as other convective complexes (Magnusson et al., 2019) usually due to lack of enough data for assimilation as is the case over this region. As such it is not surprising that day time heating played a very huge role in the model to produce convective precipitation that was biased towards afternoon hours.

As figure 9.14 depicts, the real precipitation (inferred from TRMM) occurred much later in the afternoon, at 2100 UTC. Moisture flux convergence anomaly was such that a moisture flux convergence surplus characterised the entire period between 09 UTC 27 Dec. –12 UTC 28 Dec. This surplus was in phase with the peak ERA5 precipitation, the latter lagging it by a few hours. In fact, throughout the three days shown in figure 9.14, precipitable water anomaly was positive within the ERA5 climatology indicating that the moisture flux convergence contributed to high amounts of precipitable water that enabled the moistening of the column as observed in the sounding diagram shown in figure 9.12. A hovmöller diagram shown in figure 9.15 corroborates the theory about moisture flux to the region. A three-day moving average of this quantity as well as its convergence indicate that the region was characterised by a quite persistent easterly moisture flux prior to the day of event originating from the nearby Indian Ocean as has been demonstrated under section 9.8. The resulting moisture flux convergence contributed to high amounts of total column water that moistened the troposphere even beyond the most critical convective period.

Dew point anomalies were above zero throughout the period (27th – 29th Dec. 2012) with temperature anomalies oscillating in tandem with surface diurnal heating. Of interest was the fact that there was a nocturnal positive anomaly in temperature. This anomaly was as a result of a nocturnal warm temperature advection from the Indian Ocean (figure 9.13). The Indian Ocean was indeed very warm with SSTs of about 30°C (figure 9.11). Advection of warm temperatures during the day was neutralized and exceeded by the afternoon cooling as a result of the diurnal precipitation occurring during the afternoon. ERA5 model seemed to respond to intense day heating and the presence of the highlands to produce convective precipitation in the afternoon. This eventually caused after-rain cooling in the lower levels. CAPE anomaly values were relatively low throughout the period prior to the event but peaked substantially two hours before the event in ERA5. This served to provide considerable impetus for convective activity. Indeed, as mentioned before under section 9.6, CAPE values were observed to be relatively low spatially throughout the duration of the event. This was presumably due to the absence of large-scale forcings like tropical waves during the initiation of the event which are usually associated with widespread convection under the right atmospheric conditions.

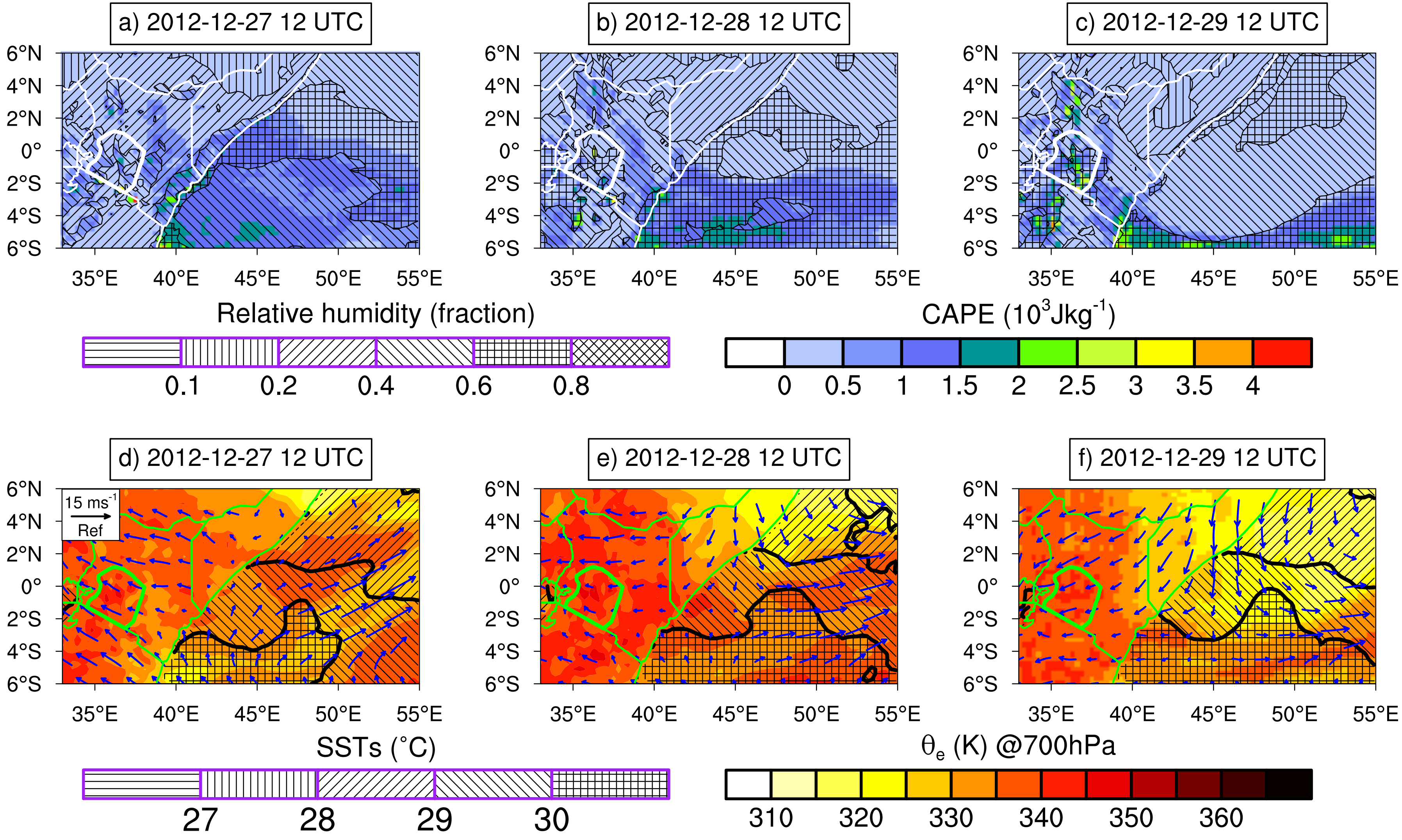

Figure 9.11: *(a-c): Evolution of ERA5 Convective Available Potential Energy (filled contours; 10^{-3} Jkg^{-1}) and relative humidity (shaded contours; no units) at 12 UTC between 27 and 29 Dec. 2012. (d-f): Evolution of 975 hPa level equivalent potential temperature, θ_e (filled contours; K) and sea surface temperatures (shaded contours; K) with 700 hPa wind field overlaid on the contours.*

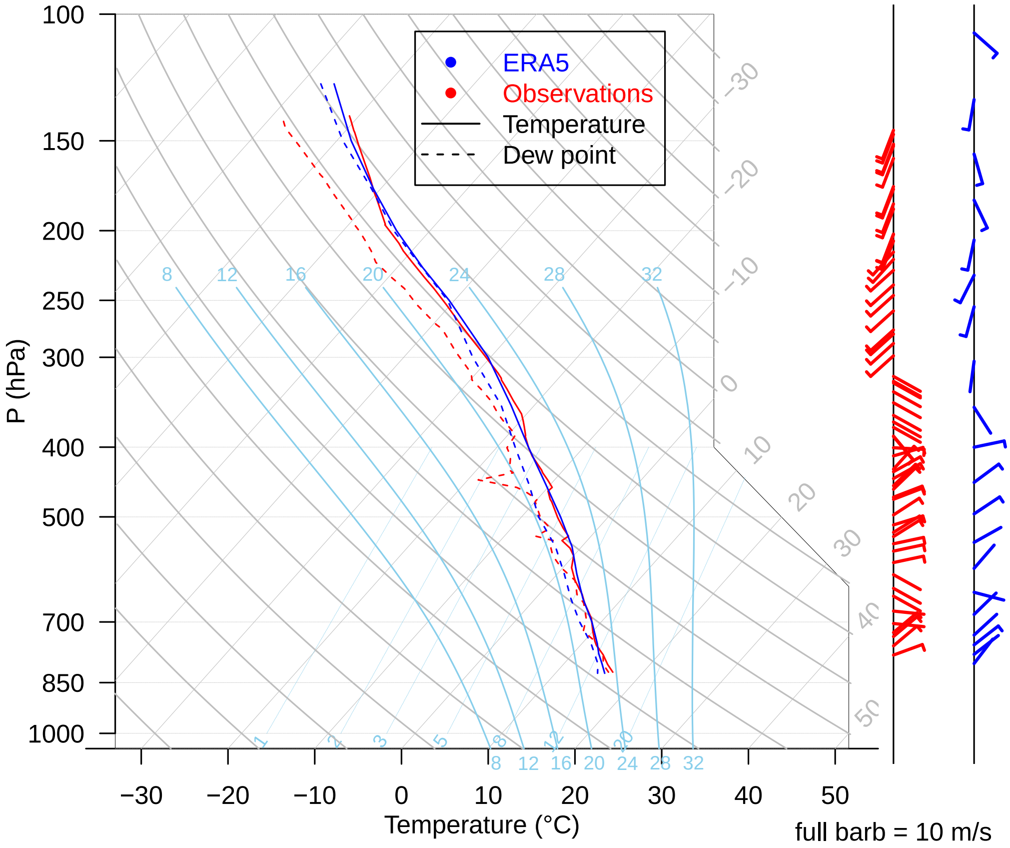

Figure 9.12: SkewT-logP plot of a rainy sounding taken from Dagoretti Meteorological station in Nairobi at 2242 UTC 28 Dec. 2012 (red attributes) and a corresponding ERA5 sounding from the vertical level data of the reanalyses model (blue attributes) at 2300 UTC 28 Dec. 2012.

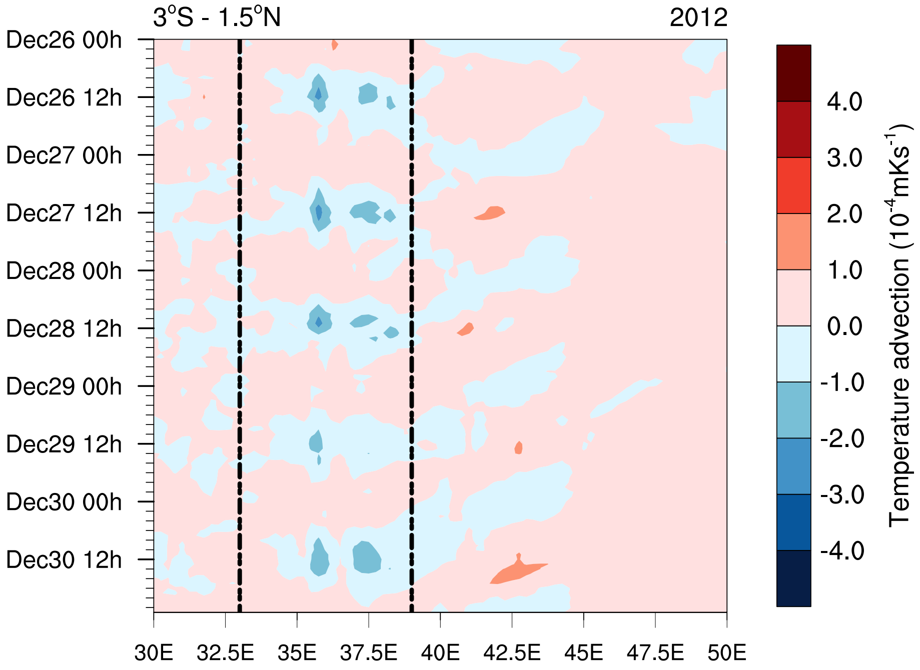

Figure 9.13: A hovmöller diagram over the Central Highlands averaged between 3°S – 1.5°N showing temperature advection (colors; $10^{-1}mKs^{-1}$) between 26 and 30 Dec 2012. A nocturnal positive advection of temperature from the Indian Ocean is visible. Vertical dotted lines demarcate the Central Highlands.

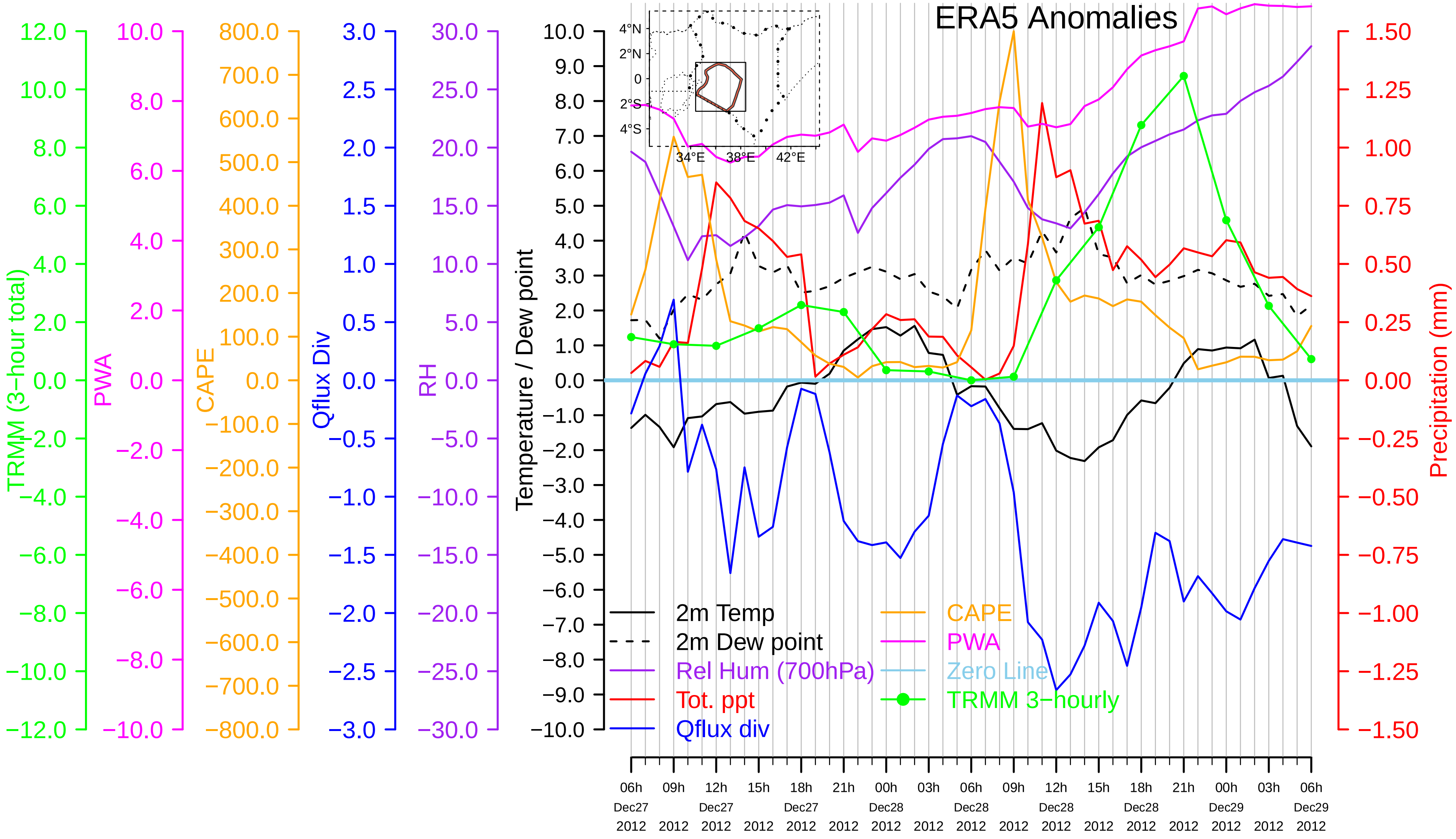

Figure 9.14: *Anomalies of various ERA5 variables namely 2-meter temperature (solid black curve), 2-meter dew-point (dashed black curve), relative humidity at 700 hPa level (purple curve), total precipitation (red curve), vertically integrated moisture flux divergence (blue curve) and Convective Available Potential Energy (CAPE; orange curve).The variables are calculated as hourly means between 26 and 30 Dec. 2012 averaged within the 1979–2018 ERA5 climatology. Note that every variable is color-coded. TRMM 3-hourly totals averaged over the Central Highlands spatial domain are shown in green.*

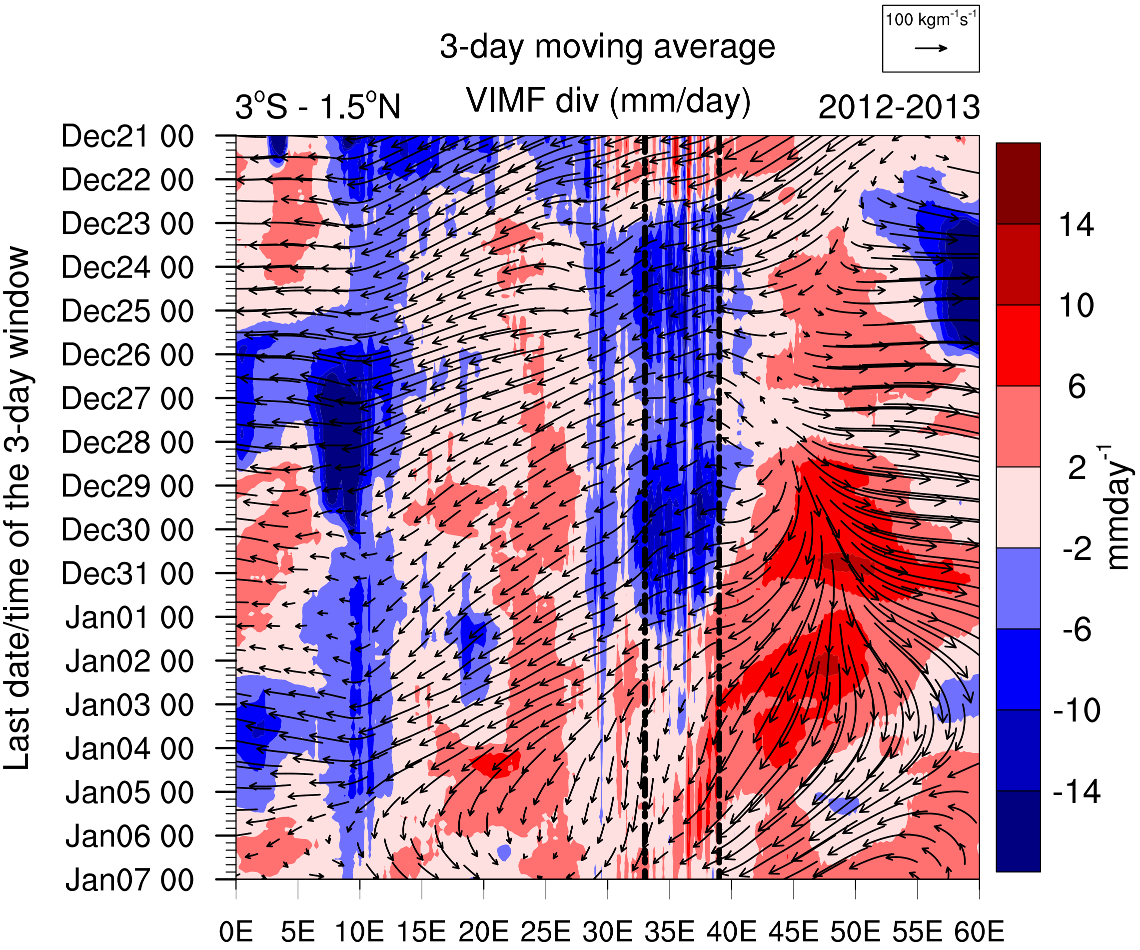

Figure 9.15: *A hovmöller diagram showing the three-day running mean of ERA5 vertically integrated moisture flux (vectors; kgm*$^{-1}$*s*$^{-1}$*) and its convergence (colors; mmday*$^{-1}$*) between 18 Dec. 2012 to 07 Jan 2013 averaged between 3°S – 1.5°N within the Central Highlands.*

9.8 Moisture sources: Lagrangian analysis

In section 9.6, the eulerian approach in the analysis of moisture transport is discussed where snapshots of moisture flux at specific times are analysed. This section presents results obtained from the Lagrangian moisture transport using the Lagranto model which attempts to follow an air parcel in space. This is discussed at a relative detail in section 5.2.7. u and v wind components at various pressure levels were used as forcing variables to the Lagranto tool. The mode chosen was the backward trajectory one which traces an air parcel back to its source. Levels chosen to start the backward trajectories were 500 to 1000 hPa in intervals of 50 hPa. However, due to the region of study being in a highlands zone, the lowest level above the surface for the grid point chosen was 800 hPa. Just like in other cases studied in this thesis, specific humidity was tracked along the trajectory in order to identify the sources of moisture as well as the physical mechanisms triggering its release over the region of study. The backward tracing illustrated that five days prior to the event, the parcels of air that arrived in the region emanated from the eastern flanks of the Arabian Sea located to the northern side of the western equatorial Indian Ocean. The parcels were carried predominantly in the lower levels of the atmosphere, first rising within the horn of Africa five days prior, sinking along the Somali coast north of the equator four days prior and finally ascended until the moisture was released within the region of study (figure 9.16a). The moisture was collected along the track consistently at every point within the five days until it was released near the region at grid point 36.25°E and 0.1°S (figure 9.16b) at 15 UTC 28 Dec. by virtual of the air parcels undergoing expansion. This grid point was chosen based on the amount of precipitation received and as a way to trace back moisture that contributed to the deep convection producing the A06 on 29 Dec 2012 over the region. To quantify the heat changes in the air parcels, $T-\theta$ diagrams were

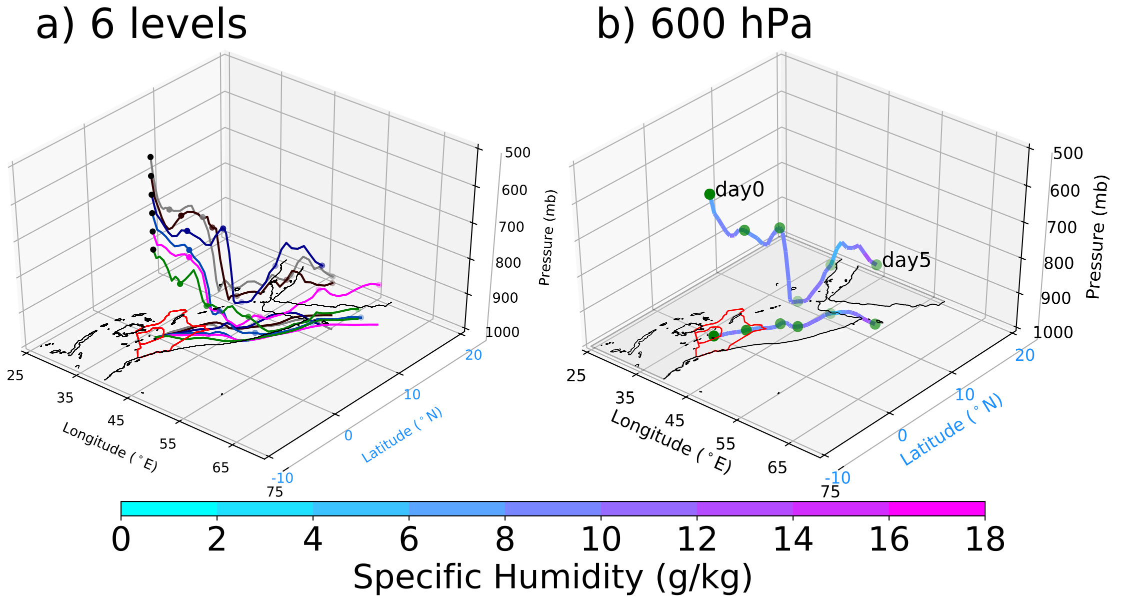

Figure 9.16: ***a)*** *Three dimensional 5-day backward Lagranto trajectories showing air mass sources for various starting levels using ERA5 model data over the Central Highlands initialized at 15 UTC 28 Dec. 2012. The starting levels are namely, 500, 550, 600, 650, 700 and 750 hPa shown by grey, darkbrown, darkblue, blue, magenta, and green lines respectively. The color markers indicate every day lapsed. Black markers represent the initial grid point namely, 36.25°E, 0.1°S.* ***b)*** *Specific humidity traced along the backward trajectory starting from the 600hPa level. Notice that each trajectory in both* ***a*** *and* ***b*** *is mapped onto the surface too using the same color configuration.*

analysed. Five starting levels were chosen in this diagnosis namely, 500, 600, 650 and 700 and 750 hPa levels. Consistent with the Lagrangian analysis in figures 9.16a and 9.16b, the backward trajectory that began at 500 hPa continued to rise by virtue of decreasing T while θ increased by about 5°C per day until two days before the event. In this case, adiabatic cooling exceeded diabatic heating and the parcels are said to have undergone expansion due to lifting. However, two days to the event, these parcels underwent compression by virtue of increasing T and decreasing θ hence adiabatic heating exceeding diabatic cooling which could only be explained by subsidence. Just before the event, the temperature T decreased while θ decreased too rendering conclusion about vertical motion somewhat difficult. However, examination of figure 9.16a shows that these air parcels rose. The conclusion is that the parcels lost heat through either radiative cooling or evaporation. The backward trajectory that started at 600 hPa was similar to the 500 hPa one save for the fact that between day three and day two before the event, the parcels underwent a purely diabatic heating process at constant temperature. Until the last day when the latent heat was released, the parcels underwent lifting as temperature, T decreased while θ increased thus adiabatic cooling exceeding diabatic heating. For trajectories started at 650, 700 and 750 hPa, the initial stages (one day to the event) were such that they all had their T and θ increase creating uncertainty as to whether they were rising, remaining at constant level or decreasing. However, examination of figure 9.16a shows that all these parcels rose initially. Eventually three days to the event, their T decreased while θ increased which could only be explained by lifting. Conclusion drawn is that parcels started at every level may have undergone different heating processes four to five days before the event of 29 Dec., but responded in a similar nature at most three days before the event by undergoing lifting caused by an increase in θ with a corresponding decrease in T.

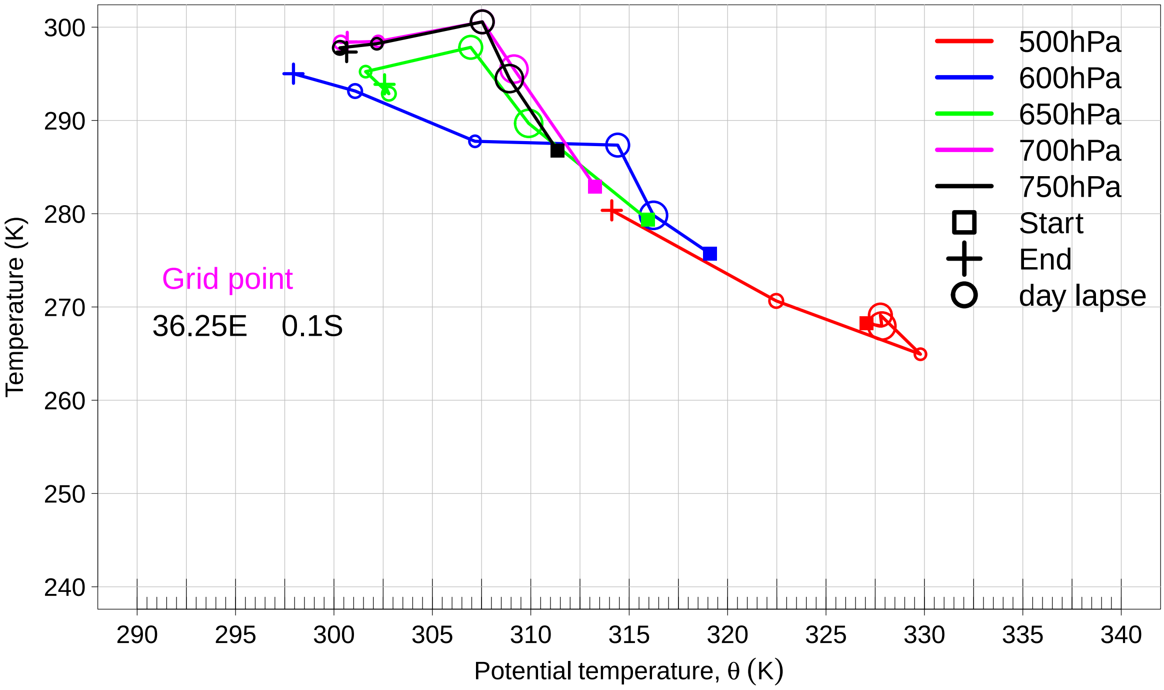

Figure 9.17: *Temperature-Potential temperature ($T - \theta$) curves showing the evolution of T and θ each day for 5 days since the beginning of the backward trajectory at 15 UTC 28 Dec. 2012 (shown by the diamond marker) until the end of the trajectory 5 days later (shown by the cross marker). Rings indicate every day lapsed and their size diminish further away from the event every 24 hours. The starting levels are 600, 650 and 700hPa and each curve represents a specific starting level of the trajectory.*

9.9 ICON simulations

In this section, results obtained after the simulation of precipitation using the ICON model discussed in section 5.3.1 are presented. The model was initialized at various times (12 UTC 27 Dec., 18 UTC 27 Dec. and 00 UTC 28 Dec.) using both the ERAI and IFS operational model to compare which combination of initial conditions best produced precipitation structures of A06 that closely matched the observed patterns from TRMM. Once this overall best combination of initial condition was identified, the diurnal cycle of precipitation from ICON was investigated.

9.9.1 Simulation of the 24-hour accumulated precipitation between 0600–0600 UTC (A06)

A06 for the various initial conditions are shown in figure 9.18a – 9.18d. Based on an *eye-ball* approach alone, it can be deduced that neither of the combinations of initial conditions produced an optimal A06 structure observed in TRMM. The model at every stage was found to produce an incoherent spatial structure that paid little semblance to the organisation found in TRMM. However, a closer look at the ERAI forced ICON at 12 UTC Dec. 27, though tending to underestimate the magnitude of the precipitation, had a few pixels that tended to organise in a way that resembled the TRMM A06 structure. One grid point especially produced almost the same amount of precipitation as observed in TRMM. For the rest of the ERAI-driven initialization times, the structure was found to be non-representative of the observed patterns with larger precipitation objects produced just next to Lake Victoria. As for the IFS initialized model, the subjective *eye-ball* method reflected a similar structure where the 12 UTC simulation appeared to be more representative of the observed structures than the rest of the initialization times with a spatial bias towards the lake basin just as observed by the ERAI-driven ICON. However, eye-judgement is not entirely skillful and a more objective approach was adopted in the next subsection.

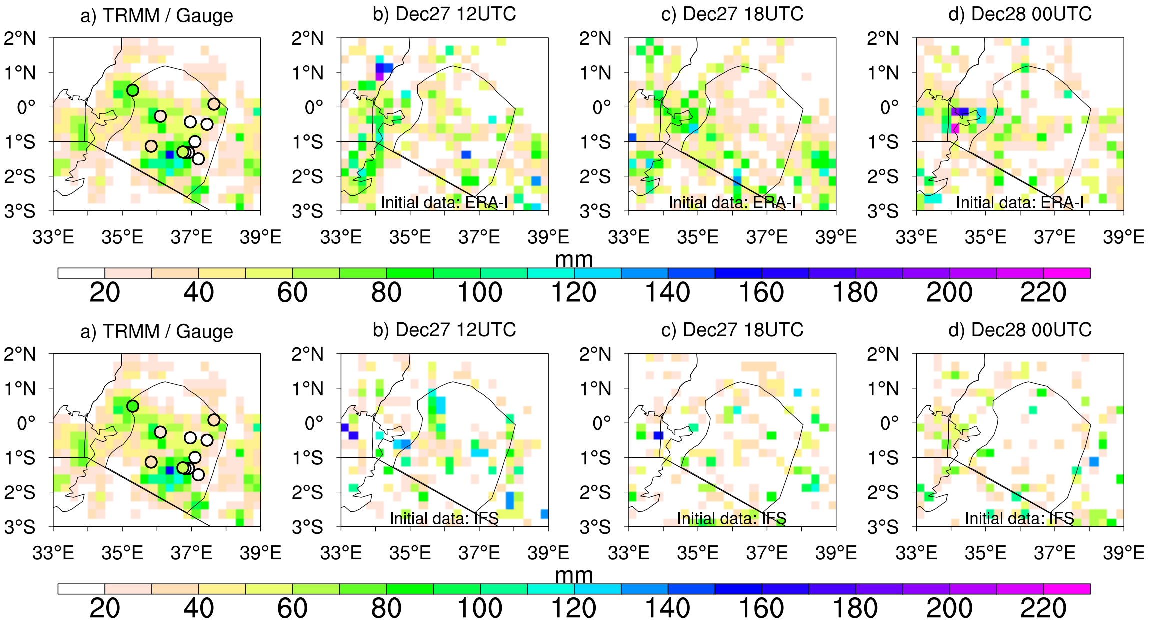

Figure 9.18: *A06 for* ***a:*** *Gauges (markers) overlaid on TRMM (filled contours).* ***b–d:*** *ICON simulated precipitation initialized at 12 UTC 27 Dec., 18 UTC 27 Dec. and 00 UTC 28 Dec. respectively using ERAI (upper row) and IFS (bottom row).*

9.9.2 Spatial evaluation of 24-hour accumulated precipitation between 0600–0600 UTC (A06)

Based on section 9.9.1, the subjective approach of evaluating the skill of the A06 ICON forecast pointed to a poor representation while making the comparison with TRMM. The eye approach identified the 12 UTC Dec. 27 ERAI-driven simulation as the most ideal under the circumstances. The SAL method was adopted to identify the most representative simulation. From figure 9.19a which is the ERAI-driven simulation, the model is observed to have overestimated the magnitude of precipitation by some margin ($A > 0$). As for the structure, all the simulations produced scattered precipitation patterns ($S < 0$) with the 12 UTC simulation producing the least scattered structure. The locations for all the ERAI-driven simulations were not found to have a significant bias. As seen from the observations, the 12 UTC simulation from ERAI was found to be objectively superior to the others especially on structure producing the least scattered rains. The IFS-driven simulation in figure 9.19b was poorer by a small margin compared to its ERAI-driven counterpart with the most scattered rains ($S < 0$), magnitude overestimation ($A > 0$) and largest location bias produced by the 18 UTC initialization. Thus, based on this objective evaluation, the 12 UTC 27 Dec. ERAI-driven simulation was adopted as the most ideal in representing A06 structure over the Central Highlands. The next section investigates the diurnal cycle of precipitation between 06 and 06 UTC 28–29 Dec. 2012 using this adopted simulation.

9.9.3 Sub-daily precipitation

The ERAI-driven ICON model forecast initialized on 12 UTC 27 Dec. 2012 was adopted to examine the diurnal evolution of precipitation in the model compared to TRMM. A striking difference was observed during the periods of most intense precipitation (15 UTC to 00 UTC). The model was found to underestimate the magnitude of precipitation by as much as 30–35 mm during this period as opposed to the beginning of the day when the differences were close to zero with the model overestimating precipitation over some grid points (figure 9.20a – 9.20h). The model produced too high but isolated convection cells outside the boundaries of the region and especially within the Lake Victoria basin as observed in the analysis of A06. However, a handful of ICON grid points during the onset of intense precipitation within the Central Highlands were found to have much larger values than TRMM (case in point is 15 and 18 UTC). From this *eye-view* subjective method, it can be concluded that the model failed to capture the magnitude, structure and location of the various precipitation objects especially during the period of most intense convection and precipitation. The model produced too much scattered precipitation and especially over the regions neighbouring Lake Victoria.

9.9.4 Spatial evaluation of sub-daily precipitation

Focus now turns to the assessment of spatial skill of ERAI-driven ICON model forecast in representing the various precipitation objects summing up to A06. Unfortunately, the skill was as poor as the eye-judgement revealed. Figure 9.21 demonstrates the three quantities of SAL for each of the three-hourly precipitation objects from ICON and TRMM. The magnitude of precipitation in most of the cases considered was found to have been much higher than TRMM ($A > 0$) considering the domain of 3°S–1°N and 34°–39°E. This might seem to differ from the subjective *eye-view* in figure 9.20. The

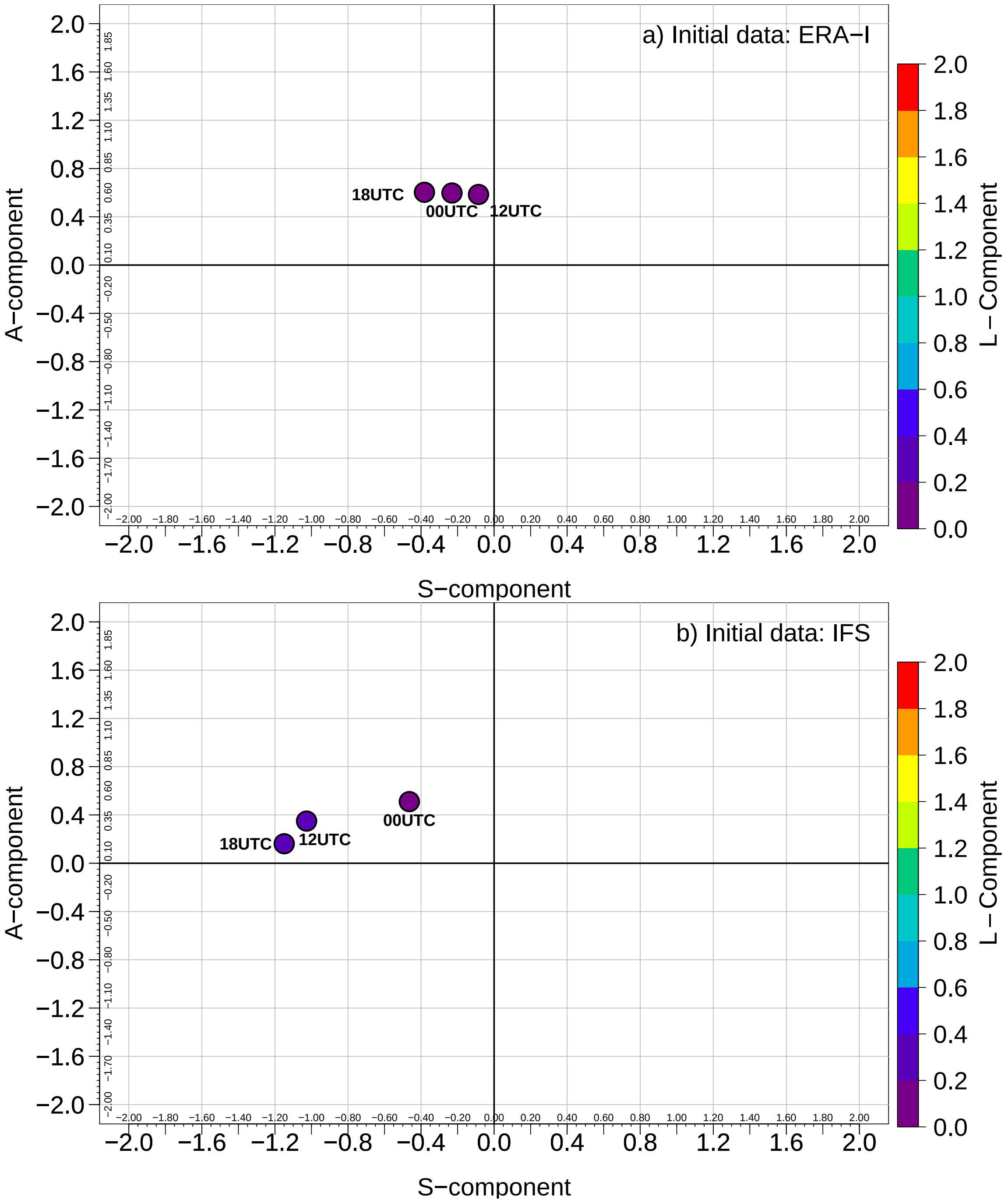

Figure 9.19: SAL diagram for A06 forecasts from the ICON model at three different initialization times namely, 12 UTC, 18 UTC 27 Dec. and 00 UTC 28 Dec. 2012. Every dot shows the value of the three components of SAL with the location component shown by color. ***a*** *shows SAL for ICON output forced by ERAI while* ***b*** *is the SAL result for ICON output forced by IFS. TRMM data was used as the verification field in both cases.*

magnitude of the difference between the observed and the model when TRMM precipitation was higher (lower) than ICON were relatively lower (higher) triggering the observed pattern. However, as observed from figure 9.20, the structure was non-coherent in nature with the model tending to produce too much isolated precipitation ($S < 0$). This was the case for a majority of the diurnal precipitation objects save for the object at 15 UTC 29 Dec. which showed an organised system contrary to what TRMM reported with a slightly

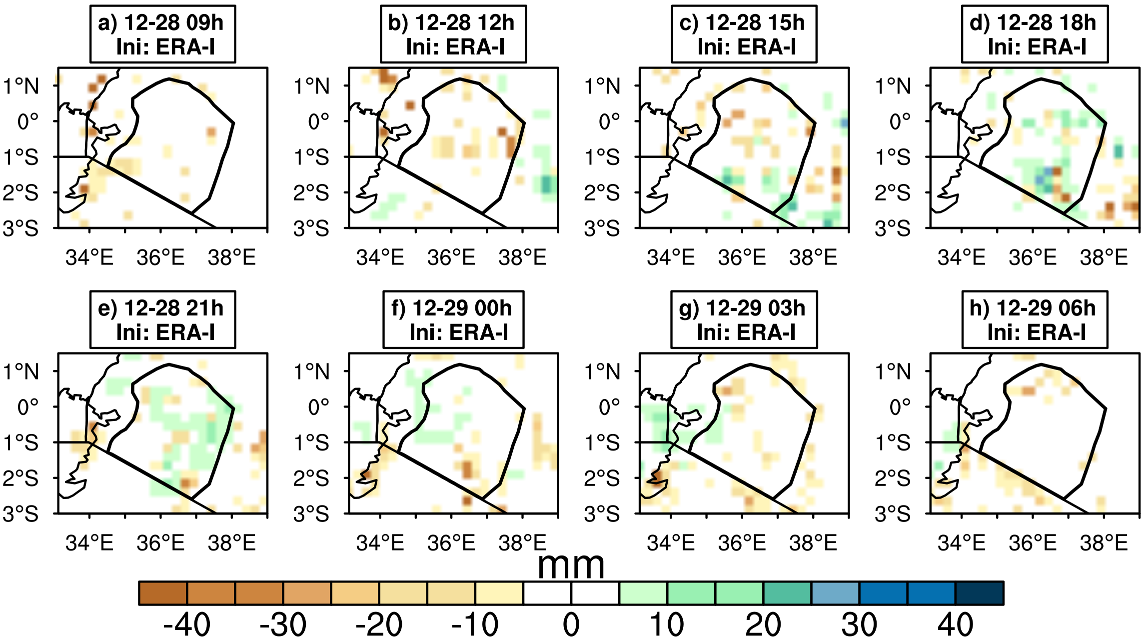

__Figure 9.20:__ __a–h:__ Sub-daily evolution of the difference between TRMM and ERAI-forced ICON (trmm − icon) between 28 Dec. 09h and 29 Dec. 06h for the 12 UTC 27 Dec. initialization.

positive value of S, a situation that is not immediately clear from 9.20c.

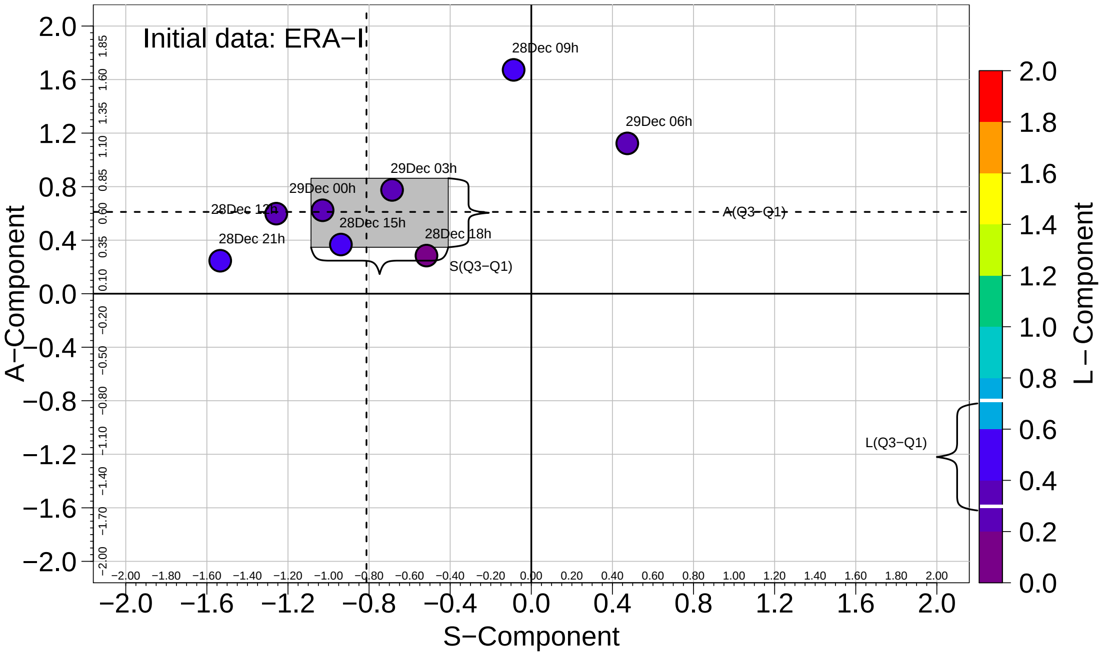

__Figure 9.21:__ SAL diagram for ICON model outputs at three-hourly interval initialized at 12 UTC 27 Dec. 2012 by ERAI. Every dot shows the value of the three components of SAL at a particular three-hour interval since initialization. The L-component is shown by color. Median values of the S and A components are shown as dashed lines while the gray box extends from the 25th to the 75th percentile of the distribution of S and A and annotated on the diagram as $S(Q_3 - Q_1)$ and $A(Q_3 - Q_1)$ respectively. The corresponding interquartile range of the L-component is shown by the two white dashes on the color scale and annotated as $L(Q_3 - Q_1)$. Notice that the individual hours of the day are annotated.

9.9.5 Simulated cloud top temperatures

This section presents results obtained after comparing cloud top temperatures from the IFS-driven ICON model initialized at 00 UTC 28 Dec. 2012 with BT. Since the focus was on deep clouds responsible for A06, temperatures above 240 K were considered too warm and shallow to produce precipitation. Therefore, temperature values below 240 K were masked for the purposes of this section. Striking differences were found between the verification field (BT) and the model field (ICON). Firstly, the strictly organised clouds found in BT within the boundaries of the region were almost absent at 18, 19, 21 and 22 UTC as shown in figure 9.22a–9.22j. The model produced deeper clouds just outside the region and to the east of the regional boundary. This might explain why the model could not adequately reproduce organised precipitation clusters as observed in TRMM. This subjective method concludes that even though the model produced some clusters of deep clouds, these clusters were not as large and occurred outside the region and therefore the model is said to have been poor in simulating cloud top temperatures.

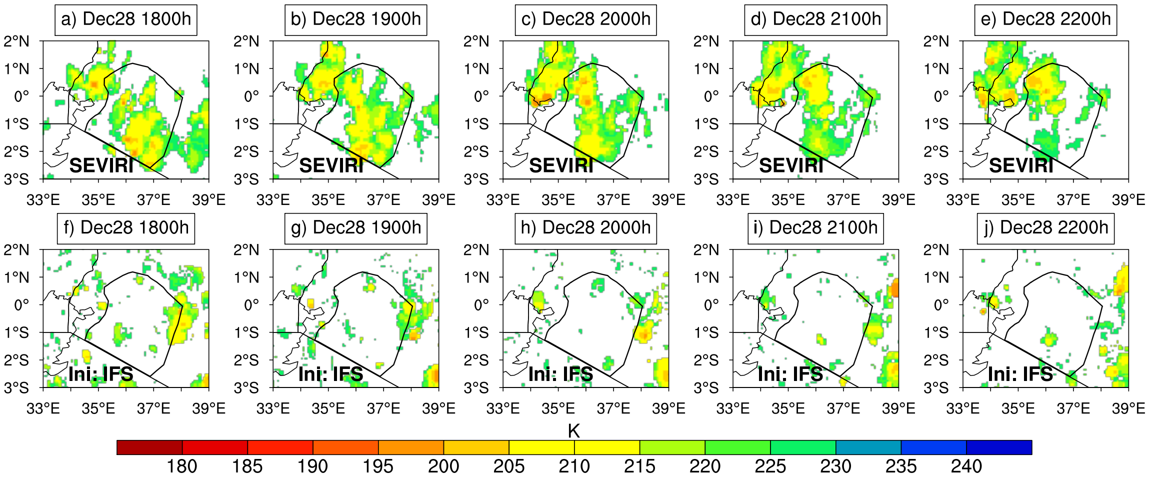

Figure 9.22: Evolution of cloud-top temperatures over the Central Highlands between 18 and 22 UTC 28 Dec. 2012. ***a–e*** *are the BT while* ***f–j*** *are the simulated cloud top temperatures from ICON initialized by IFS reanalysis data.*

9.9.6 Spatial evaluation of cloud top temperatures

The model was found to be poor in reproducing CTT over the Central Highlands from the subjective *eye-view* method discussed in section 9.9.5. However, in this section, the forecast skill of the model was objectively assessed by comparing the neighbourhood sizes in both forecast and verification fields within the entire domain (3°S – 2 °N and 33° – 39°E). The FSS method discussed in section 5.3.3.2 was adopted for this task. The times chosen for the application of the FSS were 18, 19, 20, 21, 22 and 23 UTC 28 Dec. The FSS result is shown in figure 9.23 The result showed that the skill was better during the earlier hours of 18 and 19 UTC with the skill diminishing with size (n) as the system grew. However, even for the 18 and 19 UTC when the skill was found to be better, one had to increase the spatial length to over 90 Km to realize a FSS skill of at least 0.5. This was not considered ideal since the model was run at a resolution of about 3.25 Km. For such a high resolution, and the relatively small size of the domain considered, a FSS skill of at least 0.5 would be more acceptable for spatial lengths of less than 40 Km. This goes in tandem with the proposition of Roberts and Lean (2008) to always consider the limit of scale size when interpreting results from FSS. For the rest of the times of intense convection, the skill of 0.5 was realized after increasing the spatial length to more than 350 Km. Though linear correlation by grid point can give information about how the two fields relate to one another, it does not reveal the magnitude of the respective fields. Thus, as long as there is a trend between the two fields, correlation will always be high. The inset figure within the figure 9.23 shows clearly this scenario. The high values of correlation can be misleading when making magnitude-based comparisons.

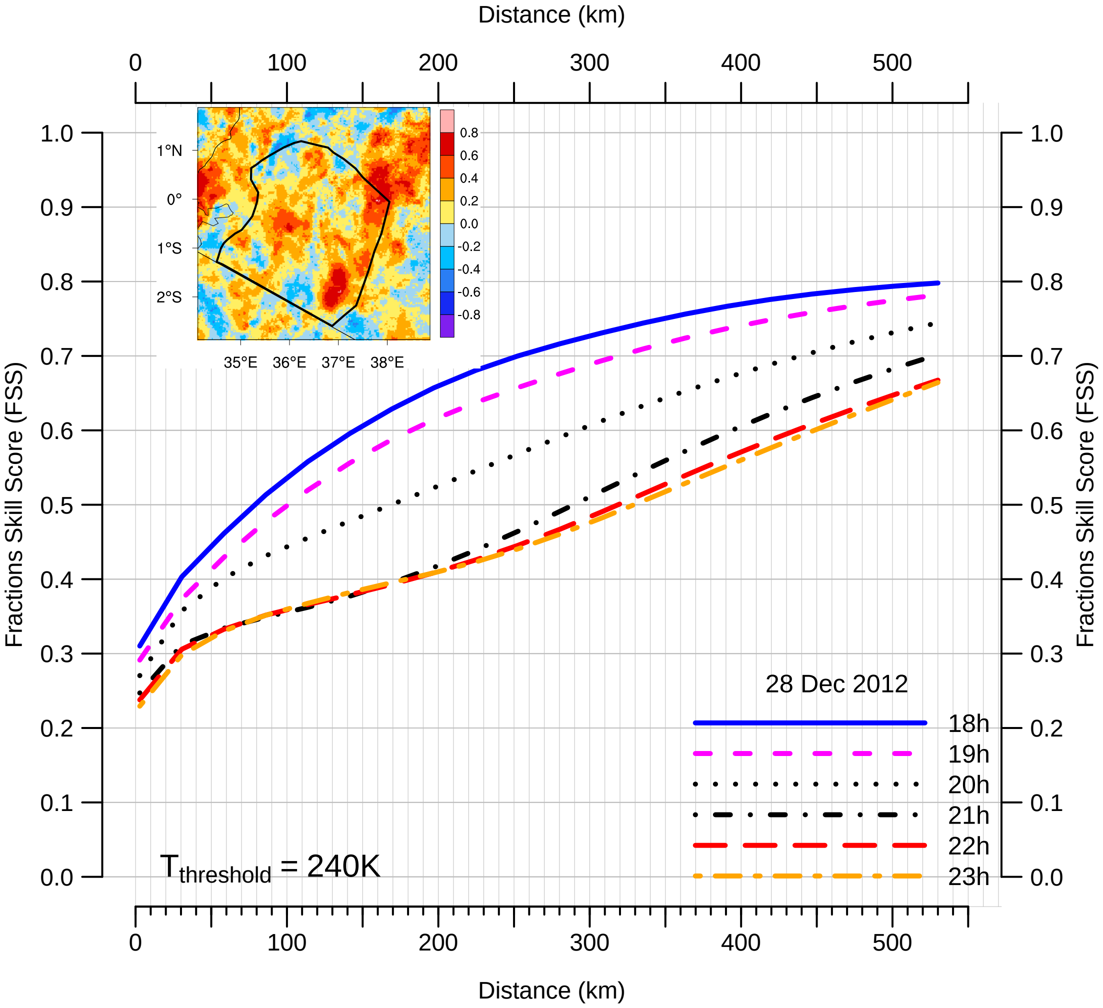

Figure 9.23: Fractions Skill Score (FSS) and grid-point based correlation coefficient between BT and ICON model simulated cloud top temperatures (CTT) initialized at 00 UTC 28 Dec. 2012 using IFS reanalysis datasets. Shown are FSS curves during the most intense convection (between 1800–2300 UTC 28 Dec., 2012). Temperatures below 240 K are deemed to be representative of deep convection to which the binary fields of FSS are defined. Inset plot is the linear correlation coefficient map between the observed (BT) and the forecasts (ICON simulated cloud-top temperatures) between 1800 UTC 27 Dec and 1200 UTC 29 Dec., 2012.

9.10 Summary and conclusions

The precipitation event of 29 Dec. 2012 was identified within the TRMM period of 1998–2014 as a contiguous and extreme event within the Central Highlands. Satellite and surface-based observational data revealed the extreme nature of the case. Diurnal cycle of precipitation indicated that the event was induced by day-time heating as the period of intense convection in ERA5 occurred in the early afternoon hours which was much earlier than in observations where precipitation occurred during evening hours. Apart from a dry Kelvin wave observed in the upper level wind divergence, no convectively coupled tropical waves could be attributed to the event. The extreme event appeared to have been locally forced by intense solar heating creating a local low pressure system. As such, the low pressure system induced low-level winds from the east which converged near the southern flank of the region due to speed convergence with the highlands acting as a barrier that decelerated the winds. The event benefited from an easterly intrusion of high θ_e-air from the Arabian Sea which moistened the region and rendered it conditionally unstable. A Lagrangian analysis corroborated this finding. This moist but unsaturated air was brought to the LFC through speed convergence and orographic lifting. Evolution of the event was characterised by anomalous variables of heat, moisture and momentum which were found to have exceeded their overall climatology for each hour considered. The magnitude of this climatological exceedance was not quantified but rather observed from the analysis and subsequent plots. However, attempts to reproduce the 24 - hour accumulated precipitation in ICON model proved unsuccessful with the model producing an extremely noisy pattern whose structure did not match the observations. The model was also found to overestimate sub-daily precipitation by producing too isolated cells of convection. A further attempt to reproduce cloud top temperatures from the model proved futile as the model was found to miss the deep and cold clouds especially during the time of most intense convection.

In conclusion, this extreme precipitation event over the Central Highlands was found to have been locally-triggered by local day-time heating, benefiting immensely from availability of moisture and heat from the neighbouring western equatorial Indian Ocean. The easterlies deposited moisture in an elevated zone releasing instability through orographic lifting and speed convergence. The resulting upward motion released moderate amounts of CAPE that promoted the development of deep convective clouds. The perpetual moisture flux ensured a continued supply of moisture rendering precipitable water in a column, the highest on record. This persistent moisture flux aided in the sustenance of the convective system. However, the ERA5 model struggled to reproduce the local scale processes but did well in reproducing the synoptic evolution of moisture and momentum. The poor network of upper level observations over the region hindered the model from performing well in forecasting precipitation events due to challenges emanating from insufficient data for assimilation as well as model errors.

Chapter 10

Summary and outlook

Extreme precipitation events over Kenya have devastating impacts on communities and economies. They wreak havoc to infrastructure, destroy crops in fields causing hunger and poverty, bring forth water-borne diseases and other catastrophic impacts. However, current NWP models fall short of forecasting these extreme events with a reasonable degree of skill. The overarching aim of this dissertation was to investigate the synoptic-dynamic preconditions that precede contiguously extreme precipitation events in Kenya by way of case studies. The cases were selected from the main rainy seasons in Kenya and East Africa namely, October-November-December (OND) and March-April-May (MAM).

Three case studies were chosen namely; the Coastal Lowlands case (14 May 2007), the Lowlands case (29 Oct. 2011) and the Central Highlands case (29 Dec. 2012). The initial stages of the analysis involved aggregating both gauge and TRMM data to create a 24-hour accumulated precipitation between 0600–0600 UTC (A06) product for each day within the TRMM's 1998–2014 period. Contiguity and extremity in both datasets were compared. However, TRMM's extremity and contiguity was, for most of the cases, preferred based on its wider spatial coverage over a region prone to data scarcity. The large-scale synoptic conditions were similar for the Coastal and Lowlands case but slightly different for the Central Highlands case. Synoptic-scale forcing was much stronger in the former two cases but weaker for the Central Highlands case. To understand the underlying synoptic-scale influences for the cases, an extensive diagnostic study was conducted in terms of preconditions for deep moist convection and representation in the ICON model. Preconditions for deep moist convection include availability of sufficient quantities of moisture content within a column of the atmosphere, a potentially unstable atmosphere and a trigger mechanism that aids in lifting of warm, moist and unsaturated air to the LFC.

As far as the Coastal Lowlands case is concerned, a Kelvin wave superposed on an equatorial Rossby wave was observed prior to the event's initiation and could have played a role in creating a low pressure system. This pressure trough induced large-scale south-easterly winds which converged over the Coastal region. The resultant frictional convergence at the coast was enough to overcome the CIN and lift the unsaturated moist air parcels in the lower levels to the LFC. A similar large-scale influence involving a Kelvin wave - equatorial Rossby wave superposition was identified for the Lowlands case too and may have triggered a surface pressure low that induced winds to the region resulting into wind convergence and lifting. A strong LSB off the Somali coast and propagating westward towards the Lowlands may have enhanced the eastward propagating convective system contributing to the enhanced afternoon convection. The Central Highlands case was not found to have been triggered by a convectively coupled tropical wave but was as a result of intense day-time heating coupled with a prevailing warm and moist easterly flow emanating from an anomalously warm (western equatorial Indian) ocean. The flow was forced to rise over the highlands aiding to break the CIN in a conditionally unstable atmosphere. In all the cases, strong vertical motion was found to precede initiation sustained by a strong and persistent convergence of moisture flux mainly emanating from the Arabian Sea. The mesoscale instabilities were poorly represented in ERA5 and conclusion was drawn that due to the scarcity of upper level air data as well as the low vertical resolution of such data, ERA5 is likely to misplace or totally miss locally induced circulations. Lagrangian analysis in all the cases indicated that the source of moisture was the northern end of the western equatorial Indian Ocean where the flow underwent diabatic processes aiding the flow to collect moisture from the ocean before the ultimate release of latent heat over the respective regions.

Representation of the three cases in the convection-permitting ICON model was found to be poor as the model reproduced too isolated convective elements, sometimes underestimating the magnitude of precipitation (as was the case for the Central Highlands event) or overestimating the magnitude of precipitation (as was the situation in the Coastal and Lowlands cases). The same verdict was drawn after an attempt to reproduce the deep convective clouds in observations through simulation of cloud top temperatures by ICON. The model was, in all the cases, found to produce too warm clouds. Objective evaluation of cloud top temperatures against BT revealed that the model could not reproduce adequately the cold cloud tops.

Since the main aim of this doctoral thesis was to diagnose extreme precipitation events over Kenya with a view to developing dynamical precursors that may aid in forecasting, the findings based on the research questions listed under chapter 4 are summarised as follows:

1. As to the research question on the most extreme precipitation event in both spatial contiguity and magnitude, the study identified three dates when both TRMM and rain-gauges agreed in both magnitude and contiguity. The dates identified are 14 May 2007, 29 Oct. 2011 and 29 Dec. 2012 for Coastal Lowlands, Lowlands and the Central Highlands respectively.

2. As to the second research question, the study found that satellite-based precipitation data compared well to the rain-gauges in spite of a few observed overestimations and underestimations. Indeed, TRMM and gauge data were found to be in phase temporally and spatially and were also found to be interchangeable in most respects.

3. As to the third research question, the study unraveled that ECMWF reanalysis model captured, to a reasonable degree, the aspect of enhanced precipitation. Interestingly, the extreme precipitation in ERA5 largely underestimated observations. These extreme rains, the analysis revealed, exceeded the 98^{th} percentile in ERA5's own climatology. This negative bias in precitation amounts was prevalent across all the cases considered. As for the contiguity of the event, ERA5 was found to concentrate precipitation within selected parts of a region. This bias was more common over large water bodies. ERA5 appeared to respond to abundance of moisture and day time heating in the tropics to produce convection over these specific areas.

4. As to the fourth research question, the study revealed that the cases were not truly related to propagating systems since the degree of organisation was low. On the Coastal Lowlands case, for example, deep convection was found to propagate from

interior regions of the western equatorial Indian Ocean a few hundred miles from the shore intensifying as it collected more moisture but dissipated a few hours after hitting the mainland probably due to a moisture cut-off. However, since there were no clear signals of cold pools recreating sister cells along its wake, the conclusion was that there was no clear indication of cold pool related convective organisation in the satellite images. The vertical extent of the convective system in the Coastal Lowlands case was found to be about 12 Km though observed early on by a flying CALIPSO/CloudSat overpass. The Lowlands system too was found to have been a long-lived one emanating from the west and propagating eastward towards the region where it was accentuated by a developing LSB. Just like the Coastal Lowlands case, it was not found to be related to any cold pool convective organisation. Due to lack of CALIPSO/CloudSat overpass flights during the evolution of the Lowlands case, the vertical height of the system could not be determined. As for the Central Highlands case, a subtle propagation could be seen emanating from shores of the Indian Ocean along the Kenyan coast. The propagation was not at all organised and as it was clear from the satellite images that there was no apparent cold pool organisation. However, ERA5 could not replicate this system's propagation but created convective systems that tended to be in phase with day time solar heating. Thus, the conclusion here was that satellite-based observations pointed to propagating organised convective systems but ERA5 variables pointed to a diurnal cycle of convection with no discernible propagation. Again, due to the absence of overflights during this system's evolution, the vertical extent of the Central Highlands case system - especially during the time window of the most intense convection - could also not be determined.

5. As to the fifth research question, the study found that indeed, the ECMWF reanalysis model was able to capture, to a great extent, the large-scale synoptic influences but struggled to reproduce local to mesoscale preconditions. As an example, the reanalysis model captured well the tropical waves that superposed to create local low pressure system for both the Coastal and the Lowlands case but struggled to reproduce the inherent thermodynamic instability aspects. The same case applied to the Central Highlands case where the model was found to respond more to the day time heating producing diurnal precipitation biased towards early afternoon hours. In the absence of sufficient upper air data, this research question could not be adequately addressed as the study relied heavily on ERA5 data that is reasonable for large-scale dynamics but poor for locally forced and mesoscale systems.

6. As to the sixth research question, the study found that tropical waves play a key role during initiation of these extreme precipitation events. Apart from the Central Highlands case where there was no discernible convectively coupled tropical waves, the Coastal and Lowlands cases were apparently found to have been influenced by convectively coupled tropical waves. What could not be answered here is whether the waves acted as trigger mechanisms or augmented the development of these convective systems. What was observed, though, was that for each of the cases where a convectively coupled wave existed, there was a drop in mean sea level pressure. For the Coastal Lowlands case, frictional convergence played a role in triggering a lift while both frictional and directional convergence were the main dynamical processes that delivered the unsaturated moist air parcels from the lower levels to the LFC in a conditionally unstable atmosphere for the Lowlands case.

CAPE was found to be important in the growth and sustenance of the systems save for the underestimation by the ERA5 model. In all the cases, strong vertical motion preceded each initiation and remained active for long hours until the system dissipated due to a drop in moisture supply.

7. As to the last research question, the state-of-the-art convection-permitting ICON model could not replicate the cases adequately. The model produced too scattered precipitation which in most cases were found to exhibit higher magnitudes than observations. The model, to some extent, was able to reproduce the location of these systems but with the poor structure of the system coupled with the too noisy isolated convection pattern, the conclusion drawn was that the model could not adequately reproduce the cases.

The novelty of this doctoral thesis lies in the use of a myriad of observational data which include remotely-sensed and surface-based observations as well as reanalysis data and the adoption of a new simple method for selecting case studies of extreme precipitation that is based on statistical percentiles in time and space. Most recent works on extreme precipitation events are based on monthly-to-seasonal accumulated precipitation and strive to unravel the intra-seasonal dynamical aspects of such events while this work investigated the distinct extreme daily precipitation extremes. The recent works of Kilavi et al. (2018) for example investigated extreme rainfall and flooding over central Kenya in terms of causes and forecasting by looking into MJO and tropical cyclones over the Indian Ocean. This study has complemented such works by looking at an extended array of dynamical aspects which included a variety of tropical waves, synoptic scale flow and thermodynamic instabilities. The study has also attempted to demonstrate the propagation of these convective systems including, where possible, their vertical extents using a variety of overpasses from CALIPSO/CloudSat, the hydrometeors using microwave data and vertical soundings of the atmosphere using both surface and reanalysed data. The use of the CLAAS product that characterises cloud types is a new attempt over the region which this study has used to examine deep convective clouds. Representation of extreme precipitation in the convection-permitting ICON model, though with negative results, has also been attempted for the first time. Some of the potential benefits of using a convective-permitting numerical models are elucidated in e.g. Finney et al. (2019) and Woodhams et al. (2018) and summarised in section 3.10.

The novel approach to use a method that first and foremost, separates contiguous extreme rainfall regimes from events which are based on single rain-gauges with little regard to remotely sensed data has been shown to be a very promising strategy in identifying case studies over data-scarce regions like Kenya. Within this doctoral work, three case studies were evaluated using the newly introduced ERA5 reanalysis data that promises to be more reliable in reproducing mesoscale events based on its higher spatial and temporal resolution. Indications are that this combination of synoptic and convective-scale diagnosis over Kenya and probably over the tropical region could be an appropriate strategy to determine forcings for heavy precipitation events. It is recommended that further cases be evaluated using a similar methodology to improve the findings about the preconditions of extreme precipitation over Kenya drawn from this work. A future initiative should also be put in place to mount more observational platforms especially upper air platforms that could provide a three-dimensional picture of the atmosphere. This would reinforce data assimilation to greatly improve future forecasts of extreme events as the reanalysis model would be adequately trained to make meaningful forecasts.

The author wishes to clarify that the ICON model inadequacy to reproduce the event was partly due to the model set-up. It is argued that perhaps with a higher quality initial and boundary data, the results could improve. It is therefore left as an open question and perhaps a future endeavor, whether a different ICON model set-up would greatly improve the results.

Appendix A

Rainfall Stations

Table A.1: *A summary of the Kenyan synoptic stations extracted from KASSD and used for the selection of cases between 2014-12-31 and 1998-01-01.*

No	KASSD ID	Name	Lat	Lon	Alt	No	KASSD ID	Name	Lat	Lon	Alt
1	636120	Lodwar	3.12	35.60	515.0	16	637370	Narok	-1.09	35.88	1890.0
2	636190	Moyale	3.52	39.05	1097.0	17	637400	JKIA (Nairobi)	-1.32	36.93	1624.0
3	636410	Marsabit	2.34	38.00	1345.0	18	63740001	Machakos	-1.52	37.26	1646.0
4	636240	Mandera	3.94	41.85	231.0	19	63740004	Thika	-1.04	37.08	1463.0
5	636610	Kitale	1.02	35.00	1875.0	20	637410	Dagoretti (Nairobi)	-1.30	36.76	1798.0
6	636710	Wajir	1.75	40.06	244.0	21	637420	Wilson (Nairobi)	-1.32	36.81	1679.0
7	636860	Eldoret	0.51	35.27	2133.0	22	637660	Makindu	-2.28	37.82	1000.0
8	636870	Kakamega	0.28	34.75	1530.0	23	63766100	KampiYaMawe	-0.18	37.65	-999.0
9	636950	Meru	0.05	37.65	1554.0	24	63717101	OlMaisorFarm	-0.41	36.66	-999.0
10	637080	Kisumu	-0.09	34.77	1146.0	25	637720	Lamu	-2.27	40.90	6.0
11	63708103	KariKiboko	0.21	37.67	999.0	26	637930	Voi	-3.40	38.34	579.0
12	637140	Nakuru	-0.30	36.08	1901.0	27	637990	Malindi	-3.22	40.12	23.0
13	637170	Nyeri	-0.44	36.96	1759.0	28	63799100	Msabaha	-3.27	40.05	91.0
14	637200	Embu	-0.54	37.46	1493.0	29	638200	Mombasa	-4.04	39.67	55.0
15	637230	Garissa	-0.45	39.65	147.0	30	63820100	Mtwapa	-3.94	39.75	200

Table A.2: *Statistical scores between A06 of synoptic gauges over Kenya and TRMM between 1998 and 2014. TRMM A06 is the 9-pixel average surrounding a station.* ***ID*** *is the KASSD identification number for* ***station****,* ***Obs (%)*** *is the percentage of the number of non-missing gauge observations between 1998 and 2014,* ***r****,* ***r^2****,* ***P-Value****,* ***RMSE*** *and* ***BIAS*** *are the linear correlation coefficient, variance explained by correlation, p-value, root mean square error and bias respectively.*

	Station	**ID**	**Obs (%)**	**r**	**r^2**	**P-Value**	**RMSE**	**BIAS**
1	Lodwar	63612	99.44	0.52	0.28	0.00	3.70	-0.48
2	Moyale	63619	99.95	0.55	0.31	0.00	5.15	0.50
3	Mandera	63624	99.28	0.61	0.38	0.00	3.74	-0.17
4	Marsabit	63641	99.47	0.61	0.37	0.00	6.50	0.92
5	Kitale	63661	98.97	0.45	0.20	0.00	7.25	-0.08
6	Wajir	63671	98.47	0.68	0.46	0.00	4.13	-0.05
7	Eldoret	63686	98.97	0.54	0.29	0.00	6.65	-0.80
8	Kakamega	63687	93.94	0.45	0.20	0.00	8.91	0.98
9	Meru	63695	99.29	0.56	0.31	0.00	8.86	1.48
10	Kisumu	63708	99.97	0.49	0.24	0.00	8.27	-0.66
11	Nakuru	63714	99.24	0.46	0.21	0.00	5.88	-0.17
12	Nyeri	63717	98.66	0.40	0.16	0.00	6.90	-0.04
13	Embu	63720	99.90	0.53	0.28	0.00	8.65	0.92
14	Garissa	63723	99.90	0.48	0.23	0.00	4.81	-0.26
15	Narok	63737	99.47	0.56	0.32	0.00	5.27	-0.67
16	Machakos	63740001	99.82	0.59	0.34	0.00	5.91	0.02
17	N.hortic.res. Thika	63740004	95.78	0.57	0.32	0.00	7.24	0.26
18	Jomo Kenyatta Intl	63740	98.47	0.57	0.32	0.00	5.84	-0.23
19	Dagoretti Corner	63741	99.95	0.56	0.31	0.00	7.32	0.61
20	Wilson	63742	98.97	0.55	0.30	0.00	7.48	0.42
21	Makindu	63766	99.97	0.39	0.15	0.00	7.32	-0.27
22	Lamu	63772	99.50	0.64	0.41	0.00	7.85	0.72
23	Voi	63793	99.08	0.53	0.28	0.00	6.44	-0.03
24	Msabaha	63799100	97.71	0.61	0.37	0.00	7.18	0.75
25	Malindi	63799	99.40	0.62	0.39	0.00	7.36	0.73
26	Mtwapa	63820100	99.92	0.59	0.35	0.00	8.56	1.33
27	Mombasa	63820	99.81	0.62	0.39	0.00	6.67	0.45

Appendix B

Selection of Cases

B.1 Selection of Cases

To select cases for investigation in this study, the following steps are carried out and implemented using R Core Team (2018):

i) Assemble both TRMM-B42 and gauge data between 1998–2014.

ii) Calculate A06 for each dataset.

iii) Calculate the 98^{th} percentile from TRMM A06 by considering only pixels which have at least 1 mm of rainfall.

iv) Repeat bullet iii) for gauges but also compute the 80^{th} percentile.

v) For each day in both TRMM and gauge percentile, calculate the exceedance (A06 - percentile).

vi) Create a boolean from bullet v) by assigning 1 to all values above zero and 0 elsewhere.

vii) Sum-up each day's frame (2D matrix) and note its date.

viii) Identify the frames having the highest sum total for both TRMM and gauges and sort them in an alphabetical order.

ix) Consider the first ten frames in bullet viii) and compare the two results from each data set.

x) Select corresponding dates between TRMM and gauge with the highest number of pixels and gauges respectively.

xi) In case of a vast region e.g. the lowlands regions which has localised convection and hence no coherence in-between gauges, use the first date in the sorted TRMM sum-totals.

xii) Based on dates selected from x) and xi) , settle on one ideal case that realistically satisfies the objectives of this work e.g. a date must be within a rainy season.

B.2 Computation of percentile anomalies

Throughout this work, anomalies are computed using R Core Team (2018) as follows:

i) Collect the data containing all years in climatology.

ii) Split the dataset by year.

iii) For each year, select ten dates centered around the the case study event.

iv) Compute the 98^{th} percentile for each hour by splitting the data by hour.

v) Subtract the percentile above from the main file containing all selected timesteps.

Appendix C

Conversions

C.1 Brightness Temperature

The equivalent brightness temperature of a satellite observation, is defined as the temperature of a black body which emits the same amount of radiation as observed.

$$R_{rad} = \frac{\int_{\Delta k_\lambda} \phi_{k_\lambda} R_b(k_\lambda, T_b) dk_\lambda}{\int_\Delta \phi_{k_\lambda} dk_\lambda} \tag{C.1}$$

R_{rad} is the observed radiance in mWm^{-2}sr^{-1}
R_b is the Plank function
T_b is the equivalent brightness temperature (in K)
k_λ is the wavenumber (in cm^{-1})
ϕ is the instrument spectral response.

The relation between the radiance (B) and T for the MSG thermal IR channels is given by the Planck function as follows: (Lensky and Rosenfeld, 2008).

$$B(T) = \frac{C_1 v_c^3}{\exp\left(\frac{C_2 v_c}{aT+b}\right) - 1} \tag{C.2}$$

The brightness temperature (T) in SEVIRI is calculated using the inverse Planck function:

$$T = \frac{\left(\frac{C_2 v_c}{(c_1 v_c^3 + 1)} - b\right)}{a} \tag{C.3}$$

Where:
C_1 = 1.19104 x 10^{-5} mWm^{-2}sr^{-1} (cm^{-1})
C_2 = 1.43877K (cm^{-1})
v_c is the central wave number
a and b are coefficients.

Appendix D

Supplementary plots

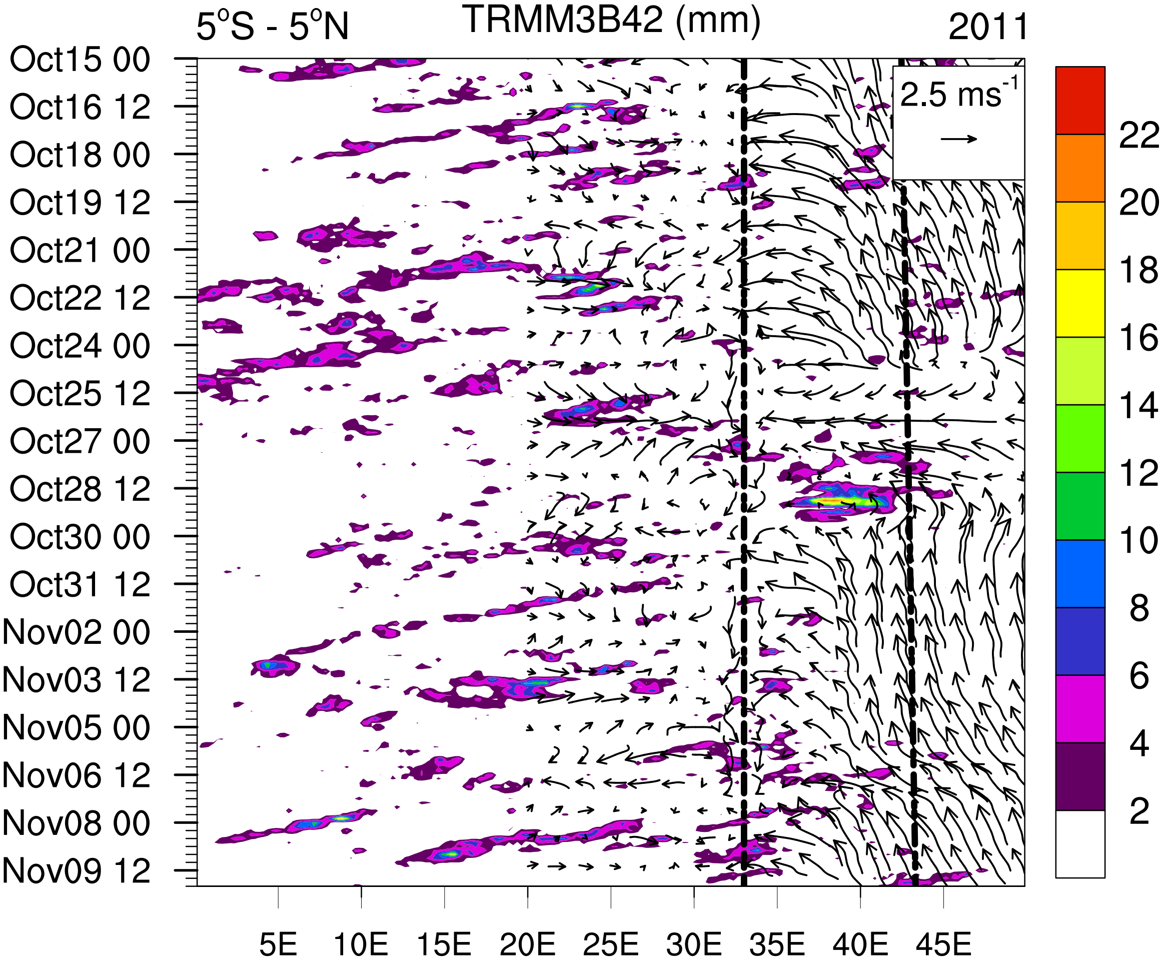

Figure D.1: *A hovmöller diagram of TRMM-3B42 (contours) and ERA5 winds at 100 meter height on a 3-hourly basis averaged between 5°S–5°N*

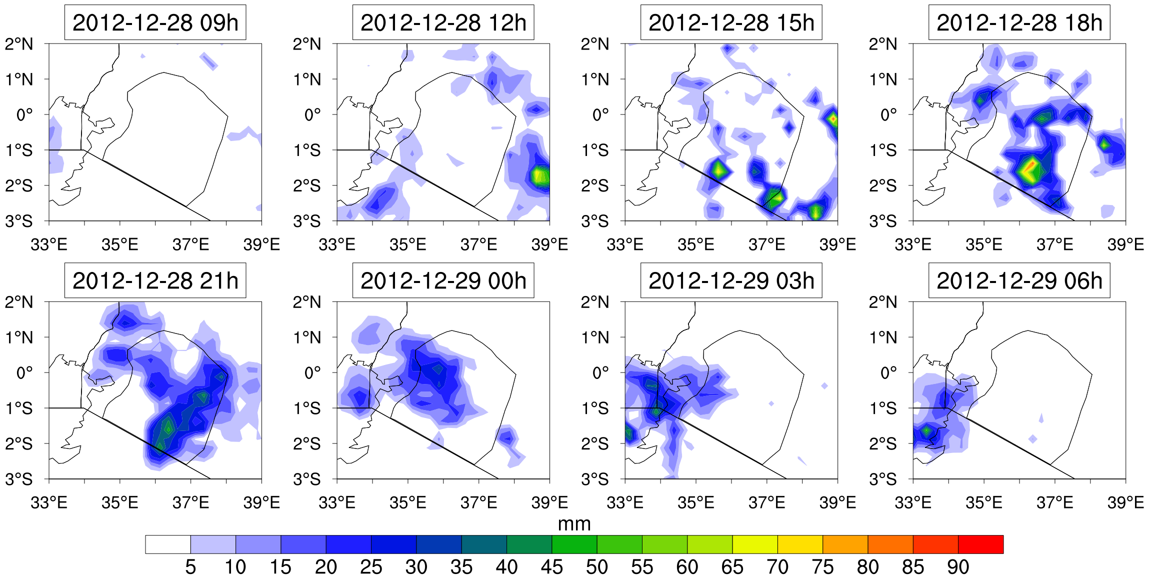

Figure D.2: *Three hourly evolution of TRMM precipitation (in mm) within the time window summing up to A06 during the extreme and contiguous event of 29 Dec 2012 over the central region.*

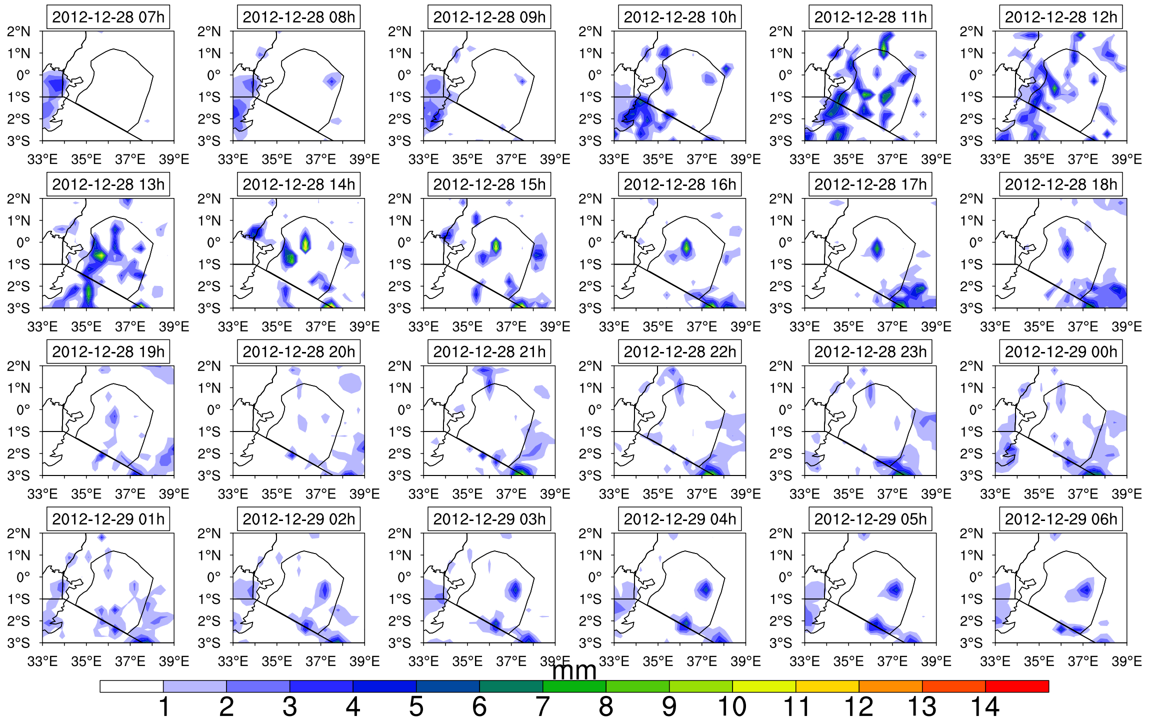

Figure D.3: *Hourly evolution of ERA5 precipitation (in mm) within the time window summing up to A06 during the extreme and contiguous event of 29 Dec 2012 over the central region.*

Bibliography

Anyah, R. O. and Semazzi, F. H. M. (2007). Variability of East African rainfall based on multiyear Regcm3 simulations. *International Journal of Climatology*, 27(3):357–371.

Anyah, R. O., Semazzi, F. H. M., and Xie, L. (2006). Simulated Physical Mechanisms Associated with Climate Variability over Lake Victoria Basin in East Africa. *Monthly Weather Review*, 134(12):3588–3609.

Asnani, G. and Kinuthia, J. (1979). Diurnal variation of precipitation in East Africa. , Research Report No. 8/79, 1–58. *Kenya Meteorological Department, Research Report*, 64A(8/79):1–58.

Azarian, T., Grant, L. R., Arnold, B. J., Hammitt, L. L., Reid, R., Santosham, M., Weatherholtz, R., Goklish, N., Thompson, C. M., Bentley, S. D., O'Brien, K. L., Hanage, W. P., and Lipsitch, M. (2018). The impact of serotype-specific vaccination on phylodynamic parameters of Streptococcus pneumoniae and the pneumococcal pan-genome. *PLOS Pathogens*, 14(4):1–25.

Bärring, L. (1988). Regionalization of daily rainfall in Kenya by means of common factor anlaysis. *Int. J. Climatol*, 8:371–389.

Basalirwa, C. P. K. (1995). Delineation of Uganda into climatological rainfall zones using the method of principal component analysis. *International Journal of Climatology*, 15(10):1161–1177.

Bechtold, P., Köhler, M., Jung, T., Doblas-Reyes, F., Leutbecher, M., Rodwell, M. J., Vitart, F., and Balsamo, G. (2008). Advances in simulating atmospheric variability with the ECMWF model: From synoptic to decadal time-scales. *Quarterly Journal of the Royal Meteorological Society*, 134(634):1337–1351.

Benas, N., Finkensieper, S., Stengel, M., van Zadelhoff, G.-J., Hanschmann, T., Hollmann, R., and Meirink, J. F. (2017). The MSG-SEVIRI-based cloud property data record CLAAS-2. *Earth System Science Data*, 9(2):415–434.

Berhane, F. and Zaitchik, B. (2014). Modulation of Daily Precipitation over East Africa by the Madden–Julian Oscillation. *Journal of Climate*, 27(15):6016–6034.

Bhat, G., Srinivasan, J., and Gadgil, S. (1996). Tropical Deep Convection, Convective Available Potential Energy and Sea Surface Temperature. *Journal of the Meteorological Society of Japan. Ser. II*, 74(2):155–166.

Bieli, M., Pfahl, S., and Wernli, H. (2015). A Lagrangian investigation of hot and cold temperature extremes in Europe. *Quarterly Journal of the Royal Meteorological Society*, 141(686):98–108.

Black, E., Slingo, J., and Sperber, K. R. (2003). An Observational Study of the Relationship between Excessively Strong Short Rains in Coastal East Africa and Indian Ocean SST. *Monthly Weather Review*, 131(1):74–94.

Bolton, D. (1980). The Computation of Equivalent Potential Temperature. *Monthly Weather Review*, 108(7):1046–1053.

Bowden, J. H. and Semazzi, F. H. M. (2007). Empirical Analysis of Intraseasonal Climate Variability over the Greater Horn of Africa. *Journal of Climate*, 20(23):5715–5731.

Camberlin, P. and Philippon, N. (2002). The East African March–May Rainy Season: Associated Atmospheric Dynamics and Predictability over the 1968–97 Period. *Journal of Climate*, 15(9):1002–1019.

Chen, C.-J. and Georgakakos, A. P. (2015). Seasonal prediction of East African rainfall. *International Journal of Climatology*, 35(10):2698–2723.

Climate Prediction Center, National Centers for Environmental Prediction, N. W. S. N. U. D. o. C. (2011). NOAA CPC Morphing Technique (CMORPH) Global Precipitation Analyses.

Cook, B. I. and Seager, R. (2013). The response of the North American Monsoon to increased greenhouse gas forcing. *Journal of Geophysical Research: Atmospheres*, 118(4):1690–1699.

D'Abreton, P. and Tyson, P. (1996). Three-dimensional kinematic trajectory modelling of water vapour transport over Southern Africa. *Water SA*, 22(4):297–306.

Doms, G. and Schättler (2004). A description of the nonhydrostatic regional model LM. Part II: Physical parameterization. *Technical report, Deutscher Wetterdienst, Offenbach, Germany. (available from http://www.cosmo-model.org/public/documentation.htm.*

Doswell, C. A., Brooks, H. E., and Maddox, R. A. (1996). Flash Flood Forecasting: An Ingredients-Based Methodology. *Weather and Forecasting*, 11(4):560–581.

Doswell, C. A., Ramis, C., Romero, R., and Alonso, S. (1998). A Diagnostic Study of Three Heavy Precipitation Episodes in the Western Mediterranean Region. *Weather and Forecasting*, 13(1):102–124.

Dyer, T. G. J. (1977). The assignment of rainfall stations into homogeneous groups: An application of principal component analysis. *Q. J. R. Meteorol. Soc*, 101:1005–1013.

Emanuel, K. (1993). The Effect of Convective Response Time on WISHE Modes. *Journal of the Atmospheric Sciences*, 50(12):1763–1776.

Emanuel, K. A. (1987). An Air-Sea Interaction Model of Intraseasonal Oscillations in the Tropics. *Journal of the Atmospheric Sciences*, 44(16):2324–2340.

Emanuel, K. A., David Neelin, J., and Bretherton, C. S. (1994). On large-scale circulations in convecting atmospheres. *Quarterly Journal of the Royal Meteorological Society*, 120(519):1111–1143.

Endris, H. S., Omondi, P., Jain, S., Lennard, C., Hewitson, B., Chang'a, L., Awange, J. L., Dosio, A., Ketiem, P., Nikulin, G., Panitz, H.-J., Büchner, M., Stordal, F., and Tazalika, L. (2013). Assessment of the Performance of CORDEX Regional Climate Models in Simulating East African Rainfall. *Journal of Climate*, 26(21):8453–8475.

Engel, T., Fink, A. H., Knippertz, P., Pante, G., and Bliefernicht, J. (2017). Extreme Precipitation in the West African Cities of Dakar and Ouagadougou: Atmospheric Dynamics and Implications for Flood Risk Assessments. *Journal of Hydrometeorology*, 18(11):2937–2957.

Feidas, H. and Giannakos, A. (2012). Classifying convective and stratiform rain using multispectral infrared Meteosat Second Generation satellite data. *Theoretical and Applied Climatology*, 108(3):613–630.

FEWSNET (2011). East Africa: Past year one of the driest on record in the eastern Horn June 14, 2011.

Fink, A., Emert, V., Linden, R., Pinto, G. Seregina, L., and Njeri, K. (2018). Daily Rainfall Modulation of the Long and Short Rains in East Africa By the Madden Julian Oscillation and Convectively Coupled Equatorial Waves. Presented at the 33rd Conference on Hurricanes and Tropical Meteorology: African Weather and Climate 1.

Finney, D. L., Marsham, J. H., Jackson, L. S., Kendon, E. J., Rowell, D. P., Boorman, P. M., Keane, R. J., Stratton, R. A., and Senior, C. A. (2019). Implications of Improved Representation of Convection for the East Africa Water Budget Using a Convection-Permitting Model. *Journal of Climate*, 32(7):2109–2129.

Flohn, H. and Burkhardt, T. (1985). Nile run-off at Aswan and Lake Victoria: A case of discontinuous climate time series. *Z. Gletscherk. Glazialgeol*, 21:125–130.

Forsdyke, A. (1944). Synoptic analysis in the western Indian Ocean. *East Af. Met. Dept. Memoirs*, II(3).

Fraedrich, K. (1972). A simple climatological model of the dynamics and energetics of the nocturnal circulation at Lake Victoria. *Quarterly Journal of the Royal Meteorological Society*, 98(416):322–335.

Gitau, W., Ogallo, L., Camberlin, P., and Okoola, R. E. (2013). Spatial coherence and potential predictability assessment of intraseasonal statistics of wet and dry spells over Equatorial Eastern Africa. *Int. J. Climatol*, 33:2690–2705.

Grabowski, W. W. and Moncrieff, M. W. (2004). Moisture–convection feedback in the tropics. *Quarterly Journal of the Royal Meteorological Society*, 130(604):3081–3104.

Gruber, A. (1974). The Wavenumber-Frequency Spectra of Satellite-Measured Brightness in the Tropics. *Journal of the Atmospheric Sciences*, 31(6):1675–1680.

Haddad, Z. S., Smith, E. A., Kummerow, C. D., Iguchi, T., Farrar, M. R., Durden, S. L., Alves, M., and Olson, W. S. (1997). The TRMM "Day-1" Radar/Radiometer Combined Rain-Profiling Algorithm. *Journal of the Meteorological Society of Japan. Ser. II*, 75(4):799–809.

Hastenrath, S. (2000). Zonal Circulations over the Equatorial Indian Ocean. *Journal of Climate*, 13(15):2746–2756.

Hastenrath, S., Polzin, D., and Mutai, C. (2010). Diagnosing the Droughts and Floods in Equatorial East Africa during Boreal Autumn 2005–08. *Journal of Climate*, 23(3):813–817.

Hastenrath, S., Polzin, D., and Mutai, C. (2011). Circulation Mechanisms of Kenya Rainfall Anomalies. *Journal of Climate*, 24(2):404–412.

Heise, E., Ritter, B., and Schrodin, E. (2006). Operational implementation of the multilayer soil model TERRA. *Technical report, Deutscher Wetterdienst, Offenbach, Germany. (available from http://www.cosmo-model.org/public/documentation.htm)*.

Held, I. M. and Soden, B. J. (2006). Robust Responses of the Hydrological Cycle to Global Warming. *Journal of Climate*, 19(21):5686–5699.

Hendon, H. H. and Salby, M. L. (1994). The Life Cycle of the Madden–Julian Oscillation. *Journal of the Atmospheric Sciences*, 51(15):2225–2237.

Hersbach, H. and Dee, D. (2016). ERA-5 reanalysis is in production. *Spring 2016*, (147):7.

Hogan, E., Shelly, A., and Xavier, P. (2015). The observed and modelled influence of the Madden–Julian Oscillation on East African rainfall. *Meteorological Applications*, 22(3):459–469.

Holton, J. R. and Gregory, J. H. (2012). *An Introduction to Dynamic Meteorology*, volume 88. Academic Press, University of Washington, Seattle, WA, USA, 5th edition.

Hong, G., Heygster, G., Miao, J., and Kunzi, K. (2005). Detection of tropical deep convective clouds from AMSU-B water vapor channels measurements. *Journal of Geophysical Research: Atmospheres*, 110(D5).

Houze, R. A., Rasmussen, K. L., Zuluaga, M. D., and Brodzik, S. R. (2015). The variable nature of convection in the tropics and subtropics: A legacy of 16 years of the tropical rainfall measuring mission satellite. *Rev Geophys*, 53(3):994–1021. ROG20083[PII].

Hu, Y., Winker, D., Vaughan, M., Lin, B., Omar, A., Trepte, C., Flittner, D., Yang, P., Nasiri, S. L., Baum, B., Holz, R., Sun, W., Liu, Z., Wang, Z., Young, S., Stamnes, K., Huang, J., and Kuehn, R. (2009). CALIPSO/CALIOP Cloud Phase Discrimination Algorithm. *Journal of Atmospheric and Oceanic Technology*, 26(11):2293–2309.

Im, E., Durden, L., and Wu, C. (2006). Cloud profiling radar for the CloudSat mission. *Proc. 2005 IEEE int. Radar Conf., Arlington, VA, Institute of Electrical and Electronics Engineers*, pages 483–486.

Indeje, M., Semazzi, F. H. M., and Ogallo, L. J. (2000). ENSO signals in East African rainfall seasons. *Int. J. Climatol*, 20(1):19–46.

Ininda, J. M. (1995). *Numerical simulation of the influence of SST anomalies on the East African seasonal rainfall*. Ph.D Thesis. University of Nairobi, Kenya.

Johnson, D. H. (1962). Rain in East Africa. *Quarterly Journal of the Royal Meteorological Society*, 88(375):1–19.

Karanja, F. and Mutua, F. (2000). Reducing the Impacts of Environmental Emergencies Through Early Warning and Preparedness: The Case of El-Ninõ - Southern Oscillation (ENSO), Nairobi: UNFIP, UNEP, NCAR, WMO, IDNDR, UNU. *University of Nairobi*.

Karianjahi, J. N. (2012). *Potential predictability of the March to May rainfall over East Africa using ITCZ indices*. M.Sc Thesis. University of Nairobi, Kenya.

Kidwell, K. B., Goodrum, G., and Winston, W. (2009). NOAA KLM user's guide, with NOAA-N, -N' supplement. Technical report, National Environmental Satellite, Data, and Information Services, Silver Spring, MD.

Kiladis, G. N., Wheeler, M. C., Haertel, P. T., Straub, K. H., and Roundy, P. E. (2009). Convectively coupled equatorial waves. *Reviews of Geophysics*, 47(2).

Kilavi, M., MacLeod, D., Ambani, M., Robbins, J., Dankers, R., Graham, R., Titley, H., Salih, A. A. M., and Todd, M. C. (2018). Extreme Rainfall and Flooding over Central Kenya Including Nairobi City during the Long-Rains Season 2018: Causes, Predictability, and Potential for Early Warning and Actions. *Atmosphere*, 9(12).

Kinuthia, J. H. and Asnani, G. C. (1982). A Newly Found Jet in North Kenya (Turkana Channel). *Monthly Weather Review*, 110(11):1722–1728.

KMD (2013). The outlook for the Mar to May (MAM) 2013 "Long-Rains" season in Kenya and review of the performance of the Oct to Dec (OND) 2012 "short rains" season as well as the weather during Jan to Feb 2013. [Online; seen on Jan-04-2019].

Knippertz, P., Fink, A. H., Deroubaix, A., Morris, E., Tocquer, F., Evans, M. J., Flamant, C., Gaetani, M., Lavaysse, C., Mari, C., Marsham, J. H., Meynadier, R., Affo-Dogo, A., Bahaga, T., Brosse, F., Deetz, K., Guebsi, R., Latifou, I., Maranan, M., Rosenberg, P. D., and Schlueter, A. (2017). A meteorological and chemical overview of the DACCIWA field campaign in West Africa in June–July 2016. *Atmospheric Chemistry and Physics*, 17(17):10893–10918.

Kummerow, C., Barnes, W., Kozu, T., Shiue, J., and Simpson, J. (1998). The Tropical Rainfall Measuring Mission (TRMM) Sensor Package. *Journal of Atmospheric and Oceanic Technology*, 15(3):809–817.

Kutty, G. and Gohil, K. (2017). The role of mid-level vortex in the intensification and weakening of tropical cyclones. *Journal of Earth System Science*, 126(7):94.

Laing, A. G., Carbone, R. E., and Levizzani, V. (2011). Cycles and Propagation of Deep Convection over Equatorial Africa. *Monthly Weather Review*, 139(9):2832–2853.

Latif, M., Dommenget, D., Dima, M., and Grotzner, A. (1999). The role of Indian Ocean sea surface temperature in forcing east African rainfall anomalies during December-January 1997/98. *J.Climate*, 12(12):3497–3504.

Lensky, I. M. and Rosenfeld, D. (2008). Clouds-Aerosols-Precipitation Satellite Analysis Tool (CAPSAT). *Atmospheric Chemistry and Physics*, 8(22):6739–6753.

Lloyd, C. D. (2010). *Spatial Data Analysis: An Introduction for GIS Users*. Oxford University Press".

Lott, F. and Miller, M. J. (1997). A new subgrid-scale orographic drag parametrization: Its formulation and testing. *Quarterly Journal of the Royal Meteorological Society*, 123(537):101–127.

Lyon, B. (2014). Seasonal Drought in the Greater Horn of Africa and Its Recent Increase during the March–May Long Rains. *Journal of Climate*, 27(21):7953–7975.

Lyon, B. and DeWitt, D. G. (2012). A recent and abrupt decline in the East African long rains. *Geophysical Research Letters*, 39(2):n/a–n/a. L02702.

Mace, G. G., Marchand, R., Zhang, Q., and Stephens, G. (2007). Global hydrometeor occurrence as observed by CloudSat: Initial observations from summer 2006. *Geophysical Research Letters*, 34(9):n/a–n/a. L09808.

Mace, G. G., Zhang, Q., Vaughan, M., Marchand, R., Stephens, G., Trepte, C., and Winker, D. (2009). A description of hydrometeor layer occurrence statistics derived from the first year of merged Cloudsat and CALIPSO data. *Journal of Geophysical Research: Atmospheres*, 114(D8):n/a–n/a. D00A26.

Madden, R. and Julian, P. (1971a). Detection of a 40-50 day oscillation in the zonal wind in the tropical Pacific. *J. Atmos. Sci.*, 28(5):702–708.

Madden, R. and Julian, P. (1994a). Observations of the 40-50 day Tropical oscillation–A review. *Mon. Wea. Rev.*, 122(5):814–837.

Madden, R. A. and Julian, P. R. (1971b). Detection of a 40–50 Day Oscillation in the Zonal Wind in the Tropical Pacific. *Journal of the Atmospheric Sciences*, 28(5):702–708.

Madden, R. A. and Julian, P. R. (1972). Description of Global-Scale Circulation Cells in the Tropics with a 40–50 Day Period. *Journal of the Atmospheric Sciences*, 29(6):1109–1123.

Madden, R. A. and Julian, P. R. (1994b). Observations of the 40–50-Day Tropical Oscillation—A Review. *Monthly Weather Review*, 122(5):814–837.

Magnusson, L., Bidlot, J.-R., Bonavita, M., Brown, A., Browne, P., De Chiara, G., Dahoui, M., Lang, S. T. K., McNally, T., Mogensen, K. S., Pappenberger, F., Prates, F., Rabier, F., Richardson, D. S., Vitart, F., and Malardel, S. (2019). ECMWF activities for improved hurricane forecasts. *Bulletin of the American Meteorological Society*, 0(0):null.

Marchand, R., Mace, G. G., Ackerman, T., and Stephens, G. (2008). Hydrometeor Detection Using Cloudsat—An Earth-Orbiting 94-GHz Cloud Radar. *Journal of Atmospheric and Oceanic Technology*, 25(4):519–533.

Matsuno, T. (1966). Quasi-Geostrophic Motions in the Equatorial Area. *Journal of the Meteorological Society of Japan. Ser. II*, 44(1):25–43.

McBride, J. L. and Frank, W. M. (1999). Relationships between Stability and Monsoon Convection. *Journal of the Atmospheric Sciences*, 56(1):24–36.

Mekonnen, A. and Rossow, W. B. (2011). The Interaction Between Deep Convection and Easterly Waves over Tropical North Africa: A Weather State Perspective. *Journal of Climate*, 24(16):4276–4294.

Mekonnen, A. and Rossow, W. B. (2018). The Interaction between Deep Convection and Easterly Wave Activity over Africa: Convective Transitions and Mechanisms. *Monthly Weather Review*, 146(6):1945–1961.

Mekonnen, A. and Thorncroft, C. D. (2016). On mechanisms that determine synoptic time scale convection over East Africa. *International Journal of Climatology*, 36(12):4045–4057.

Miltenberger, A. K., Pfahl, S., and Wernli, H. (2013). An online trajectory module (version 1.0) for the nonhydrostatic numerical weather prediction model COSMO. *Geoscientific Model Development*, 6(6):1989–2004.

Mlawer, E. J., Taubman, S. J., Brown, P. D., Iacono, M. J., and Clough, S. A. (1997). Radiative transfer for inhomogeneous atmospheres: RRTM, a validated correlated-k model for the longwave. *Journal of Geophysical Research: Atmospheres*, 102(D14):16663–16682.

Monkam, D. (2002). Convective available potential energy (CAPE) in Northern Africa and tropical Atlantic and study of its connections with rainfall in Central and West Africa during Summer 1985. *Atmospheric Research*, 62(1):125 – 147.

Mörth, H. (1967). Investigations into the Meteorological Aspects of the variations in the level of Lake Victoria. *East African Met. Dept. Memoirs*, (4):1–22.

Mukabana, J. R. and Piekle, R. A. (1996). Investigating the Influence of Synoptic-Scale Monsoonal Winds and Mesoscale Circulations on Diurnal Weather Patterns over Kenya Using a Mesoscale Numerical Model. *Monthly Weather Review*, 124(2):224–244.

Murugavel, P., Pawar, S. D., and Gopalakrishnan, V. (2012). Trends of Convective Available Potential Energy over the Indian region and its effect on rainfall. *International Journal of Climatology*, 32(9):1362–1372.

Mutai, C., Polzin, D., and Hastenrath, S. (2012). Diagnosing Kenya Rainfall in Boreal Autumn: Further Exploration. *Journal of Climate*, 25(12):4323–4329.

Mutai, C. and Ward, M. (2000). East African Rainfall and the Tropical Circulation/Convection on Intraseasonal to Interannual Timescales. *J.Climate*, 13(22):3915–3939.

NCL (2018). *The NCAR Command Language (Version 6.5.0) [Software]. http://dx.doi.org/10.5065/D6WD3XH5*. Boulder, Colorado:.

Neelin, J. D., Held, I. M., and Cook, K. H. (1987). Evaporation-Wind Feedback and Low-Frequency Variability in the Tropical Atmosphere. *Journal of the Atmospheric Sciences*, 44(16):2341–2348.

Ngecu, W. and Mathu, E. (1999). The El-ninõ triggered landslides and their socioeconomic impact on Kenya. *Environmental Geology*, 38(4):227–284.

Nguyen, H. and Duvel, J.-P. (2008). Synoptic Wave Perturbations and Convective Systems over Equatorial Africa. *Journal of Climate*, 21(23):6372–6388.

Nicholson, S. E. (1996). A Review of Climate Dynamics and Climate Variability in Eastern Africa. The Limnology, Climatology and Paleoclimatology of the Eastern African Lakes. *Gordon and Breach: New York*.

Nicholson, S. E. (2016). An analysis of recent rainfall conditions in eastern Africa. *International Journal of Climatology*, 36(1):526–532.

Odada, E. O. and Olago, D. O. (2002). *The East African Great Lakes: Limnology, Palaeolimnology and Biodiversity*, chapter Extreme Rainfall Events and Lake Level Changes in East Africa: Recent Events and Historical Prec edents, pages 63–92. Springer Netherlands, Dordrecht.

Odingo, R. (1962). The abnormal and unseasonal rains in East Africa. *The Geographical Review*, 52(3):25–37.

Ogallo, L. J. (1988). Relationships between seasonal rainfall in East Africa and the Southern Oscillation. *Journal of Climatology*, 8(1):31–43.

Ogallo, L. J. (1989). The spatial and temporal patterns of the East African Seasonal rainfall derived from the Principal Component Analysis (PCA). *Int. J. Climatol.*, 9(2):145–167.

Okamoto, K. (2003). A Short History of the TRMM Precipitation Radar. *Meteorological Monographs*, 51:187–195.

Okeyo, A. E. (1986). The impact of lake victoria on the convective activities over the kenya highlands. *Journal of the Meteorological Society of Japan. Ser. II*, 64A:689–695.

Okoola, R., Camberlin, P., and Ininda, J. (2008). Wet periods along the East African Coast and the extreme wet spell of October 1997. *J.Kenya Meteorol. Soc.*, 2(1):67–83.

Okoola, R. E. (1999a). A diagnostic study of the Eastern African Monsoon circulation during the northern hemisphere spring season. *Int. J. Climatol*, 19:143–168.

Okoola, R. E. (1999b). Midtropospheric Circulation Patterns Associated with Extreme Dry and Wet Episodes over Equatorial Eastern Africa during the Northern Hemisphere Spring. *Journal of Applied Meteorology*, 38(8):1161–1169.

Orr, A., Bechtold, P., Scinocca, J., Ern, M., and Janiskova, M. (2010). Improved Middle Atmosphere Climate and Forecasts in the ECMWF Model through a Nonorographic Gravity Wave Drag Parameterization. *Journal of Climate*, 23(22):5905–5926.

Owiti, Z., Ogallo, L., and Mutemi, J. (2008). Linkages between the Indian Ocean Dipole and East African Seasonal Rainfall Anomalies. *J.Kenya Meteorol. Soc.*, 2(1):3–17.

Peppler, R. A. and Lamb, P. J. (1989). Tropospheric Static Stability and Central North American Growing Season Rainfall. *Monthly Weather Review*, 117(6):1156–1180.

Pohl, B. and Camberlin, P. (2006a). Influence of the Madden–Julian Oscillation on East African rainfall. I: Intraseasonal variability and regional dependency. *Quarterly Journal of the Royal Meteorological Society*, 132(621):2521–2539.

Pohl, B. and Camberlin, P. (2006b). Influence of the Madden–Julian Oscillation on East African rainfall: II. March–May season extremes and interannual variability. *Quarterly Journal of the Royal Meteorological Society*, 132(621):2541–2558.

Puranik, D. M. and Karekar, R. N. (2004). Classification of Thunderstorms over India Using Multiscale Analysis of AMSU-B Images. *Journal of Applied Meteorology*, 43(4):595–611.

R Core Team (2018). *R: A Language and Environment for Statistical Computing*. R Foundation for Statistical Computing, Vienna, Austria.

Raschendorfer, M. (2001). The new turbulence parameterization of LM.. *COSMO Newsletter 1, 89–97. (available from http://www.cosmo-model.org).*

Redl, R., Fink, A. H., and Knippertz, P. (2015). An Objective Detection Method for Convective Cold Pool Events and Its Application to Northern Africa. *Monthly Weather Review*, 143(12):5055–5072.

Reiff, J., Forbes, G. S., Spieksma, F. T. M., and Reynders, J. J. (1986). African Dust Reaching Northwestern Europe: A Case Study to Verify Trajectory Calculations. *Journal of Climate and Applied Meteorology*, 25(11):1543–1567.

Rempel, M., Senf, F., and Deneke, H. (2017). Object-Based Metrics for Forecast Verification of Convective Development with Geostationary Satellite Data. *Monthly Weather Review*, 145(8):3161–3178.

Reverdin, G., Cadet, D., and Gutzler, D. (1986). Inter-annual displacements of convection and surface circulation over the equatorial Indian Ocean. *Q. J. R. Met. Soc.*, 112(471):43–67.

Riehl, H. (1945). *Waves in the Easterlies and the Polar Front in the Tropics*. University of Chicago Misc. Rep. 17, 79 pp.

Roberts, N. (2008). Assessing the spatial and temporal variation in the skill of precipitation forecasts from an NWP model. *Meteorological Applications*, 15(1):163–169.

Roberts, N. M. and Lean, H. W. (2008). Scale-Selective Verification of Rainfall Accumulations from High-Resolution Forecasts of Convective Events. *Monthly Weather Review*, 136(1):78–97.

Rowell, D., Ininda, J., and Ward, M. (1996). The impacts of global sea surface temperature patterns on seasonal rainfall in East Africa. In *Proceedings International Conference on Monsoon Variability and Prediction, Trieste, Italy*, pages 9–13. WMO/WCRP no.3.

Röhner, L. (2016). *Heavy precipitation events in the Western Mediterranean area: physical Processes and predictability*. Karlsruhe Institute of Technology (KIT) - KIT-Bibliothek, Karlsruhe.

Saji, N., Boswami, B., Vinayachanran, P., and Yamagata, T. (1999). A dipole mode in the tropical Indian Ocean. *Nature*, 401:360–363.

Satti, S., Zaitchik, B. F., Badr, H. S., and Tadesse, T. (2017). Enhancing Dynamical Seasonal Predictions through Objective Regionalization. *Journal of Applied Meteorology and Climatology*, 56(5):1431–1442.

Schemm, S., Nummelin, A., Kvamsto, N. G., and Breivik, O. (2017). The Ocean Version of the Lagrangian Analysis Tool LAGRANTO. *Journal of Atmospheric and Oceanic Technology*, 34(8):1723–1741.

Schlueter, A., Fink, A. H., Knippertz, P., and Vogel, P. (2019). A Systematic Comparison of Tropical Waves over Northern Africa. Part I: Influence on Rainfall. *Journal of Climate*, 32(5):1501–1523.

Schmetz, J., Pili, P., Tjemkes, S., Just, D., Kerkmann, J., Rota, S., and Ratier, A. (2002). An Introduction to METEOSAT Second Generation (MSG). *Bulletin of the American Meteorological Society*, 83(7):977–992.

Schreck, C. J. and Semazzi, F. H. M. (2004). Variability of the recent climate of eastern Africa. *International Journal of Climatology*, 24(6):681–701.

Schumacher, C. and Houze, R. A. (2003). The TRMM Precipitation Radar's View of Shallow, Isolated Rain. *Journal of Applied Meteorology*, 42(10):1519–1524.

Seifert, A. (2008). A revised cloud microphysical parameterization for COSMO-LME. *COSMO Newsletter 8, 25–28. (available from http://www.cosmo-model.org*.

Sinclaire, Z., Lenouo, A., Tchawoua, C., and Janicot, S. (2015). Synoptic Kelvin type perturbation waves over Congo basin over the period 1979–2010. *Journal of Atmospheric and Solar-Terrestrial Physics*, 130-131:43 – 56.

Sobel, A. H., Yuter, S. E., Bretherton, C. S., and Kiladis, G. N. (2004). Large-Scale Meteorology and Deep Convection during TRMM KWAJEX. *Monthly Weather Review*, 132(2):422–444.

Sprenger, M. and Wernli, H. (2015). The LAGRANTO Lagrangian analysis tool - version 2.0. *Geoscientific Model Development*, 8(8):2569–2586.

Stengel, M., Kniffka, A., Meirink, J. F., Lockhoff, M., Tan, J., and Hollmann, R. (2014). CLAAS: The CM-SAF cloud property data set using SEVIRI. *Atmospheric Chemistry and Physics*, 14(8):4297–4311.

Sun, L., Semazzi, F. H. M., Giorgi, F., and Ogallo, L. J. (1999a). Application of the NCAR regional climate model to Eastern Africa. Part I: Simulations of autumn rains of 1988. *J. Geophys. Res.*, 104(D6):6529–6548.

Sun, L., Semazzi, F. H. M., Giorgi, F., and Ogallo, L. J. (1999b). Application of the NCAR regional climate model to Eastern Africa. Part II: Simulations of interannual variability. *J. Geophys. Res.*, 104(D6):6549–6562.

Taylor, K. E., Stouffer, R. J., and Meehl, G. A. (2012). An Overview of CMIP5 and the Experiment Design. *Bulletin of the American Meteorological Society*, 93(4):485–498.

Tobin, I., Bony, S., and Roca, R. (2012). Observational Evidence for Relationships between the Degree of Aggregation of Deep Convection, Water Vapor, Surface Fluxes, and Radiation. *Journal of Climate*, 25(20):6885–6904.

Trenberth, K. E. (1976). Spatial and temporal variations of the Southern Oscillation. *Quarterly Journal of the Royal Meteorological Society*, 102(433):639–653.

Vanden, J. and Bernacsek, G. (1990). *Source Book for the Inland Fishery Resource of Africa*, volume 1, page 291. Food and Agriculture Organization, United Nations.

Wan, H., Giorgetta, M. A., Zängl, G., Restelli, M., Majewski, D., Bonaventura, L., Fröhlich, K., Reinert, D., Rípodas, P., Kornblueh, L., and Förstner, J. (2013). The ICON-1.2 hydrostatic atmospheric dynamical core on triangular grids - Part 1: Formulation and performance of the baseline version. *Geosci Model Dev.*, 6(3):735–763.

Wang, Y., Leung, L. R., McGregor, J. L., Lee, D.-K., Wang, W.-C., Ding, Y., and Kimura, F. (2004). Regional Climate Modeling: Progress, Challenges, and Prospects. *Journal of the Meteorological Society of Japan. Ser. II*, 82(6):1599–1628.

Ward, M. N., Folland, C. K., Maskell, K., Colman, A. W., Rowell, D. P., and Lane, K. B. (1993). Experimental seasonal forecasting of tropical rainfall at the uk meteorological office. In Shukla, J., editor, *Prediction of Interannual Climate Variations*, pages 197–216, Berlin, Heidelberg. Springer Berlin Heidelberg.

Webster, P., Moore, A., Loschnigg, J., and Lebden, R. (1999). Coupled Ocean-Atmosphere Dynamics in the Indian Ocean during 1997-1998. *Nature*, 401:356–360.

Wernli, B. H. and Davies, H. C. (1997). A lagrangian-based analysis of extratropical cyclones. I: The method and some applications. *Quarterly Journal of the Royal Meteorological Society*, 123(538):467–489.

Wernli, H., Paulat, M., Hagen, M., and Frei, C. (2008). SAL—A Novel Quality Measure for the Verification of Quantitative Precipitation Forecasts. *Monthly Weather Review*, 136(11):4470–4487.

Wernli H. and Sprenger M. (2018). LAGRANTO: The Langrangian Analysis Tool. http://iacweb.ethz.ch/staff//sprenger/lagranto//. Accessed: 2018-09-26.

Wheeler, M. and Kiladis, G. N. (1999). Convectively Coupled Equatorial Waves: Analysis of Clouds and Temperature in the Wavenumber–Frequency Domain. *Journal of the Atmospheric Sciences*, 56(3):374–399.

Wheeler, M. C. and Hendon, H. H. (2004). An All-Season Real-Time Multivariate MJO Index: Development of an Index for Monitoring and Prediction. *Monthly Weather Review*, 132(8):1917–1932.

Wilheit, T. (2003). The TRMM Measurement Concept. *Meteorological Monographs*, 51:197–200.

Williams, A. P. and Funk, C. (2011). A westward extension of the warm pool leads to a westward extension of the walker circulation, drying eastern africa. *Climate Dynamics*, 37(11):2417–2435.

Woodhams, B. J., Birch, C. E., Marsham, J. H., Bain, C. L., Roberts, N. M., and Boyd, D. F. A. (2018). What Is the Added Value of a Convection-Permitting Model for Forecasting Extreme Rainfall over Tropical East Africa? *Monthly Weather Review*, 146(9):2757–2780.

Wyrtki, K. (1973). An Equatorial Jet in the Indian Ocean. *Science*, 181(4096):262–264.

Xu, K.-M. and Emanuel, K. A. (1989). Is the Tropical Atmosphere Conditionally Unstable? *Monthly Weather Review*, 117(7):1471–1479.

Yang, W., Seager, R., Cane, M. A., and Lyon, B. (2015). The Annual Cycle of East African Precipitation. *Journal of Climate*, 28(6):2385–2404.

Yano, J.-I., Chaboureau, J.-P., and Guichard, F. (2005). A generalization of CAPE into potential-energy convertibility. *Quarterly Journal of the Royal Meteorological Society*, 131(607):861–875.

Yano, J.-I. and Emanuel, K. (1991). An Improved Model of the Equatorial Troposphere and Its Coupling with the Stratosphere. *Journal of the Atmospheric Sciences*, 48(3):377–389.

Zängl, G., Reinert, D., Rípodas, P., and Baldauf, M. (2015). The ICON (ICOsahedral Non-hydrostatic) modelling framework of DWD and MPI-M: Description of the non-hydrostatic dynamical core. *Quarterly Journal of the Royal Meteorological Society*, 141(687):563–579.

Zhang, G. J. (2002). Convective quasi-equilibrium in midlatitude continental environment and its effect on convective parameterization. *Journal of Geophysical Research-Atmospheres*, 107(D14). n/a.

Zschenderlein, P., Fragkoulidis, G., Fink, A. H., and Wirth, V. (2018). Large-scale Rossby wave and synoptic-scale dynamic analyses of the unusually late 2016 heatwave over Europe. *Weather*, 73(9):275–283.

Acknowledgements

First and foremost, I thank the almighty God for his guidance throughout my four-year doctorate period at the Institute of Meteorology and Climate Research, Karlsruhe Institute of Technology (IMK-KIT) in Germany. Secondly, I thank the DAAD and the Kenyan Government through NACOSTI for providing the funding that made this work feasible. Thanks too to the University of Eldoret, Kenya, for granting the much needed study leave to pursue my doctorate studies away from my station. Heartfelt appreciation to my immediate family and especially to my wife Everline Ogola for her patience through the many days and nights I was away in the four-year period as well as my son, Emmanuel Karianjahi, for the long hours I stayed away from him. I can't forget to thank my supervisor Prof. Andreas H. Fink for his continued guidance and support and for the many suggestions he made to make this work a success. I am also indebted to Prof. Peter Knippertz, the leader of our research group, for his critique and the many suggestions and recommendations he provided towards this work. I am also highly indebted to Dr. Gregor Pante and Dr. Florian Pantillon for their invaluable assistance in setting up of the ICON model for my nested simulations. I can't forget to mention Dr. Philipp Zschenderlein, Dr. Anke Kniffka and Dr. Gregor Pante for reviewing my work and highlighting areas that needed strengthening. To my office-mates and by extension, my fellow PhD colleagues led by Dr. Titike Bahaga and Dr. Marlon Maranan for making the working atmosphere livable through the exchange of code as well as their tantalizing sense of humuor. To the administrative staff led by our director Prof. Dr. Christoph Kottmeier for their academic and non-academic facilitation. The author is finally indebted to the *Open Access* R Core Team (2018) and NCL (2018) for providing the tools necessary for big data manipulation, data analysis and the production of high quality graphics which forms the backbone of this work.